Optimisation of cycle and turbine designs for transcritical cycles of CO_2-based working fluids

Omar Aqel

CITY UNIVERSITY
LONDON

Submitted for the degree of Doctor of Philosophy

City University of London
School of Science and Technology
Department of Mechanical Engineering & Aeronautics

May 2023

This page is left intentionally blank.

Acknowledgement

First and foremost, I would like to thank my supervisors, Professor Abdulnaser Sayma and Dr Martin White, for their invaluable guidance, support, and encouragement throughout my research journey. Their expertise, dedication, and constructive feedback have been instrumental in shaping my ideas and improving the quality of my work. If it weren't for their compassion, my journey would have been much more difficult.

I would also like to extend my heartfelt appreciation to my colleagues and friends who have provided me with their valuable insights and assistance, especially my PhD comrades, Salma and AbdelRahman.

Furthermore, I am grateful to my family for their support, and encouragement. Their constant motivation and understanding have been a source of inspiration for me. Lastly, I would like to express my deepest gratitude and love to my wife, Yara, whose unwavering support, patience, and encouragement have been the driving force behind my success. Her sacrifices, understanding, and love have sustained me during the most challenging times of my research journey, and I am blessed to have her in my life.

Thank you all for your invaluable contributions to my academic and personal growth.

This page is left intentionally blank.

Declaration

I hereby declare that this thesis has not been and will not be submitted in whole or in part to another University for the award of any other degree. I also grant powers of discretion to the University Librarian to allow the thesis to be copied in whole or in part without further reference to the author. This permission covers only single copies made for study purposes, subject to normal conditions of acknowledgement.

Signature:

Omar Aqel

This page is left intentionally blank.

Abstract

Since their inception, CO_2 power cycles have gained prominence for their excellent performance and compactness. Among their benefits, CO_2 power cycles may reduce the levelised cost of electricity (LCoE) of Concentrated Solar Power (CSP) plants. Integrating them into CSP plants may require doping CO_2 with other molecules to adapt the working fluid to dry cooling in locations with a high ambient temperature. The implications of doping CO_2 on the design of the cycle and its components have not yet been fully explored, nor has there been an investigation into its implementation in small- to medium-scale power plants (0.1 – 10 MW). The aim of this thesis is to determine the implications of doping CO_2 on the design of a simple recuperated transcritical cycle and the design of radial inflow turbine for small- to medium-scale CSP plants.

The study focuses on three dopants: $TiCl_4$, SO_2, C_6F_6. First, a thermodynamic model of a transcritical cycle was developed to compare the effect of doping CO_2 with different dopants on the thermal efficiency of the cycle, the recuperator size, the expansion process, and the design of the turbine. The sensitivity of cycle conditions, specifically turbine boundary conditions, to the dopant fractions was also analysed. The maximum achievable cycle efficiencies were found to be 48.1%, 46.5%, and 42.2% for dopant molar fractions of 0.17 of $TiCl_4$, 0.21 of SO_2, and 0.17 of C_6F_6.

The effect of the choice of dopant and its molar fraction on the performance of recompression cycles was also investigated by considering six additional dopants. It was found that the benefit of a recompression cycle diminishes as the aggregate molecular complexity of the working fluid increases. For simple dopants, such as H_2S and SO_2, the recompression cycle will outperform the simple recuperated cycle, regardless of the dopant molar fraction. On the other hand, more complex dopants may achieve thermal efficiencies in simple recuperated cycles that are comparable to a recompression cycle. The dopant molar fraction at which both cycles achieve a similar performances depends on the molecular complexity of the dopant; the more complex the dopant, the lower the molar fraction at which this occurs.

Having established the intrinsic thermodynamic differences between the dopants, the consequences on the design of radial turbines was explored across power scales. This required the development of a mean line model based on experimentally formulated loss equations, which was validated using data from the literature and computational fluid dynamics simulations. Performance estimates from the mean line model were then used to update cycle design in a conjugate optimisation model that

accounts for the achievable turbine performance of the mixtures across scales. This led to the identification of dopant properties that are advantageous to small-scale power plants.

In terms of radial inflow turbine design, variations in the achievable total-to-static efficiency amongst the fluids stem from variations in their clearance-to-blade height ratio, their pressure ratios, rotational speed limits, and, to a lesser degree, differences in their viscosity. Although doping CO_2 has little effect on the aerodynamic behaviour of CO_2, it is the consequence of the change in cycle conditions along with the design limitations of radial inflow turbines that lead to differences in the performance of the turbines amongst the fluids.

Finally, the modelling of binary mixtures requires the intramolecular interactions between the mixture components to be considered, usually through an equation of state supplemented by a binary interaction coefficient. The uncertainty in cycle and turbine designs associated with the choice of the equation of state and its calibration was found to be dependant on the mixture and power capacity. Cubic equations of state showed the most consistency in thermodynamic model results considering the choice and calibration of the fluid model, thus they are recommended for when using thermodynamic models to compare CO_2-based mixtures.

Overall, this thesis successfully identifies the source of the differences between CO_2-based working fluids, in terms of cycle design, turbine design, and modelling uncertainty.

This page is left intentionally blank.

Publications

Part of the work performed during this PhD resulted in peer-reviewed publications, which are listed here.

Journal articles

- **Aqel, O.**, White, M., Sayma, A. (2023), Loss Analysis in Radial Inflow Turbines for Supercritical CO2 Mixtures. ASME Turbo Expo 2023: Turbomachinery Technical Conference and Exposition (recommended for journal publication), scheduled on June 26-30 2023, Boston, Massachusetts, USA.

- **Aqel, O.**, White, M., Khader, M. Sayma, A. (2021), Sensitivity of transcritical cycle and turbine design to dopant fraction in CO2-based working fluids, Applied Thermal Engineering, Volume 190,2021.

Conference papers

- A. AbdElDayem, S. I. Salah, **O. Aqel**, M. T. White, and A. I. Sayma, Design of a 130 MW axial turbine operating with a supercritical carbon dioxide mixture for the SCARABEUS project, In 15th European Turbo-machinery conference, 24-28th April 2023, Budapest, Hungry.

- **Aqel, O.**, Salah, S., Abdeldayem, A., White, M., Sayma, A., 2022. Blended supercritical carbon dioxide turbines: opportunities and challenges. Proceedings of the 14th International Conference on Sustainable Energy and Environmental Protection, Brunel University London, London, UK.

- **Aqel, O.**, White, M., Sayma, A., 2021. Binary interaction uncertainty in the optimisation of a transcritical cycle: consequences on cycle and turbine design. 4th European sCO2 Conference for Energy Systems.

Technical reports

- M. Khader, S. I. Salah, **O. Aqel**, M. T. White, and A. I. Sayma, D3.1 preliminary design of the full-scale axial turbine and pump, tech. rep., SCARABEUS Consortium, May 2020

Contents

List of Figures

List of Tables

Nomenclature

Acronyms

BIP	Binary interaction parameter
BK	Blade blockage
BWRS	Benedict-Webb-Rubin-Starling-Nishiumi
C	Absolute velocity
CFD	Computational fluid dynamics
CR	Concentration ratio
CSP	Concentrated solar power
EoS	Equation of state
HTM	Heat transfer medium
HTR	High-temperature recuperator
IEA	International Energy Agency
IRENA	International Renewable Energy Agency
LCoE	Levelized cost of electricity
LMTD	Log-mean temperature difference
LTR	Low-temperature recuperator
MAE	Mean absolute error
MAPE	Mean absolute percentage error
MITA	Minimum internal temperature approach

ORC	Organic Rankine cycle
PC-SAFT	Perturbed chain statistical associating fluid theory
PCHE	Printed circuit heat exchanger
PHE	Primary heat exchanger
PIT	Pump inlet temperature
PR	Peng-Robinson
PV	Photovoltaic
RANS	Reynolds averaged Navier-Stokes
RIT	Radial inflow turbine
RMS	Root mean square
SPT	Solar power tower
SRK	Soave-Redlich-Kowng
SW	Span-Wanger
TES	Thermal energy storage
TIT	Turbine inlet temperature
VdW	Van der Waal
W	Relative velocity

Greek Symbols

α	Absolute flow angle	deg
β	Relative flow angle	deg
η	Efficiency	%
γ	Adiabatic coefficient	
Λ	Degree of reaction	
λ	Thermal conductivity	$W^1m^{-1}K^{-1}$
μ	Dynamic viscosity	$N^1s^1m^{-2}$

ω	Acentric factor	
ϕ	Flow coefficient	
ψ	Loading coefficient	
ρ	Density	$\mathrm{kg^1m^{-3}}$
σ	Molecular complexity	
σ_{ct}	Centrifugal tensile stress	Pa
σ_{gb}	Gas bending stress	Pa
θ_{c}	Camber angle	
ξ	Meriodnal velocity ratio	

Roman Symbols

ΔT_{m}	Log-mean temperature difference	K
A	Area	$\mathrm{m^2}$
b	Blade height	m
c	Chord length	m
C_{p}	Isobaric specific heat capacity	$\mathrm{JK^{-1}kg^{-1}}$ or $\mathrm{JK^{-1}mol^{-1}}$
C_{v}	Isobaric specific heat capacity	$\mathrm{JK^{-1}kg^{-1}}$ or $\mathrm{JK^{-1}mol^{-1}}$
h	Specific enthalpy	$\mathrm{Jkg^{-1}}$
I	Rothalpy	$\mathrm{Jkg^{-1}}$
k_{ij}	Binary interaction parameter	
m	Mass	kg
N	Rotational speed	RPM
N_{s}	Specific speed	
P	Pressure	Pa
P_{c}	Critical pressure	Pa
P_{r}	Reduced pressure	

Q	Heat load	J
R	Specific gas constant	$\mathrm{Jkg^{-1}}$
r	Radius	m
S	Pitch	m
T	Temperature	K
t	Thickness	m
T_c	Critical temperature	K
T_r	Reduced temperature	
U	Blade velocity	$\mathrm{ms^{-1}}$
U	Overall heat transfer coefficient	$\mathrm{Wm^{-2}K^{-1}}$
V	Volume	$\mathrm{m^3}$
W	Work	J
s	Pitch	
Z	Blade count	

Subscripts

θ	Tangential velocity component
H	Heat source
L	Heat sink
P	Pump
s	Isentropic
sat	Saturation conditions
t	Turbine
h	Rotor hub
le	Leading edge
le	Trailing edge

m	Meridional velocity component
n	Stator (nozzle)
r	Rotor
rel	Relative conditions
sh	Rotor shroud

This page is left intentionally blank.

Chapter 1

Introduction

1.1 CO_2 power cycles

A heat engine, or power cycle, receives heat from a reservoir of arbitrarily high temperature, converts part of this heat to work, and then rejects the waste heat to another reservoir of lower temperature. The process is cyclic and uses a fluid as the energy carrier. In its most basic form, a heat engine involves four processes, each of which commonly employs a specialised equipment.

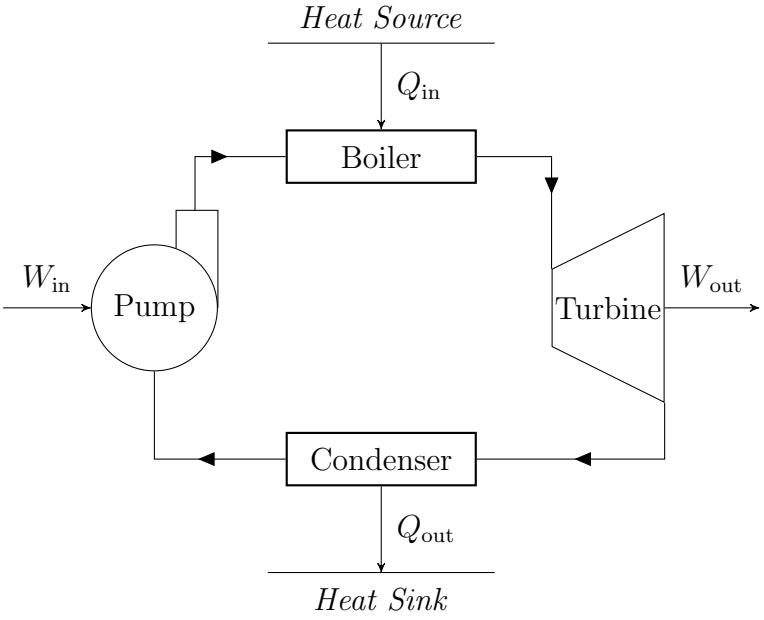

Figure 1.1: Schematic of a basic steam power plant

For example, in a simple steam power plant:

- Heat (Q_{in}) is transferred from the heat source to the steam in the boiler.
- The steam expands in the turbine to produce work (W_{out}).
- A condenser cools the steam and rejects the waste heat (Q_{out}) to a energy sink, such as the atmosphere.
- A pump consumes work (W_{out}) to compress water to boiler pressure.

The net work output from this power plant is the difference between the output and input work, or between the consumed and wasted heat.

$$W_{\text{net}} = W_{\text{out}} - W_{\text{in}} = Q_{\text{in}} - Q_{\text{out}} \tag{1.1}$$

Depending on the critical temperature of a working fluid relative to the heat source and sink temperatures, a heat engine can be operated under four main cycle variations, as seen in Figure 1.2. If both heat rejection and addition occur below the critical pressure, then the cycle is subcritical. Such cycles can either be a Rankine cycle, with condensation, or a Brayton cycle, without condensation. If heat rejection occurs below the critical pressure, but heat addition above it, then the cycle is said to be transcritical (sometimes dubbed as supercritical Rankine cycle). Finally, if both heat rejection and addition occur above the critical pressure then the cycle is supercritical (normally referred to as the supercritical Brayton cycle).

Condensing Rankine cycles often adopt water or organic compounds as their working fluids. Most coal power plants with high heat source temperatures operate on steam Rankine cycles, while applications with lower grade heat sources such as geothermal or waste heat utilize organic Rankine cycles (ORC). Open loop Brayton cycles, on the other hand, are mostly employed in gas power plants or jet engines where the working fluid is predominantly composed of air.

CO_2 has been considered as a working fluid in heat engines because it is abundant, cheap, non-toxic, and non-flammable (Feher 1968). The versatility of sCO_2 cycles is made possible by the low critical temperature of CO_2 (31.1 °C) which allows for compression near ambient conditions. Moreover, sCO_2 cycles benefit from a good

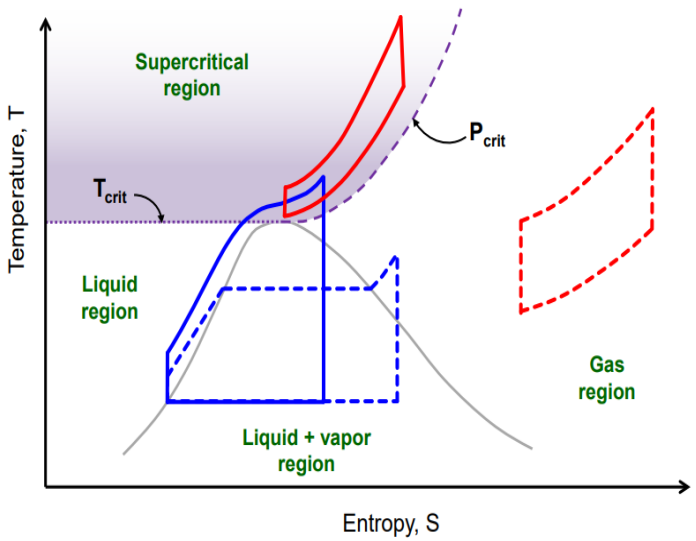

Rankine cycle
Brayton cycle
Transcritical cycle
Supercritical cycle

Heat addition	Heat rejection	Type of cycle
Below Pc	Below Pc	Subcritical
Above Pc	Below Pc	Transcritical
Above Pc	Above Pc	Supercritical

Figure 1.2: Differentiation between power cycles. From (Musgrove et al. 2016)

temperature profile match during both heat addition and rejection. By taking advantage of the fluid properties near the critical point, sCO_2 cycles are able to achieve comparatively high-power conversion efficiencies. Because the working fluid can be compressed without much rise in its temperature, a lower compression work and a higher efficiency are achievable. Moreover, the density of sCO_2 remains comparatively high at turbine inlet, which translates to a lower volume flow rate and smaller turbomachinery. The compactness of the turbine leads to a smaller plant footprint and lower plant cost compared to steam or gas power stations. With low volume flow rates, the size of the pipework ad heat exchangers are also reduced.

sCO_2 cycles operate with a supercritical fluid throughout the cycle. A supercritical fluid behaves as a dense gas phase but is neither a liquid nor a gas. Compared to the liquid state, a supercritical fluid has a higher diffusion coefficient and a lower viscosity. While compared to the gas state, it has a high thermal conductivity, high specific heat capacity, and high thermal diffusivity. These properties enable efficient heat and mass transfer compared to the liquid and gas states (Smith et al. 2013).

Although operating near the critical point increases the power cycle's efficiency, it is not without its challanges. As seen in Figure 1.3, CO_2 exhibits drastic variations in its thermodynamic and transport properties such as density, viscosity, speed of sound, and thermal conductivity near the critical region. Therefore, equipment operating

near the critical region, such as compressors or heat exchangers, are especially vulnerable to slight variations in temperature or pressure. Properties like density, the speed of sound, and viscosity affect the flow velocities, Mach number, and Reynolds number, which influence turbomachinery performance. Likewise, thermal conductivity alters the heat transfer coefficient in heat exchangers. The sensitivity to fluctuations in pressure and temperature means that the off-design performance of such equipment deteriorates as they operation approaches the critical region.

At temperatures below 120 °C the isobaric specific heat of CO_2 in the high-pressure side is considerably higher than that in the low-pressure side (Kim et al. 2012). Therefore, the cycle is subject to irreversibilities in the recuperator where heat from the low-pressure high-temperature fluid is recuperated, which effectively limit the cycle's maximum achievable efficiency. As will be seen in Section 2.2, modification of cycle architecture can alleviate the recuperator irreversibility.

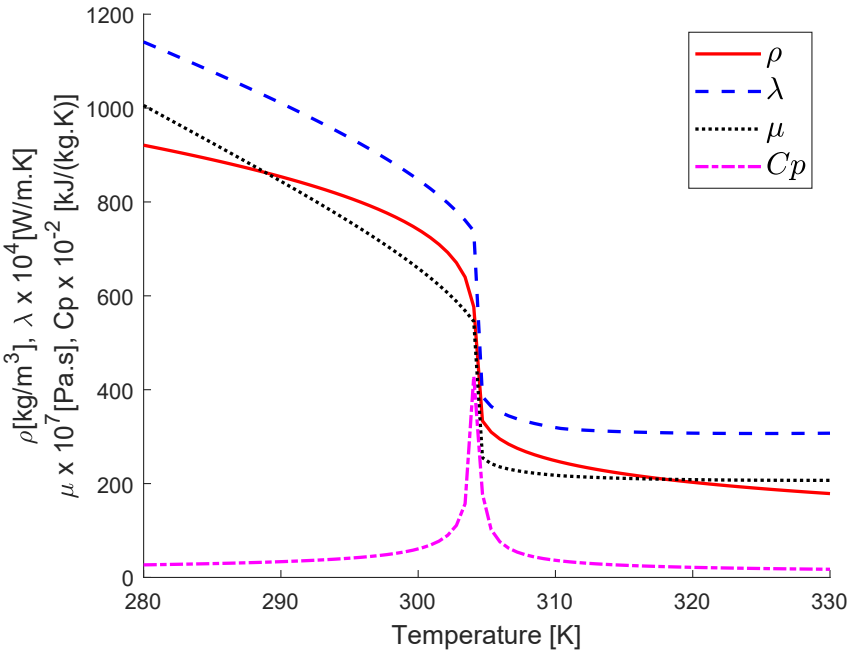

Figure 1.3: Properties of CO_2 near the critical region

In its simplest form, a sCO_2 power cycle consists of a compressor, heater, turbine, and cooler. But because of the low pressure ratios that are typical of these cycles which lead to elevated turbine outlet temperatures, and because of the large irreversibilities in heat recuperation, various modifications of the cycle have been

proposed which are explorerd in Chapter 2.

sCO_2 Brayton cycles have been studied for a variety of heat sources with a wide range of turbine inlet temperatures (Ahn, Bae, Kim, Cho, Baik, Lee & Cha 2015). In their review of sCO_2 systems for power generation, White et al. (2021) mapped the expected applications of this technology based on the ranges of heat source temperature and power output, as shown in Figure 1.4.

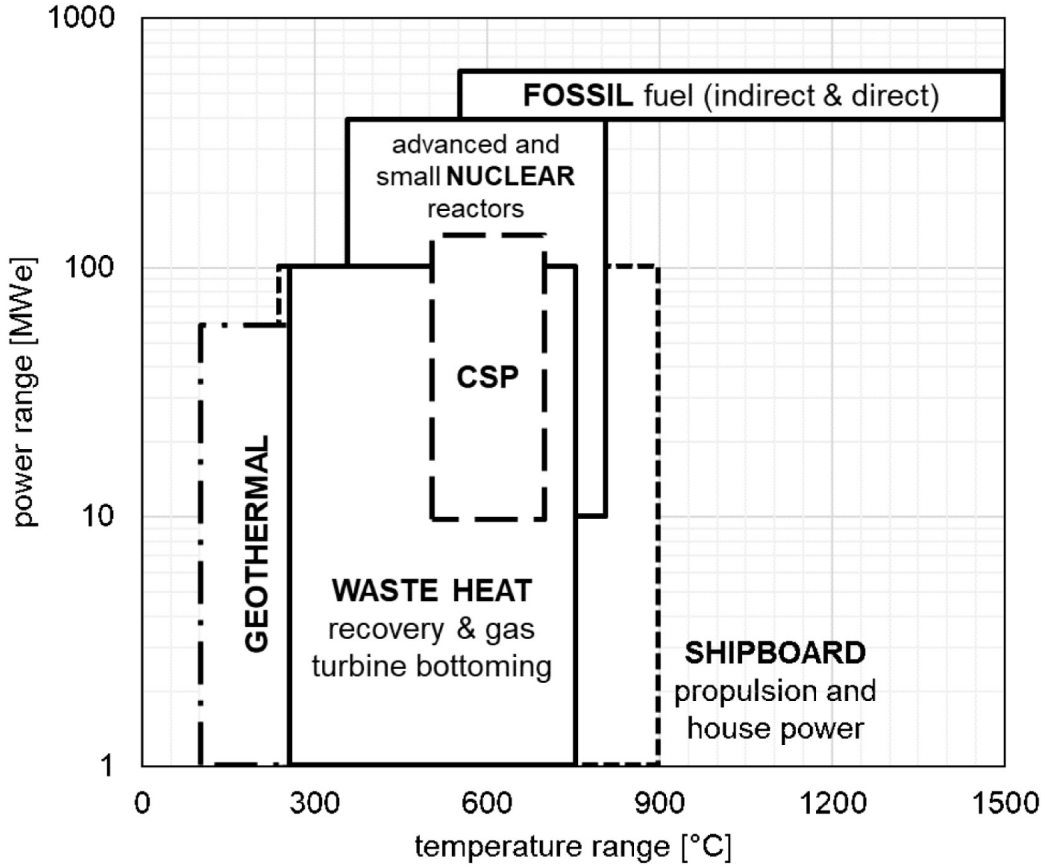

Figure 1.4: Overview of sCO_2 power applications according to White et al. (2021), which was based on data from Mendez & Rochau (2018)

1.2 The sun as an energy source

The sun is an unrelenting fusion reactor constantly turning hydrogen into helium. Energy transfer from the sun to Earth takes the form of thermal radiation. Using the Stefan-Boltzmann Law (σT^4), the intensity of the solar radiation of Earth may be estimated.

$$I_o = \frac{r_{Sun}^2 \epsilon \sigma (T_{Sun}^4 - T_{Earth}^4)}{d^2} = 1340\ W/m^2 \tag{1.2}$$

where

- I_{o} – Solar Constant (W/m^2)
- r_{Sun} – Radius of the sun ($\sim 6.95 \times 10^8\ m$)
- ϵ – emissivity of the sun ($\epsilon = 1$ since the sun is considered a black hole)
- σ – Stefan-Boltzman constant ($5.6703 \times 10^{-8}\ W/m^2K^4$)
- T_{Sun} – Average surface temperature of the sun ($\sim 5760\ K$)
- T_{Earth} – Average surface temperature of Earth ($\sim 300\ K$)
- d – Distance between the sun and Earth ($\sim 1.5 \times 10^{11}\ m$)

This is a rough, but fairly accurate, estimate as most recent experimental measurements of the average solar constant have been found to be around 1367 W/m^2. This value varies around the year within a margin of 3.3% depending on Earth's position and orientation relative to the sun (Bhatia 2014). As an estimate, the amount of solar energy reaching the Earth's surface is about 885 million TWh per year, which dwarfs the total global annual electrical energy consumption of 23 thousand TWh (based on estimates by IRENA (2022)).

Due to the nature of the Earth's atmosphere not all of the direct solar radiation penetrates through to reach its surface. The atmosphere provides a shield protecting Earth from harmful radiation and meteors. Knowing that about one ton of atmosphere resides above each square foot of Earth's surface puts this into perspective. Consequently, as direct solar radiation passes through the atmosphere it is absorbed, scattered, and reflected as diffuse radiation.

Direct radiation or "Beam radiation" is defined as radiation that has not experienced scattering in the atmosphere, is directionally fixed, and shadows are formed when it is blocked (Sorensen 2017). Diffuse solar radiation is the radiation which has been scattered by molecules and particles in the Earth's atmosphere. Diffuse radiation has no specific direction as it scatters randomly through the atmosphere. The nature of the radiation available informs the collector technology selection, which will be elaborated on in Section 1.3 of this chapter.

1.3 Harvesting solar power

Solar energy can be utilized directly by photovoltaics or thermal solar conversion systems, or indirectly through solar induced secondary energy sources such as biofuels, fossil fuels, wind, or waves. Directly collected solar radiation can be converted into electricity using Photovoltaic (PV) cells, which convert sunlight into electricity using semi-conductors and the photovoltaic effect. Unlike thermal conversion systems, PV cells do not require the intervention of heat engines or rotating equipment. Thermal conversion, on the other hand, converts the sun's radiation into thermal energy, which is then used to run a power plant. After using collectors to harvest solar heat radiation, thermal solar systems transfer heat to a fluid via conduction, convection, radiation, or a combination of the three. Solar collectors can either be non-concentrating or concentrating. Whereas non-concentrating collectors have the same area for intercepting and absorbing radiation, concentrating collectors have reflecting surfaces to intercept and focus the sun's beam to a smaller receiving area, thereby increasing the radiation flux (Kalogirou 2013).

Table 1.1: Presents a fundamental comparison between the different types of solar collectors (Kalogirou 2003).

Motion	Collector/Reflector Type	Absorber Type	Concentration Ratio (CR)	Indicative temperature (°C)
Stationary	Flat Plate	Flat	1	30-80
	Evacuated Tube		1	50-200
	Compound Parabolic		1-5	60-200
Single Axis Tracking		Tubular	5-15	80-300
	Linear Fresnel		10-40	80-250
	Parabolic trough		15-45	80-300
	Cylindrical trough		10-50	80-300
Two Axis Tracking	Parabolic dish	Point	100-1000	100-500
	Tracking Heliostat field		100-1500	150-2000

As a general rule, higher concentration ratios (CR) achieve higher temperatures, thus higher thermal efficiencies, but at increasing cost and complexity. Therefore, selection of a solar collector is largely dependent on the application in question. For applications requiring relatively low temperature such as domestic water heating, air heating, or crop drying, a flat plate collector is most convenient. This is because flat plate collectors can deliver sufficient heat for bulk quantities of air or water. However,

due to their lower temperatures, non-concentrating collectors (CR = 1) have lower heat engine efficiencies.

The theoretical efficiency of a heat engine increases with the temperature of the heat source for a fixed heat sink temperature, as described by the Carnot efficiency:

$$\eta_{\text{Carnot}} = 1 - \frac{T_{\text{L}}}{T_{\text{H}}} \tag{1.3}$$

where T_{L} and T_{H} are the heat sink and heat source temperatures, respectively. Therefore, concentration of solar energy (CR >1) will increase the heat source temperature, and with it the heat engine's Carnot efficiency. As shown in Table 1.1, Heliostat Field Collectors (Solar Power Towers) can deliver the highest concentration ratios and temperatures among all available technologies, thus show potential for efficient electricity generation. It should also be noted that the maximum temperature is also dependent on the heat extraction rate as well.

A solar power tower (SPT) system (also known as “central receiver” or “heliostat” power plant) is a form of CSP that consists of an array of tracking mirrors, or heliostats, spaced in a field to reflect and focus incident direct-beam sunlight onto an elevated heat exchanger (or receiver) (Alvin F. Hildebrandt 1977). The receiver sits on top of a tower at the centre of the field and is designed to effectively intercept the concentrated sunlight and absorb it as high-temperature heat. This energy is collected by a heat transfer medium (HTM) which is directed in a closed loop among the receiver, storage, and power conversion system. A thermal energy storage (TES) system typically stores the collected energy as sensible heat for later delivery to the power conversion system, as shown in Figure 1.5. It also decouples the collection of solar energy from its conversion to electricity, which allows the plant to maintain design point operation during solar transients and improves its electrical energy dispatchability.

The optical design and optimisation of solar tower systems are somewhat complicated by the multitude of variables one must consider and the continuous variation in configuration and performance of each of the heliostats as they track the sun and

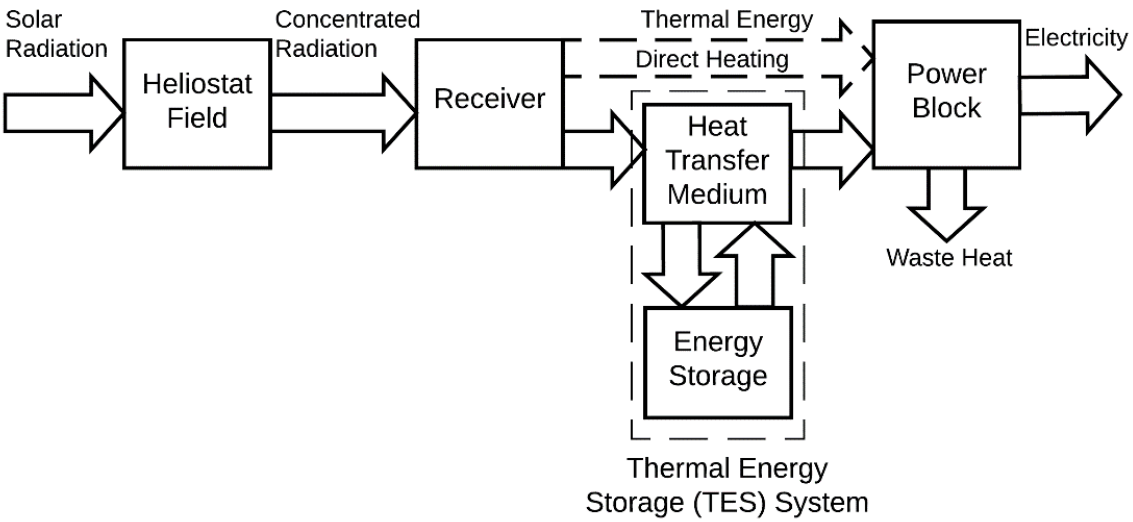

Figure 1.5: Schematic representation of the component parts of a solar power tower

interact with one another (Stein & Wes 2012). However, SPT systems offer many advantages because (Kalogirou 2013):

1. They collect solar energy and transfer it to a single receiver, thus minimizing thermal energy transport requirements
2. They typically achieve concentration ratios of 300 to 1500 and so are highly efficient, both in collecting energy and in converting it to electricity.
3. They can conveniently store thermal energy.
4. They are suitable for utility-scale power generation (generally more than 10 MWe) and thus benefit from economies of scale.

The efficient collection, high concentration, and high temperature of collected heat render SPT compatible with power cycles that operate at elevated temperatures. Traditionally, SPT plants are coupled with steam power plants. However, CO_2 cycles have been identified as a possible solution that can make CSP more competitive with traditional power sources such fossil fuelled power plants (Osorio et al. 2016, Cerio Vera 2015, Neises & Turchi 2014, Polimeni et al. 2018, Wang et al. 2017, Al-Sulaiman & Atif 2015, Feher 1968, Ahn, Bae, Kim, Cho, Baik, Lee & Cha 2015, Smith et al. 2013, Cayer et al. 2009, Yamaguchi et al. 2006). It does so by increasing the power block efficiency whilst decreasing its complexity and size, thus lowering its capital cost. Review of literature studying CO_2 cycle adaptations for CSP will be

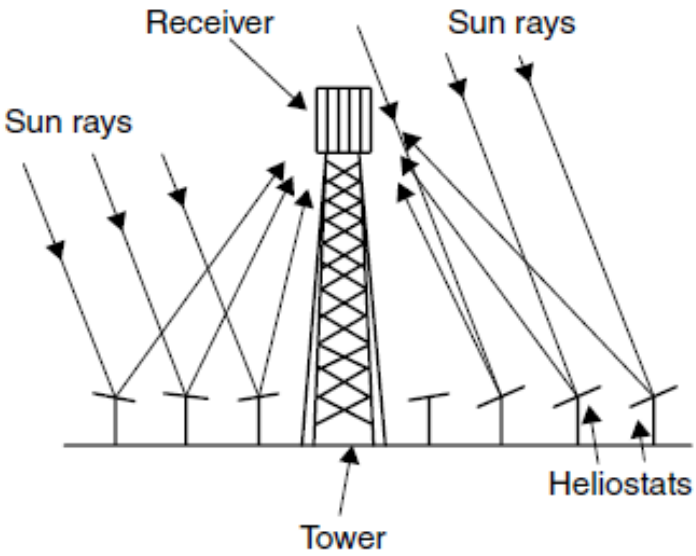

Figure 1.6: Schematic of fundamental SPT layout (Kalogirou 2013)

investigated, but first, a glance at CO_2 power cycle fundamentals and history is in order. However, as will be explained next, a few challenges must be addressed before the adoption of sCO_2 cycles in CSP plants.

1.4 Motivation

Recent studies of sustainable power generation by international agencies such as the International Renewable Energy Agency (IRENA 2022) and the International Energy Agency (IEA 2022) point towards the need for a diverse global energy portfolio that encompasses a variety of energy resources, while de-carbonising the power generation system. They agree that there cannot be a single solution to meet the ever growing global electrical energy demand. Fortunately, there is an abundance of renewable energies which are practically inexhaustible and are proven to be sufficient to provide sustainable electricity for future generations. Amongst the line-up, solar energy is the most abundant and ubiquitous, therefore it has enjoyed the focus of many research and commercial endeavours over the years.

Thermomechanical energy transformation systems like heat engines are expected to play a pivotal role in future energy sustainability. Heat engines employing steam, air, or organic compounds have allowed the utilization of a variety of high and low temperature energy sources such as fossil fuels, geothermal, and waste heat recovery.

Owing to their high thermal performance and compactness, heat engines employing carbon dioxide (CO_2) may enhance solar to electrical energy conversion systems and reduced their Levelized Cost of Electricity (LCoE).

CO_2 power cycles were first explored during the mid-20^{th} century. Since then, research has progressed towards adapting them to different energy sources; but their domain of application remains in the range of 350 to 800 °C (White et al. 2021). The most common adaptation is cycle layout modification. Numerous cycles have been studied for applications within a concentrated solar power (CSP) plant. Because of its excellent performance and simplicity, the condensing transcritical cycle (tCO_2) is one of the most promising cycle layouts (Crespi et al. 2017). However, the relatively low critical temperature of CO_2 (31.1 °C) inhibits the use of condensing cycles in dry-cooled CSP plants, since they are usually located in warm arid climates where cooling water is not a commercially feasible option.

Another more recently proposed adaptation is doping CO_2 to create a binary mixture working fluid tailored towards a specific application. Firstly, a distinction must be made between a CO_2 mixture and its dopant. The latter is any chemical additive that is added to CO_2 to produce the former. For instance, a mixture of $CO_2/TiCl_4$ consists of CO**2** as its base fluid and $TiCl_4$ as the dopant. The addition of dopants of higher critical temperature can increase the working fluid's critical temperature to above 50 °C, thus allowing the use of condensing cycles in hot dry climates. Effective implementation of this technology requires an understanding of the effect of doping CO_2 on power cycle and equipment design.

This PhD thesis is part of the Supercritical CARbon dioxide/Alternative fluids Blends for Efficiency Upgrade of Solar power plants (SCARABEUS) project. SCARABEUS is a research endeavour by a consortium of European institutes which aims to identify ways of reducing the capital and operating costs of CSP technology through an innovative power cycle based on CO_2 blends. Although the SCARABEUS project is mainly concerned with utility-scale power plants ($> 100MW_e$), this thesis will investigate if the use of CO_2 will benefit small-scale power plants.

For the purpose of this thesis, small- to medium-scale is defined as power plants with electrical power output ratings from 0.1 MWe to 10 MWe. From biomass combustion, to industrial waste-heat recovery, to concentrated solar power, small- to medium-scale power plants provide modular electrical power generation solutions to a variety of consumer needs. They are key to the establishment of power generation islands and distributed grid networks, which promote electrical power accessibility and affordability. Doping of CO_2 is one of the ways through which the working fluid may be engineered to match different applications. Therefore, although the main focus of this thesis will be small-scale CSP plants, this study contributes to the knowledge of small- to medium-scale power plants operating with CO_2-based working fluids in other applications as well.

1.5 Knowledge gap and novelty

Even though there has been substantial prior research into Supercritical CO_2 (sCO_2) power cycles, the area of CO_2-based mixtures has not been exhaustively explored. It remains to be seen how doping CO_2 will affect the design of the cycle and its components. Research into CO_2-based mixtures has shown that dopants have a non-trivial effect on cycle behaviour, namely on the cooling temperature and on the irreversibility in the recuperation process. Although complex cycle layouts are often implemented to increase thermodynamic performance, the choice of best cycle layout has been shown to depend on the CO_2 mixture employed (Khatoon & Kim 2019). Therefore, the cycle layout for a newly proposed mixture cannot be readily assumed based on available literature. Cycle layout is not the only uncertain design decision, the design space of cycle components such as heat exchangers and turbomachinery for CO_2-based working fluids is also unknown.

Thus far, there has not been an investigation into the design space of radial inflow turbines for CO_2-based mixtures within the range of CSP inlet conditions. Previous attempts at pure CO_2 turbine design have identified key challenges related to aerodynamic loading and losses. The effect of dopants on these parameters and on the turbine design space in general is yet to be determined. Moreover, scaling down

to small scale power plants must account for the effect of plant size and operating conditions on turbine efficiency (Romei et al. 2020), rather than erroneously assuming a constant efficiency.

A question open for investigation is: *which mixtures, dopant fractions, and design conditions result in the optimal cycle efficiency for small- to medium-scale CSP plants, whilst enabling a feasible turbine design space in which turbine efficiency can be maintained within challenging operating conditions?*

Generally, the modeling of working fluids requires the use of thermophyscial property estimation equations that account for non-ideal fluid behaviours. The choice of the property model is known to affect the results of thermodynamic cycle modelling. For mixtures, additional mixing rules must be used to capture the interactions between the components of the mixture, which entail the specification of binary interaction parameters. It is expected that, in addition to the uncertainty due to the choice of the property model, the choice of the binary interaction model may also lead to additional uncertainty in the results of the thermodynamic model. The magnitude of this uncertainty and its effect on the cycle and turbine design of CO_2-based working fluids has not yet been quantified.

Overall, the novelty of this work lies in the following:

- The study of dopants as performance enhancers of sCO_2 cycles employing radial inflow turbines across power scales.
- The study of the effect of dopant molecular complexity on the choice of cycle layout.
- The study of the uncertainty in the equation of state on modelling results.

Moreover, the investigation presented in this thesis contributes to the wider field of power cycle design for non-conventional working fluids. A framework for predicting the suitability of an additive for CO_2 power cycles has been developed including turbine performance in small scale installations, power cycle layout complexity, and modelling uncertainty.

1.6 Thesis objectives

Considering the knowledge gap, the overarching aim of this thesis is to determine the feasibility of small- to medium-scale power cycles operating with CO_2-based mixtures. In an attempt to do so, this thesis should also complete the following objectives:

- **Identify the dopant molar fractions which yield the highest efficiency in a transcritical cycle whilst considering the achievable turbine efficiencies across power scales;**
- **Determine the effect of dopant molecular complexity on the choice between simple recuperated and recompression cycles;**
- **Determine the effect of doping CO_2 on the design of radial inflow turbines and on their feasible design space when adapted to a small- to medium-scale power plants;**
- **Quantify the uncertainty in the optimisation of the cycle and turbine design due to the method of thermophysical property calculation.**

Overall, the aim of this work lies in the study of dopants as performance enhancers of sCO_2 cycles employing radial inflow turbines across power scales.

1.7 Thesis outline

This thesis consists of eight chapters, including the present introduction. Chapter 2 provides a literature review of relevant research into concentrated solar power, CO_2 power cycles, CO_2-based mixtures, and CO_2 turbines. Chapter 3 presents the approach to cycle modelling and optimisation, in addition to a sensitivity study to determine the effect of different dopants on cycle and preliminary turbine design.

Chapter 5 introduces the theory of turbomachiney before describing the mean line model used to produce preliminary radial inflow turbine designs. This chapter also presents turbine model validation efforts based on data from the literature and CFD simulations.

Chapter 6 investigates the design space of radial inflow turbines under practical design constraints. The design space is first explored in a parametric study which determines the plausible range of the variables used to design the turbine, such as the flow and loading coefficient, to name a few. Next the optimal designs of radial inflow turbines for three mixtures with three dopants are compared based on their geometry and performance, including loss profiles. This chapter also includes a fluid-agnostic study of loss models to determine their mathematical behaviour and their response to changes in design parameters.

Radial inflow turbines are expected to suffer performance deterioration as their size reduces, which will affect the cycle efficiency. In Chapter 6 the cycle and turbine models are coupled through a conjugate optimisation approach which iterates the cycle optimisation based on the turbine performance estimates from the mean line model. The purpose of the conjugate optimisation is to account for practical limitations on the performance of the radial inflow turbine in small-scale plants and highlight the differential effect across the mixtures studied here.

In Chapter 7, the effects of the choice of the fluid model parameters, namely the equation of state (EoS) and the binary interaction parameter (k_{ij}), are studied. The analysis aims to highlight the uncertainty associated with the modelling of CO_2 mixtures using equations of state, and to quantify the effect of the uncertainty on the consistency of cycle and turbine modelling efforts.

Finally, the conclusion and recommendations for future work are presented in Chapter 8.

Chapter 2

Literature Review

2.1 Introduction

This chapter begins by highlighting the significance of solar power for the security of future energy supplies. It then describes Solar Power Tower (SPT) as a proven application of Concentrated Solar Power (CSP) concepts and the role CO_2 power cycles may play in advancing the technology.

Before delving into the details of CO_2 power cycles in the context of CSP, a brief history of CO_2 power cycles is presented, namely the early works of the 1960's & 1970's which paved the way for later research efforts in the 21^{st} Century. Subsequently, the progress made in three main directions: cycle architecture, CO_2-based working fluids, and turbine design, is reviewed.

Since a cycle's architecture greatly influences its behaviour, the most promising architectures are compared, setting the stage to reveal key design limitations that are inherent to CO_2 power cycles. The novelty of this work lies in the study of the effect of adding dopants to CO_2 on optimal cycle and turbine designs. This direction has not been exhaustively examined yet and remains relatively new. Nonetheless, a few examples and their implications are presented. Lastly, previous attempts at turbine design are examined to identify key challenges that will be heeded in subsequent chapters.

2.2 A brief history of sCO_2 power cycles

The first recorded reference to a sCO_2 heat engine is in a 1948 patent by Sulzer AG in Switzerland. Years later, in the 1960's and 1970's, interest in the prospects of sCO_2 implementation in nuclear power plants was expressed through the independent works of Dekhtiarev in Russia, Angelino in Italy, and Feher in the USA. The subject went out of focus until it was renewed in the early 2000's at Massachusetts Institute of Technology (MIT), Idaho National Laboratory (INL), and Sandia National Laboratories (SNL). Since then, there has been a growth in the amount of research investigating the potential applications of sCO_2 power cycles, in addition to the establishment of multiple testing facilities worldwide. The following are summaries of the most pivotal works in the field.

In the lesser known work of Dekhtiarev (1962), a recuperative tCO_2 cycle with reheat and precompression was designed, which is reintroduced as a "new" cycle in a later work (Purjam et al. 2017). Dekhtyarev's cycle operated between 21 °C / 60 bar and 650 °C / 210 bar as shown in Figure 2.1.

The work presented preliminary condenser, boiler, and turbine designs based on existing industrial equipment. It postulated that plant size will be smaller than an equivalent steam power plant. For instance, the boiler would be 8 to 10 times smaller. Dekhtyarev also introduced intricacies to the cycle by adding an additional recuperator and compressor and splitting the flow to improve recuperation and lower the compressor work, resulting in a 52% theoretical thermal efficiency. This layout was described in later works as the precompression cycle with reheat. Dekhtyarev concluded that sCO_2 cycles may have higher efficiencies and smaller power blocks when compared with contemporary steam power cycles.

Often credited for initiating the interest in sCO_2 cycles, Feher hypothesized that a supercritical cycle would alleviate some of the limitations facing Rankine and Brayton cycles at the time. Such limitations for a Rankine cycle included:

1. Maximum temperature range restrictions that entailed a compromise between

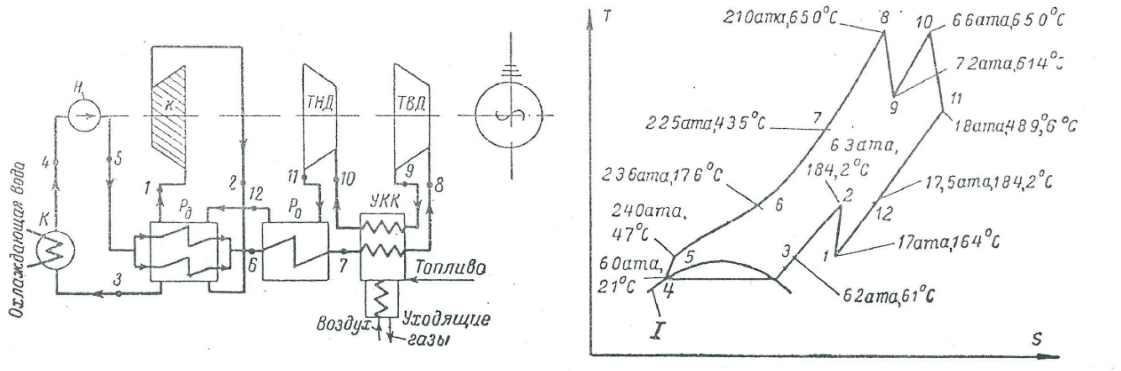

Figure 2.1: Schematic and Temperature-Entropy diagram of Dekhtyarev's cycle (Dekhtiarev 1962)

superheating (non-isothermal heat addition) and wet expansion. This usually requires multiple reheat stages that add to the cost and complexity of the plant.

2. Inadequate recuperation attributed to the relatively low steam temperatures exiting the turbine (100 - 120 °C).
3. Large expansion ratios that require many turbine stages; up to 30 stage at times.
4. Blade erosion from steam.

Brayton cycles also had their share of drawbacks, such as:

1. High compression work of gas.
2. Sensitivity of cycle efficiency to compression work.
3. Large heat exchanger surfaces due to the inferior heat transfer properties of gas at typical Brayton cycle operating pressures.

In his paper, Feher (1968) studied the behaviour of a supercritical carbon dioxide cycle over a wide range of temperatures and pressures. The cycles he studied operated entirely above the critical pressure varying from 13.7 MPa to 48.2 MPa, while the temperatures varied below and above the critical temperature, between 20 and 870 °C. All cycles allowed compression in the liquid phase and benefited from reduced compression work, thus improving overall efficiency. Compression was assumed to be achieved using a pump rather than a compressor. The main difference

is that a pump operates with an incompressible liquid whereas a compressor with a compressible gas. This cycle is supercritical by our earlier definition since both heat addition and rejection occur at pressure higher than the critical pressure. A schematic of the T-s diagram as depicted by Feher is shown in Figure 2.2.

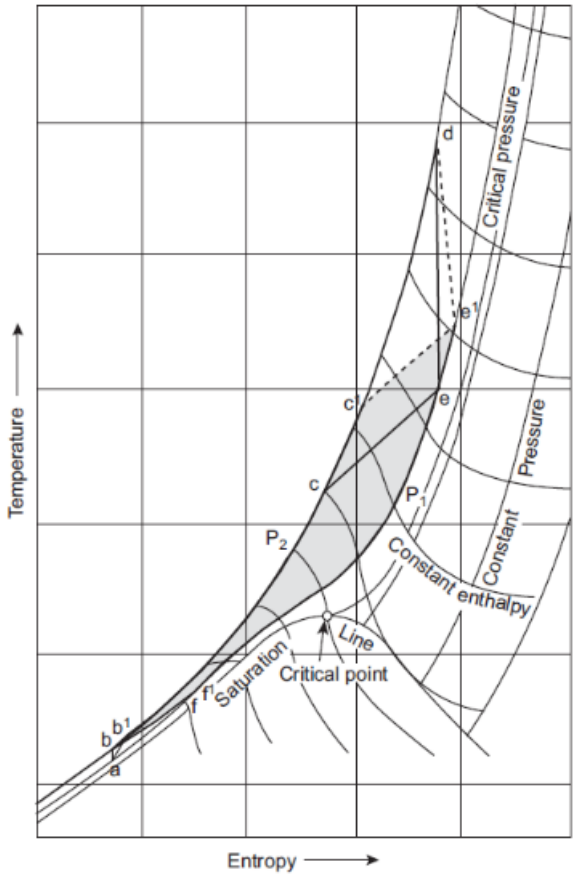

Figure 2.2: T-s Diagram of a supercritical cycle (Musgrove & Wright 2017)

Feher's work provided insights into the sensitivity of the cycle's efficiency towards its parameters. For instance, even though cycle efficiency reaches a maximum above a pressure ratio of 3.5, an almost similar value can be obtained at a pressure ratio of 2, since efficiency increases only slightly after that. However, this is only true when the recuperator's pinch temperature is relatively low. His results also demonstrate the reduced consequence of compression efficiency on cycle efficiency, as the pump efficiency is only half as significant as that of the turbine in the efficiency range of 60% - 100%, which is within the usual design efficiency range. Lastly, he compared the effect of the turbine and pump inlet temperatures (TIT and PIT) on the efficiency of the sCO_2 and Brayton cycles. Both behave similarly with regard to TIT; almost

linear positive correlation. However, the sCO_2 cycle efficiency is greatly affected by the PIT. A nonlinear decrease in efficiency is observed upon transitioning from below to above the critical point, which is attributed to the increased compressibility of the fluid, and thus the need for more compression work.

Although Feher hinted at the potential applications of sCO_2 by providing an overarching analysis of a simple recuperated cycle, he did not delve into the possible improvements of the cycle's configuration; an endeavour which Angelino carried out.

Angelino conducted an exhaustive study of the real gas behaviour, namely the change in compressibility and specific heat capacity, and the performance of different CO_2 cycle configurations such as the recompression, and partial cooling, to name a few (Angelino 1967, 1968, 1969). In contrast to an ideal gas, a real gas is a non-idealized model that accounts for the physical space occupied by gas particles and the intermolecular attraction between them, which imposes a physical limit to its compressibility. A gas is expected to exhibit real gas behaviour the closer it is to the saturation dome by becoming increasingly resistant to compression (incompressible).

Angelino postulated that sCO_2 cycles will be able to compete with contemporary steam cycles in high and low temperature ranges, that real gas behaviour can be exploited to improve cycle efficiency, that variations in specific heats can prove detrimental to efficiency, and that there will be a trade-off between the fluid-dynamic and heat transfer losses in a sCO_2 cycle.

In his first paper, Angelino (1967) highlighted the importance of regeneration on cycle efficiency and studied the effect of specific heats and pressure on its effectiveness. He concluded that higher specific heats reduced the surface area and log mean temperature difference in the recuperator. In that regard, the work showed that fluids with higher ideal gas specific heats tend to have lower temperature drops across the turbine, thus carry greater regenerative potential. Most importantly, it described how the significant difference between the heat capacities of the two streams in a recuperator degrade cycle efficiency. The feasibility of CO_2 as a working fluid was also questioned because of its relatively low critical point. A condensation cycle would

be impossible without heat sink temperatures lower than the working fluid's critical temperature; a challenge which was later addressed by doping CO_2 with impurities.

The study of condensing cycles continued in Angelino's second paper with a focus on improving cycle efficiency (Angelino 1968). He developed four cycle configurations including the recompression, precompression, partial cooling, and split expansion. By reducing the difference in heat capacities between the high- and low-pressure streams, the first three layouts served to reduce the irreversibility in the recuperator. These will be elaborated on in the next section. On the other hand, the split expansion layout was used to reduce the thermal stresses in the turbine. Figure 2.3 compares the efficiencies of the cycles. In the same paper, Angelino recognized the benefit of reheating in improving efficiency and presented a preliminary design of a 1 MW CO_2 turbine compared with a 600 MW steam turbine to demonstrate its compactness.

In his third work, Angelino (1969) explored the influence of real gas effects on various cycle architectures. He recognized the benefit of the reduction in specific volume on the compression work, and the potential degradation of efficiency due to the change in specific heat capacities. Also, he identified nuclear and solar energy sources as potential applications for sCO_2 cycles. Moreover, he postulated that sCO_2 cycle may rival steam cycles in low temperature ranges 400 - 550 °C based on economic merits, and in high temperature ranges above 600 °C based on superior efficiency.

In his PhD thesis at the Massachusetts Institute of Technology (MIT), Dostal et al. (2004) built upon the earlier work of Angelino in more detail via a systematic design and optimisation of multiple supercritical Brayton cycle's in advanced nuclear reactor applications. In that respect, he compared sCO_2 with Steam and Helium cycles to show that sCO_2 power plants have lower capital costs than either. Unlike Angelino, he found that sCO_2 outperforms supercritical steam cycles for temperatures above 550 °C rather than 600 °C, as seen in Figure 2.4.

Dostal also compared sCO_2 cycles with ideal gas Brayton cycles and found that they do not benefit as much from increases in turbine inlet temperatures. They are also much more sensitive to the compressor inlet temperature since they operate

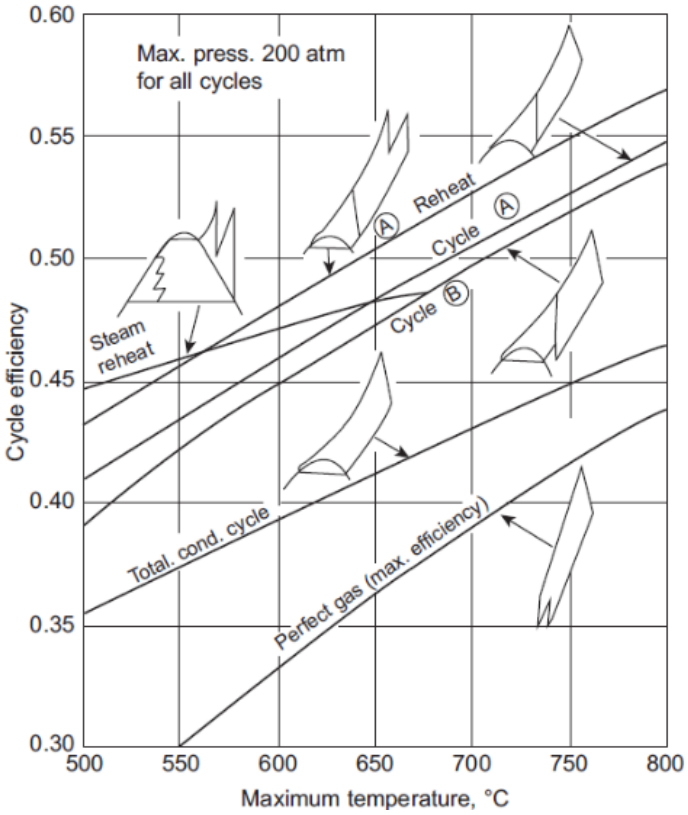

Figure 2.3: Cycles efficiency comparison. Cycle A and B are recompression and partial cooling (Musgrove & Wright 2017)

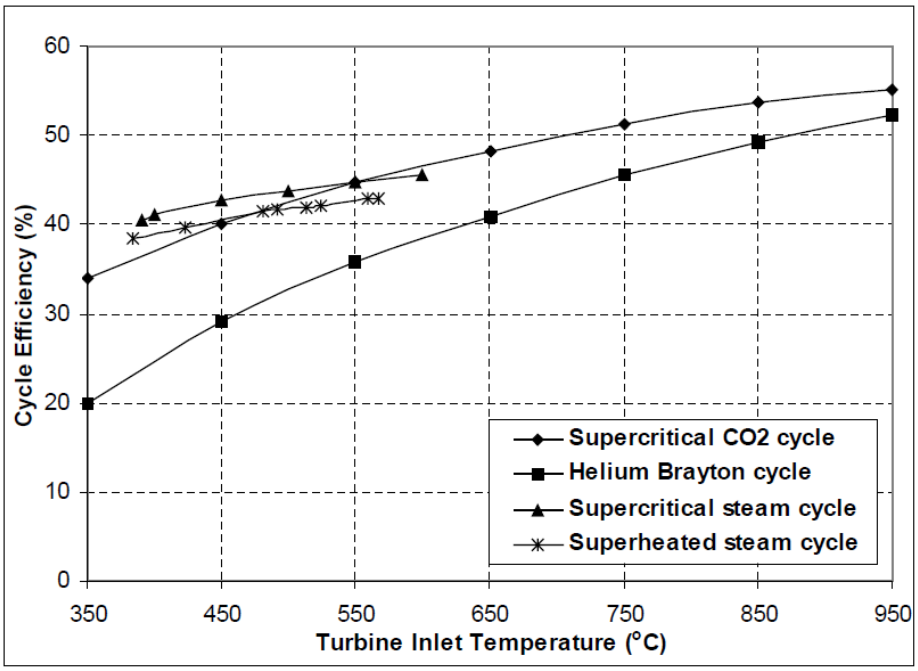

Figure 2.4: Cycle efficiency comparison. From (Dostal et al. 2004)

near the critical point. The work included a preliminary turbine design for a 246 MWe power plant. The turbine body was 1.2 m in diameter and 0.55 m long, which

translates into a high-power density of 395 MWe/m^3. Figure 2.5 compares the sizes of steam, helium, and sCO_2 turbines.

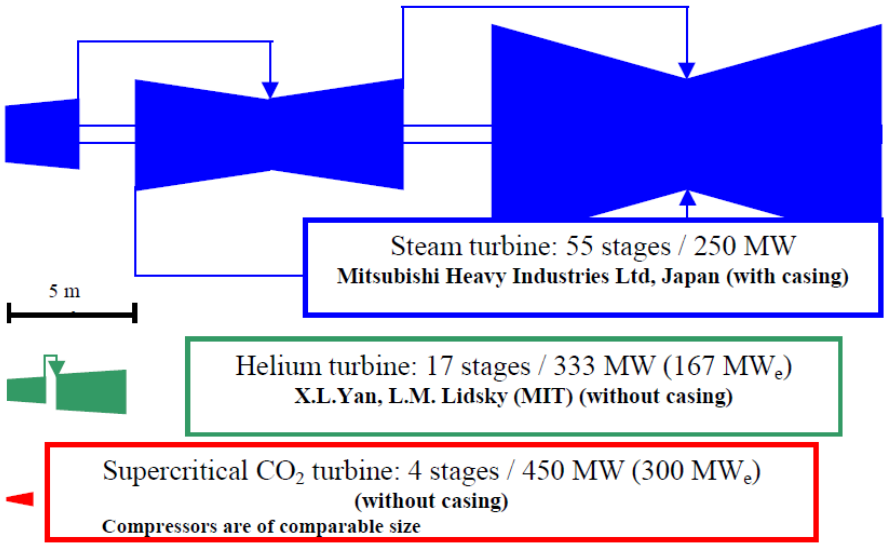

Figure 2.5: Turbine size comparison. From (Dostal et al. 2004)

Most importantly, Dostal recognized the demanding size of sCO_2 recuperators due the internal pinch point and its associated irreversibility which requires larger heat transfer areas, which might offset the appeal of smaller turbomachinery. As a possible way of maintaining cycle compactness, he proposed the use of Printed Circuit Heat Exchangers (PCHE).

The research conducted at MIT in the early 2000's re-triggered interest in sCO_2 power cycles. Since then, a plethora of scientific works covering many facets and applications of sCO_2 power cycle have emerged. Some of these looked into cycle design optimisation (Kim et al. 2016, Padilla et al. 2016), or were motivated by the need to improve heat exchanger or turbomachinery performances (Chu et al. 2017, Albrecht & Ho 2019, Keep 2018, Crespi et al. 2018). While others focused on heat source specific applications in nuclear (Moisseytsev & Sienicki 2009), solar (Crespi et al. 2018, Neises & Turchi 2014), (Neises & Turchi 2019), geothermal (Kim et al. 2016), waste heat recovery (Li et al. 2014, Novales et al. 2019), or fossil fuel (Bruno 2019). Moreover, several experimental rigs have been constructed, including those at Cranfield University UK (Anselmi et al. 2018), Sandia National Laboratory (SNL) USA (Pasch et al. 2012), and most recently at Centrum vzkumu e (CVR) Czech

Republic (Vojacek et al. 2018), the details of which are discussed in Section 2.7. The next section serves to summarize the findings of more than a decade of work that are most relevant to the focus of this thesis, starting with the fundamental cycle architectures.

A recent review of sCO_2 systems for power generation by White et al. (2021) showed the growing interest in this technology, which was indicated by the growth in research and patents, as shown in Figure 2.6.

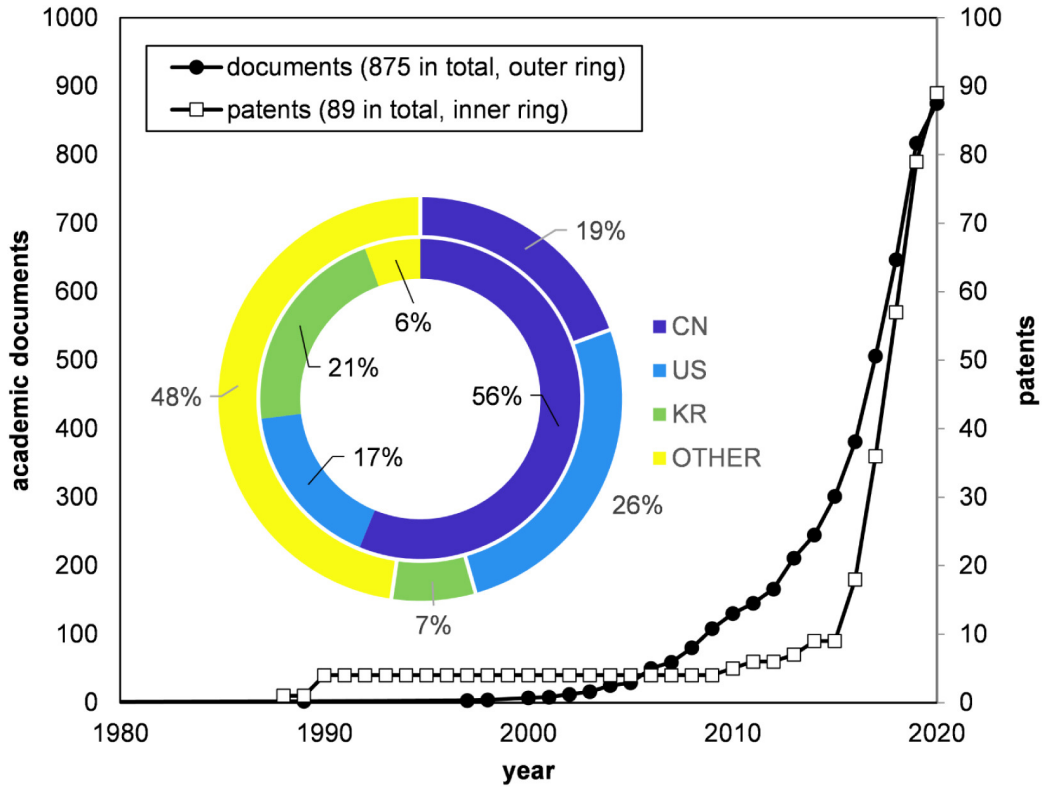

Figure 2.6: Historical evolution and geographical distribution of intellectual property outputs in the field of sCO_2 power systems. Elaboration from Scopus and Espacenet world databases between January 1988 and March 2020. The doughnut charts refer to the total number of outputs in the period surveyed while their legend shows the shares in the Peoples Republic of China (CN), the United States of America (US), the Republic of Korea (KR) and the rest of the world (OTHER) (White et al. 2021)

It was noticed early on that CO_2 exiting the turbine maintains a relatively high temperature, and thus has a high heat recuperation potential. Therefore, the simplest practical layout for the sCO_2 cycle includes a recuperator. As seen in Figure 2.7, CO_2 is first compressed by the compressor (MC) and passed through a recuperator (REC) where it recovers heat, then it is heated in the primary heat exchanger (PHE) before

entering the turbine (TB). After the fluid is expanded in the turbine it is passed through the recuperator to transfer some of its heat to the cold stream before being cooled in the precooler (PCR) and compressed to repeat the cycle.

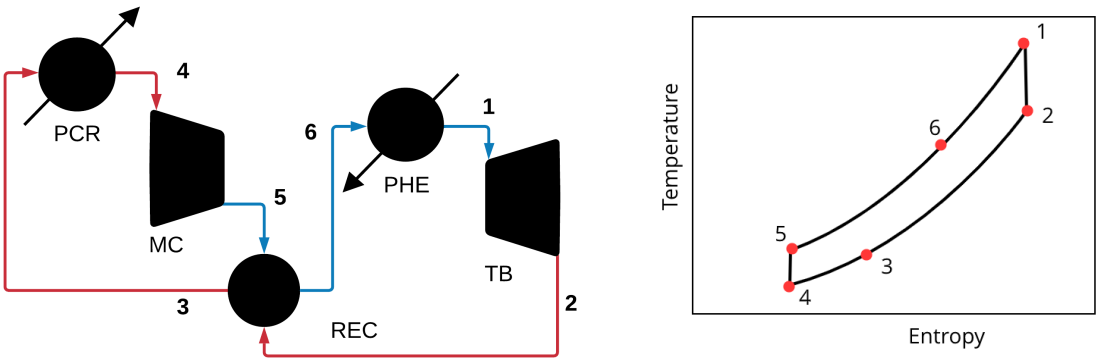

Figure 2.7: Schematic and T-s diagram of the simple cycle.

It was also noticed early on that the recuperator exhibits high irreversibility and an internal pinch-point because of the significant difference between the specific heat capacities of the high- and low-pressure streams. The pinch-point is the minimum temperature difference between the two streams in a heat exchanger as depicted in Figure at least one of the fluids. cle configurations.

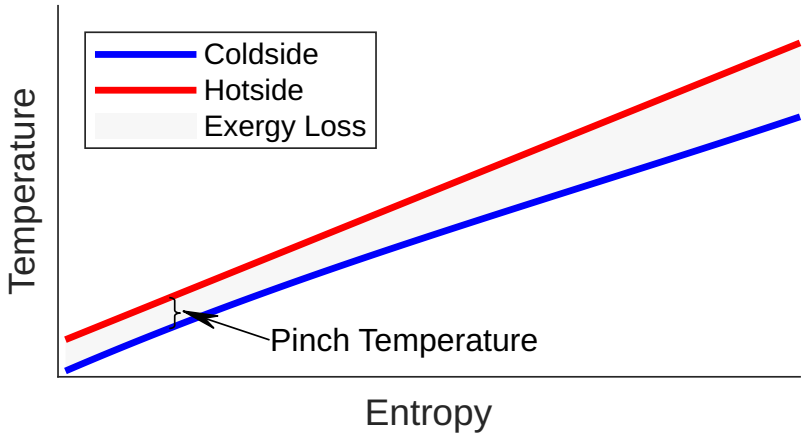

Figure 2.8: An example of the temperature profiles of the hot and cold streams in a simple recuperated sCO_2 Brayton cycle. The exergy loss (irreversibility) due to the internal pinch point and mismatch between the two streams is indicated by the shaded area

The recompression cycle, shown in Figure 2.9, avoids the pinch-point problem by dividing the recuperator into two; the high-temperature recuperator (HTR) and

the low-temperature recuperator (LTR), while adding a recompressor (RC) after the low-temperature recuperator. The difference in heat-capacity rates is reduced by decreasing the mass flow rate of the high-pressure stream and allowing a smaller flow into the low temperature recuperator. The two high-pressure streams are then mixed before the high temperature recuperator where their combined heat-capacity rate is not too different from the low-pressure stream. This is by far the most widely studied cycle layout due to its high performance especially in high-temperature applications (Dostal et al. 2004).

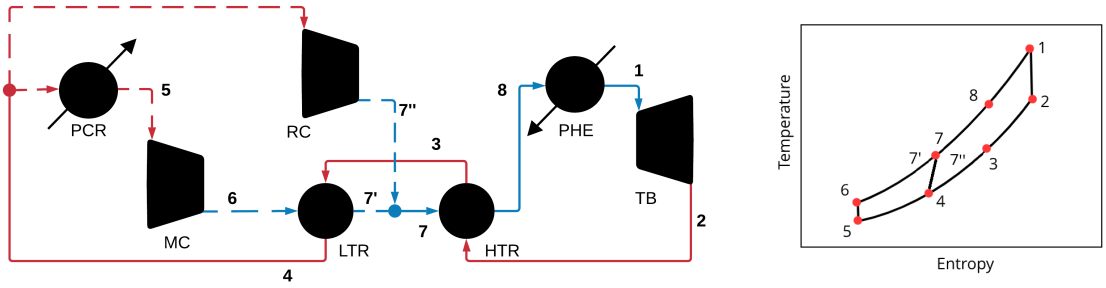

Figure 2.9: Schematic and T-s diagram of the recompression cycle.

Like the recompression cycle, the precompression cycle splits the recuperator, but adds a precompressor (PC) as seen in Figure 2.10. Unlike the recompression cycle, it reduces the heat-capacity rates between the two streams by compressing the low-pressure stream between the recuperators to increase its heat capacity rather than reduce the flow of the high-pressure stream. This layout also decouples the turbine outlet pressure from the heat rejection temperature, which allows for higher expansion ratios and higher specific work. The decoupling of the turbine outlet pressure also gives more operational flexibility; a benefit for off-design operation of CSP plants.

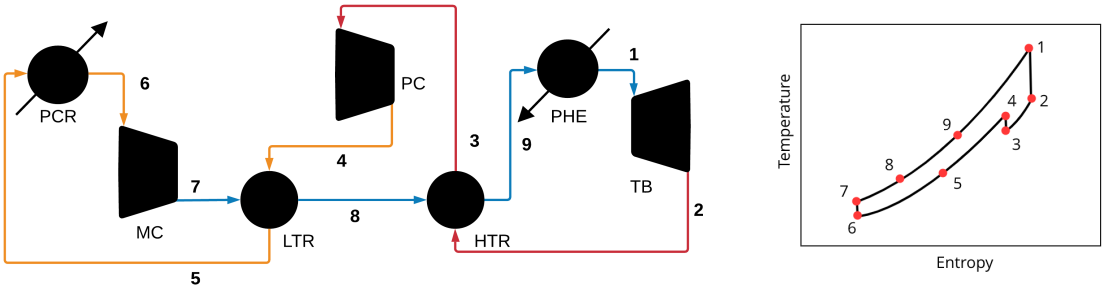

Figure 2.10: Schematic and T-s diagram of the precompression cycle.

Apart from reducing the recuperator irreversibility as intended by the three fundamental cycles described above, other alterations may be adopted to modify the performance of the cycle. The compression work may be further reduced by using an intercooler (ICR) between compression stages. For example, in a recompression cycle, the low-pressure stream can either be split after or before the first stage of compression. If split after, then the layout becomes a partial-cooling cycle, shown in Figure 2.11. If split before, then it becomes an intercooling cycle depicted in Figure 2.12. In either case, the turbine outlet pressure is decoupled from the heat rejection temperature which allows for greater operational flexibility. Furthermore, the specific work can be increased by introducing a reheat stage with an additional turbine, which is illustrated in Figure 2.13. Essentially, the addition of intercooling or reheat stages brings the compression or expansion process closer to the isothermal conditions experienced in an ideal Carnot heat engine. These alterations have been studied in the past and have proved to increase cycle efficiency depending on operating conditions, but at a higher capital cost and added complexity.

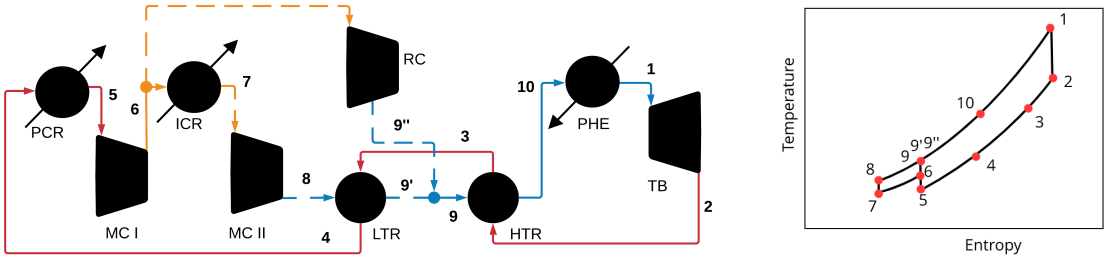

Figure 2.11: Schematic and T-s diagram of the partial-cooling cycle.

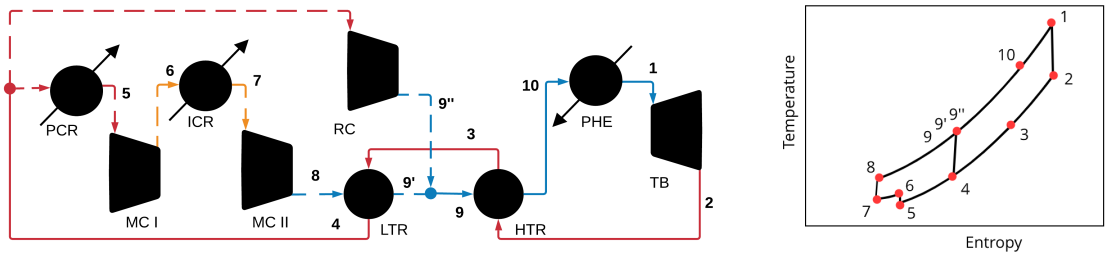

Figure 2.12: Schematic and T-s diagram of the intercooling cycle.

These configurations have been widely studied for sCO_2 Brayton cycles, but may be adapted to tCO_2; according to the minimum cycle temperature and pressure. In fact, they were originally proposed by Angelino as condensing cycle with a combina-

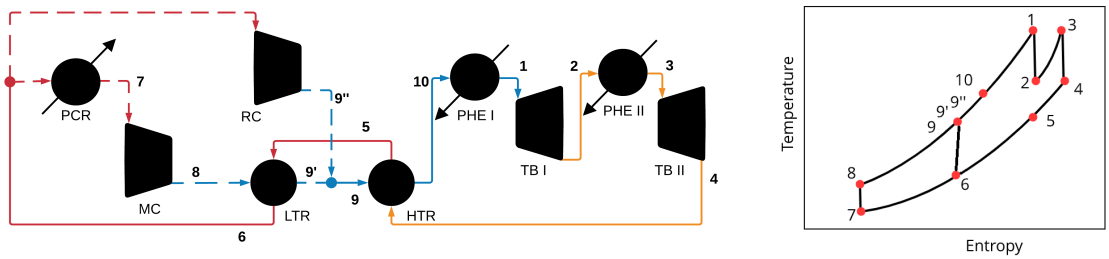

Figure 2.13: Schematic and T-s diagram of the reheat cycle.

tion of pumps and compressors.

Recovering waste heat from a sCO_2 cycle via a bottoming power cycle tailored for low-grade heat is also a viable method of increasing its efficiency. Studies have shown that ORC and tCO_2 can both be employed as bottoming cycles within a combined sCO_2 power plant.

Depending on the working fluid and cycle layout, a combined sCO_2/ORC or sCO_2/tCO_2 plant may increase overall thermal efficiency by 3-8% compared to a stand-alone sCO_2 power plant (Besarati & Yogi Goswami 2014, Chacartegui et al. 2011, Wang, Wang, Zhao & Dai 2016). For example, a combined simple sCO_2/ORC operating with R245fa plant can be 8.23% more efficient than a stand-alone simple cycle and 2.43% more efficient than a stand-alone recompression cycle operating at the same temperature (Chacartegui et al. 2011). Even higher efficiencies are possible with a combined recompression cycle, with increases of 9% and 4% compared to stand-alone simple and recompression cycle, respectively (Wang, Wang, Zhao & Dai 2016). The same trend is observed when comparing simple and recompression sCO_2/tCO_2 cycles with their stand-alone counterparts. The gains in efficiency are 7.24% for a simple cycle and 4.34% for a recompression cycle.

The difference in efficiency gains between cycle architectures is a result of higher bottoming cycle efficiencies in simple cycles since they provide more waste heat than complex cycles. Therefore, a simple sCO_2 layout will benefit more from a bottoming cycle than a recompression layout might. The same is true for the partial cooling layout (Besarati & Yogi Goswami 2014). It is for that reason that simple cycles were found to be more feasible from a technoeconomic viewpoint (Wang, Zhao, Wang, Li & Dai 2016).

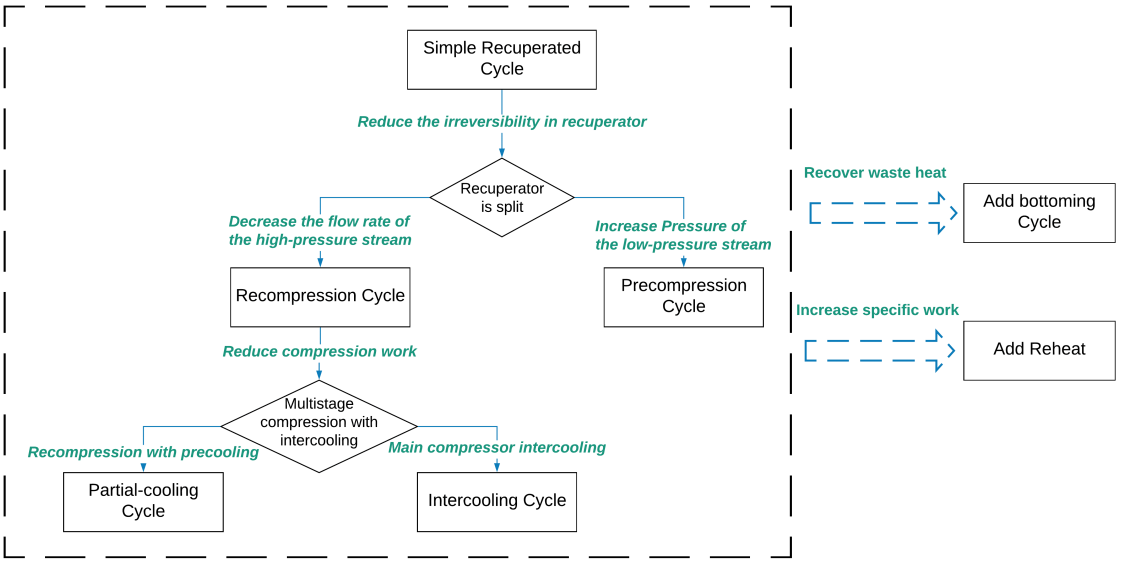

Figure 2.14: Sketch of the relationships of different CO_2 layouts ((adapted from (Wang et al. 2017)

2.3 sCO_2 power cycles for solar power towers

As mentioned earlier, sCO_2 power cycles have been identified as the most promising power block solution that can help CSP compete with other power sources (Besarati & Goswami 2016). The potential cost saving is mainly owed to the possible gains in efficiency, compact turbomachinery and its compatibility with heat storage and direct heating. Among CSP power plants, solar tower power plants were deemed the most suitable for sCO_2 applications owing to their higher receiver temperatures compared to other CSP applications.

The performance metrics of a power plant depends on the thermal resource being utilized. For example, efficiency is paramount in a gas or coal fired power plant, while the total power output is a crucial factor in waste heat recovery systems. For SPT, additional factors must be accounted for, namely its incorporation ability with thermal storage and compatibility with dry cooling. The following section will review the literature investigating the performance of CO_2 power cycles for SPT plants.

In a SPT plant, transfer of thermal energy from the central receiver to the power block can be achieved either by direct or indirect receiver configurations, as seen in Figure 2.15. Direct configuration uses CO_2 both as the heat transfer medium and as

the power block working fluid by circulating it directly through the central receiver. This removes the need for intermediate heat exchangers and their associated exergy losses and costs (Silva-Pérez 2016). However, it poses a challenge for efficient thermal energy storage, which is a vital factor in the dispatchability of CSP electricity and the reduction of its LCoE (up to 50% reduction according to one estimate (Alsagri et al. 2019)). Indirect configurations, on the other hand, are able to efficiently store thermal energy and may use air, molten salt mixtures, liquid metals, or solid particles as the heat transfer medium (Ho et al. 2014).

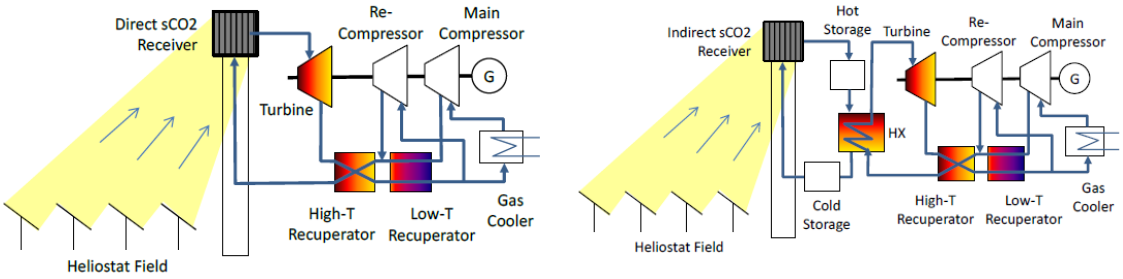

Figure 2.15: (left) direct receiver, (right) indirect receiver (Ho et al. 2014)

As mentioned earlier, sCO_2 gain comparative advantage against current CSP technologies employing steam at temperatures above 550 °C, and so studies have investigated the feasibility of achieving high temperatures using indirect heating. A receiver temperature of 750 °C may be achieved by the adoption of liquid sodium or KCl-$MgCl_2$ as the heat transfer medium instead of Solar-Salts (mixture of 60 wt% $NaNO_3$ and 40 wt% KNO_3). Results show that plants using sodium can achieve overall plant efficiencies above 25%, whereas the use of Solar Salts at 565 °C and KCl-$MgCl_2$ at 750 °C reach 21.5% and 24%, respectively (Polimeni et al. 2018).

An inherent trade-off between the thermal performance of the heating loop and that of the power block persists in indirectly heated SPT plants. Higher turbine inlet temperatures yield greater efficiencies in the power block. However, they also promote greater thermal losses in the receiver and reduce the thermal efficiency of the heating loop. Likewise, a narrower temperature difference in the primary heat exchangers indicates a greater recuperation in the power block, thus higher efficiencies. However, it also increases the required flow rate and overall inventory of the heat transfer medium, thus requiring larger and more expensive sensible heat storage facilities.

The relationship between the energy released, mass, and temperature of the heat transfer medium is described by

$$\dot{Q} = \dot{m} C_{\mathrm{p}} \Delta T_{\mathrm{PHE}} \tag{2.1}$$

where $\dot{Q}$ is the thermal energy released (W), $\dot{m}$ is the mass flow rate of the medium (kg/s), c_{p} is its specific heat capacity (J/kgK), and ΔT_{PHE} is the temperature difference across the primary heat exchanger (in Kelvin). The same equation can be used to calculate the amount of energy stored in the heating loop by replacing the mass flow rate with the total mass of the medium inventory.

The trade-off is evident when comparing the overall efficiency of several sCO_2 configurations operating with SolarSalts. Figure 2.16 shows that increasing maximum temperature leads to an increase in power cycle efficiency and a decrease in the receiver efficiency. Since overall efficiency is dependent on both the power cycle and the receiver, the maximum overall efficiency is achieved around 650 to 700 °C for all cycles (Wang et al. 2017).

Compared to steam cycle, sCO_2 cycles operate with a narrow temperature difference across the primary heat exchanger in CSP plants. For example, the temperature difference for all layouts considered in Figure 2.16 are around 100 to 120 °C for a maximum temperature of 565 °C, as opposed to the 290 °C temperature difference in a steam CSP plant operating at the same temperature. This indicates that the thermal storage system for a SPT operating with sCO_2 at these temperatures will be bulkier than that of a similar SPT operating with steam, which might oppose the reduction in overall plant size due to compact turbine and piping (Wang et al. 2017).

Evaluating the trade-off from an economic point of view is essential to sizing its influence in determining the plant's design point. In general, plants that achieve the highest power block efficiency, thus require the least amount of heat input, have the lowest cost. Although the lower temperature differences across the primary sCO_2 heater increase the required mass flow rate of the sensible heat-transfer/storage media, the resulting cost increase is relatively small compared to the costs of the he-

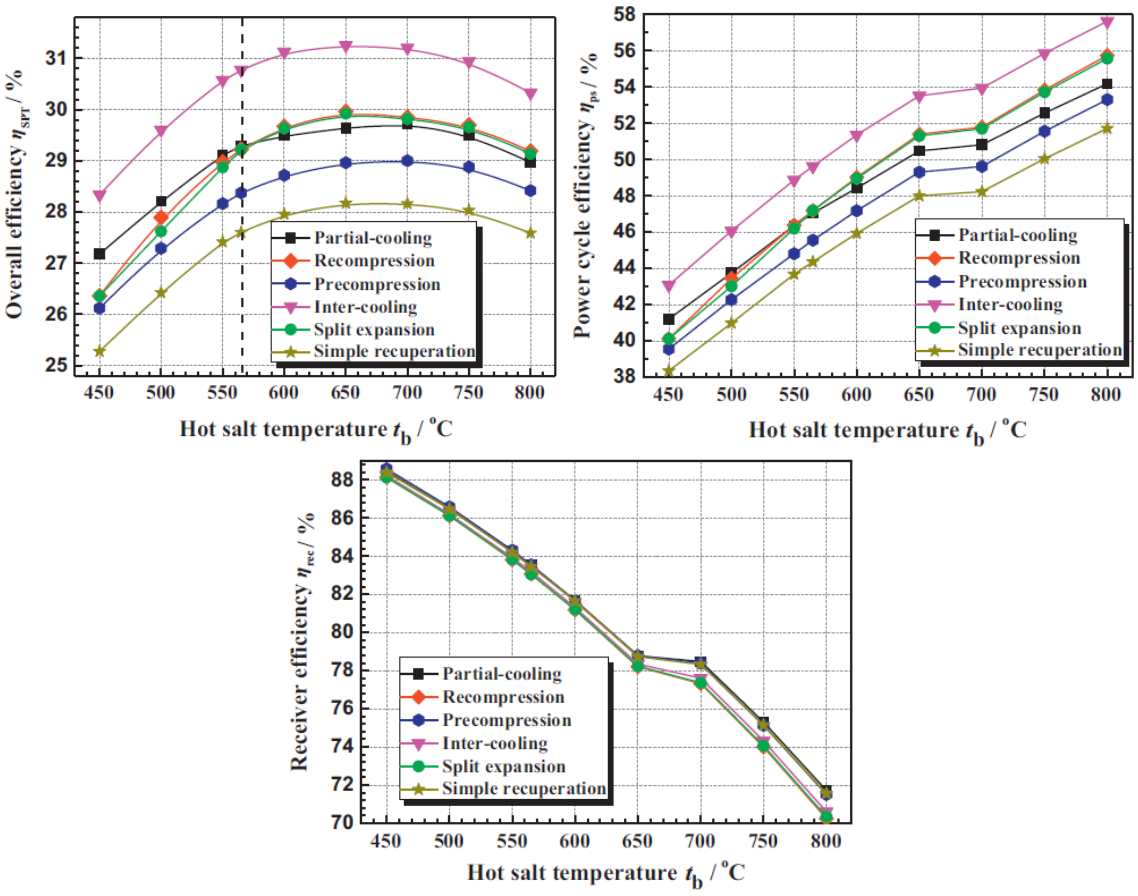

Figure 2.16: Comparison of efficiencies between SPT systems integrated with different S-CO_2 cycles at various hot salt temperatures (left: overall efficiency, middle: cycle efficiency, right: receiver (Wang et al. 2017)

liostats and solar receiver (Ho et al. 2015).

Because the heat capacity of CO_2 is the limiting factor in the pre-cooler (Cerio Vera 2015), wet cooled sCO_2 cycles in CSP plants require more cooling water than their steam counterparts. In dry coolers, on the other hand, the heat capacity of ambient air is the limiting factor, therefore both CO_2 and steam coolers should have similar sizes (Garg et al. 2014). However, dry cooling is especially prone to weather fluctuations since they depend on ambient air for cooling (Sorbet et al. 2019). Since sCO_2 cycles operate near the critical point to exploit real gas effects during compression, then slight changes in the compressor inlet temperature may have dramatic effects on cycle performance and reduce its competitive advantage over steam (Sorbet et al. 2019). To avoid such dramatic effects, it is recommended to operate slightly above the critical temperature and pressure in CSP applications (Saeed & Kim 2018).

A comparison between different sCO_2 cycle layouts for SPT plants shows the varying advantages of each. In Figure 2.17, the comparison is presented based on five criteria: efficiency, specific work, simplicity, incorporation ability with thermal storage, and compatibility with dry cooling. Efficiency and specific work ranking are based on the maximum achievable value by each configuration, not annually averaged, and they do not necessarily coincide with each other. Simplicity is judged based on how many extra components are added compared to a simple cycle. Incorporation ability is based on the temperature difference across the primary heat exchanger; the higher the difference the better suited the layout is to thermal storage. Finally, compatibility with dry cooling depends on the layout's performance sensitivity to compressor inlet temperature fluctuations. The first three criteria are common to all heat sources i.e. nuclear, fossil fuel, solar, etc. However, the last two are of special interest to SPT power plants. For example, although the recompression cycle achieves the highest efficiency, it is more sensitive to compressor inlet temperatures compared to the precompression or partial-cooling cycle. Consequently, it yields lower annual efficiencies in hot climates with ambient temperature fluctuations away from design considerations (Sorbet et al. 2019). The partial-cooling cycle also offers a larger temperature differential across the primary heat exchanger which allows for more cost effective sensible thermal energy storage systems and smaller internal recuperators (Cerio Vera 2015, Neises & Turchi 2014).

In terms of exergy destruction, the recuperator, hot thermal energy storage, and solar receiver are the main sources of exergy destruction in a SPT plant, accounting for around 70% of total destruction (Osorio et al. 2016).

2.4 Working fluid characterization

The selection of the working fluid is known to be an influential factor in optimizing closed power cycles. In this section we will explore several considerations involved in working fluid selection.

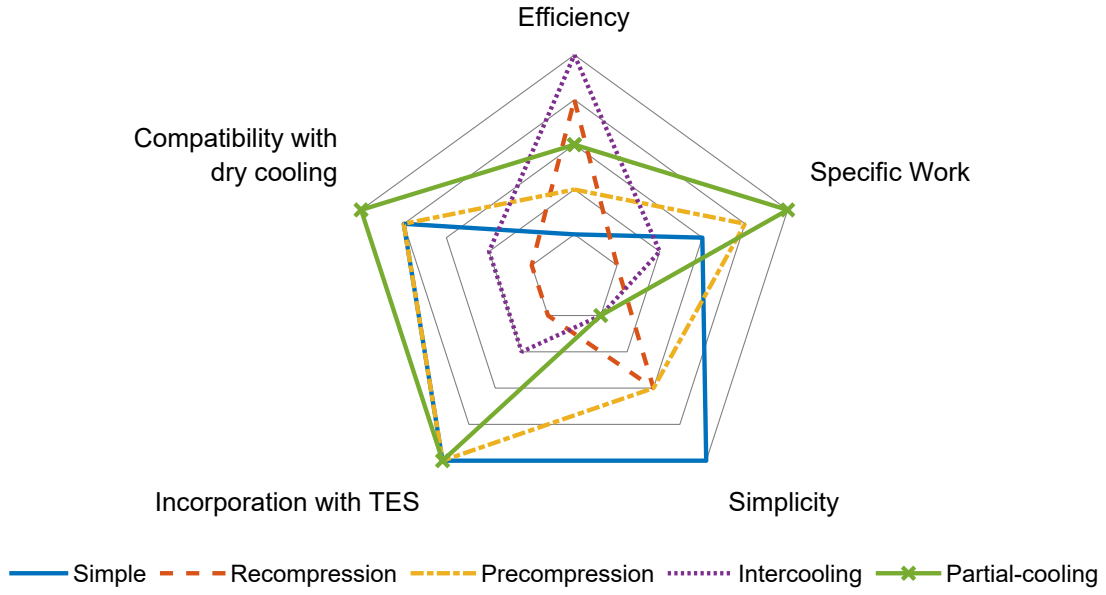

Figure 2.17: Comparison of performance of different cycles in SPT power plant (Wang et al. 2017)

2.4.1 Types of working fluids

Working fluids may be pure or multicomponent, inert or reactive fluids. Inert fluids may be pure, such as water, or multicomponent fluids, such as water-ammonia mixtures. Reactive fluids, on the other hand, can only be multicomponent fluids, as they are mixtures by definition, such as N_2O_4 (Lasala et al. 2018).

The choice of the working fluid type depends on the desired cycle behaviour. Inert fluids help reduce the irreversibilities occurring along the cycle. Conversely, owing to the conversion of its chemical energy —in addition to the change in its enthalpy—reactive fluids allow a significant increase in the work extracted during fluid expansion. However, the continuous state of chemical disequilibrium in reactive fluids entails greater sophistication in modelling their behaviour. Therefore, thermochemical driving forces must be accounted for within the components of a power cycle employing reactive fluids.

In this thesis, binary CO_2-based mixtures will be investigated for applications in CSP. Before exploring the possible candidate working fluids, it is worth assessing

the possible implications of the change in the working fluid's molecular weight and complexity as a result of doping.

2.4.2 Effect of molecular weight and complexity

A molecule's complexity increases with the number atoms it contains; its weight with the mass of those atoms. According to Lasala et al. (2018), weight and complexity affect the fluid's response to energy interactions with the environment. With increasing complexity, the isochoric heat capacity (C_{v}) increases at a higher rate than the isobaric heat capacity (C_{p}), thus the adiabatic coefficient ($\gamma = \frac{C_{\mathrm{p}}}{C_{\mathrm{v}}}$) is lower for more complex molecules. Applied to the isentropic expansion of an ideal gas through a turbine, expressed by Equation 2.3, lower values of γ result in a smaller temperature drop, but higher expansion ratio, for a given pressure ratio. Using the same relation, but for a fixed temperature ratio, compression or expansion of complex molecules yields higher pressure and expansion ratios.

$$\frac{P_{\mathrm{in}}}{P_{\mathrm{out}}} = \left(\frac{T_{\mathrm{in}}}{T_{\mathrm{out}}}\right)^{\frac{\gamma}{\gamma-1}} = \left(\frac{\nu_{\mathrm{out}}}{\nu_{\mathrm{in}}}\right)^{\gamma} \tag{2.2}$$

The molar heat capacity of a fluid is strongly dependant on its molecular complexity. In brief, and without delving into statistical mechanics, the molar heat capacity depends on the degrees of freedom (kinematics) of a molecule i.e. rotation, bending, vibration, and translation. The more degrees of freedom of the molecule, the greater is its molar heat capacity. This explains why monatomic molecules have lower heat capacities than polyatomic molecules. The same effect can be extended to different phases of the same fluid. Because gas molecules are less bound by intermolecular forces, they lose their intermolecular vibrational freedom. Therefore, gases have a lower capacity than liquids; which may vibrate, rotate, and translate (J. Richard Elliott 2012).

Within the context of simple recuperative supercritical Brayton cycle, it was noted early on that a fluid with a high molar heat capacity would be preferable to minimize the difference of heat capacities between the cold and hot streams in the recuperator (Angelino 1967). This was deduced from the principle of corresponding states which

asserts that all fluid properties are similar if expressed properly in reduced variables:

$$\left(C_{\mathrm{p}} - C_{\mathrm{p}}^{o}\right)_{\mathrm{P_r,T_r}} = -T \int_0^p \left(\frac{\partial^2 V}{\partial T^2}\right) dp \tag{2.3}$$

where C_{p}^{o} is the isobaric molar heat capacity at the reference state (see Section 3.2.3) and the ratio of the pressure and temperature to the critical pressure and temperature are expressed as the reduced pressure $P_{\mathrm{r}} = \frac{P}{P_{\mathrm{c}}}$, and temperature $T_{\mathrm{r}} = \frac{T}{T_{\mathrm{c}}}$ is the reduced temperature.

The departure of the fluid molar heat capacity from the ideal gas value is the same for all substances at a given reduced pressure and temperature. Fluids having a large ideal molar heat capacity exhibit a small difference in liquid and vapor state heat capacities. As the heat capacity rates of the two streams grow closer, internal irreversibilities in the regeneration process of the cycle decrease.

Unlike molar heat capacity, mass heat capacity not only relies on complexity, but it also on molecular weight. The lower the weight, the more moles there are per unit mass, the higher the specific heat capacity. Therefore, light-weight complex molecules are expected to have the highest specific heat capacities.

Increasing the mass heat capacity increases the turbine specific work. For a fixed maximum enthalpy drop per stage, higher specific work requires a greater number of stages, thus a larger turbine. In contrast, a lower mass heat capacity reduces the specific work and allows for greater pressure and expansion ratios per stage. Therefore, it is recommended to use simple heavy fluids to reduce the turbomachinery size and increase its efficiency, at the cost of higher inlet pressures for simple molecules.

Another way in which the complexity of a fluid's molecules affects turbomachinery is through the shape of its saturation curve in the T-s plane. Complex fluids tend to have skewed 'dry' dew lines which permit dry expansion in the turbine. However, this is only of concern when expanding close the dew curve, which is not the case for $\mathrm{sCO_2}$ or $\mathrm{tCO_2}$.

The nature of the working fluid also affects the design of heat exchangers. The

molar mass should preferably be low (light molecule) to maximise the heat transfer coefficients. Heavy molecules would instead entail the adoption of heavy and expensive heat exchanger. Moreover, the molecular weight indirectly affects the heat exchanger by influencing the pressure ratio of the power cycle, thus changing the pressure in the heat exchanger. This effect also encourages the use of light molecules as they have lower optimal pressure ratios.

The same generalities about the effect of the molecular character of pure fluids on power cycles extends to binary mixtures as well. A study of these effects will help in understanding the influence of certain dopants of CO_2-based binary mixtures on cycle performance and equipment design. However, there are additional influences in mixture working fluids that should be accounted for when deciding on a choice of mixture, as investigated in the next section.

2.4.3 Mixture types

The P-T relation during a vapour-liquid transition is more complex in mixtures than that in a pure substance. Mixtures are either zeotropic, also known as non-azeotropic, or azeotropic. Zeotropic mixtures are the general cases of mixtures for which the liquid and vapor coexisting phases have unequal molar compositions of the constituent fluids. Azeotropic mixtures, on the other hand, may be formed by certain mixtures at specific compositions where molar compositions in the liquid and vapor phases are equal. When the saturation pressure (P_{sat}) and temperature (T_{sat}) are the same for both components, azeotropes will occur in ordinarily zeotropic mixtures. The closer the boiling temperatures of the two components are to each other the more likely that this will happen; normally they have to be 30K apart for an azeotrope to form. (Radermacher & Hwang 2005)

2.4.4 Mixture classification

Several classifications have been proposed for binary mixtures based on their miscibility and the shape of their critical loci. A classification of five types (I to V) of binary mixtures derived from Van der Waals's equation of state was first introduced

by van Konyneneburg & Scott (1980). The classification is based on the presence or absence of three-phase lines and the way critical lines connect with these lines. Conveniently, this classification focuses on the fluid part of the phase diagram, whilst neglecting solid phases (Gray et al. 2011). Since then the classification has been extended to eight types, some with their own sub-classes based on whether or not they form azeotropes. A thorough examination of the phase phenomenology was presented by Privat & Jaubert (2013).

In general, a mixture's type is governed by the intermolecular forces between its components and their relative molecular sizes (also referred to as molecular asymmetry (J. Richard Elliott 2012)); the further apart they are the more complex the phenomenology. For instance, mixtures of roughly similar particles with comparable critical temperatures ($T_{c1}/T_{c2} < 2$), such as Ar/Kr, exhibit Type I phase behaviour with a single continuous critical locus connecting the liquid-vapor critical points of the two components. Mixtures that include particles capable of intermolecular forces, such as H-bonding or dipoles, lead to liquid-liquid immiscibility at low temperatures when mixed with those that don't form such bonds, such is the case of Xe-HCl mixtures (Type II). As the disparity between the components increases they exhibit liquid-liquid immiscibility at higher temperatures and transition to Type III. In some cases even gas-gas immescibility have been found. Therefore, the categorization extends to more elaborate types that exhibit convoluted phase behaviour. Because the working fluid selection will be confined to simple mixtures, complex binary mixtures will not be studied in this thesis.

Transition between the different types of binary mixtures has been shown to be continuous by Privat & Jaubert (2013). They demonstrated that calibrating the binary interaction parameter k_{ij}—a correction factor applied to account for intermolecular interactions in mixture which is introduced in Section 3.2.1—could influence the classification of a mixture and transition it from one type to another. Therefore, k_{ij} has a direct and potentially significant consequence on the physiochemical description of the working fluids.

The presented taxonomy applies to CO_2-based mixtures as well. Compounds that

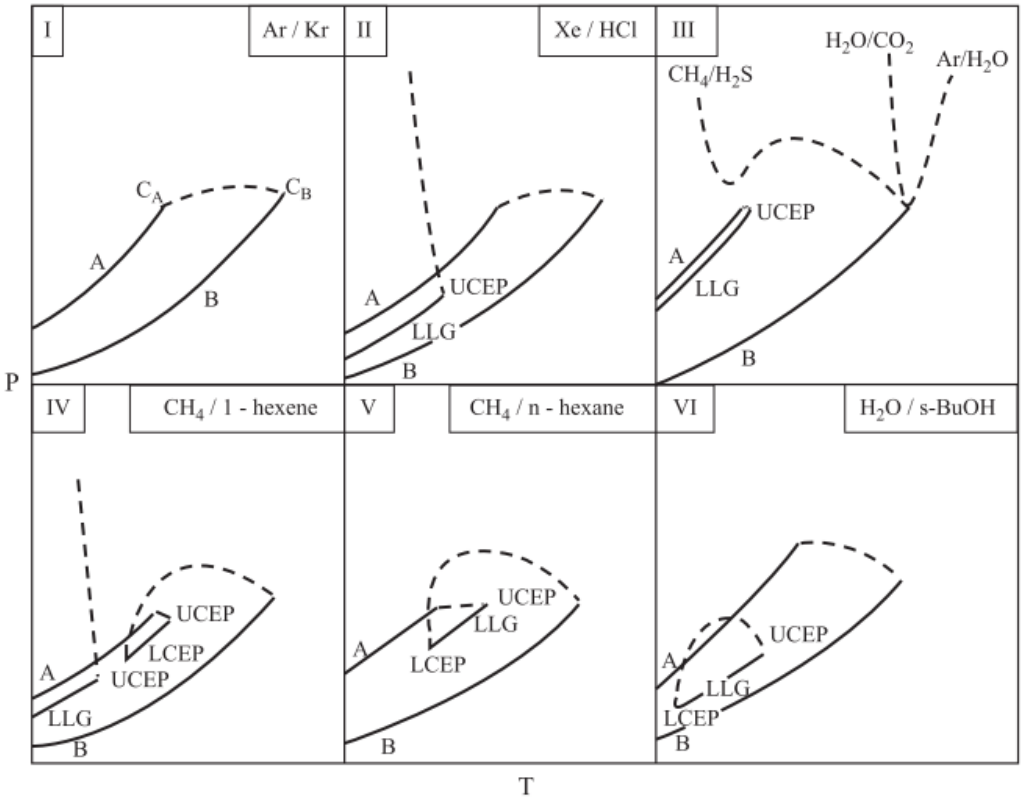

Figure 2.18: Classification of binary phase diagrams for a mixture of components A and B. Here solid lines labelled A and B are the pure component vapour pressure curves and dashed curves show the composition dependence of critical points for the mixture. Solid lines labelled LLG are the three-phase liquidliquidgas coexistence lines. UCEP = upper critical end point and LCEP = lower critical end point denotes the ends of critical lines. s-BuOH = secondary butanol. (From (Gray et al. 2011))

are expected to have poor solubility in CO_2 are those with high molecular weights, thus requiring high pressure to dissolve in CO_2. Moreover, CO_2 does not have a dipole moment, thus it is a poor solvent for polar compounds. But, because it has a quadripole moment it can dissolve compounds that are only slightly polar. Immiscibility in CO_2 will prohibit the formation of a homogeneous mixture which may manifest in the formation of a Liquid-Liquid phases. From a practical perspective, it is preferable to use working fluids of Type I mixture in order to increase the certainty in thermodynamic modelling and to avoid phase immiscibility, which may deteriorate the power cycle performance.

2.4.5 Temperature glide

Azeotropes exhibit a coexistence line in a P-T diagram, similar to that of pure fluids. Consequently, they undergo isothermal phase change similar to pure fluids (no temperature glides), while zeotropes do not. A qualitative description of zeotropic mixture phase change is shown in the T-s and T-x charts in Figure 2.19. The molar compositions in the vapour and liquid vary continuously along the isobar, and are unequal. Moreover, the temperature is not constant during a constant-pressure phase change, producing a temperature glide (Angelino & Colonna Di Paliano 1998).

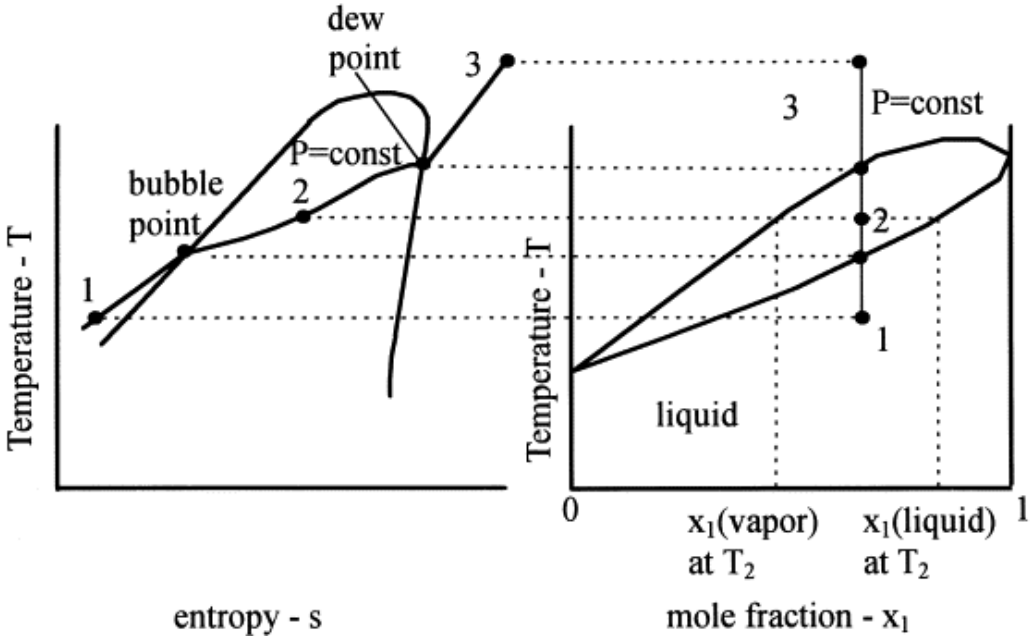

Figure 2.19: Qualitative representation of an isobaric phase change for a binary mixture in the T-s and T-x ($x = molefraction$) planes (From (Angelino & Colonna Di Paliano 1998))

Temperature glides affect the design of two-phase heat exchangers. With a linear glide, the pinch point is located at either end of the heat exchanger, or it does not exist when the two process lines are parallel (equal heat capacities). These cases are indicated in Figure 2.20a.

For a given logarithmic mean temperature difference, the parallel case produces the least entropy. The location of the pinch point can be controlled by balancing the heat capacity rate (mass flow rate times specific heat capacity) for both fluids. Since the pinch point limits the heat transfer rate, its existence and location severely

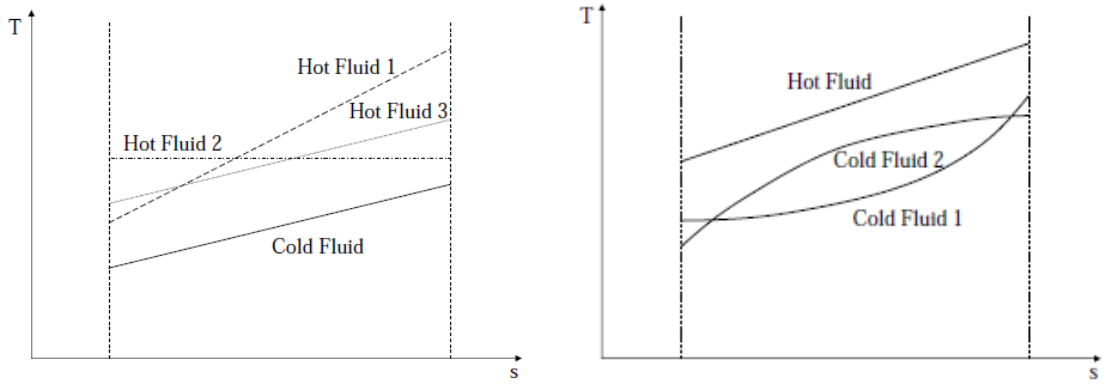

(a) (b)

Figure 2.20: (left). Temperature glide of a cold fluid and three different hot fluids. (right). Temperature glide matching between a hot fluid and two cold fluids with non-linear glides. (From (Radermacher & Hwang 2005))

affect heat exchanger performance. When the glides are parallel (no pinch point), the entropy production can be theoretically reduced to zero by increasing the heat exchange area. Increasing the heat exchange area in the presence of a pinch point reduces the approach temperature, but a large temperature difference continues to exist at other points of the heat exchanger. Therefore, even with an infinitely large area where the pinch point approaches zero, the entropy production of the heat exchanger may never be eliminated.

In general, glides are not linear, although ternary mixtures—those consisting of three types of molecules—tend to have a more linear glide than binary mixtures. With a nonlinear glide, the pinch point can occur at any location within the heat exchanger. Figure 2.20b shows two examples with a concave and convex glide. For the concave case, the pinch point occurs at the end of the heat exchanger, while it occurs somewhere in the middle for the convex case. Therefore, its location can no longer be controlled by selecting the thermal capacity alone. Also, the existence of this pinch point cannot be observed by calculating the inlet and outlet stream temperatures.

The temperature glide depends on the difference in each components saturation temperature at a given pressure; the greater the difference the steeper the glide. However, the latent heat of each component and its molar fraction determines the temperature glide shape. Consequently, modifying the composition of the mixture

enables the transformation of the glide shape.

As seen in Figure 2.21, increasing the molar fraction of the less volatile component (higher latent heat) reshapes the glide from concave, to s-shaped, and ultimately to convex. For example, at a molar fraction of (0.9), the component with the smaller latent heat (more volatile) boils first, indicating a local boost in the temperature glide. However, as more heat is added the liquid phase becomes more saturated with the component of higher latent heat, thus smaller increments of temperature will occur when the same amount of heat is added. On the other hand, when the molar fraction is (0.1), the local boost in glide temperature results from the evaporation of the less volatile component at higher enthalpy levels.

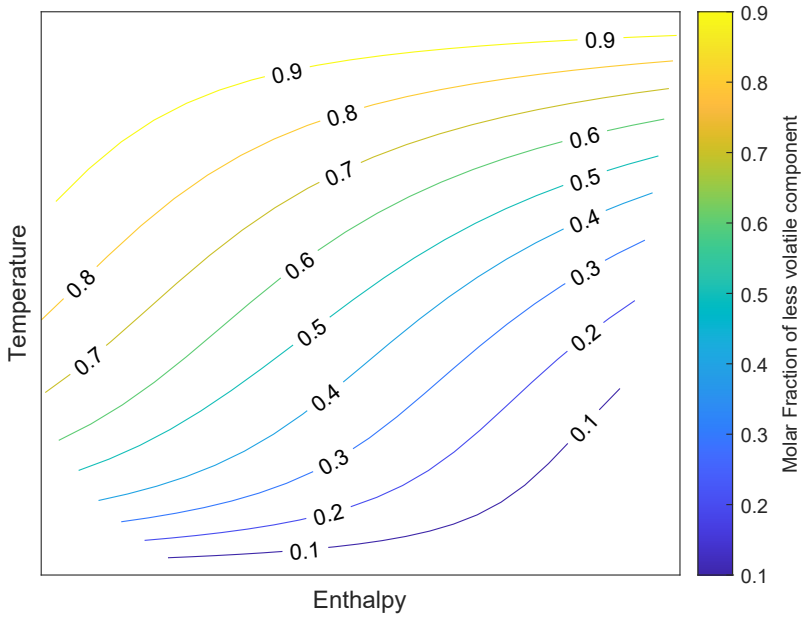

Figure 2.21: Comparison between the temperature glides at different CO_2/SO_2 mixture compositions

Temperature glide nonlinearity introduces opportunities in the design of heat exchangers. A glide may provide a better 'match' of heat profiles between streams, thus reducing entropy generation in a heat exchanger, such as a dry-cooled condenser. The engineering of the mixture composition may also be useful in matching with heat transfer medium that have non-linear glides. This is especially true in transcritical cycles, where a significant amount of the heat is recuperated internally

between a supercritical cold stream and subcritical hot stream. With a pure fluid, energy recuperation is limited by a fixed saturation temperature, whereas a zeotropic mixture increases the range of recuperation while simultaneously matching the heat profile of the supercritical stream.

Temperature glide nonlinearity also introduces it own challenges. A high glide temperature value may cause the fractionation of the mixture during the phase change process, namely heat recovery and condensation in transcritical cycles. If a leak occurs, fractionation would result in a rapid change in the working fluid's composition, which would negatively impact the cycle operation (Noriega Sanchez et al. 2019).

2.4.6 Mixture phase behaviour

The critical point of mixtures does not necessarily coincide with the maximum temperature and pressure above which the two phases merge into a supercritical phase. The critical point is no longer at the apex or peak of the two-phase region; hence, vapor and liquid can coexist in equilibrium at $T > T_c$ and $P > P_c$. Instead two new maxima are identified: the cricondenbar (P_{cc}) and cricondentherm (T_{cc}), which are the maximum conditions at which two phases can coexist.

The shape of the coexistence region gives rise to the phenomenon of retrograde vaporization when the fluid is heated along an isobar between P_c and P_{cc}. This should be regarded when optimizing a power cycle because it may occur during heat addition if the pump outlet pressure is below P_{cc}. Such a condition would thus give rise to two-phase flow in the heat exchangers, which may cause an internal pinch-point in the primary heat exchanger. Likewise, retrograde condensation may occur in isothermal or near isentropic expansion at temperatures between T_c and T_{cc}, however, this is unlikely in CSP power cycles operating with CO_2 based working fluids as the turbine inlet temperature will be higher than T_{cc}.

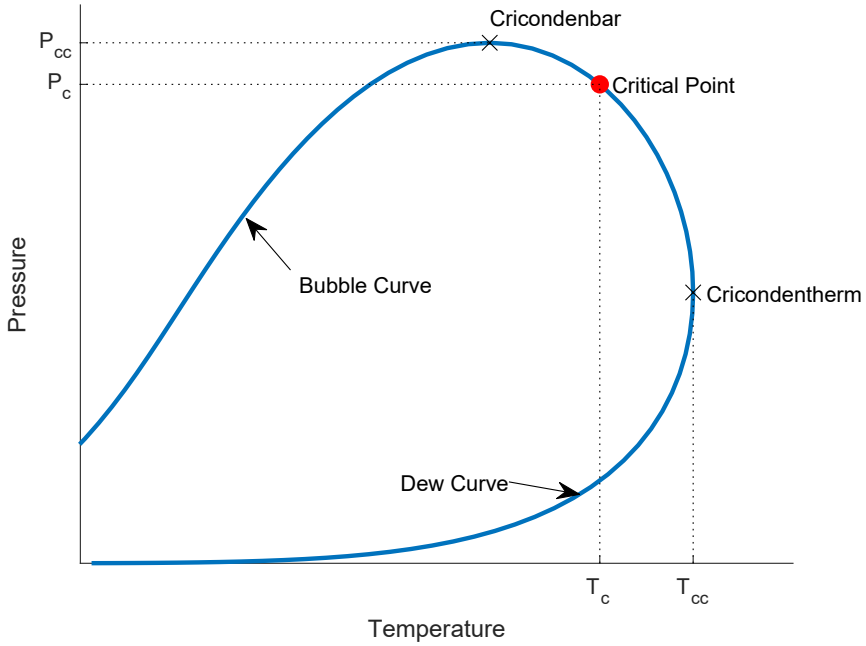

Figure 2.22: Pressure-Temperature coexistance region for a generic binary mixture

2.4.7 The supercritical state space

The physical conditions of the working fluid at each junction in a power cycle are not readily obvious, especially upon crossing into the supercritical phase. This section serves to demystify, at least in a broad sense, the state space in which the power cycles are expected to operate.

Recent research has shown that the supercritical state is not entirely homogeneous as previously thought. Instead it is divided into two broad regions distinguished by their thermodynamic and dynamic features; one liquid-like and the other gas-like. The two regions are separated by a set of lines known as the Widom lines, which are loci of maximum response functions (specific heat capacity, isothermal compressibility, thermal expansion, etc.). Different properties have different lines. The region encompassed between those line is known as the Widom region, or the pseudo-boiling region, which resembles a wedge pointing towards the critical point in a P-T plane (Imre et al. 2015). The transition between the states is reflected in macroscopic properties such as density. There is no precise limiting pressure, but a universal weakening in the thermodynamic character of the transition is observed to the point of being negligible at $P_{\mathrm{r}} \approx 3$ (Banuti et al. 2018). The Widom 'transitional'

region is shown in Figure 2.23.

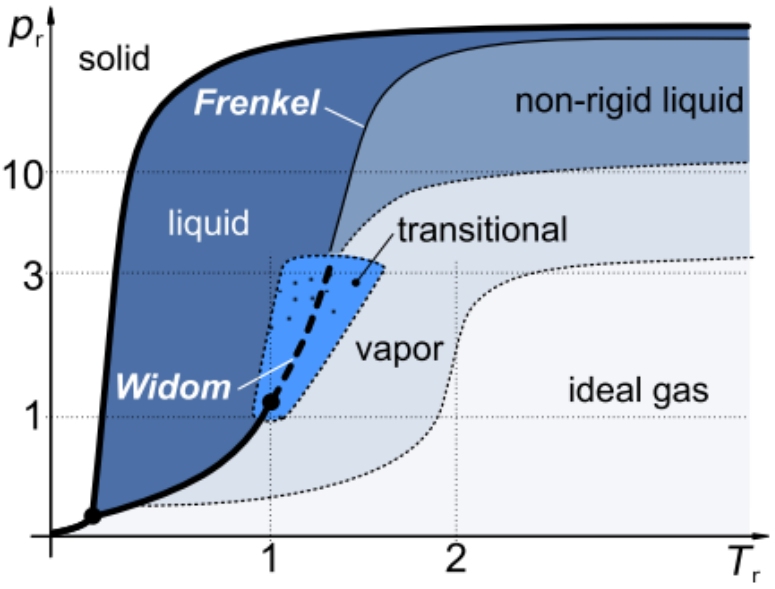

Figure 2.23: Revised phase state $P_r - T_r$ structure for a Argon according to Banuti et al. (2018)

Using Molecular Dynamics modelling Raju et al. (2017) were able to study the supercritical state space of binary mixtures of varying miscibility. They concluded that highly miscible Type I mixtures exhibit a single set of Widom lines similar to pure fluids. On the other hand, immiscible Type III mixtures exhibit two distinct Widom lines indicating separate phase transitions. They also note that cubic equations of state are only able to detect a single set of Widom line, regardless of the mixture type.

The abrupt change in the heat capacity at the pseudo-boiling region will likely result in an internal pinch point in the heat exchanger, thus limiting its performance and increasing entropy generation. Therefore, Type I mixtures are expected to have better heat exchange performance than Type III mixtures. The ideal gas behaviour of a fluid may be predicted by studying the compressibility function within a P_r-T_r plane, shown in Figure 2.24. As suggested by Banuti et al. (2017), if deviations of 5% in compressibility are acceptable for ideal gas behaviour, then supercritical fluids with $T_r > 2$ and $P_r < 3$ can be considered as ideal gases.

Transcritical cycles operate across these regions. The pump is expected to operate

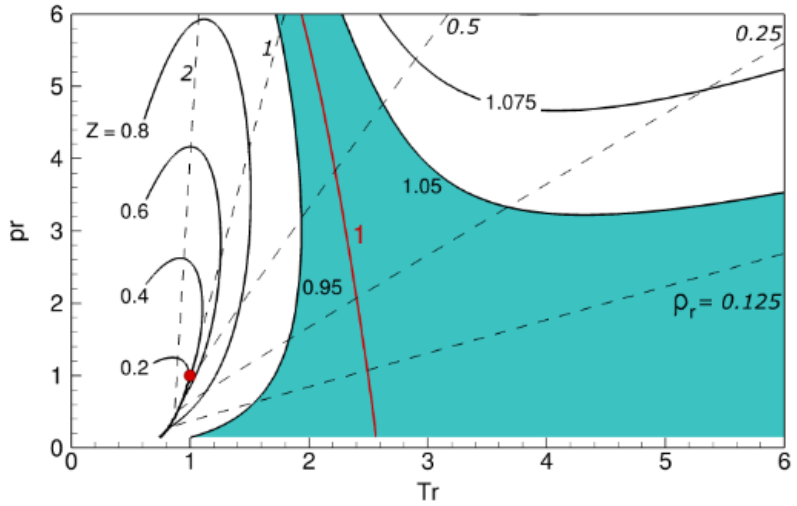

Figure 2.24: Real gas compressibility Z (solid lines) in pure Nitrogen $P_r - T_r$ diagram. Dashed lines are isochores. Regions of less than 5% deviation from ideal gas behaviour are shaded. The critical point is marked by the red circle (From (Banuti et al. 2017))

in the liquid region ($T_r < 1$, $P_r < 1$), while expansion in the turbine will most likely occur in the vapor or ideal gas region, depending on optimal cycle parameters. Heat exchangers will inevitably cross the Widom transitional region during heating in the recuperators or primary heat exchangers, but most probably in the former. Therefore, recuperator internal pinch points will exist in transcritical cycles with pump outlet pressures $P_r < 3$. On the other hand, heat rejection occurs at a reduced pressure lower than unity, which is below the transitional region. Yet, the working fluid will exhibit abrupt changes in its specific heat capacity as it crosses into the two-phase region. Consequently, if condensation starts in the recuperator, then it will have an internal pinch that is more severe than that resulting from crossing the Widom region.

2.4.8 Working fluid selection

This work is part of a research effort that aims to explore the use of CO_2-based working fluids in CSP plants. Therefore, the choice of dopants is focused on those that increase the critical temperature of CO_2 to enable the operation of transcritical cycles in CSP plants. Although the list of chemical compounds is virtually endless, the choice of dopant can be focused by a set of desirable dopant properties, some of which are essential, while others are preferable. The three essential properties are: (1)

critical temperature above 70 °C (2) thermal stability above 700 °C and (3) solubility in CO_2 in all cycle conditions. The minimum critical temperature is set to ensure compression occurs far enough from the critical point that the liquids properties are not drastically affected by small changes in temperature. A critical temperature of 70 °C is a safe distance away from the design pump inlet temperature of 52 °C that liquid compression is ensured. Other, preferable, properties include:

- Condensation pressure above ambient pressure to prevent air infiltration into the cycle;
- Melting temperature lower than the lowest ambient temperature to avoid issues associated with solidification;
- High molecular complexity to reduce recuperator irreversibility;
- High thermal conductivity to reduce heat exchangers sizes;
- Low viscosity to reduce pressure losses in pipes;
- Non-toxicity and non-flammability;
- Low global warming potential (GWP), low ozone depletion potential (ODP), and atmospheric life (ALT).
- Low cost.

The working fluid selection criteria can be translated into the selection criteria for the type and amounts of dopants in CO_2 mixtures. Preference should be given to compounds that are miscible in CO_2 and are able to form Type I mixtures. They should have high molecular complexity to minimize the heat capacity difference between the two sides of the recuperator. The resulting temperature glide of the mixture should be lower than 50 °C to avoid fractionation during heat recovery and condensation.

2.5 CO_2-based mixtures

As mentioned earlier, the critical temperature of pure CO_2 is 31.10 °C. Therefore, for a sCO_2 cycle to operate near the critical point and take advantage of real gas

effects during compression, the heat sink must cool the working fluid to around its critical temperature. Transcritical or Rankine cycles require even lower temperatures for CO_2 to condensate below its critical temperature and pressure. Consequently, assuming a pinch temperature of 10 °C, the cooling medium must have a relatively low temperature below 20 °C. This may be achieved in locations where there is a large and reliable body of cooling water such as a river, lake, sea, or ocean. It is also possible in cool climates where the ambient temperature is normally below 20 °C. However, these conditions rarely apply where CSP applications are most viable.

CSP plants are mostly feasible in dry arid regions with hot climates. Viable locations such as deserts have limited access to bodies of water and ambient temperatures are relatively high throughout the year. Therefore, the efficient operation of water cooled SPT plants with CO_2 power blocks is not possible or would require costly cooling solutions, which negate the economic feasibility of such plants. A possible remedy to this challenge is to raise the critical temperature of the working fluid.

Doping of CO_2 has been explored as a means to engineer the working fluid properties to diversify the operational range of the power cycle whilst maintaining near-critical point compression. In theory, if the heat sink allows it, the minimum cycle temperature range of the cycle can be extended by lowering the working fluid's critical temperature, thus lowering the heat rejection temperature. Alternatively, an increase in the critical temperature raises the lower temperature limit of the cycle and allows it to operate at elevated heat sink temperatures. With a higher critical temperature, dry cooling becomes possible, thus expanding the cycle's operation into arid environments (Lewis et al. 2011), which is of special interest for CSP plants.

Dopants can have varying effects on the properties of CO_2 based working fluids. Along with the change in critical temperature, dopants may also change the critical pressure. Assuming that an upper limit is set for the highest pressure within the cycle, an increase in the critical pressure will narrow the pressure ratio and decrease the available work, while a decrease in the critical pressure will have the opposite effect, assuming compression occurs near the critical pressure.

Working fluids consisting of CO_2-based mixtures can be categorized into four groups based on their critical temperature and pressure relative to pure CO_2:

- Group A: lower critical temperature and pressure;
- Group B: lower critical temperature but higher pressure;
- Group C: higher critical temperature and pressure;
- Group D: higher critical temperature but lower pressure.

Although some mixture may move amongst the groups depending on the molar fraction of the dopant as seen in Figure 2.25, the grouping shown in Figure 2.26 is based on the fractions considered in previous studies.

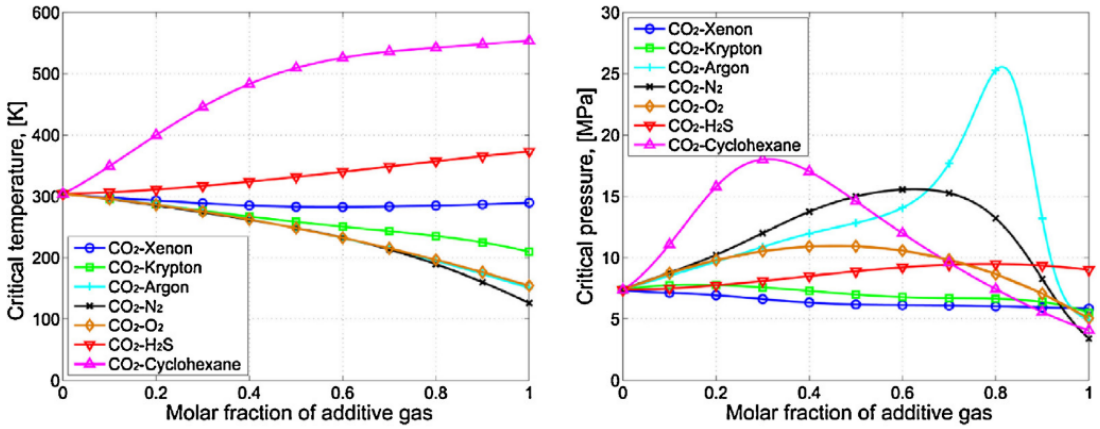

Figure 2.25: Critical properties vs molar fraction of dopant gases in CO_2-based mixture (Jeong & Jeong 2013)

Elements in groups A and B are all naturally found in their gas state since they have relatively low critical temperatures. Group A mixtures like He, Xe, and Kr have both lower critical temperatures and pressures compared to pure CO_2. Therefore, they widen the temperature range of the sCO_2 cycle and may achieve efficiencies 0.7% to 1.7% higher than pure sCO_2 simple cycles (Jeong & Jeong 2013, Jeong et al. 2011). Also, mixtures of He and Kr reduce the amount of recuperated heat, which on its own would have been detrimental to the cycle efficiency since more thermal energy would be required to fuel it. However, the decrease in recuperation is accompanied by an increase in the specific work of the turbine, thus the overall effect is an increase in the cycle efficiency (Hu et al. 2015). Moreover, the gain in efficiency compared to pure

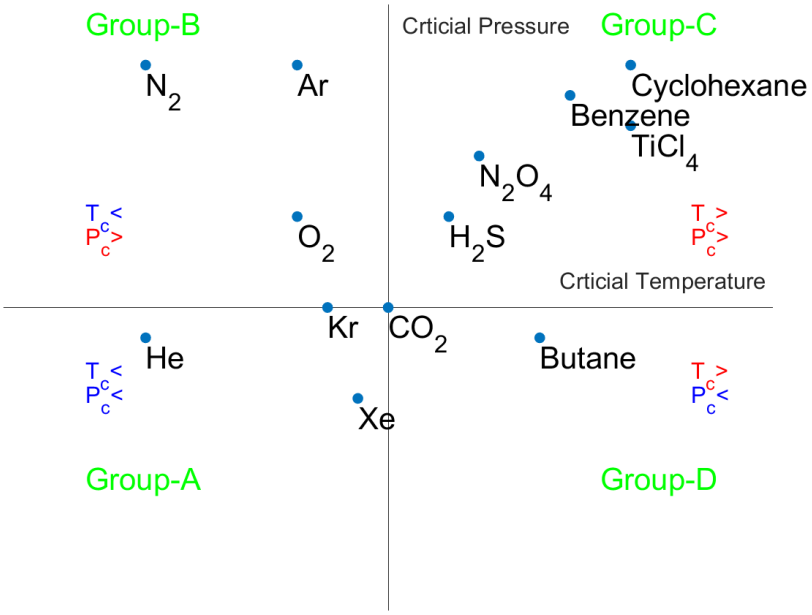

Figure 2.26: Abstract comparison between the critical properties of pure CO_2 and binary CO_2 mixtures

CO_2 is lesser in recompression cycles than in simple cycles because the re-compressor operates away from the critical point, thus benefits less from real gas effects (Jeong & Jeong 2013). These mixtures require cooler heat sinks and are unlikely to be feasible for CSP applications in arid regions were dry cooling is required.

Group B mixtures like N_2, O_2, and Ar have lower critical temperatures but higher pressures compared to pure CO_2. Although they widen the operating temperature range, the increase in the mixture's critical pressure reduces the pressure ratio and offsets the gains in efficiency. Therefore, such mixtures lead to reduced cycle efficiencies (Jeong & Jeong 2013).

Group C mixture like H_2S, N_2O_4, $TiCl_4$, benzene, and cyclohexane should reduce the efficiency of a sCO_2 Brayton Cycle by narrowing its temperature range and reducing its pressure ratio, assuming operation near the critical point. However, they outperform pure sCO_2 power cycles under the practical limitations of warm heat sink temperatures of CSP applications (Hu et al. 2015, Manzolini et al. 2019). Mixtures $TiCl_4$ have even been shown to operate in a tCO_2 Rankine cycle with dry cooling and have achieved efficiency improvements of 3% and 2% in simple and recompression cycle efficiencies, respectively (Manzolini et al. 2019).

Out of all the dopants studied, only Butane can be considered part of Group D. CO_2-Butane mixtures can have higher critical temperatures and lower critical pressures than pure CO_2. The deterioration of the cycle's efficiency because of the narrowing of its temperature range is counterbalanced-and even exceeded-by an increase in its pressure ratio. Consequently, CO_2-butane mixtures increase the efficiency the power cycle and also adapt it to dry cooling in arid climates (Hu et al. 2015, Guo et al. 2019). However, organic mixture are not practical for high grade heat application.

Organic compounds, namely hydrocarbons, have been considered as possible dopants to pure CO_2 working fluid. CO_2-based mixtures with organic compounds could achieve better performances and lower LCoE than those of pure CO_2 under both low and medium temperature heat source conditions (Xia et al. 2018). However, the highest temperatures considered for organic mixtures was around 350 °C, which is much lower than those achievable by CSP applications. This is a consequence of the limited thermal stability of hydrocarbons, which usually does not exceed 400 °C (Invernizzi & Van Der Stelt 2012). Therefore, it is prudent to exclude hydrocarbon mixtures from SPT application as they limit the exploitation of its available exergy.

Apart from efficiency, modifying the working fluid will affect other key cycle behaviour metrics such as specific work, integration ability with thermal energy, and others for which the assessment criteria was presented in Section 2.3. For example, using a CO_2-Benzene mixture has different effects depending on the cycle layout used as is evident in Figure 2.27. This indicates that the findings of previous studies of pure sCO_2 cycle behaviours comparison should not be blindly generalized to working fluids with CO_2 based mixtures. Therefore, a reassessment of cycle parametric studies for CO_2 based mixture working fluids is necessary.

Studies under the umbrella of the SCAREBEUS project have posited that mixtures of $CO_2/TiCl_4$, CO_2/SO_2, and CO_2/C_6F_6 may achieve cycle efficiencies above 50% depending on the cycle layout, turbine inlet temperature, and minimum cycle temperature; which may be as high as 60°C in the case of CO_2/SO_2 (Crespi et al. 2021, Morosini et al. 2022, Crespi et al. 2022, Manzolini et al. 2022). Most recently, it was found that mixtures outperform pure sCO_2 or steam cycles in both energy

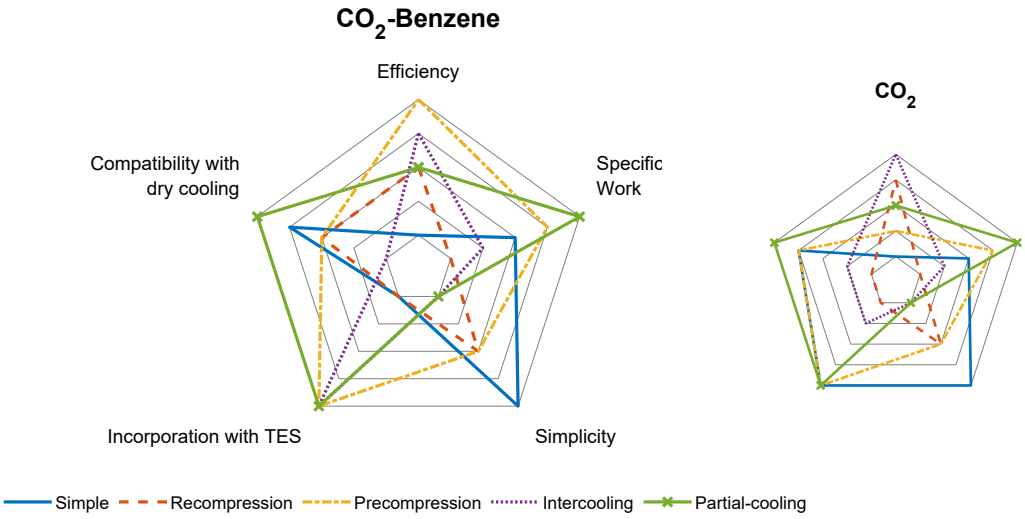

Figure 2.27: Comparison of performance metrics of different cycles in a SPT power plant for pure CO_2 and CO_2-Benzene mixture (based on results from (Khatoon & Kim 2019))

and exergy efficiencies, a difference which increases at higher ambient temperatures (Rodríguez-deArriba et al. 2022).

Another line of CO_2-mixture research is being pursued by Valencia-Chapi and co-authors. In a group of 4 studies, they investigated 16 mixtures for CSP power blocks. All of their studies show the increase in cycle efficiency compared to pure sCO_2. Similar to the SCARABEUS project, they found that the gains in efficiency depend on the choices of dopant, cycle layout, heat sink temperature, and mode of cooling (Valencia-Chapi et al. 2020*b*, Tafur-escanta et al. 2021, Valencia-Chapi et al. 2020*a*, 2022). In Tafur-escanta et al. (2021) they noted that the split fraction in a recompression cycles depends on the relative flow heat capacities of the hot and cold side of the recuperator; the greater the difference the more of the flow must be diverted and the lower the thermal efficiency. In Valencia-Chapi et al. (2022) efficiencies up to 60% were theoretically possible depending on the mixture and cycle.

Research into CO_2-mixture power blocks has also been gaining momentum with other research groups, some of which attest to the potential benefits of the technology for plants with elevated cooling temperatures (Ma et al. 2023, Bai et al. 2022, Tang et al. 2022, Niu et al. 2022, Wang et al. 2022, Bertini et al. 2021, Sun et al. 2021). Niu et al. (2022) compared pure CO_2 with CO_2-Butane, CO_2-H_2S, and CO_2-Propane

recompression cycles for SPT plants to find that all mixtures achieve greater thermal efficiencies than pure CO_2, with CO_2-Propane the favoured choice. Overall, this technology seems promising for CSP plants with relatively high heat sink temperatures (above 40 °C).

2.6 Supercritical CO_2 turbines

Amongst a power plant's equipment, turbines are known to suffer from the highest drops in efficiency when downsizing to small-scale plants. Although this is true for ORC plants (Tocci et al. 2017), because the drop in efficiency is caused by the decrease in gas flow rate and the amplification of turbine losses, there is no reason to believe that CO_2 turbines will not undergo a similar performance deterioration. Therefore, part of this thesis will be focused on the design and performance optimization CO_2 turbines from small- to medium-scales, specifically radial inflow turbines. The reason for the choice of radial inflow turbines over axial turbines will become apparent later in this section.

Research has determined that turbine performance influences the overall efficiency of sCO_2 cycles considerably (Novales et al. 2019, Dostal et al. 2004, Allison et al. 2017). One study estimated that sCO_2 Brayton cycles can only compete with state-of-the-art supercritical steam Rankine cycles in high temperature (above 600 ^oC) utility scale (150 MWe) CSP plants if turbine efficiencies are above 93%, among other conditions. They also estimated that a 1% efficiency change in turbine results in 0.31 - 0.38% change in cycle efficiency, depending on cycle type and conditions (Novales et al. 2019). While another put the figure at around 0.5% cycle efficiency for every 1% turbine efficiency (Allison et al. 2017). Therefore, it's safe to say that the path to commercial realization of CO_2 power cycles entails a better understanding of turbine behaviour.

The primary purpose of the turbine is to extract energy from the working fluid which has previously been pressurized and heated. The thermal energy of the working fluid is converted into kinetic energy in the turbine by passing it through a set of rotating blades. In axial flow type turbine, the inlet and outlet streams are parallel

to the axis of rotation. Alternatively, radial flow turbines may be used wherein the inlet flow is introduced into the turbine along the axis of rotation and the outlet flow leaves the turbine through a circumferential outlet. These two types of turbines are illustrated in Figure 2.28.

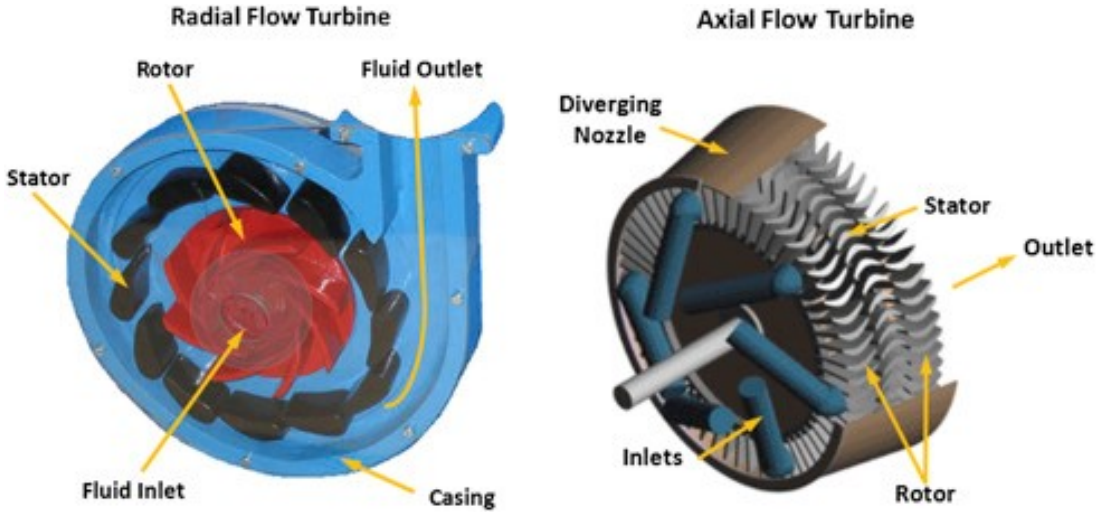

Figure 2.28: Illustration of radial and axial Turbines (from (William Emrich 2016))

There are two main ways of calculating a turbine's efficiency: total-to-static efficiency or total-to-total efficiency. The difference between the two is based on whether the kinetic energy of exhaust gas is considered to be useful or not. Total-to-static efficiency considers the kinetic energy of the turbine exhaust gas to be lost energy. Total-to-total efficiency, on the other hand, considers the kinetic energy of the gas to be useful energy which can be employed.

Dimensionless parameters are commonly used in the design of turbomachinery. Some dimensionless parameters rely on external quantities, while others rely on internal quantities. External quantities may be measured externally without probing the machine, such as the volume flow rate of the fluid, the enthalpy (calculated using pressure and temperature measurements), and rotational speed. Conversely, internal properties require knowledge of the flow characteristics inside the machine such as the flow velocity vectors. Both the flow (ϕ) and loading (ψ) coefficients, which will be defined in Chapter 5, rely on internal properties which makes them a useful reference for determining the velocity diagrams of a turbomachine. However, the specific speed relies exclusively on external parameters, which can be readily measured, and may be

used to characterise a machine regardless of its size or type; thus the specific speed has a broad application. For turbines, the conventional definition of specific speed is:

$$N_{\mathrm{s}} = \frac{N\dot{V}_4^{0.5}}{\Delta h_{\mathrm{s}}^{0.75}} \tag{2.4}$$

where [rad/s] is the rotational speed, $\dot{\mathrm{V}}[\mathrm{m}^3/\mathrm{s}]$ is the volume flow rate at outlet, and $\Delta \mathrm{h_s}[J/kg]$ is the total-to-static isentropic enthalpy change across the turbine. Other sources, such as Rohlik (1968), Kofskey & Nusbaum (1972), and Wood (1963), defined the specific speed using the total-to-total isentropic enthalpy drop. However, all specific speed values calculated in this thesis are based on Eq. 2.4, unless stated otherwise.

Although originally conceived for machines working with incompressible fluids, namely water, Balje demonstrated that the specific speed may also characterize machines that use compressible fluids. As shown in Figure 6.10, the theoretical optimal efficiency of turbines lies between a specific speed of 0.4 to 1.0. In theory, charts like this can be generated by surveying all turbines ever produced and including the most efficient of them for a given specific speed. Although Balje did rely on real turbine data to validate the chart in Figure 6.10, it is based on theoretical designs generated by advanced preliminary design methods. Because Baljes model was verified for a limited number of test machines, the diagram he produced are only partially reliable, but provide a good benchmark against which future designs may be compared.

Because volumetric flow rate is dependent on scale, to maintain the specific speed within a favourable range at smaller scales, the rotational speed of the machine must increase to balance the decrease in the volume flow rate. This is depicted in Figure 2.30.

High rotational speeds are undesirable because they are accompanied by higher windage losses in around the rotor, and more importantly in the electric generator cavity which reduces efficiency. Moreover, the diameter must also decrease to maintain an optimal value for blade tip speeds. As the diameter decreases, tip leakage losses gain significance and also penalise turbine performance. Compact-high speed

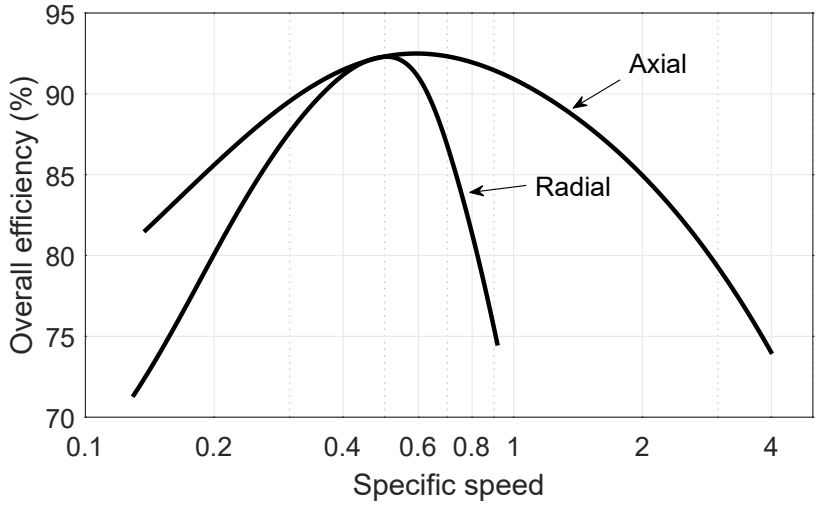

Figure 2.29: Maximum total-to-static efficiency as a function of the specific speed (Balie 1981)

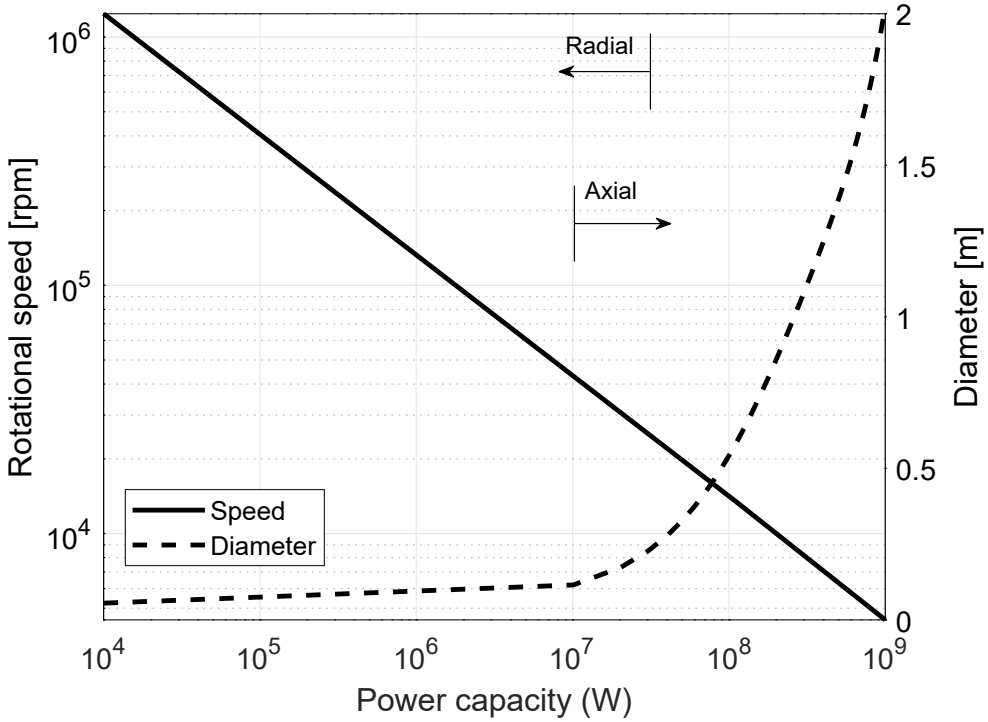

Figure 2.30: Rotational speed and diameter of a single stage turbine as a function of power capacity: small sized turbines require high rotational speeds, whereas greater power capacities require larger diameters. The turbine types recommended by Sienicki et al. (2011) are marked according to the power capacity

turbomachines may also bring forth a host of challenges regarding bearings and seals selection, rotor mechanical stresses, containment, rotor dynamics, and electric generator limitations.

On the other hand, as the plant scale increases, the speed of the turbine de-

creases and its diameter increases. However, utility scale turbines are designed for rotational speeds of 3000 or 3600 rpm, depending on the grid frequency. Gearing could be used to allow for higher rotational speeds, but it would increase the capital, operational, and maintenance costs of the turbine. Moreover, the turbine diameter cannot grow indefinitely and must be restrained for cost and mechanical integrity. Therefore, multi-staging is a common method of optimising performance within these constraints.

Supercritical carbon dioxide turbines are introduced in the literature with both radial, and axial configurations. For low volume high enthalpy drop applications resulting in comparatively low specific speeds, radial turbines are preferred while in high specific speed machines with large volume flow rates, axial turbines are preferred. Although radial machines can accommodate higher enthalpy drops per stage, they cannot lend themselves easily to multi-staging the way that axial machines can. This is because dedicated channels are required to realign the flow from the outlet of a stage to the inlet of the next, which incurs additional losses in the intermediate piping. A study of the turbine architecture types was presented by Sienicki et al. (2011) in which they proposed radial turbines for power rating from 100 kW to 30 MW and axial turbines for power rating above 10 MW. The same is marked in Figure 2.30.

To decide on the choice between radial inflow and axial turbine architectures in sCO_2 power plants, Seshadri et al. (2022) analysed turbomachinery losses for power scales between 100 kW and 1 GW using the commercial software AxStream. The turbine efficiencies increase from 76% to above 90% with an increase in power output from 100 kW to 1 GW. The corresponding optimal low side pressure decreases from 95 bar to 75 bar with an increase in power scale. Although this trend was not explained by the authors, it is likely due to the trade-off between cycle and turbomachinery efficiency; the former prefers higher pressure ratios, whereas the latter prefers the opposite. In small-scale turbines the increase in a few points of turbomachinery efficiency is more significant than at higher power levels. Therefore, the benefit of higher turbomachinery efficiency at lower pressure ratio to the overall cycle performance outweighs that of cycle efficiency gains from higher pressure ratio. However, as the power plants are scaled up, the trade-off leans in favour of higher pressure

ratios.

As posited by Sienicki et al. (2011) earlier, Seshadri et al. (2022) predicted that the transition from radial to axial machines occurs at approximately 10 MW for plants operating at turbine inlet temperatures of 550 ^{o}C. At sub-MW scales, the cycle efficiency is 27% due to poor turbomachinery efficiencies. Windage and stator losses due to high shaft speed and stator fluid velocities were identified as major losses at the sub-MW scale. As the power scale increases, the cycle efficiency reaches 38% at the GW scale. The dominant turbomachinery loss mechanism at this scale was profile loss.

For axial turbines, the optimal aerodynamic efficiency of the turbine covers a wide range of specific speeds ($0.5 < N_s < 1.0$), as seen in Figure 6.10. Axial turbines can handle high mass-flow rates efficiently and accommodate multiple expansion stages on a single shaft. The improvement in efficiency with increments in stage count may be deduced from the improvement in the specific speed of the turbine. As an example, consider the specific speeds shown in Figure 2.31 for 100 MW turbines with fixed speeds of 3600 RPM. In the figure, the specific speed of for CO_2-based mixtures is superimposed on the traditional specific speed vs efficiency chart introduced by Balje (1981). The left and right terminals of each horizontal line represent the specific speeds of the first and last stages of the turbine, while the specific speeds of intermediate stages lie in-between the two ends. The number of stages is indicated on the right vertical axis.

According to Balje (1981), as the exit density increases the volume flow rate and the specific speed decreases for a given power and rotational speed; therefore sCO_2 are expected to operate at a lower specific speeds compared to air turbines, which is evident in Figure 2.31. In all turbines, the specific speed of all stages increases with increments in the number of stages. However, air turbines reach specific speeds that are favourable for axial turbines with as low as 4-stages. Whereas, the 4, 12, and 8 stages are required to reach favourable specific speeds for CO_2 mixtures of $CO_2/TiCl_4$, CO_2/SO_2, and CO_2/C_6F_6, respectively. Therefore, it is expected that CO_2-based mixtures will require more stages than traditional air turbines. This is corroborated

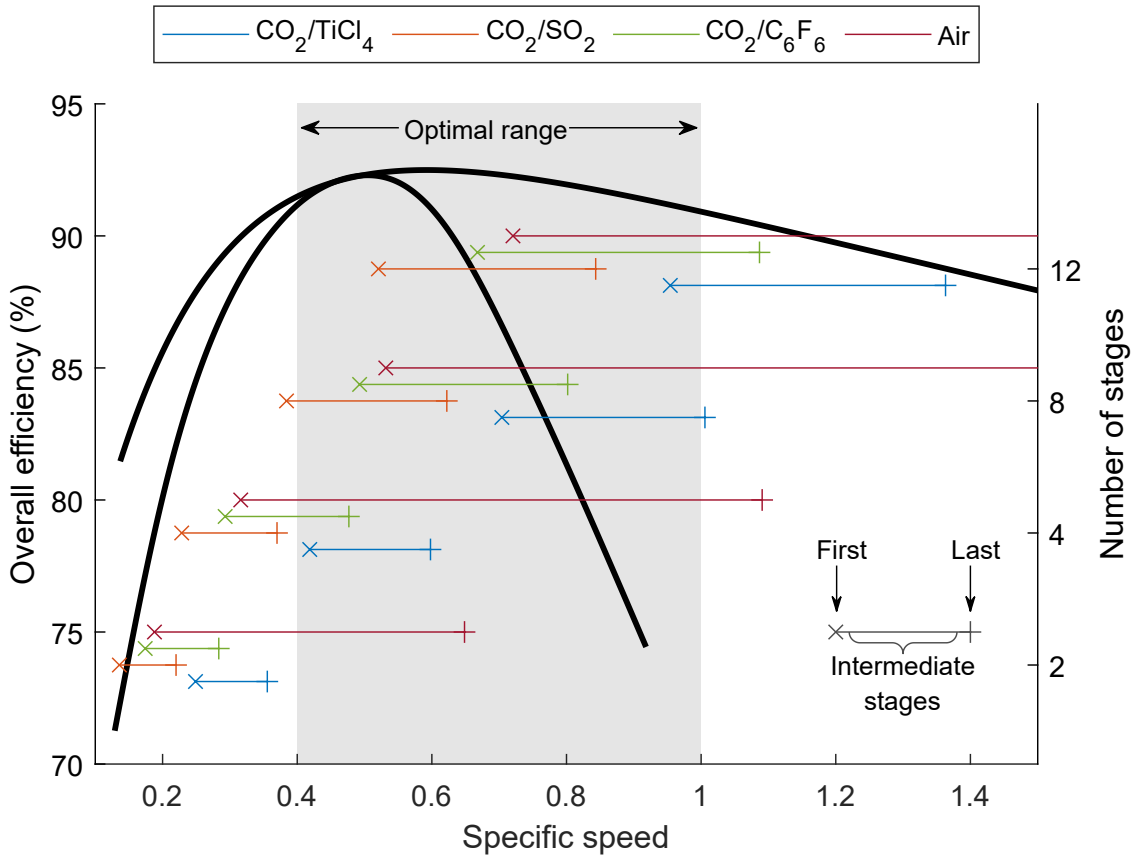

Figure 2.31: Expected turbine efficiency for a range of stages. The left axis marks the turbine efficiency as a function of the specific speed according to Balje (1981). The right axis marks the increase in specific speed with an increase in the number of stages. Compared to air turbines of equivalent power capacity, turbines operating with sCO_2 blends require more stages for the same efficiency. The curves were produced assuming a uniform enthalpy drop across all stages

by recent research by Abdeldayem et al. (2023), in which they showed that as high as 14 stages may be required in highly efficient axial turbines for sCO_2/SO_2 100 MWe power plants.

The design of a sCO_2 turbines can be quite different from those of conventional steam or gas turbines given the difference in the fluid's properties. The density of sCO_2 at the turbine outlet is 10,000 and 100 times greater than that of condensing steam turbines and combustion gas turbines, respectively. So, sCO_2 turbines tend to be smaller in size than either (Allison et al. 2017). Consequently, the operating speeds of sCO_2 turbine are much higher than conventional turbines of the same power output and may be in the range of a few hundred thousand RPM for small scale cycles.

Moreover, the high density of sCO_2 at the turbine outlet results in relatively low

volumetric flow rates compared to the enthalpy head. Scaling up the power plant maintains the enthalpy head across the turbine while increasing volume flow rate (Allison et al. 2017). Therefore, a transition from radial inflow to axial flow turbine design is expected when scaling up because axial turbines exhibit better performance at high flow rates and lower enthalpy heads. This is shown in Figure 2.32 which favours radial turbines below 10 MWe, and axial machines between 30 MWe and 100 MWe. It also shows that the speed reduces with increasing scale.

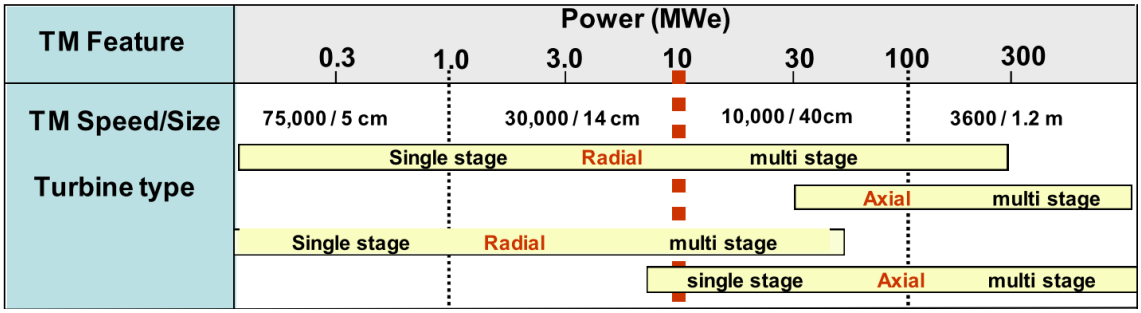

Figure 2.32: Scaling effect on turbine speed and type (Sienicki et al. 2011)

sCO_2 turbines are expected to operate at high temperatures and pressures, and thus face a metallurgical challenge in terms of thermal and mechanical stresses. This combination of high pressure, high temperature, and small size is comparable to that of rocket turbopumps and is unique to sCO_2 within the domain of power generation as seen in Table 2.1. Even advanced ultra-supercritical steam turbines which operate at similar conditions are far larger in size, and thus are subject to less strenuous thermomechanical stresses. Consequently, the combination of high pressure and small diameter in sCO_2 turbines result in fluid stresses that are comparable to centrifugal induced stresses (Fuller et al. 2012).

Table 2.1: Comparison of normal operating range of different turbines

Parameter	**Steam Turbines**	**Gas Turbines**	**sCO_2 Turbines**
Inlet Temperature [°C]	250 to 550	900 to 1200	450 to 700
Pressure Ratio	~50	7 to 15	2 to 6
Inlet Pressure [Bar]	3 to 250	~60	250 to 350

Owing to its relative infancy, research into CO_2 mixture turbines is limited. Although there is an existing body of literature on turbines operating with organic mixtures for organic Rankine cycles, they do not encounter the same technical challenges

as those facing CO_2 turbines; namely aerodynamic and rotordynamic constraints imposed by a high power density, high rotational speeds, and high operating temperatures. Nonetheless, there have been many investigations into pure supercritical CO_2 turbines.

It is customary to non-dimensionalise the kinematics of fluid flow in turbines to describe dynamic similarity between turbomachinery. In doing so, we may compare between turbines of various sizes and operating conditions. By mapping the flow (ϕ) and loading (ψ) coefficients, a group of turbine designs from the literature are compared with the widely used air turbine efficiency contours shown in the background of Figure 2.33. Generally, the relation between coefficients and efficiency for medium to large turbines (above 1 MW) is similar to that of the air turbine efficiency contours. A notable exception is Persky et al. (2015), which achieves 86% efficiency at a non-optimal value for the loading coefficient. Upon inspection, the original paper does not disclose details about the loss models used whilst presenting non-ideal flow angles for the turbine. Therefore, an informed judgment about this outlier cannot be made. Nevertheless, outliers were also present in the initial data set used to plot these contours (Chen & Baines 1994).

For small-scale (<1 MW) turbines, the efficiency is lower than that suggested by the contours. Seeing that these contours were originally created with test data from small scale air turbines, they should still be able to predict the efficiency of future small scale turbine designs. Although this may be true for air turbines, it may not be the case for sCO_2 because of its high-power density. Because aerodynamic losses, namely clearance loss, become a greater drain on small scale sCO_2 turbines than they would for air turbines, the discrepancy between the data points and the contours is warranted.

The agreement between the trend in sCO_2 turbine efficiencies and the contours suggests that the loss models developed for air turbines may be implemented to the design of sCO_2 turbines. Although they overestimate small scale turbine efficiencies, they still provide a sense of the optimal turbine design space. The same was corroborated by Unglaube & Chiang (2020) in their conclusion that the same design

principles of air turbines may be followed for sCO_2 turbines. Moreover, Cho, Lee, Lee & Cha (2016) attempted to validate a 1D mean-line design code with the scarce experimental data that was made public by Sandia Laboratory in the USA. The efforts were challenging because windage losses in the experimental data were excessive and were not predictable by the 1D model. However, by applying a correction factor to windage loss, they concluded that the loss models traditionally used for air gas turbines may accurately predict the losses in sCO_2 turbines because the working fluid behaves as an ideal gas in both cases.

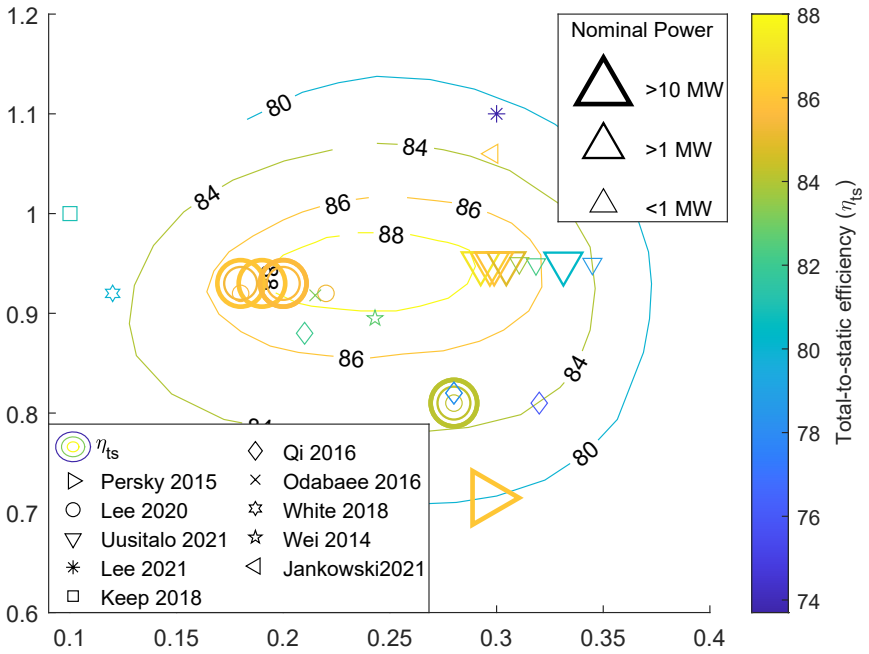

Figure 2.33: Smith-type chart showing the efficiency of RIT turbines from literature based on their flow and loading coefficients (Persky et al. 2015, Lee & Gurgenci 2020, Uusitalo & Turunen-saaresti 2021, Lee et al. 2021, Keep 2018, Qi et al. 2017, Odabaee et al. 2016, White & Sayma 2018*a*, Wei 2014, Jankowski et al. 2021)

Based on the available literature, RITs range from the very small (tens of kW), to the medium scale (1 to 10 MW), to fewer examples of larger designs (above 10 MW). Predictably, small to medium sized turbines have been actualised in several prototypes, while large RIT are yet to be demonstrated experimentally. The histogram of Figure 2.34 illustrates this by accentuating the numbers of conceptual and experimental designs. According to a review of expander designs by Du et al. (2022), the radial inflow turbine is the most studied architecture in sub-200kW sCO_2 power

applic

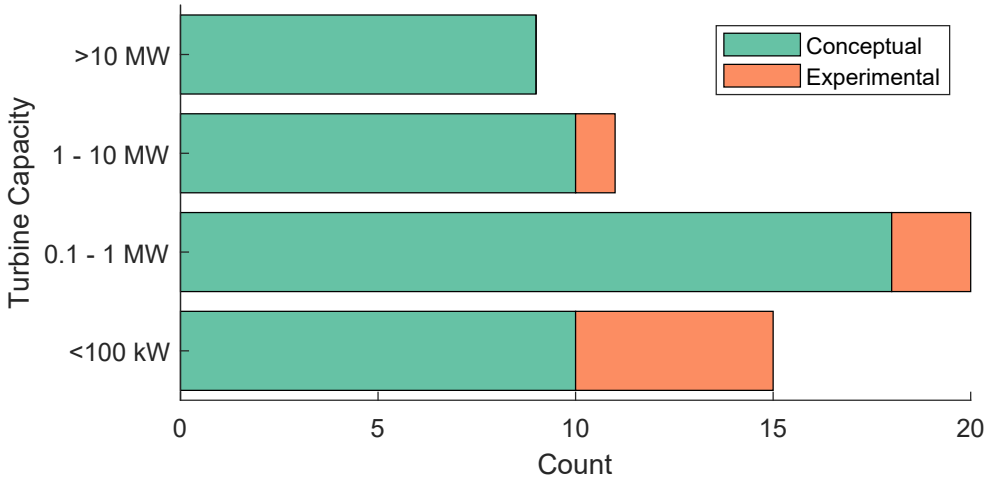

Figure 2.34: Histogram illustrating the current count of RIT designs in the literature (Bianchi et al. 2019, Steven et al. 2011, Pasch & Stapp 2018, Clementoni et al. 2014, Held 2014, Utamura et al. 2012, Ahn, Lee, Kim, Lee, Cha & Lee 2015, Shin et al. 2017, Hacks et al. 2018, Bianchi et al. 2019)

Several authors have investigated the design of sCO_2 turbines of varying scales to reveal its critical design considerations and the expected range of efficiencies. The largest RIT thus far was investigated by El Samad et al. (2020) who assessed the performance of a 100 MW utility scale RIT operating within an Allam cycle. Depending on the pressure ratio, the designed turbine may achieve total-to-static efficiencies of up to 86%, with lower pressure ratios improving efficiencies. A similar observation was made by Uusitalo & Grönman (2021). In that study, the turbine efficiency ranged between 80% to 87% for 0.1 MW and 3.5 MW capacity RIT. Moreover, passage and exit losses had the greatest adverse effect on turbine efficiency. While predictions of single stage 1.5 MW radial and 15 MW axial turbines were able to achieve 83.96% and 80.02%, respectively (Zhang et al. 2015).

A mean-line design is an effective step to home in on a proximate turbine design with little computational cost compared to refined numerical analysis and optimisation using CFD. Using a 1D mean line design code called TOPGEN, Qi et al. (2017) explored the radial inflow design space within the confines of performance and geometric constraints . The design space was mapped on a (ϕ) vs (ψ) coordinate to show the effects of power- and speed-scaling based on three cases: 100kW at 160kRPM, 200kW at 113 kRPM, and 100kW at 120 kRPM.

Among their conclusions, they posited that constant specific speed scaling would maintain the same loss breakdown; however, as will be shown in Chapter 6, specific speed scaling does not maintain the same loss breakdown if the turbine power capacity is scaled in orders of magnitude. Moreover, they identified the rotor absolute and relative inlet angles and the blade height to be among the most stringent constraints of sCO_2 radial turbine design space in the 100 kW to 200 kW range. According to the same study total-to-static efficiencies up to 82% are possible and that the most significant sources of loss were passage and tip clearance losses. However, in an attempt to simulate the results of Qi et al. (2017) it was found that those efficiencies were likely underestimated by at least 2% because the authors of that paper had doubled the passage losses based on an erroneous implementation of the passage loss model. Therefore, the efficiency quoted in Figure 2.33 was adjusted by adding 2% to the efficiency claimed in the original source.

Uusitalo & Turunen-saaresti (2021) investigated the effect of clearance gap height on the performance of sCO_2 radial inflow turbines by designing cases with gap heights of 0.1 mm, 0.3 mm, and 0.5 mm for mass flow rates between 1 kg/s and 25 kg/s . It was shown that clearance loss increases with gap height, especially for smaller designs. For example, an increase in gap height from 0.1mm to 0.5mm decreases total-to-static efficiency by 10% for a small turbine with a mass flow rate of 1 kg/s. On the other hand, the same increase in blade height would only decrease efficiency 2% for a turbine with a mass flow rate of 25 kg/s.

There have been some studies addressing aerodynamic losses in sCO_2 RITs. Zhou, Wang, Xia, Guo, Zhao & Dai (2020) pointed out the vulnerability of sCO_2 RIT to tip clearance due to their relatively compact size. They demonstrated this by analysing a 1 MW RIT using computational fluid dynamics (CFD). An increase in the dimensionless tip clearance of 6% (from 2% to 8% of the leading edge height) was shown to decrease efficiency by 3.84%. They also showed that the addition of a volute may reduce efficiency by 2%.

Lv et al. (2018) analysed loss correlations using 1D generated designs and CFD simulation results. Based on their analysis, a specific set of nozzle and rotor loss

models was recommended. An even more comprehensive rotor loss assessment study, including 30 different models (some of which with their own variations), was conducted by Persky & Sauret (2019). Both studies agree that the best choice of passage loss model is that developed by Wasserbauer & Glassman (1975) at NASA; however, Persky & Sauret (2019) noted that the CETI model, presented by Moustapha et al. (2003), is more accurate in estimating design-point efficiency. On the other hand, a study by Uusitalo & Grönman (2021) concluded that the CETI model was a better option for modelling passage loss in sCO_2 turbines, specifically for specific speeds in the range of 0.4-0.65. Alternatively, Ventura et al. (2012) used a combination of both approaches and averaged their results.

Because of the diminishing significance of aerodynamic losses, scaling up the axial turbine and adding more stages increases the turbine's total-to-total efficiency to around 90% for varying scales of 10 MWe, 50 MWe, and 450 MWe (Shi et al. 2019, Bidkar et al. 2016).

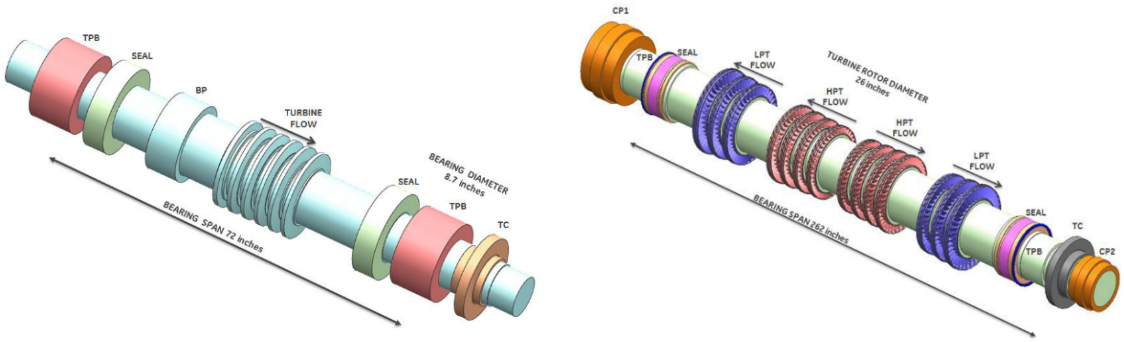

Figure 2.35: Conceptual model of turbines; (left) 50 MWe, (right) 450 MWe

Kalra et al. (2014) designed a four-stage axial turbine for a 10 MW CSP plant. The study focused on practical considerations such as mechanical integrity, vibrational damping, sealing, shaft assembly, and operational transients. It highlighted the unique challenges imposed by sCO_2 turbines such as high torque transmission requirements, small airfoil design and fabrication, aero-design optimisation with mechanically safe blade design, and high cycle fatigue life of the rotor.

Turbine performance can either be measured through an experimental rig employing a built prototype, or estimated using CFD or loss models. Among these options,

loss models require the least resources and rely upon one-dimensional modelling of fluid flows. Understanding the loss mechanisms not only requires an understanding of the underlying fluid mechanic and thermodynamic process that generate entropy in the turbine, but they also need to be refined by empirical formulas validated with test results. Such mechanisms are well established for steam and gas turbine models, but are virtually non-existent for sCO_2 due to the lack of empirical data. However, some authors have attempted to predict the performance of sCO_2 turbines either by utilizing existing gas models in CFD and comparing the results with preliminary design predictions or by using what little data is available to adapt existing models.

Vane et al. (2014) designed the first stage of a sCO_2 axial turbine by mean-line design and 3D design using STAR-CCM+ CFD package. They found that both methods predict similar vane geometries, but mean-line design overestimates the efficiency of the stage when compared to the CFD analysis. The reason for the discrepancy was attributed to the inadequacy of Soderberg loss calculations to capture all primary losses. They also observed that the fluid's high density at turbine inlet will result in relatively short blades, which promote secondary flow and tip clearance losses that reduce efficiency. Additionally, the loading coefficient was found to be high enough to warrant a 6-stage turbine.

Vilim (2011) developed a 1D design model for small scale radial inflow turbines using experimental data published by Sandia National Laboratory. They altered existing models by adding a heat loss model in the volute and applying multiplicative factors to the Euler head and pressure loss. Another study by Lv et al. (2018) also visited the data published by SNL, but opted to identify the most accurate existing loss models rather than develop new ones. That was achieved by systematic comparison between 1D design performance predictions of each model and the predictions of 3D CFD simulation based on SNL data. They concluded that the selected loss models provide a very high prediction accuracy for sCO_2 radial inflow turbines, and thus may be used for turbine design optimisation.

Currently, the work done by Keep (2018) is the most detailed published examination of sCO_2 radial inflow turbines. In his PhD, Keep recognised that rotational

speed will limit sCO_2 radial inflow turbines to low to medium specific speeds; away from the optimal range. To that end, he studied the nature of losses radial inflow turbine at in such a design space. He concluded that preliminary design calculations can be relied upon for turbine efficiency approximations as the geometry optimisations validated with CFD post-optimisation were able to achieve the predicted efficiencies for low specific speed radial turbines. Examples of geometry optimisations include minimizing the interspace between stator and rotor to reduce stator losses, adding splitter blades to reduce secondary flow losses. Indeed, Keep & Jahn (2019) conducted a numerical loss investigation of a 300-kW low-specific speed RIT operating with CO_2 and concluded that endwall viscous losses in the stator are more significant than predicted using gas turbine derived preliminary design methods. In the same study, they showed that optimisation of the stator-rotor interspace and blade profile, along with the addition of splitter blades an efficiency of 81% is possible (7.5% higher than the baseline). They also showed that the clearance loss is the predominant source of entropy generation and suggested using a shroud to reduce it.

Using experimental data of three turbines, Glassman (1995) calibrated the turbine losses to obtain total-to-static efficiencies within $\pm 1\%$. Using a different set of loss models and experimental data, Rodgers (1987) matched turbine efficiency to within $\pm 2\%$, and Baines (1998, 2005) validated a set of loss correlations to within $\pm 3.2\%$ using the data of more than 30 turbines. Meroni et al. (2018) calibrated the experimental coefficients of analysis of nozzle passage, rotor incidence, and rotor passage loss models using experimental data six well-documented turbines available in the open literature and CFD simulations. The calibration method employed a multi-objective optimisation based on a genetic algorithm, which resulted in a significant reduction in the deviation between the numerical model and the experimental data compared to the baseline case (no calibration). Specifically, the root mean square error across the range of turbine operating conditions decreased from 5.9% to 2.1% in the prediction of isentropic efficiency and from 2.4% to 1.5% in the prediction of the mass flow rate.

Unglaube & Chiang (2020) recommended a specific speed range between 0.2 and 0.5 for small-scale sCO_2 turbines. They had reached a similar conclusion in an earlier

study in which Unglaube & Chiang (2018) investigated the effect of the specific speed (N_s) and velocity ratio (ν_s) on the efficiency of small-scale radial inflow turbine using CFD simulations. They concluded that efficiency is maximised in the range of $0.2 < N_s < 0.4$; designs with specific speed higher than 0.6 would require excessively high rotational speeds in small-scale sCO_2 turbines.

Some research into sCO_2 RIT has progressed into thermal and structural design of the impeller and shaft arrangement (Uddin et al. 2021, Li et al. 2021). Uddin et al. (2021) identified bearing and seal as critical challenges to sCO_2 radial inflow turbines. They analysed the possibility of using dry gas seals and journal bearings by isolating them from the hot gas with cooling zone. By analysing the cooling requirements and mechanical stability of 0.5 MW and 10 MW turbines, they produced generalised charts and equations to evaluate the trade-off between rotor shaft stiffness and temperature limitations.

2.7 Existing demonstration plants

The growing interest in sCO_2 cycles has encouraged the construction of many experimental facilities to investigate its technological limits. Most facilities are aimed at testing heat exchangers, but there are several that focus on turbomachinery design and testing. The test loops have provided valuable insights into the practical challenges facing sCO_2 turbomachinery; which may prove useful in future designs.

Based on the chosen control strategy, an integral loop may include turbomachinery in configurations of one or more Turbine-Alternator-Compressor (TAC), Turbine Generator (TG), or Compressor-Motor. So far, the preferred choice for small-scale machines has been radial-inflow turbines with labyrinth seals and gas journal bearings. A detailed description of all turbomachinery testing facilities is available in the literature. Table A.1 of Appendix A summarizes their design characteristics. The following section will only focus on the crucial findings of the test loops; not their technical details.

Perhaps the most prominent of all loops is that of Sandia National Laboratories

(SNL) (Clementoni et al. 2017). The results obtained at SNL confirm the compressor's performance sensitivity to inlet conditions when operating near the critical point. However, they also note that there isn't an observable degradation in compressor hardware when operating with two phase fluid; which is probably because of the similarity in density of CO_2 in liquid and vapor phases. Moreover, significant erosion of material at turbine inlet has been reported, which has been attributed to the high pressure and temperature conditions. SNL results also confirmed the applicability of standard design tools to sCO_2 turbomachinery.

A few loops have made serious attempts to quantify windage losses. The Integrated System Test (IST) at the Naval Nuclear Laboratory in the U.S. found motor-generator cavity windage losses in the turbine generator to be greater than predicted because of the small-scale coupled with high rotor speeds (Clementoni et al. 2017). They recommended using labyrinth seals and lowering the generator cavity pressure. Likewise, the Tokyo Institute of Technology (TIT) emphasized the significance of windage losses in their 10 kWe test bench (Utamura et al. 2012). They also identified possible irreversibilities caused by local vortex induced pressure drops that lead to phase change during compression.

Four loops were tested in South Korea; one at Korea Advanced Institute of Science and Technology (KAIST) (Ahn, Lee, Kim, Lee, Cha & Lee 2015), and three at Korea Institute of Energy Research (KIER) (Cho, Shin, Ra, Lee, Lee & Baik 2016). Researchers at KIER consider the high pressure at turbine outlet to be the primary characteristic of a sCO_2 cycle which causes high axial force, high windage loss, difficult turbomachinery layout design, rotordynamics, bearing, seal and leakage problems. They also emphasize the need for proper leakage management to mitigate loss of working fluid due to high pressure. Most notably, the first sCO_2 axial turbine was tested at KIER and is currently one of only two in the world. The second and larger of the two axial turbines is currently being tested at the Southwest Research Institute (SwRI) in the USA with a design capacity of 1 MWe (Allison et al. 2019).

Other notable facilities include the first commercial waste heat sCO_2 cycle built by Echogen (Clementoni et al. 2017). It validated the technical feasibility of large

scale ($> 1MW$) radial flow turbomachinery and tests claim turbine efficiencies up to 80% were achieved. There is also a small scale turbopump under testing at CVR for the European funded sCO_2 HeRO project (Hacks et al. 2018).

2.8 Summary

The abundance of solar energy will make it one of the pillars of future electricity sources. Among the proven methods of harvesting solar energy, solar power towers show the greatest potential for electricity generation thanks to their ability to achieve high aperture temperatures. However, the future wide-spread deployment of this technology necessitates a reduction in its cost.

A possible way of making SPT more competitive is to reduce the cost of the power block, or increase its efficiency. Supercritical Carbon Dioxide cycles might fulfil this requirement as they boast higher efficiencies and more compact turbines compared to current SPT power blocks operating with steam. However, they also face unique challenges when deployed in SPT plants. With a high rate of internal heat recuperation, sCO_2 cycles are less compatible with TES, thus require larger and more costly TES systems. Moreover, because wet cooling may not always be an option for SPT plants, dry cooling will likely be required. Because they exploit real gas effects near the critical point, sCO_2 power cycles are generally sensitive to fluctuations in compressor inlet temperature. This may deteriorate their performance when dry cooling is used in arid climates with ambient temperature fluctuations. To mitigate these fluctuations, compression can occur below the critical point in a transcritical cycle, whilst maintaining good efficiency.

Adopting transcritical CO_2 cycles with dry cooling requires relatively low ambient air conditions since the critical temperature of CO_2 is 31.1 ^{o}C. To overcome this, the working fluid may be doped to increase its critical temperature and allow the operation of tCO_2 power blocks in SPT plants. Studies have shown this to be a promising pathway to lower the cost of current SPT technologies, thus it is a subject worth studying in more detail. What few studies that have been conducted indicate that conventional sCO_2 cycle layouts will behave differently when operating with a

mixture.

Because turbine performance is expected to greatly influence the performance of the power block, ensuring high turbine efficiencies is an imperative part of the design process. Research into sCO_2 turbines has shown its compactness and high-performance potential. High rotational speeds, aerodynamic losses, and mechanical integrity—are amongst the possible design restrictions that must be heeded in the turbine design process, especially in small scale power plants. Nevertheless, feasible design spaces and preliminary designs have been outlined.

Thus far, efforts to study the effect of doping CO_2 on the feasible design space have not been made. Doping CO_2 will change its thermodynamic and transport properties such as heat capacity, thermal conductivity, density, and viscosity. Therefore, a more detailed comparison between dopants requires an accurate probe of their implications on all major cycle components, not only turbines.

Going forward, this thesis will focus on modelling, analysing, and optimizing CO_2 transcritical power cycles and turbines. Ultimately, the investigation aims to identify the effect of doping CO_2 on the cycle and turbine designs in CSP plants across power scales. In Chapter 3, the effect of doping CO_2 on cycle design and on the expansion process is explored through a 100 MWe CSP plant employing multistage axial turbines. On the other hand, CSP plants may offer distributed and dispatchable electricity to off-grid locations that require lower power capacities, which employ radial inflow turbines. Therefore, in Chapter 6 the effect of doping CO_2 on the design of single stage radial inflow turbines is investigated.

Chapter 3

Cycle Modelling and Optimisation

3.1 Introduction

The methodology and models introduced in this chapter are used in the subsequent chapters. First, the available methods for calculating the thermophysical properties of the working fluids are explored presented. Thereafter, the models that are used to simulate transcritical cycles, both simple and recompression layouts, and their components are detailed. A description of a mean-line model that is used to generate preliminary designs of multistage axial turbines for large scale CSP plants is also included; however, Chapters 5 and 6 will focus on radial inflow turbines for small- to medium-scale plants. Lastly, a brief description of the optimisation algorithm and the computer software used in this thesis is included at the end.

3.2 Working fluid model

In this section the thermodynamic basis of working fluid property estimation by means of Equations of State (EoS) is explored. A previous study by Zhao et al. (2017) concluded that the choice of EoS has a trivial effect on the overall thermal efficiency of a pure sCO_2 cycle, but has a measurable effect on equipment sizing and subsequent cost. An elaboration on the EoS is of particular interest when modelling multicomponent working fluids; because it may account for the disparity in intermolecular

interaction among its components and its non-ideality.

Thermodynamic and physical properties of real fluids needed for process design are usually calculated through various thermodynamic models and equations. Generally, there are four categories of thermodynamic models:

1. Equations of state model.
2. Empirical equations and generalized correlations.
3. Activity coefficient models.
4. Specific models.

Equations of State (EoS) are usually used for vapor phase calculations, but still yield sufficiently accurate results in the liquid, if well calibrated. The equations in common use can be classified as being of the Van der Waals family of cubic equations (SRK, PR, etc.), of the extended virial family of equations (BWRS), or equations based more closely on results from statistical mechanics and computer simulations (SAFT or MD) (I. Sandier & Orbey 2000). Activity coefficient models, on the other hand, use free excess enthalpy to model liquid phase thermodynamics. Examples of activity models include van Laar, Non-Random Two Liquid (NRTL), and UNIQUAC.

The approach to thermodynamic modelling may adopt either an EoS or an activity model, or a combination of both. A homogeneous approach applies an EoS for both phases, while a heterogeneous approach limits the EoS to the vapor phase and uses activity models to predict liquid phase properties. A combined approach is one which incorporate activity models within complex mixing rules of the EoS.

3.2.1 The equation of state

In describing the thermodynamics of substances, we begin with the most basic model; that of the perfect gas. A perfect gas is macroscopically defined as a theoretical fluid obeying the equation of state $pV_{\mathrm{m}} = RT$. From a molecular viewpoint, a perfect gas is a fluid in which the individual gas particles have no interaction upon one another (neither attraction, nor repulsion). In reality, there exist attractive and repulsive forces between particles, which manifest in the macroscopic properties of a

fluid.

Theoretically, real fluids may behave like a perfect gas if their pressure is reduced to zero. In such a state, the molecules of a fluid occupy an infinite volume, therefore interactions with other molecules become unlikely. Real gas behaviour is demonstrated when intermolecular interactions are accounted for, which leads to deviations from perfect gas behaviour like incompressibility. The equation of state formulated by Van der Waals (VdW) in 1873 has been the most influential in the development of popular successive engineering equations. VdW EoS uses the principle of corresponding states to describe the properties of any fluid, which requires only the critical temperature (T_c) and critical pressure (P_c) of the fluid.

$$P = \frac{RT}{(V-b)} - \frac{a}{V^2} \tag{3.1}$$

$$a = \frac{27}{64}\frac{R^2T_c^2}{P_c} \tag{3.2}$$

$$b = \frac{RT_c}{8P_c} \tag{3.3}$$

where a and b represent the attractive and co-volume (repulsive) terms. Thus, the VdW EoS differs from the ideal gas equation by acknowledging the impact of intermolecular forces.

Many approximate equations of state have been proposed based on VdW original work. One of the most popular is the Peng-Robinson EoS (1976), which incorporates the dependency of the attractive term 'a' on the molecular shape and temperature.

$$P = \frac{RT}{(v-b)} - \frac{a\alpha}{(v^2+2bv-b^2)} \tag{3.4}$$

$$a = 0.45724\frac{R^2T^2}{P_c} \tag{3.5}$$

$$b = 0.07780\frac{RT_c}{P_c} \tag{3.6}$$

$$\alpha = \left[1 + K\left(1 - \sqrt{(T_r) - 1}\right)^2\right] \tag{3.7}$$

$$K = 0.37464 + 1.54226\omega - 0.26992\omega^2 \tag{3.8}$$

$$\omega = -1 - log\left(\frac{P_{\text{sat}}}{P_{\text{c}}}\right);\ @T_{\text{r}} = 0.7 \tag{3.9}$$

$$T_{\text{r}} = \frac{T}{T_{\text{c}}} \tag{3.10}$$

where, ω is the acentric factor first introduced by Pitzer (1955) to help specify the vapor pressure curve. It is equal to zero for spherical molecules like argon and methane, but deviate from zero with deviations from spherical symmetry. Moreover, the alpha function presented in Equation 3.7 was introduced by Soave (1972*a*). Alternate forms of the function have been suggested in the literature, including some which are specific to certain mixtures or certain fluid phases.

When extended to mixtures, the rudimentary form of the equation of state does not change. The properties of mixtures are estimated based on the same equation of state parameters as for pure fluids; however, parameters like a and b become dependent on composition. To incorporate compositional dependence of such parameters, mixing rules are employed. The VdW mixing rules assume random mixing with compositional dependant interaction probabilities expressed by these equations:

$$a_{\text{m}} = \sum_{\text{i}}^{NC}\sum_{\text{j}}^{NC} x_{\text{i}}x_{\text{j}}a_{\text{ij}} \tag{3.11}$$

$$b_{\text{m}} = \sum_{\text{i}}^{NC}\sum_{\text{j}}^{NC} x_{\text{i}}x_{\text{j}}b_{\text{ij}} \tag{3.12}$$

where i and j denote the pure components in a binary mixture, NC is the number of mixture components, and x is the molar fraction. The attractive and co-volumes terms are calculated based on the following combining rules:

$$a_{\text{ij}} = \sqrt{(a_{\text{i}}a_{\text{j}})\,(1 - k_{\text{ij}})} \tag{3.13}$$

$$b_{\text{ij}} = \frac{(b_{\text{i}} + b_{\text{j}})}{2}\,(1 - l_{\text{ij}}) \tag{3.14}$$

where a_i, a_j are calculated using 3.5, b_i, b_j are calculated using 3.6, and l_{ij} and k_{ij} are termed binary interaction coefficients (BIP). However, for many mixtures of roughly equal-sized molecules, the BIP l_{ij} is assumed to be zero.

The description of the macroscopic behaviour of fluids is based on a microscopic model of dynamic interacting particles. The same system may be applied to understand mixtures, specifically the way in which similar and dissimilar particles interact. In a pure fluid, all intermolecular potentials are assumed to be uniform, wherein the attractive and repulsive forces between particles are similar throughout a given phase. However, this is not true for mixtures as the size and "stickiness" of different molecules are not equal. In binary systems, a binary interaction coefficient (k_{ij}) is used as a measure of the intermolecular forces between unlike constituents of a binary mixture.

If k_{ij} is equal to zero then the attraction is assumed to be neutral and equal to the square root of the product of their intermolecular attractions. If it is negative that means that the unlike molecules attract each other more strongly than they attract their own kind. While a positive value means that, although they still attract each other, their attraction is not favourable and each would rather stick to its own kind. Moreover, positive k_{ij} may lead to reduced miscibility and liquid-liquid equilibrium like that of water and oil (Lasala 2016). In general, the interaction parameters are low for non-polar mixtures, but can be very high for mixtures containing polar and especially hydrogen bonding fluids (Kontogeorgis & Folas 2010).

There are two ways of obtaining a value for k_{ij}. The first is by regressions based on empirical Vapor-Liquid Equilibrium (VLE) data, where k_{ij} is calibrated to fit EoS predictions with empirical results. The second is through predictive models, of which there are several. Typically, k_{ij} decreases with increasing temperature, since polar and other intermolecular forces become less important at high temperatures (Kontogeorgis & Folas 2010). While, some predictive models accommodate this temperature dependency to improve their accuracy, empirically regressed k_{ij} are constant and temperature independent by definition, which may reduce their range of applicability. In by far most cases, positive k_{ij} are needed, but negative values are required for several

solvating systems, e.g. chloroformacetone. The significance of k_{ij} on EoS accuracy may be appreciated by examining Fig 3.1.

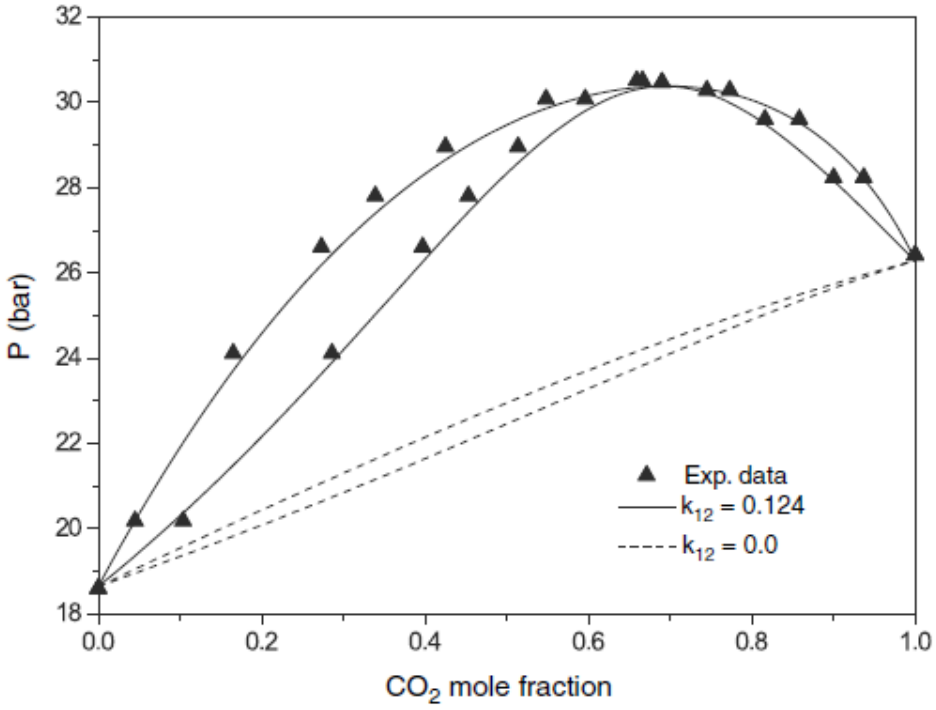

Figure 3.1: Prediction and correlation of VLE for CO_2ethane ($T = 263.15K$) with the PR EoS using the VdW1f mixing rules and the classical combining rules. From (Kontogeorgis & Folas 2010)

To summarize, the EoS offer swift and simple models capable of describing properties of compounds in both liquid and vapor phases over a wide range of pressures and temperatures. However, equations of state, by all accounts, are not perfect. They are susceptible to the interaction parameter value (k_{ij}), which may be temperature dependent. Moreover, EoS are known to overestimate liquid densities (Kontogeorgis & Folas 2010) and are inaccurate in the vicinity of the critical point (Deiters & Kraska 2012). They require system specific empirical data for their calibration, and even then, they will likely deviate from an accurate representation of the fluid's properties. At present, because a universal theory on molecular interaction is not available, no rigorous generalised theory exists for mixing rules (Angelino & Colonna Di Paliano 1998). However, cubic EoS such as PR provide a good balance between accuracy and ease of calculation, which makes them conveniently suited for the purpose of this study.

3.2.2 The binary interaction parameter

In this thesis, k_{ij} was calculated against regressed Vapor-Liquid Equilibrium (VLE) empirical data and used to tune the mixing models of all the mixtures. Determining the value of k_{ij} required an optimisation problem. By tuning k_{ij}, the calculated VLE lines were manipulated and compared with experimental data to find the best-fit k_{ij} value. An unconstrained gradient-based optimisation approach was adopted, where $h\left(k_{\mathrm{ij}}\right) = g(k_{\mathrm{ij}}) \ = \emptyset$. The weighted least mean square method was used as the objective function. Like the simple least square method, it minimizes the residuals between experimental and calculated data, but it also weighs each residual with the experimental uncertainty of the experimental data. The objective function is reduced or expanded depending on the availability of experimental data.

$$f(k_{\mathrm{ij}}) = \frac{1}{n_{\mathrm{e}}} \sum_{\mathrm{i}=1}^{n_{\mathrm{e}}} \left[\left(\frac{\hat{x}_{1,\mathrm{i}} - \widetilde{x}_{1,\mathrm{i}}}{u^{e}_{\mathrm{x}_{1,\mathrm{i}}}} \right) + \left(\frac{\hat{y}_{1,\mathrm{i}} - \widetilde{y}_{1,\mathrm{i}}}{u^{e}_{\hat{\mathrm{y}}_{1,\mathrm{i}}}} \right) + \left(\frac{\hat{T}_{\mathrm{i}} - \widetilde{T}_{\mathrm{i}}}{u^{e}_{\hat{\mathrm{T}}_{\mathrm{i}}}} \right) + \left(\frac{\hat{P}_{\mathrm{i}} - \widetilde{P}_{\mathrm{i}}}{u^{e}_{\hat{\mathrm{P}}_{\mathrm{i}}}} \right) \right] \quad (3.15)$$

where x_1 and y_1 are the liquid and vapour molar fractions of CO_2, respectively. The accents ($\wedge$) and ($\sim$) indicate the measured and calculated values, respectively. Experimental uncertainty is represented by the term u^e. The number of experiments is denoted by n_{e}.

As with any experimental data, the measurements of the VLE properties carry an uncertainty. Consequently, the value of k_{ij} that is calculated using experimental data is bound to have an uncertainty associated with it. A Monte Carlo technique similar to that used by Hajipour et al. (2014) was employed to estimate the uncertainties of the binary interaction parameters. The main four steps in applying this technique are (1) specification of probability density functions for the uncertain input variables involved in the study based on the knowledge of their uncertainty, (2) probabilistic sampling of the uncertainty space, (3) simulation and calculation of output parameters by passing each sample set through the model, and (4) statistical analysis of the results to evaluate the uncertainty of the model outputs.

In this study, the experimental data was assumed to be normally distributed in accordance with the declared uncertainty (Step 1). Random sampling with replace-

ment was repeatedly conducted for a total of 1,000 trials (Steps 2 & 3). Finally, the mean value is taken as k_{ij}, while its uncertainty is based on the 95% confidence interval from the mean (Step 4).

3.2.3 Thermodynamic property calculation

Temperature, pressure, and volume —these are properties that are calculated as absolute values using an equation of state. However, other state functions, like enthalpy and entropy, are calculated relative to a reference state using departure functions derived from the equation of state.

State functions are pathway independent, therefore calculation of real fluids properties can be computed by translations between real and hypothetical reference states. These translations are called residual functions. Sequential residual function transitions combine to formulate a departure function. Although the reference state may not be a perfect gas, the following is an explanation of the process using a perfect gas reference state.

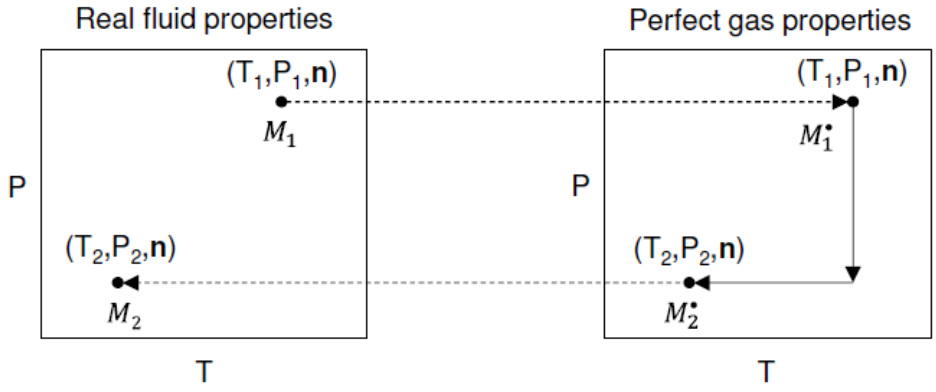

Figure 3.2: Pathway for calculating state of changes for a generic property M for a fluid of n number of moles, using departure functions. From (Lasala 2016)

In short, a departure function involves three mathematical steps: (1) turning the real fluid into a perfect gas (reference state), (2) transitioning from one perfect gas state to another, (3) turning the newly calculated perfect gas to a real fluid. A general departure function is shown in Equation 3.16, and the process is visualized in Figure 3.2, where M denotes any fundamental property, such as enthalpy or entropy,

and the subscript '*' indicates the reference state.

$$\Delta M = M_2 - M_1 = (M_2 - M_2^*) + (M_2^* - M_1^*) + (M_2^* - M_1) \tag{3.16}$$

Each quantity $(M - M^*)$ is called the residual function and represents the deviation of the real fluid property from the perfect gas property.

Two pathways are possible when formulating property departure functions; either pressure or volume dependant. The latter is more conveniently expressed in cubic equations of state. Equation 3.16 can be expounded in more detailed volume dependant thermodynamic terms as in Equation 3.17.

$$(M - M^*)_{(\mathrm{T,P,n})} = \int_{\infty}^{V} \left[\left(\frac{\partial M}{\partial V} \right)_{\mathrm{T,n}} - \left(\frac{\partial M^*}{\partial V} \right)_{\mathrm{T,n}} \right] dV - \int_{\mathrm{V}}^{V^*} \left(\frac{\partial M^*}{\partial V} \right)_{\mathrm{T,n}} dV \tag{3.17}$$

Considering, for example the entropy, the generalised form in Equation 3.17 results in Equations 3.18 and 3.21.

$$(s - s^*)_{(\mathrm{T,P,n})} = \int_{\infty}^{v} \left[\left(\frac{\partial s}{\partial v} \right)_{\mathrm{T,n}} - \left(\frac{\partial s^*}{\partial v} \right)_{\mathrm{T,n}} \right] dv - \int_{\mathrm{v}}^{v^*} \left(\frac{\partial s^*}{\partial v} \right)_{\mathrm{T,n}} dv \tag{3.18}$$

According to Maxwell's relation:

$$\left(\frac{\partial s}{\partial v} \right)_{\mathrm{T,n}} = \left(\frac{\partial P}{\partial T} \right)_{\mathrm{v,n}} \tag{3.19}$$

Therefore,

$$(s - s^*)_{(\mathrm{T,P,n})} = \int_{\infty}^{v} \left[\left(\frac{\partial P}{\partial T} \right)_{\mathrm{v,n}} - \left(\frac{\partial P^*}{\partial T} \right)_{\mathrm{v,n}} \right] dv - \int_{\mathrm{v}}^{v^*} \left(\frac{\partial P^*}{\partial T} \right)_{\mathrm{v,n}} dv \tag{3.20}$$

Since for an ideal gas $\left(\frac{\partial P}{\partial T}\right)_{\mathrm{v,n}} = \frac{R}{v}$, then:

$$(s - s^*)_{(\mathrm{T,P,n})} = \int_{\infty}^{v} \left[\left(\frac{\partial P}{\partial T} \right)_{\mathrm{v,n}} - \frac{R}{v} \right] dv + R \ln \frac{v}{v^*} \tag{3.21}$$

Likewise, the generalised form in Equation 3.17 may also be used to find the

internal energy.

$$(u-u^*)_{(\mathrm{T,P,n})} = \int_{\infty}^{v} \left[\left(\frac{\partial u}{\partial v} \right)_{\mathrm{T,n}} - \left(\frac{\partial u^*}{\partial v} \right)_{\mathrm{T,n}} \right] dv - \int_{\mathrm{v}}^{v^*} \left(\frac{\partial u^*}{\partial v} \right)_{\mathrm{T,n}} dv \tag{3.22}$$

where $\left(\frac{\partial u^*}{\partial v}\right)_{\mathrm{T,n}} = 0$ because the internal energy of a perfect gas is independent of volume, and:

$$\left(\frac{\partial u}{\partial v} \right)_{\mathrm{T,n}} = T \left(\frac{\partial P}{\partial T} \right)_{\mathrm{v,n}} \tag{3.23}$$

Therefore,

$$(u-u^*)_{(\mathrm{T,P,n})} = \int_{\infty}^{v} \left[T \left(\frac{\partial P}{\partial T} \right)_{\mathrm{v,n}} - P \right] dv \tag{3.24}$$

By definition $h = u + Pv$; therefore, the enthalpy is then determined based on Equation 3.25.

$$(h-h^*)_{(\mathrm{T,P,n})} = \int_{\infty}^{v} \left[T \left(\frac{\partial P}{\partial T} \right)_{\mathrm{v,n}} - P \right] dv - Pv - P^*v^* \tag{3.25}$$

This concludes the section on working fluids modeling. In Section 3.3, the approach used to model thermodynamic cycles is described.

3.3 Cycle thermodynamic model

In this section, the equations involved in modeling the simple recuperated cycle is described, followed by a description of the approach used to model the major cycle components and the recompression cycle model. The analysis of the cycle assumes the following:

- The changes in kinetic and potential energies are negligible.
- Components are modelled under steady conditions.
- The pump and turbine are modelled using a fixed isentropic efficiency.
- The pressure drop in both sides of a heat exchanger is divided proportional to the heat duty.

- Heat losses are neglected.

3.3.1 Simple recuperated cycle

A schematic of a simple recuperative tCO_2 cycle and its Temperature - Entropy (T-s) diagram are shown in Figure 3.3.

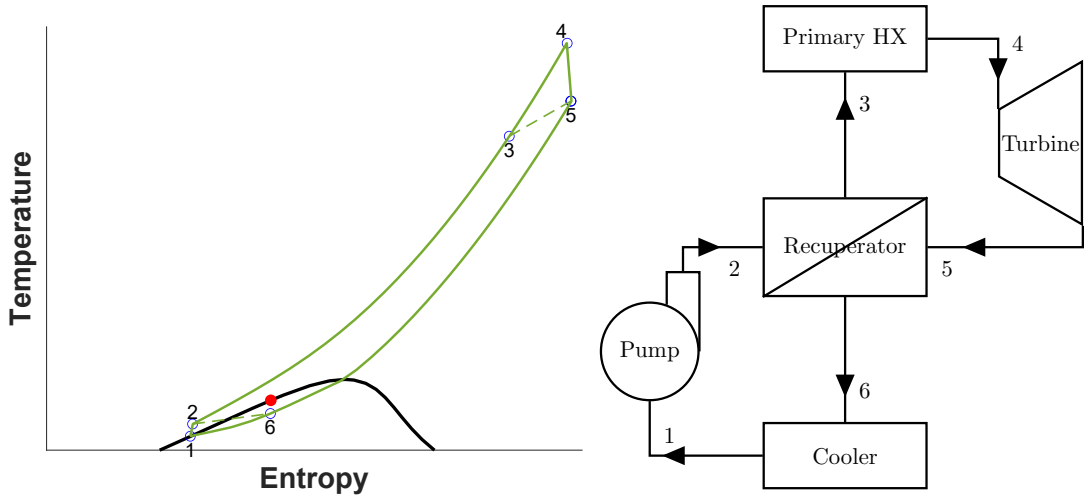

Figure 3.3: T-s diagram and schematic of a simple recuperated tCO_2 cycle

The cycle is modelled by applying the first law of thermodynamics across each component. Throughout equations 3.26 to 3.31 the terms W, Q, h, and $\dot{m}$ refer to shaft power, heat power, specific enthalpy, and mass flow rate, respectively. Subscripts are used to denote the cycle components: P for pump; T for turbine; R for recuperator; H for primary heat exchanger; and L for condenser. Numerical subscripts are also used to denote points along the cycle. The ideal cycle consists of five main processes as follows:

(1-2) Isentropic compression in the pump. The pressure of the condensate is raised in the feed pump.

$$\dot{W}_{\mathrm{p}} = \dot{m}(h_2 - h_1) \tag{3.26}$$

(2-3) Isobaric heat addition in the recuperator. High pressure liquid enters the recuperator and recovers heat from low pressure gas exiting the turbine.

$$\dot{Q}_{\mathrm{R}} = \dot{m}(h_3 - h_2) \tag{3.27}$$

(3-4) Isobaric heat addition in the primary heat exchanger. High pressure liquid enters the primary heat exchanger where it receives heat directly from the tower receiver or from an intermediate heat transfer fluid.

$$\dot{Q}_{\mathrm{H}} = \dot{m}(h_4 - h_3) \tag{3.28}$$

(4-5) Isentropic expansion in the turbine. The vapor is expanded in the turbine, thus producing work which may be converted to electricity.

$$\dot{W}_{\mathrm{t}} = \dot{m}(h_4 - h_5) \tag{3.29}$$

(5-6) Isobaric heat rejection in the recuperator. Low pressure gas enters the recuperator and loses heat to the high-pressure liquid exiting the pump.

$$\dot{Q}_{\mathrm{R}} = \dot{m}(h_5 - h_6) \tag{3.30}$$

(6-1) Isobaric heat rejection in the condenser.

$$\dot{Q}_{\mathrm{L}} = \dot{m}\,(h_6 - h_1) \tag{3.31}$$

The assumption of isobaric and isentropic processes, along with the cycle's boundary conditions and pressure ratio are key to determining the temperature and pressure at each point in the cycle. The temperature and pressure are then used in the EoS to calculate the specific properties (enthalpy and entropy) of the working fluid.

By applying the conservation of mass principle, the above energy terms can be expressed in a per unit mass basis expressed in small letters ($w_{\mathrm{p}}, w_{\mathrm{t}}, q_{\mathrm{R}}, q_{\mathrm{H}}, q_{\mathrm{L}}$). The thermal efficiency, which is often the main thermodynamic performance indicator, can be expressed as the ratio of the useful work produced to the heat consumed by the cycle:

$$\eta_{\mathrm{th}} = \frac{w_{\mathrm{t}} - w_{\mathrm{p}}}{q_{\mathrm{H}}} \tag{3.32}$$

Although isentropic compression, isontropic expansion, and isobaric heat exchange are assumed, in reality, losses in cycle components deviate its behaviour from the

ideal case. Once detailed design and analysis of each component are made, a good estimation of these losses becomes more reliable. However, for the sake of preliminary cycle design, assumptions about losses can be made. After assuming the pressure-drop within heat exchangers, pressure difference between inlet and outlet can be estimated.

$$\Delta P = P_{\text{in}} - P_{\text{out}} \tag{3.33}$$

The losses through the pump and turbine are estimated by assuming isentropic efficiencies for each, expressed as:

$$\eta_{\text{p}} = \frac{h_2 - h_1}{h_2 - h_{1\text{s}}} \tag{3.34}$$

$$\eta_{\text{t}} = \frac{h_4 - h_5}{h_4 - h_{5\text{s}}} \tag{3.35}$$

where the subscript 's' denotes the outlet conditions assuming isentropic compression and expansion.

3.3.2 Pump model

Survey of the literature of CO_2 power cycles reveals that CO_2 pumps have not been of primary concern to researchers. This is partly due to the fact that compression in most supercritical CO_2 cycles occurs near the critical point using a compressor, not a pump. Also, studies of transcritical cycles conclude that the power consumed by the pump is relatively small compared to the turbine work, thus its performance, within reasonable variations, is of little consequence (Garg et al. 2014, Li & Zhang 2011, Kim et al. 2012). Therefore, a constant isentropic efficiency is assumed for the pump throughout this study.

3.3.3 Heat exchanger model

Heat exchangers, especially the recuperator, are of special interest in CO_2 cycles. In its most basic form, a heat exchanger model disregards the temperature variations of the fluids and represents their interactions through the amount of energy they exchange. Such an approach is employed to model the primary heat exchanger and condenser in this thesis. Therefore, the behaviour of the external fluid (HTM or

coolant) is ignored, whilst only the amount of energy they exchange with the working fluid (q_{H} or q_{L}) is considered. However, this approach cannot be applied for the recuperator because the interaction is between two streams internal to the cycle.

Alternatively, a recuperator effectiveness is assumed to permit the calculation of the terminal temperatures of both streams. The recuperator effectiveness is defined as the ratio of the actual heat load to the maximum attainable heat load from the stream with the lowest heat-capacity rate. The equation for effectiveness depends on the heat exchanger flow arrangement (counter or parallel). Because it allows for higher heat recuperation, a counterflow heat exchanger is better suited for this application than a parallel flow heat exchanger. The effectiveness of a counterflow recuperator is described by:

$$\varepsilon = \frac{q_{\mathrm{R}}}{q_{\mathrm{R,max}}} = \frac{h_5 - h_6}{\min\left[\left(h_{@\mathrm{T5,P3}} - h_{@\mathrm{T2,P2}}\right), \left(h_{@\mathrm{T5,P5}} - h_{@\mathrm{T2,P6}}\right)\right]} \tag{3.36}$$

where, ε is the recuperator effectiveness and $h_{@\mathrm{T,P}}$ is the specific enthalpy evaluated at a certain temperature and pressure. Therefore, effectiveness depends on the maximum heat lost or gained by the stream with the lowest heat-capacity rate.

This approach of does not recognize the geometric implications of the assumed effectiveness, only its thermodynamic potential. In practice, the size of a heat exchanger increases with increasing effectiveness. For example, an effectiveness value of unity is an idealized case that produces an infinitely long heat exchanger. To avoid large heat exchangers, proper assessment of design feasibility must therefore account for its size. As an estimate, the overall conductance can be used:

$$Q_{\mathrm{R}} = UA\Delta T_{\mathrm{m}} \tag{3.37}$$

$$\Delta T_{\mathrm{m}} = \frac{\Delta\vartheta_1 - \Delta\vartheta_2}{\ln \Delta\vartheta_1/\Delta\vartheta_2} \tag{3.38}$$

where U is the overall heat transfer coefficient, A_{s} is the heat exchange surface area, and their product UA is the overall conductance, which is independent of the reference area and is an indicator of the recuperator size. The overall ΔT_{m} is the averaged temperature difference between the two streams, usually expressed as the log-mean

temperature difference (LMTD), and $\Delta\vartheta_i$ is the difference in the temperature between the two streams at a specified location 'i'.

As mentioned previously, an internal pinch point is expected in the recuperator, which must be observed to avoid physically impossible temperature profiles. In order to do so, the recuperator is discretized into cells, like Figure 3.4, each with an equal heat load. Pressure drop is also assumed to be equally divided along all nodes, although this is not entirely true since the transport properties of the fluids and the length of each segment differ. However, the variation in pressure drop is not expected to notably change the value of the pinch point temperature. The first law equation is then applied between the nodes to calculate the change in enthalpy based on the exchanged heat. Finally, the enthalpy and pressure are fed into the equation of state to calculate the temperature at each node.

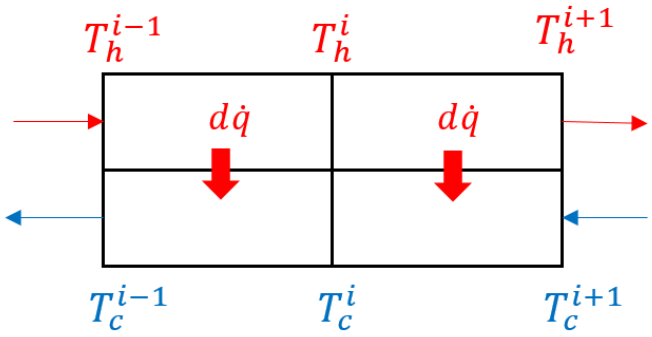

Figure 3.4: Illustrative example of recuperator discretisation

3.3.4 Axial turbine model

As previously mentioned, this thesis is part of the SCARABEUS project which is focused on large scale CSP plants. In Chapter 4, the sensitivity of cycle and turbine design to dopant selection will be first explored through a 100 MWe plant. Based on the literature review of turbine designs presented in Section 2.6, particularly Figure 2.32, an axial turbine is the most suitable for a 100 MWe power rating. The model described in this section is used to generate preliminary turbine designs to study the effect of doping CO_2 on the expansion process and overall turbine dimensions; however, optimisation of multistage axial turbines is not within the scope of this work.

An axial turbine consists of one or more sequential stages. Each stage contains one row of stator blades that accelerate and direct the flow, and one row of rotor blades that deflect the flow. As the stream of gas pushes the rotor's blades, it changes the rotor's angular momentum and produces work.

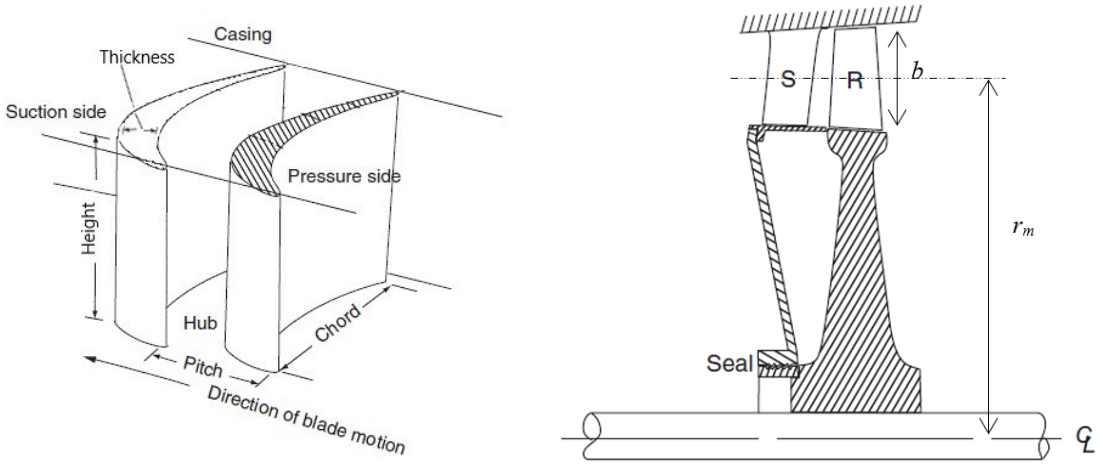

Figure 3.5: (Left) Flow channel between two adjacent turbine blades. (Right) Axial-Radial view of axial turbine. Adapted from (Korpela 2019)

The geometry of a turbine blade is shown in Figure 3.5. The foremost tip of the blade is the leading edge and the rearmost point is the trailing edge. The straight-line distance connecting the two edges has a chord length 'c'. The blade thickness 't' is the distance between the pressure and suction surfaces. The pitch or spacing 'S' is the circumferential separation between two adjacent blades. The height or span 'b' is the height of the blade from hub to casing, and is defined as:

$$b = r_{\mathrm{h}} - r_{\mathrm{c}} \tag{3.39}$$

Analysis of stage physics is commonly made for fluid properties at the mean radius, defined as the arithmetic mean of the hub and casing radii for axial turbines.

$$r_{\mathrm{m}} = \frac{r_{\mathrm{c}} + r_{\mathrm{h}}}{2} \tag{3.40}$$

The annular region formed from the blade passage areas is called the flow annulus. The annulus area is calculated as:

$$A = 2\pi r_{\mathrm{mb}} \tag{3.41}$$

The geometry of the rotor cascade can be further defined by specifying relations between its dimensions such as the blade aspect ratio 'b/c', the thickness to chord ratio 't/c', and the pitch to chord ratio 'S/c'. Moreover, the number of blades can be calculated using Equation 3.42 and rounding off to the nearest prime number.

$$N_{\mathrm{R}} = \frac{2\pi r_{\mathrm{m}}}{S} \tag{3.42}$$

A schematic of a turbine stage is shown in Figure 3.6. It consists of a stator followed by a rotor. As is conventional, the inlet to the stage is station 1, and the outlet from the stator is station 2, which is also the inlet to the rotor. The outlet from the rotor, and hence the stage, is station 3. In the figure, the absolute velocities and flow angles are denoted by V and α, the relative velocities and flow angles by W and β, and the rotor local blade speed by U.

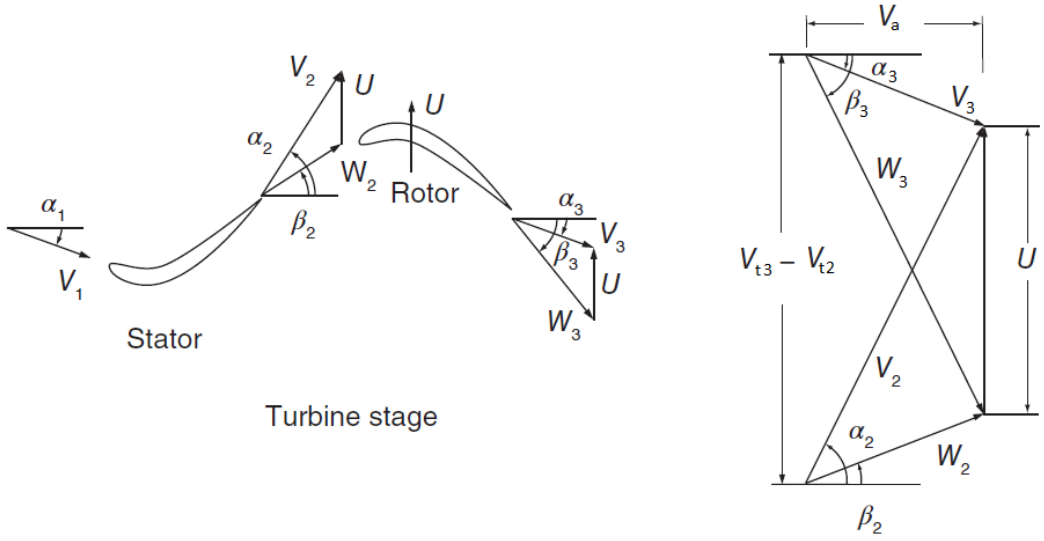

Figure 3.6: A single axial turbine stage from the meridional plane (Axial-Tangential). Adapted from (Korpela 2019)

The fluid enters the stage inlet with a static temperature and pressure T_1 and P_1 and an absolute velocity V_1 at an angle of α_1. It is then expanded in the stator blade passages to T_2, P_2, and leaves with a greater velocity V_2 at an angle α_2. The stator outlet conditions are the same as the rotor inlet conditions. In addition, since the rotor has a speed U, the relative velocity and angle between the fluid and the rotor may be derived by vectorial subtraction. The fluid is then deflected and expanded in

the rotor blade passage and leaves at T_3, P_3, and relative velocity W_3 at an angle β_3.

A constant axial velocity will be assumed to turbines designed in this report. Repeating stages are also assumed, which implies identical absolute stage inlet and outlet velocities and angles ($V_1 = V_3$, $\alpha_1 = \alpha_3$). With both of these assumptions, a generalized superimposed velocity triangle taken at mean radius can be described as seen in Figure 3.6. The velocity triangles' trigonometric relations reveal the relationships between their magnitudes and angles.

$$V_{\mathrm{t}} = V_{\mathrm{a}} \tan(\alpha) \tag{3.43}$$

$$W_{\mathrm{t}} = W_{\mathrm{a}} \tan(\beta) \tag{3.44}$$

$$\frac{U}{V_{\mathrm{a}}} = \tan(\alpha_2) - \tan(\beta_2) = \tan(\beta_3) - \tan(\alpha_3) \tag{3.45}$$

Work delivered by the stage is deduced by applying the principle of conservation of angular momentum per unit mass flow, leading to Euler's turbine equation:

$$w = U\,(V_{\mathrm{t}2} - V_{\mathrm{t}3}) = U\,(W_{\mathrm{t}2} - W_{\mathrm{t}3}) \tag{3.46}$$

If the axial velocity remains constant throughout the stage, then the stage work can be expressed as:

$$w = \; U\; V_a(\tan(\alpha_2) - \tan(\alpha_3)) = U\; W_a(\tan(\beta_2) - \tan(\beta_3)) \tag{3.47}$$

For the rotor, a deflection is the difference in the swirl velocities ($V_{\mathrm{t}2} - V_{\mathrm{t}3} = W_{\mathrm{t}2} - W_{\mathrm{t}3}$). It is also measured by the amount of turning, $\beta_2 - \beta_3$. The amount of turning across the stator is given by $\alpha_1 - \alpha_2$. From Equation 3.46, it can be seen that a stage may deliver a greater amount of work, for a given velocity, by increasing the flow deflection.

The work produced by the stage is also equal to the change in the fluid's total enthalpy $w = (h_{03} - h_{01})$. Since no work is done in the stator, total enthalpy remains constant across it ($h_{01} = h_{02}$), and the change in total enthalpy is thus confined to the rotor. Therefore, using Equation 3.46 for a constant axial velocity, the function

rothalpy (I) is found as:

$$h_3 + \frac{W_3^2}{2} = h_2 + \frac{W_2^2}{2} = I \tag{3.48}$$

Rothalpy remains constant across the rotor blade, and so it can be thought of as being the relative total enthalpy function within the rotor ($h_{02,\mathrm{rel}} = h_{03,\mathrm{rel}}$).

The degree of reaction (Λ), the flow coefficient (ϕ), and the loading coefficient (ψ) are three non-dimensional terms commonly used to characterize a turbine stage. The degree of reaction is defined as the ratio between the static enthalpy drop in the rotor to the static enthalpy drop in the stage. Reaction falls in the range $0 \leq \Lambda \leq 1$, where a value of zero indicates a purely impulse stage where the static enthalpy is constant across the rotor.

$$\Lambda = \frac{h_2 - h_3}{h_1 - h_3} \tag{3.49}$$

The flow coefficient is defined as the ratio between the meridional velocity and the local blade velocity.

$$\phi = \frac{V_\mathrm{a}}{U} \tag{3.50}$$

The blade loading coefficient indicates the work capacity of the stage. It is defined as the ratio of the deflection to the local blade velocity.

$$\psi = \frac{W_{\mathrm{t}2} - W_{\mathrm{t}3}}{U} \tag{3.51}$$

These three parameters play an important role in defining the velocity diagram of the stage, and can be expressed in terms of flow angles.

$$\psi = 2\phi(\tan(\beta_2) - \tan(\beta_3)) \tag{3.52}$$

$$\Lambda = \frac{\phi}{2}(\tan(\beta_3) + \tan(\beta_2)) \tag{3.53}$$

The aerodynamic design of a turbine stage must be cross examined with the permissible level of stress in the rotor blade, which may restrict the maximum blade tip speed. The two main sources of blade mechanical stresses are the centrifugal tensile stress caused by the blade's own weight, and gas bending stresses caused by the

change in the angular momentum of the gas in the tangential direction. Centrifugal stresses are assumed to be static, but gas bending stresses fluctuate, therefore are more critical.

For a preliminary turbine design of fixed rotational speed and tapered blade profile, the centrifugal and gas bending stress may be approximated using Equations 3.54 and 3.55, respectively.

$$\sigma_{\mathrm{ct}} = \frac{4}{3}\pi N^2 \rho_{\mathrm{b}} A \tag{3.54}$$

where, N is the turbine rotational speed in rev/s, A is the annulus area in m^2, and ρ_{b} is the density of the blade material in kg/m^3.

$$\sigma_{\mathrm{gb}} = \frac{\dot{m}\left(V_{\mathrm{t2}} + V_{\mathrm{t3}}\right)}{N_{\mathrm{R}}} \frac{h}{2} \frac{1}{zc^3} \tag{3.55}$$

where 'z' is the smallest value of root section modulus of a blade of unit chord calculated using Fig 8.24 in (Saravanamuttoo et al. 2017).

3.3.5 Recompression cycle

In the recompression cycle, the flow is split into two streams after the low temperature recuperator and before the condenser. One of these two streams flows into the pump whilst the other flows to the recompression compressor. A schematic of the cycle layout is shown in Figure 3.8. The cycle modelling assumption made here are identical to those made for the simple recuperated cycle, which are listed at the beginning of Section 3.3.

The split ratio (x_s) is the fraction of the mass flow that flows into the recompressor:

$$x_{\mathrm{s}} = \frac{\dot{m}_{\mathrm{3b}}}{\dot{m}_{\mathrm{3a}} + \dot{m}_{\mathrm{3b}}} \tag{3.56}$$

where the subscripts 3a and 3b denote the flow through the pump and re-compressor, respectively. Therefore, the specific work of the pump and re-compressor are defined as:

$$w_{\mathrm{p}} = (1 - x_{\mathrm{s}})(h_2 - h_1) \tag{3.57}$$

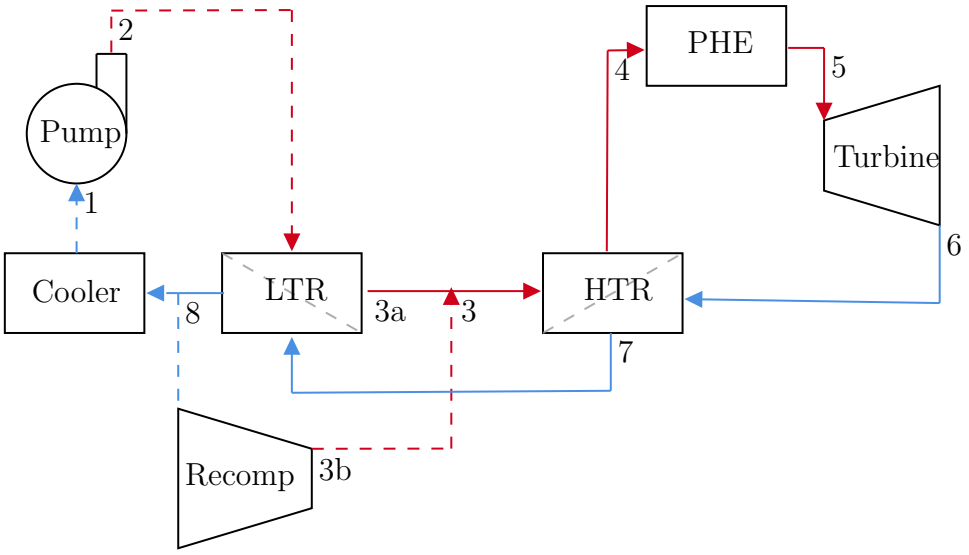

Figure 3.7: Recompression cycle. Red lines indicate high-pressure flows; blue low-pressure. Legend: low-temperature recuperator (LTR), high-temperature recuperator (HTR), primary heat exchanger (PHE), and recompressor (recomp)

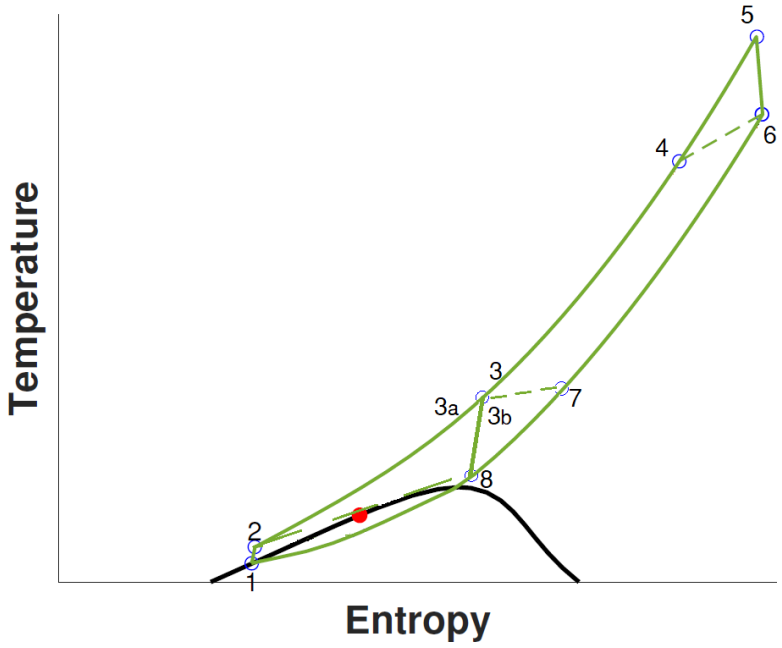

Figure 3.8: T-s diagram and schematic of a recompression tCO_2 cycle

$$w_{\mathrm{rc}} = x_{\mathrm{s}}(h_{3\mathrm{a}} - h_8) \tag{3.58}$$

Therefore, the specific net work must account for work inputs into both the pump and recompressor:

$$w_{\mathrm{n}} = w_{\mathrm{t}} - (w_{\mathrm{p}} + w_{\mathrm{rc}}) \tag{3.59}$$

The specific enthalpy at the HTR high-pressure inlet (3) is calculated by applying

the conservation of energy equation at the point where the two streams 3a and 3b converge:

$$h_3 = x_s h_{3b} + (1 - x_s) h_{3a} \tag{3.60}$$

Similarly, the energy conservation equation is applied at the LTR and HTR to produce Eqautions 3.61 and 3.62, respectively:

$$h_7 - h_8 = (1 - x_s)(h_{3a} - h_2) \tag{3.61}$$

$$h_6 - h_7 = h_4 - h_3 \tag{3.62}$$

The effectiveness of both LTR and HTR, shown in Equations 3.63 and 3.64, depend on the maximum attainable heat transfer by the flow of the lowest capacity rate; as was the case with recuperator of the simple cycle. Moreover, the recuperators are discretised to ensure that the preset minimum internal temperatures approach are not violated by in both recuperators.

$$\epsilon_{LTR} = \frac{h_7 - h_8}{\min\left[\left((1 - x_s)(h_{@T7,P3a} - h_{@T2,P2})\right), (h_{@T7,P7} - h_{@T2,P8})\right]} \tag{3.63}$$

$$\epsilon_{HTR} = \frac{h_4 - h_3}{\min\left[\left(h_{@T4,P8} - h_{@T7,P7}\right), (h_{@T6,P6} - h_{@T3,P7})\right]} \tag{3.64}$$

The system of equations for a recompression cycle is under-determined, thus requires an initial assumption of T_3 and iteration of Equations3.58, 3.63, and 3.64.

3.4 Optimisation

In this thesis, a combination of optimisation and parametric studies were performed to quantitatively probe the effect of the dopant type and amount on cycle operating conditions and turbine geometry. Parametric studies are helpful in exploring the effect of controlled parameters on any aspect of the cycle. For example, mapping the effect of varying the pump inlet pressure on its efficiency. Optimisation studies, on the other hand, are concerned with finding the best answer to an

optimisation problem. Taking the same example of a variable pump inlet pressure, an optimisation problem might be formulated to find the optimal inlet pressure that produces the highest pump efficiency.

Much of this thesis involves searching for optimal parameter values in system design problems. Any problem in which certain parameters need to be determined to satisfy constraints can be formulated as an optimisation problem. Once this has been done, a variety of optimisation methods are available to solve it.

In its basic form, a constrained optimisation problem consists of the following: (1) design variables, (2) objective function, (3) equality constraint function, and (4) inequality constraint function. The objective function is the scalar quantity to be minimized. It is a function of the set of design variables, whether directly or through intermediate variables. To limit the region of search, lower and upper boundaries are placed on the design variables, for example, setting a lower bound of unity for pressure ratio when optimizing cycle efficiency. Equality constraints must be satisfied exactly at the optimal design, and are violated if they have a non-zero value. The inequality constraints are expressed in a less than or equal to zero form by convention. Moreover, an inequality constraint is satisfied if the constraint's value is negative and is violated if its value is positive. A general mathematical model that encompasses these considerations is described in Equations 3.65 to 3.67.

Find an n-vector $\mathbf{x} = (x_1, x_2, \ldots, x_{\mathrm{n}})$ of design variables that minimize the object function:

$$f(\mathbf{x}) = f\left(x_1, x_2, \ldots, x_{\mathrm{n}}\right) \tag{3.65}$$

subject to p number of equality constraints:

$$h_{\mathrm{j}}\left(\mathbf{x}\right) = h_{\mathrm{i}}\left(x_1, x_2, \ldots, x_{\mathrm{n}}\right) = 0;\ j = 1\ to\ p \tag{3.66}$$

and m number of inequality constraints:

$$g_{\mathrm{i}}\left(\mathbf{x}\right) = g_{\mathrm{i}}\left(x_1, x_2, \ldots, x_{\mathrm{n}}\right) \leq 0;\ i = 1\ to\ m \tag{3.67}$$

Although the problem is stated as a minimization task, it can be a maximizing function by minimizing its negative transformation $f(\mathbf{x}) = -F(\mathbf{x})$. Likewise, greater than or equal to ($\geq$) constraint are expressed as the negative transformation of the inequality constraint function $g_{\mathrm{i}}(\mathbf{x}) = -G_{\mathrm{i}}(\mathbf{x})$.

Constraints are said to be explicit if they are directly dependant on the design variables, but are said to be implicit if they cannot be expressed directly as a function of design variables. Implicit constraints are indirectly influenced by the design variables through a more complex function sequence involving intermediate variables (Arora 2017). For example, the maximum turbine inlet pressure is an explicit constraint if the pressure ratio and turbine exhaust pressure are design variables. On the other hand, the minimum approach temperature of a recuperator is an implicit constraint since it cannot be directly expressed in terms of any design variable.

After an optimisation problem is formulated, a method must be chosen to solve the problem. Selection of a method depends on three main aspects: (1) The numerical nature of the design variables (continuous, discrete, or integer), (2) whether the problem functions are continuous and differentiable, and (3) the effort required to differentiate the problem functions. With continuous design variables and continuous and differentiable problem functions, gradient-based methods are most efficient. Whereas problems with discrete variables and discontinuous problem functions commonly require nature-inspired solution methods.

In the iterative gradient-based search methods, the initial design variables are assumed and improved iteratively until optimality conditions are satisfied. More particularly, for a given point in the design space, the gradients of the objective and constraints functions are calculated and used to determine a direction in which to search. This process is iterated until convergence is achieved; no further improvement of the objective is possible without violating at least one of the constraints. However, gradient-based methods are prone to converge to local optimal rather than global optimal solutions.

To promote a global optimal solution, gradient-based search may be embedded

into a global-optimisation stochastic method. Put simply, after the gradient-method converges to a local optimum, the initial parameters are changed by randomly sampling them from a given bounded set. The optimisation problem is then repeated until convergence, and its solution is compared with the previous local minimum. This process is repeated until the stopping criteria is fulfilled; such as number of repetitions or difference between solutions. This is called the multi-start method, which is used in this work, along with gradient-based method.

Nature-inspired solution methods, such as Genetic Algorithm (GA) or Simulated Annealing, use random numbers in their calculations to search for the optimum point. For example, in GA, we start with an initial set of designs and generate a new set using the initial set, random numbers, and statistical concepts. Therefore, the algorithms can lead to a different sequence of designs and a different solution, even with the same initial conditions (Arora 2017). To their credit, nature-inspired methods have the ability to converge to global optimal solutions. Although they are commonly employed for discrete problems, they may also solve continuous problems. However, the main drawback of using nature-inspired methods is the amount of time and processing power required to run them. Once an optimisation problem becomes so complex that gradient-based methods require an intolerably long time to converge to an optimal solution, nature-inspired methods become the better choice.

3.5 Computer software

Solving the multitude of mathematical models involved in this study requires the utilization of computer software. Functions and subroutines were built in *MATLAB* to execute the main thermodynamic analysis of the power cycle and the preliminary turbine design. Optimisation problems were also formulated in *MATLAB* and solved using built-in gradient-based optimisation problem solvers.

The thermodynamic cycle model described in Chapter 3 and the radial inflow turbine model described in Chapter 5, although not novel, are part of the contributions of this thesis and have been developed to specifically to achieve the goals of this thesis.

Implementation of the EoS and calculation of fluid thermophysical properties within computer software becomes increasingly necessary when studying mixture fluids. Several tools are currently available, including *REFPROP*, *Aspen Properties*, and *Simulis Thermodynamics*. The latter was used to calculate fluid properties throughout this thesis. A homogeneous approach employing the PR EoS coupled with VdW1f mixing rules was used within *Simulis Thermodynamics* software through out this thesis. As will be seen in Chapter 7, the PR equation of state is robust against fluid modelling uncertainty, and thus is a good choice for modelling mixtures. However, additonal EoS are used in Chapter 7 to quantify the effect of the fluid model on cycle and turbine design.

Calculation of fluid thermophysical properties in *MATLAB* was achieved by calls to pre-built functions in *MATLAB* format, provided as part of the *Simulis Thermodynamics* software package. *Simulis Thermodynamics* was validated through a simple recuperated cycle model for pure compounds and mixtures, respectively. A pure CO_2 cycle was simulated via a *REFPROP* based code developed in-house, while results using *Aspen* for modelling of $CO_2/TiCl_4$ mixture were obtained from Manzolini et al. (2019). The present model showed results consistent with those from *REFPROP* and Aspen with percentage variation of 0.5% in efficiency (0.2% nominal efficiency variation).

Chapter 4

CO_2 Mixtures in Transcritical Cycles

4.1 Introduction

As stated in Chapter 1, this work is part of the SCARABEUS research initiative which aims to reduce large scale CSP plant (100 MW_e) costs through the use of CO_2-based working fluids. Therefore, the majority of Chapter 4 investigates the use of CO_2-based blends as working fluids in a 100 MW_e simple recuperated transcritical cycle power plant. Later in the chapter, the study is broadened to cooling temperatures lower than those of dry-cooled CSP plants to compare the performance of the simple recuperated and recompression cycle for nine CO_2-based mixtures.

4.2 Simple recuperated cycle

The following study involves several steps. First, the optimal conditions for a simple recuperated transcritical cycle are found for a range of dopant blend fractions for each of the three mixtures considered by the SCARABEUS project. Then, the implications of the mixture composition on cycle behaviour and preliminary turbine design are explored.

4.2.1 Methodology

A parametric study was conducted by changing the dopant molar fraction and optimizing cycle conditions for the resulting mixture compositions each time. To find the optimal cycle conditions that achieve the highest overall cycle efficiency, an optimisation problem was formulated based on the mathematical models in Sections 3.3 and 3.3.3. The cycle efficiency defined by Equation 3.32 was set as the objective function, while the maximum turbine inlet pressure and minimum internal temperature approach (MITA) in the recuperator were set as constraints.

Within the optimisation problem, all cycle conditions were held constant, except for recuperator effectiveness (ε) and turbine pressure ratio (r), which were used as optimisation design variables. Recuperator effectiveness was allowed to vary in order to ensure a MITA of 5 °C at the recuperator pinch point in line with previous work on CO_2-based cycles (Manzolini et al. 2022, Rodríguez-deArriba et al. 2022, Morosini et al. 2022, Crespi et al. 2022). Variation of the effectiveness is a statement about the thermodynamic potential of the cycle away from any technical considerations, therefore the resulting recuperator size, indicated by the overall conductance (UA), was not considered during optimisation; however, the effect of dopant fraction on recuperator size was investigated.

Cycle analysis was based on a unit mass flow rate through all components. Heat exchange processes with heat source and heat sink were not considered. However, heat exchange within the recuperator was probed to ensure that the heat profiles of the two streams do not overlap and create a negative pinch point temperature. As mentioned in Section 3.3.3, the recuperator was discretised into cells in search of the internal pinch point. Based on an error sensitivity study, the number of cells was determined. As seen in Figure 4.1, the error in the calculated MITA is dependent on the chosen number of cells. It was found that dividing the recuperator into 50 cells results in $< 2\%$ error value for all mixtures at all blend fractions.

A turbine design model was used to define the turbine geometry based on optimal cycle conditions. To model the turbine, a preliminary mean line axial turbine

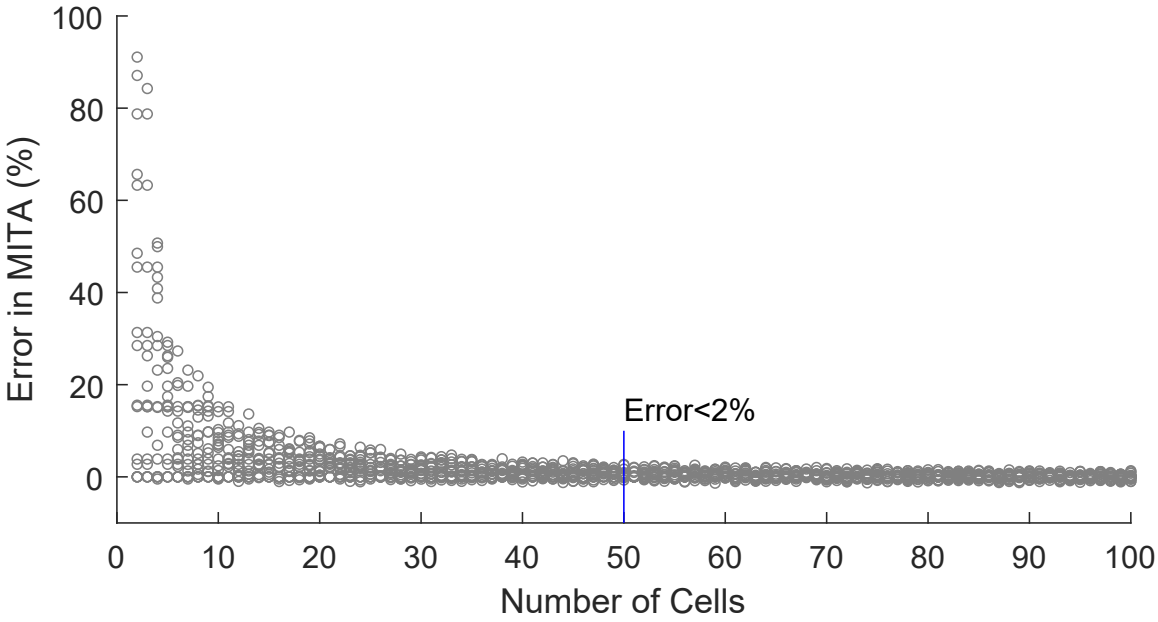

Figure 4.1: Relation between the number of recuperator cells and the associated error in the calculation of the minimum temperature difference at the pinch point. Each point represents the MITA of a working fluid with a specific dopant molar fraction based on the three mixtures and the range of molar fractions studied here. A vertical line is drawn at 50 cells

design approach was adopted, which entailed the application of basic equations and empirical relations to generate the turbine geometry based on the assumed isentropic efficiency. The turbine's shaft rotational speed was fixed at 3000 RPM. This value was determined based on the assumption that the turbine will be connected directly to a two-pole synchronous generator which feeds into the electricity grid where the frequency is 50 Hz.

Model description

A *MATLAB* program of multiple subroutines was developed to study the turbine sensitivity. The first to be deployed was the Cycle Solver Model (CSM), which is an in-house function that solves for the conditions at each point of the cycle using the equations presented in Section 3.3. The change of dopant molar fraction introduces a different mixture into the model with every iteration. To address this challenge, *Simulis Thermodynamics*, was employed to calculate the thermophysical properties of any given mixture composition and readily feed them into CSM. Lastly, the Turbine Design Model (TDM) was also developed in-house to generate the axial turbine

geometry.

The flowchart in Figure 4.2 shows two layers of optimisation corresponding to the dopant molar fraction and the two design variables; pressure ratio and recuperator effectiveness. The layers are embedded within each other, meaning that an increment in the dopant molar fraction restarts the optimisation of the design variables. The TDM is called once an optimum cycle design is found for the given mixture composition.

Two sets of data should be fed into the TDM. The first is the set of turbine boundary conditions produced by the CSM, and includes turbine inlet conditions, mass flow rate, and pressure ratio. The second set of parameters is the turbine rotational speed, its assumed efficiency, and design parameters chosen based on values recommended for high efficiency turbines (Saravanamuttoo et al. 2017).

Optimisation conditions

The pump inlet temperature (T_1) is set to 50 °C. It was chosen to be compatible with dry cooling temperatures in hot arid regions, assuming an ambient dry-bulb temperature of 40 °C and a minimum temperature difference of 10 °C in the condenser. The pump inlet was assumed to be subcooled by 2 °C below the saturation pressure. Consequently, the pump inlet pressure (P_1) is equal to the saturation pressure of the fluid at 52 °C. The turbine inlet temperature (T_4) was set to 700 °C, which is expected from an advanced CSP receiver employing sodium salt as its Heat Transfer Medium (HTM). Additionally, the turbine inlet pressure (P_4) was restricted to 25 MPa as recommended by Dostal et al. (2004).

The maximum molar fraction of the dopant was set to 0.40 to prevent it from becoming the dominant compound in the mixture. The minimum dopant blend fraction depended on the critical temperature of the mixture. Heat rejection in a transcritical cycle must occur at saturation pressures below the critical pressure of the working fluid where condensation is possible. Consequently, the critical temperature of the working fluid mixture must be equal to or greater than 57 °C to allow for the formation of liquid before pump inlet. Therefore, the minimum dopant molar fraction

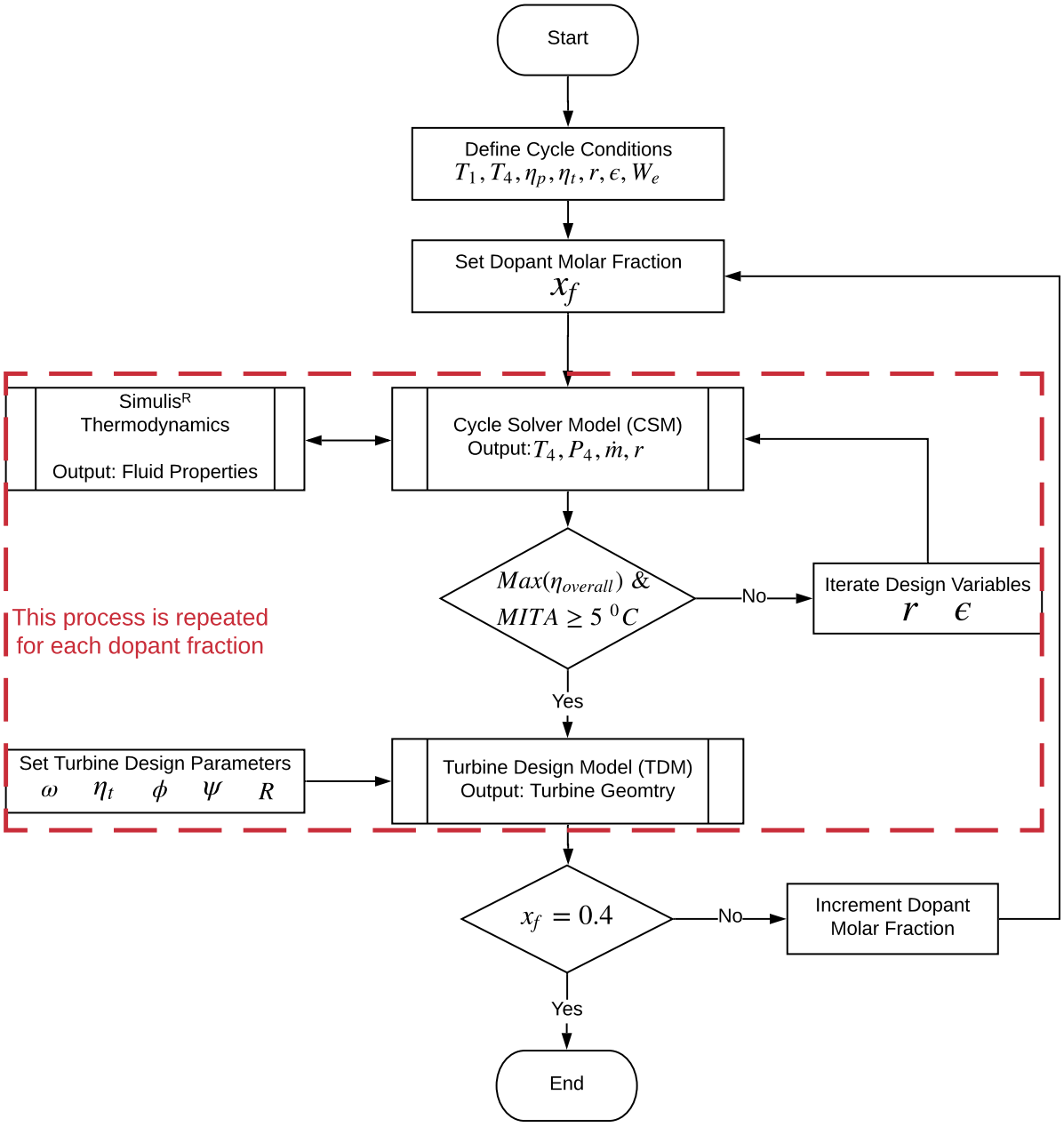

Figure 4.2: Flowchart of optimisation model

was assumed to be the value at which the critical temperature of the mixture is equal to or slightly exceeds 57 °C. A summary of the assumptions is provided in Table 4.1.

4.2.2 Choice of dopants

The dopants studied in Section 4.2.3 are among the candidates that have been identified by the SCARABEUS project as potential dopants for CO_2 based power

Table 4.1: Inputs required for cycle solution

Controlled Parameters		
Parameter	**Range**	**Unit**
Dopant Molar Fraction	Max(0.4)	%
Turbine Inlet Temperature (T_4)	700	°C
Pump Inlet Temperature (T_1)	50	°C
Pump Isentropic Efficiency(η_p)	85	%
Turbine Isentropic Efficiency(η_t)	90	%
Generator Efficiency(η_g)	99	%
Minimum internal temperature approach (MITA)	5	°C
Net Electrical Power(W_e)	100	MW
$\Delta p/p$ of Primary Heat Exchanger	0.015	-
$\Delta p/p$ of Recuperator High- and Low-pressure sides	0.01 and 0.015	-
$\Delta p/p$ of Condenser	0.02	-
Dependant Parameters		
Pump Inlet Pressure(P_1)	$P_{sat@(T_1+2)}$	MPa
Turbine Inlet Pressure(P_4)	Max (25)	MPa
Optimised Parameters		
Pressure Ratio (r)	2 to Max $(P_4)/P_1$	-
Recuperator Effectiveness(ϵ)	80 to 98	%

cycles operating in CSP. The main dopant thermophysical properties of interest are shown in Table 4.2.

Table 4.2: Physical and thermodynamic properties of pure compounds (collected from DIPPR database)

Compound	**Molecular Weight** (g/mol)	**Acentric Factor** (ω)	**Critical Temperature** (K)	**Critical Pressure** (MPa)	**Ideal Specific Heat** (C_p^o) ($T_r = 2$) **(J/mol.K)**
CO_2	44.01	0.2236	304.2	7.382	47.34
$TiCl_4$	189.7	0.2837	639.1	4.661	107.2
SO_2	64.06	0.2454	430.8	7.884	53.20
C_6F_6	186.1	0.3953	516.7	3.273	272.1

Although the interaction parameters are assumed constant for all conditions, they are known to be temperature dependent. A comprehensive determination of the temperature dependency of k_{ij} was not made in this study. However, the susceptibility

Table 4.3: Optimised k_{ij} with uncertainty intervals

Mixture	k_{ij}	**Uncertainty**	**Source of data**
$\mathbf{CO_2/TiCl_4}$	0.0745	± 0.0456 (57.6%)	Taken from Bonalumi et al. (2018)
$\mathbf{CO_2/SO_2}$	0.0243	± 0.0031 (12.8%)	Calculated from Coquelet et al. (2014)
$\mathbf{CO_2/C_6F_6}$	0.0312	± 0.0104 (33.3%)	Calculated from Dias et al. (2006)

of the EoS and the thermodynamic models to the k_{ij} was recognized by studying the effect of its variation within uncertainty margin on the modelling results in Chapter 7.

4.2.3 Cycle analysis

In order to fully capture the effect of mixture composition on the turbine design, it is helpful to first examine its effect on the cycle parameters as a whole. Analysis of the results will first investigate cycle behaviour, with emphasis on turbine boundary conditions and the expansion process. Then, the change in working fluid characteristics and their expected effect on the cycle and turbine design is considered. After which, turbine geometries for the SCARABEUS project case study will be discussed in more detail. Henceforth, any observations on parameter trends will be in reference to the increase in molar fraction of the dopant, unless stated otherwise. Moreover, a uniform graphical representation of the three mixtures is adopted throughout Section 4.2.3 as introduced in Figure 4.3.

The critical loci of the binary mixtures are illustrated in Figure 4.3. There is a notable difference in the shape of the critical locus of each mixture. The shape indicates the evolution of the Liquid-Vapor coexistence lines with changing composition. Since the minimum cycle pressure in a transcritical cycle is determined by the condensation pressure at the prescribed minimum temperature, the shift in the coexistence line defines a new equilibrium condensation pressure, which ultimately influences the cycle's pressure ratio. In general, as the critical pressure increases, the vapor pressure of the fluid increases, thus decreasing the cycle pressure ratio for a fixed maximum turbine inlet pressure. Whereas an increase in the critical temperature decreases the vapor pressure of the fluid and increases the cycle's pressure ratio. The change in vapor pressure is also proportional to its position relative to the critical

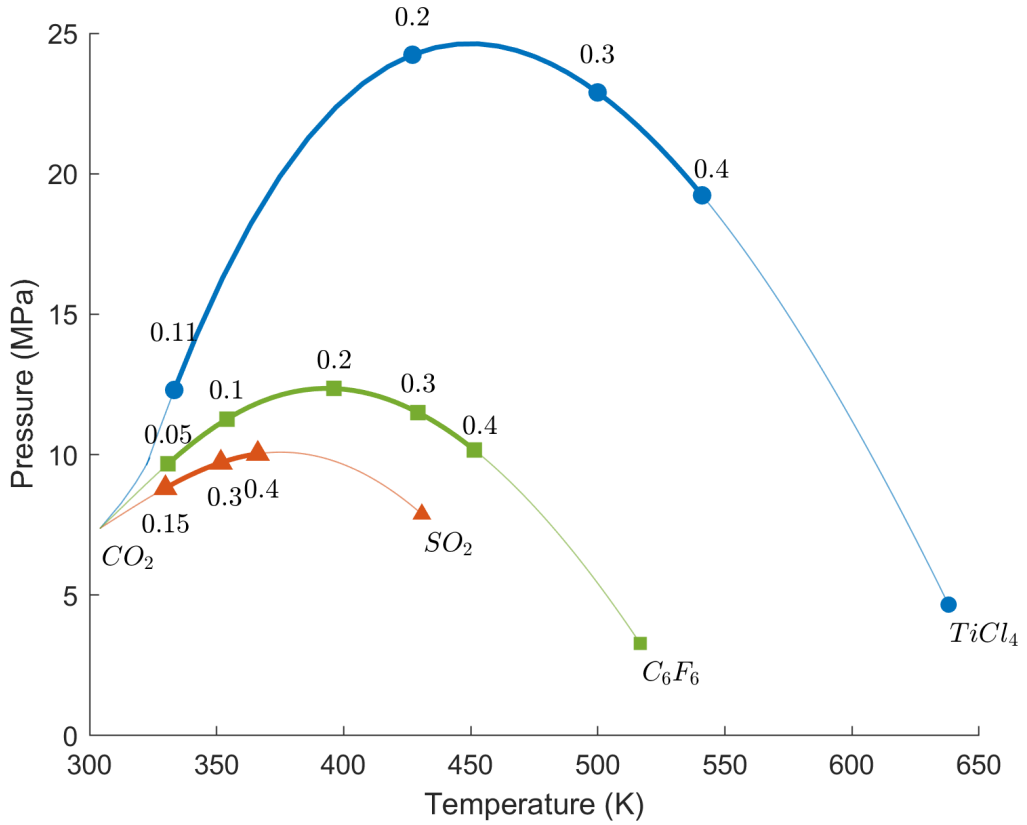

Figure 4.3: The highlighted segments represent the critical loci corresponding to the blend fractions studied for each mixture. The point labels indicate the dopant molar fraction at that point. The same styling convention is used to differentiate the three mixtures in all subsequent figures

point, and is greatest near the critical point. It is the interplay between these factors that eventually determines the aggregate change in vapor pressure, namely the pump inlet pressure.

The pump inlet pressures decrease as the dopant fractions increase as seen in Figure 4.4. Consequently, the decrease in condensation pressure induces an increase in the cycle pressure ratio in order to achieve higher levels of cycle thermal efficiency. The fall in condensation pressure is directly proportional to the increase in pressure ratio; which is greatest in CO_2/C_6F_6.

The trend in efficiency exhibits an optimal point for each mixture, as seen in Figure 4.5. The dopant molar fractions corresponding to the points of maximum efficiency are 0.174, 0.264, and 0.167 for mixtures of $CO_2/TiCl_4$, CO_2/SO_2, and CO_2/C_6F_6, respectively. Among the three blends, $CO_2/TiCl_4$ achieves the highest

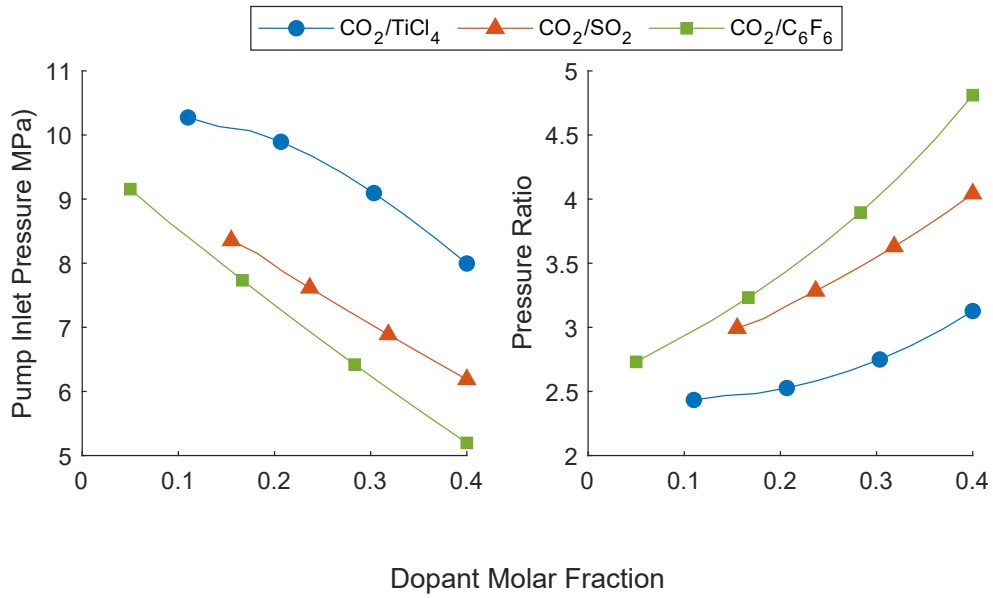

Figure 4.4: Variation of pump inlet pressure and pressure ratio with dopant molar fraction

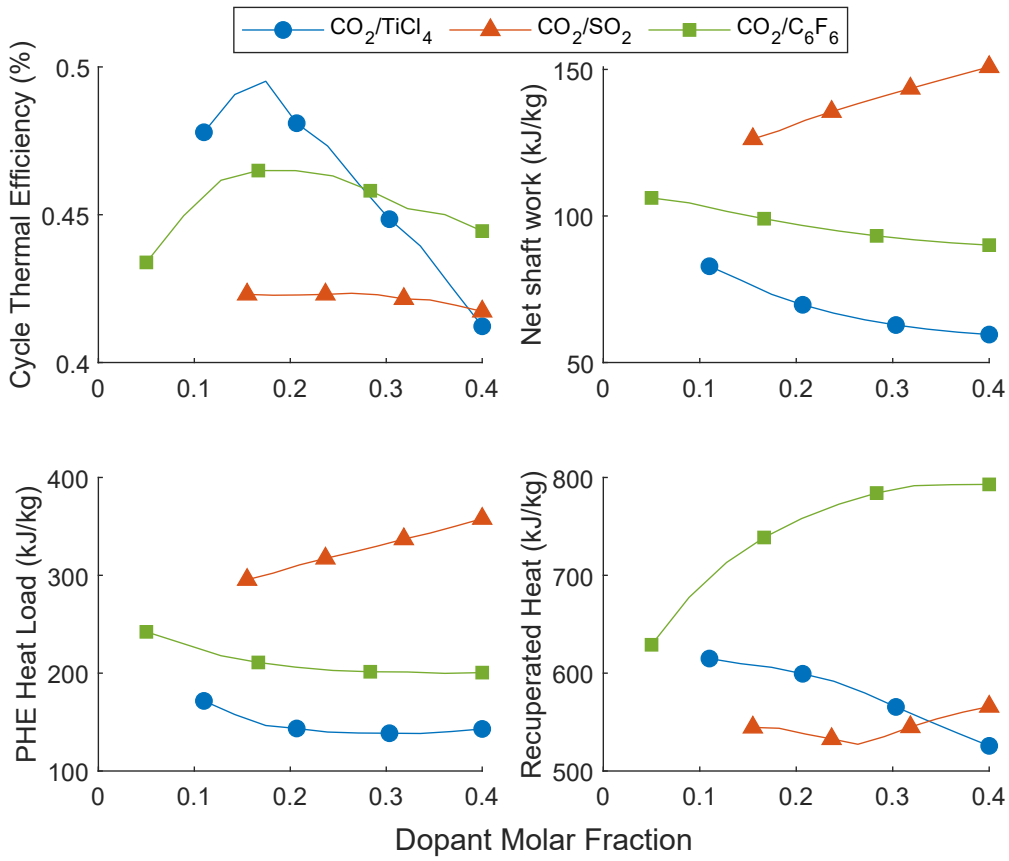

Figure 4.5: Variation of cycle thermal efficiency, net shaft work, primary heat exchanger load, and the specific recuperated heat with dopant molar fraction

thermal efficiency of 49.5%, followed by CO_2/C_6F_6 with an optimal thermal efficiency of 46.5%, while CO_2/SO_2 achieves the lowest efficiency of 42.3%. The 7.2% difference in efficiency between $CO_2/TiCl_4$ and CO_2/SO_2 cycles highlights the significant influence the choice of dopant has on cycle performance. These dopant molar fractions will later be used to compare the turbine geometries of the three mixtures.

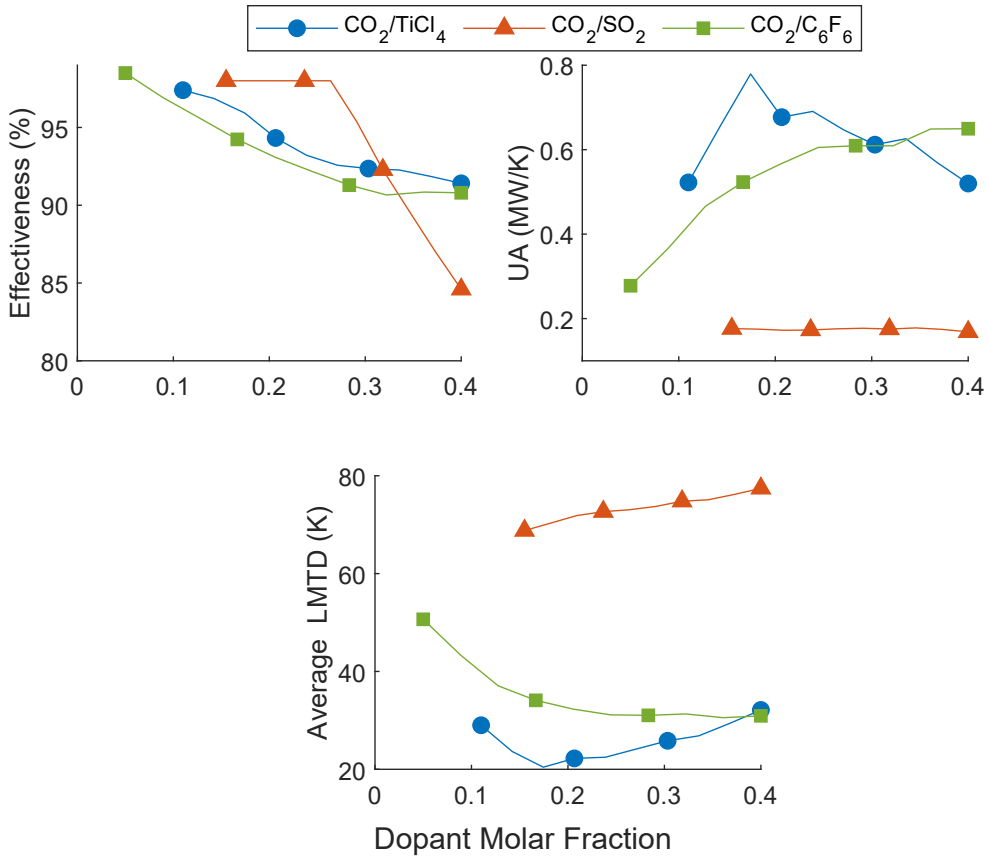

Figure 4.6: Variation of recuperator effectiveness and overall conductance with dopant molar fraction

The trend in efficiency is a consequence of the change in the net shaft work ($w_t - w_p$) and the primary heat exchanger heat load, also shown in Figure 4.5, which in turn is affected by the change in recuperated heat. By inspection of the rate of change of the two parameters (net specific work and PHE heat load) with the dopant fraction, the change in efficiency becomes clearer. For CO_2/SO_2, both parameters increase at roughly the same rate, thus maintaining a fairly constant efficiency with dopant fraction. For CO_2/C_6F_6 the PHE heat load decreases at a decreasing rate while the net specific work decreases at an almost constant rate. Therefore, the cycle efficiency exhibits an inversion point of maximum efficiency after which the PHE

heat lead decreases at a rate lower than that of the net specific work, which causes efficiency to drop. The same applies to $CO_2/TiCl_4$, but the drop in efficiency is more dramatic because the net specific work decreases at an increasing rate.

On the other hand, the trend in the net work is mainly driven by the change in the specific work, as seen in Figure 4.9. Similar to a pure sCO_2 cycle, cycles operating with CO_2 based mixtures are highly recuperative. As shown in Figure 4.5, the recuperated heat is much greater than the primary heat exchanger load for all mixture compositions. This is because of the relatively low pressure ratios and specific work across the turbine, which accompany higher turbine outlet temperatures. Recuperated heat is 3.2 to 3.5 times greater than the primary heat exchanger load for $CO_2/TiCl_4$, 2.3 to 4.0 times greater for CO_2/C_6F_6, and 1.6 to 1.8 times greater for CO_2/SO_2.

As the recuperator effectiveness increases, the MITA in the recuperator decreases. Therefore, the recuperator effectiveness is reduced to maintain a MITA of around 5 °C, whilst achieving optimal cycle thermal efficiency. Figure 4.6 shows the reduction in effectiveness with increasing dopant fractions. It was found that CO_2/SO_2 exhibits an abrupt fall in recuperator effectiveness for dopant molar fractions above 0.26, which corresponds to the SO_2 molar fraction above which condensation occurs in the recuperator. The same effect is illustrated in Figure 4.5 where the recuperated heat rises abruptly at the same SO_2 molar fraction.

The well-matched temperature profiles and higher effectiveness comes at the cost of larger recuperators. The overall conductance values of the entire recuperator are indicative of its size and were obtained by adding the overall conductance of each of its discrete cells. As seen in Figure 4.6, the overall conductance of the two heavy mixtures — $CO_2/TiCl_4$ and CO_2/C_6F_6 — are much higher than CO_2/SO_2. The trend in overall conductance with dopant molar fraction is mainly attributed to the change in the temperature profiles of the two streams, indicated by the average LMTD, also shown in Figure 4.6. The greater the LMTD the smaller is the recuperator.

A survey of the recuperator T-Q diagram for the optimal blend of each dopant is

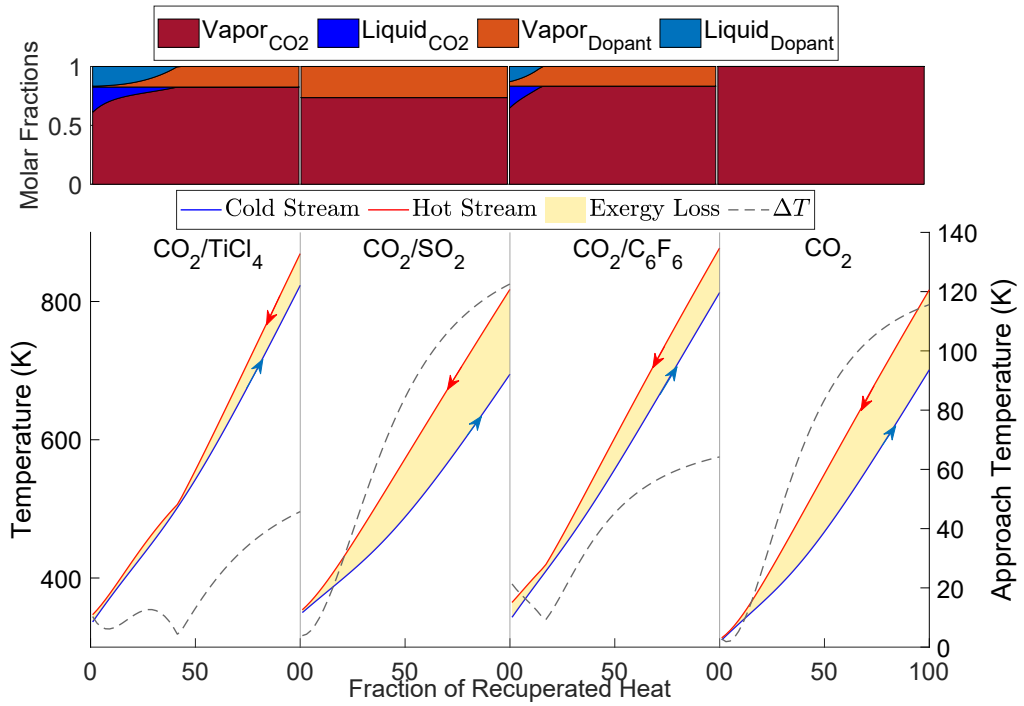

Figure 4.7: Temperature versus heat load profile of the recuperator for each working fluid at optimal dopant fraction. The plots at the top indicate the change in the liquid and vapor molar fractions of the hot stream along the recuperator.

shown in Figure 4.7. It reveals the difference between the temperature profiles of each blend and the exergy loss (irreversibility) in the recuperator. CO_2/SO_2 exhibits the greatest irreversibility and poorest match of the two streams; similar to pure CO_2. A proven solution to this issue is the adoption of more complex cycle architectures such as the recompression or partial cooling cycles (Crespi et al. 2017). The temperature profiles for CO_2/C_6F_6 and $CO_2/TiCl_4$, on the other hand, are well matched. Therefore, these mixtures work well in a simple recuperative cycle, and may not require elaborate cycle configurations, as previously noted by Manzolini et al. (Manzolini et al. 2019).

Because their profiles are almost parallel, higher effectiveness in CO_2/C_6F_6 and $CO_2/TiCl_4$ cycles will reduce the exergy loss along the recuperator length, not just at the pinch point. However, using the same argument, a CO_2/SO_2 working fluid would not benefit much from higher effectiveness since it will reduce exergy loss at the pinch point without affecting the majority of the exergy loss elsewhere in

the recuperator. Therefore, using a high recuperator effectiveness for all working fluids while discounting the pinch point approach temperature from the analysis gives CO_2/SO_2 a false advantage. It may also lead to unobserved temperature profile overlaps and the consequent misidentification of the optimal dopant fraction and turbine design point.

Figure 4.7 also shows the vapor and liquid compositions of the hot stream within the recuperator. Condensation does not occur in CO_2/SO_2 mixture at this composition, and is also trivial for all considered fractions of SO_2 below (0.4). Considerable condensation occurs in both $CO_2/TiCl_4$ and CO_2/C_6F_6 recuperators, where almost 33% and 23% of the heat is exchanged during two-phase flow, respectively. This phenomenon is directly caused by the mixture's temperature glide. As the dew temperature becomes greater than the bubble temperature, the portion of the recuperation process that occurs in the two-phase region increases. Figure 4.8, shows the temperature glide during heat rejection for the three working fluids. $CO_2/TiCl_4$ exhibits the greatest temperature glide, followed by CO_2/C_6F_6 and CO_2/SO_2. The high degree of glide in the two heavy mixtures suggests that appreciable fractionation (where one component is largely in the vapor state, while the other is still mostly liquid) occurs during cooling, which might require additional equipment such as vapor-liquid separators and separate heat exchangers for each component, hence greater pressure losses.

As seen in Figure 4.9, the turbine specific work decreases for both $CO_2/TiCl_4$ and CO_2/C_6F_6, but increases for CO_2/SO_2; the cause of which will be explained later. For a fixed electrical power output, the change in specific work causes an opposite trend in the mass flow rate. Not only does the turbine exhaust volumetric flow rate depend on the mass flow rate, but it also depends on its density. For all working fluids, the volume flow rate decreases with dopant fraction because of the increase in the fluids' density.

A zero-dimensional study of the specific speed for the whole turbine gives an indication of its shape and size. With a fixed rotational speed, any change in the specific speed will be a result of the change in the volumetric flow rate or specific enthalpy

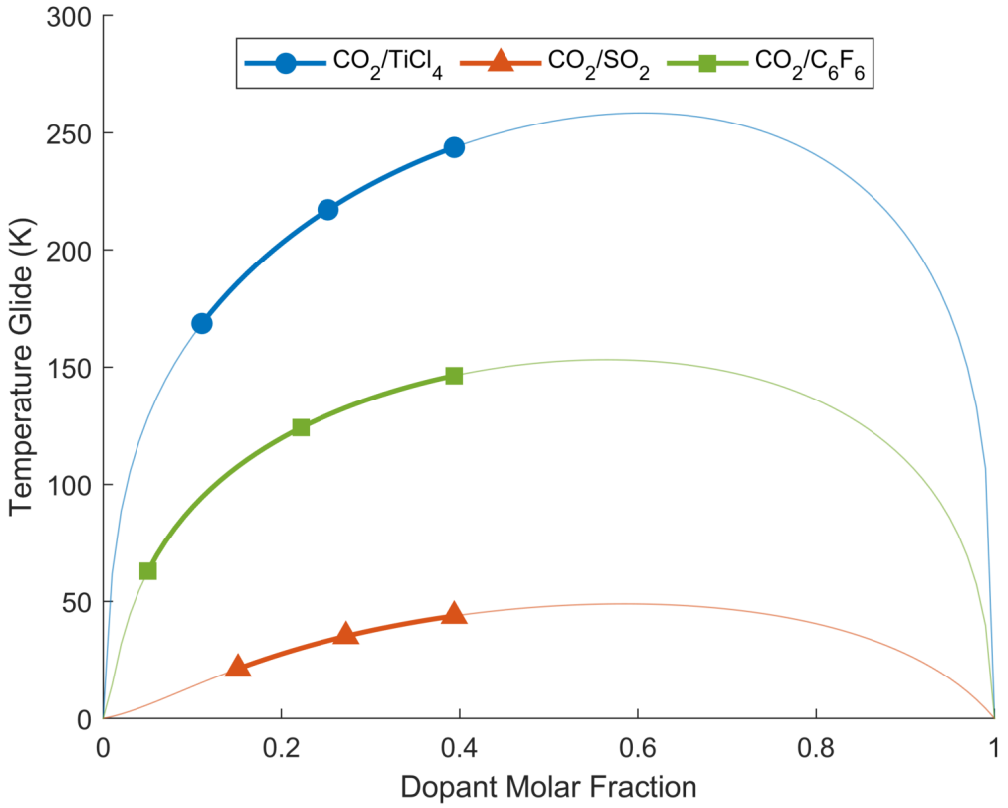

Figure 4.8: Difference between bubble and dew temperatures (temperature glide) for all compositions of the three mixtures. The highlighted segments represent the range of molar fractions studied here

drop across the turbine. As seen in Figure 4.9 the specific speed of $CO_2/TiCl_4$ and CO_2/C_6F_6 increases with blend fraction, indicating a reduction in the turbine's diameter, accompanied by an increase in the annulus area. The opposite is true for the CO_2/SO_2 mixture, where wider turbines with smaller annulus areas are expected at higher dopant fractions.

4.2.4 Incorporation into solar power towers

To compare the adaptability of the optimal working fluids to Solar Power Tower (SPT) applications, the cycles were tested for their compatibility with dry cooling. Variations in ambient temperature affect the condenser's ability to remove heat from the cycle, which will change the temperature of the working fluid at pump inlet. The more susceptible the performance of the cycle is to variations in the pump inlet temperature, the less compatible it is with dry cooling.

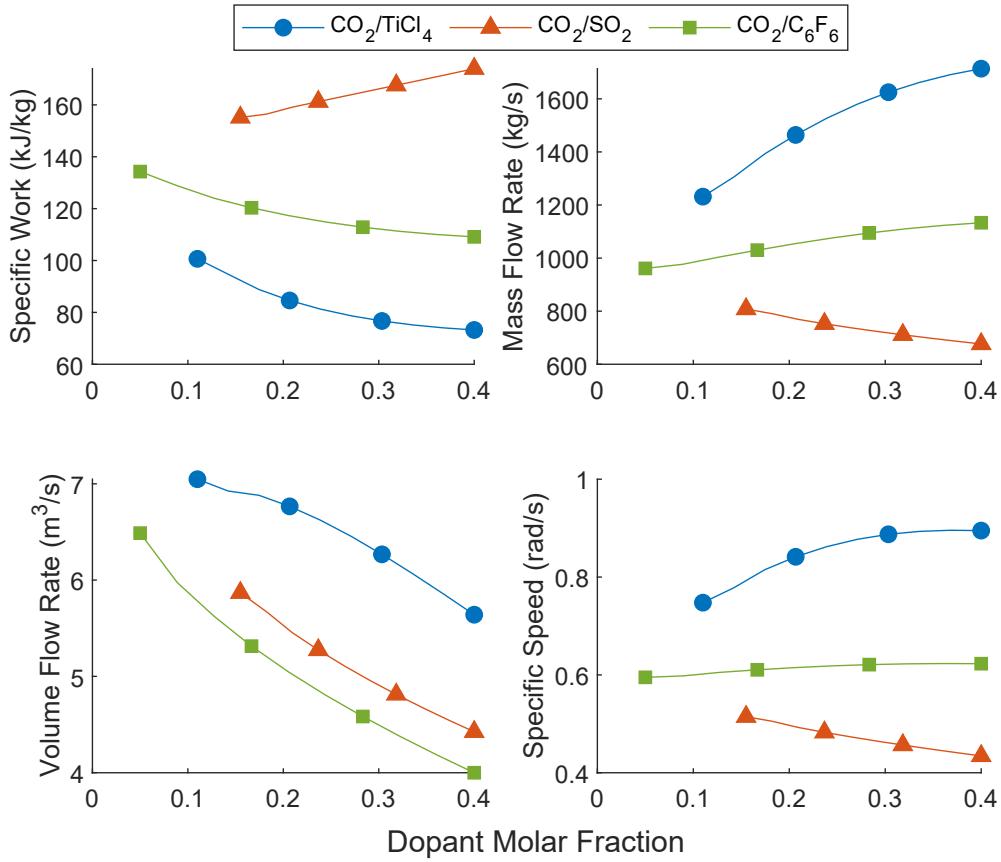

Figure 4.9: Variation of turbine specific work, mass flow rate, volume flow rate at turbine outlet, and specific speed with dopant molar fraction

Logically, the rise of ambient temperatures above the 40 °C design point is the main concern, since a drop in ambient temperatures is likely to improve the cycle's performance, and can even be mitigated by controlled cooling, if need be. However, an elevation in the cooling air temperature cannot be easily mitigated, thus it will affect the condenser's performance. Figure 4.10 reveals the loss in efficiency as the pump inlet temperature is increased by up to 10 K. The efficiency for each temperature increment is obtained by rerunning the optimisation at the elevated turbine inlet temperatures. Although, all three mixtures exhibit about 4% loss in efficiency, the effect is less pronounced in $CO_2/TiCl_4$ and CO_2/C_6F_6 because it occurs gradually over the 10 K range. Conversely, the 4% loss occurs within an increment of only 3 K for CO_2/SO_2. This is a consequence of the pump inlet conditions growing closer to the critical point where the fluid becomes more compressible, thus requires greater compression work.

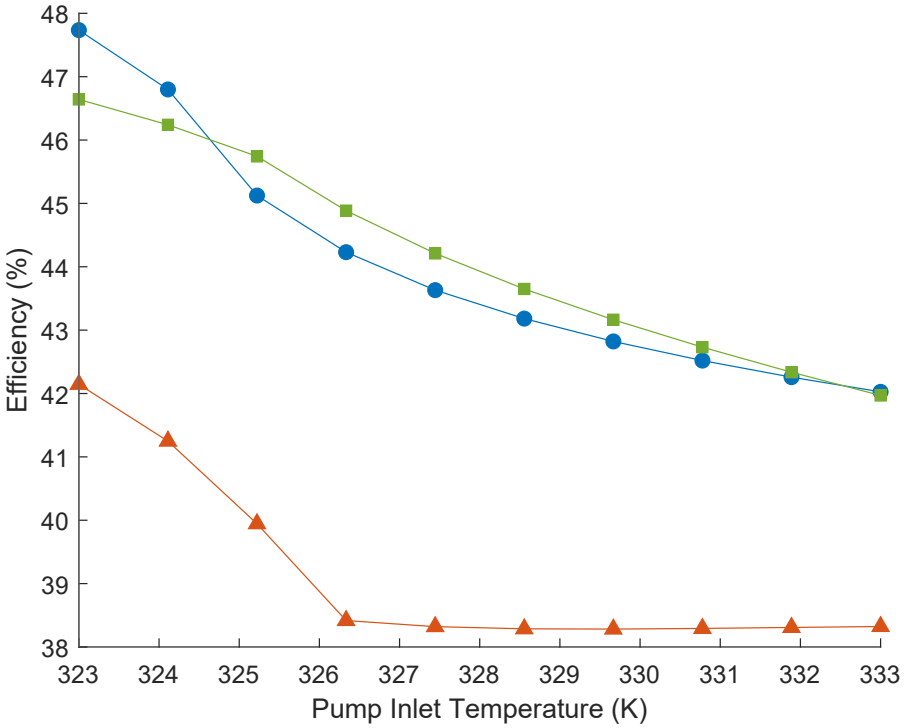

Figure 4.10: Change in thermal efficiency with pump inlet temperature variations

4.2.5 Expansion process

To characterise the expansion process, Figures 4.11 and 4.12 have been derived by assuming ideal gas behaviour throughout the expansion process and using the isentropic relations shown in Eq. 4.1 and 4.2:

$$r = \frac{P_{\text{in}}}{P_{\text{out}}} = \left(\frac{T_{\text{in}}}{T_{\text{out}}}\right)^{\frac{\gamma}{\gamma-1}} = \left(\frac{\nu_{\text{out}}}{\nu_{\text{in}}}\right)^{\gamma} \tag{4.1}$$

$$w_{\text{t}} = \left(\frac{\gamma}{\gamma-1}\right)\frac{P_{\text{in}}}{\rho_{\text{in}}}\left(1 - r^{\frac{1-\gamma}{\gamma}}\right) \tag{4.2}$$

where γ is the adiabatic coefficient ($\gamma = C_{\text{p}}/C_{\text{v}}$). The assumption of ideal gas behaviour easily permits an investigation of certain flow features without the aid of a more sophisticated EoS. This assumption is justified by the near unity (0.95 to 1.1) compressibility factor of all working fluids at both turbine inlet and outlet.

As shown in Figure 4.11, the adiabatic coefficients of $CO_2/TiCl_4$ and CO_2/SO_2 increase modestly, but significantly decrease for CO_2/C_6F_6. The trend in the adiabatic coefficient of CO_2/C_6F_6 is almost coincident with the isoline $T_1/T_2 = 1.15$, indicating

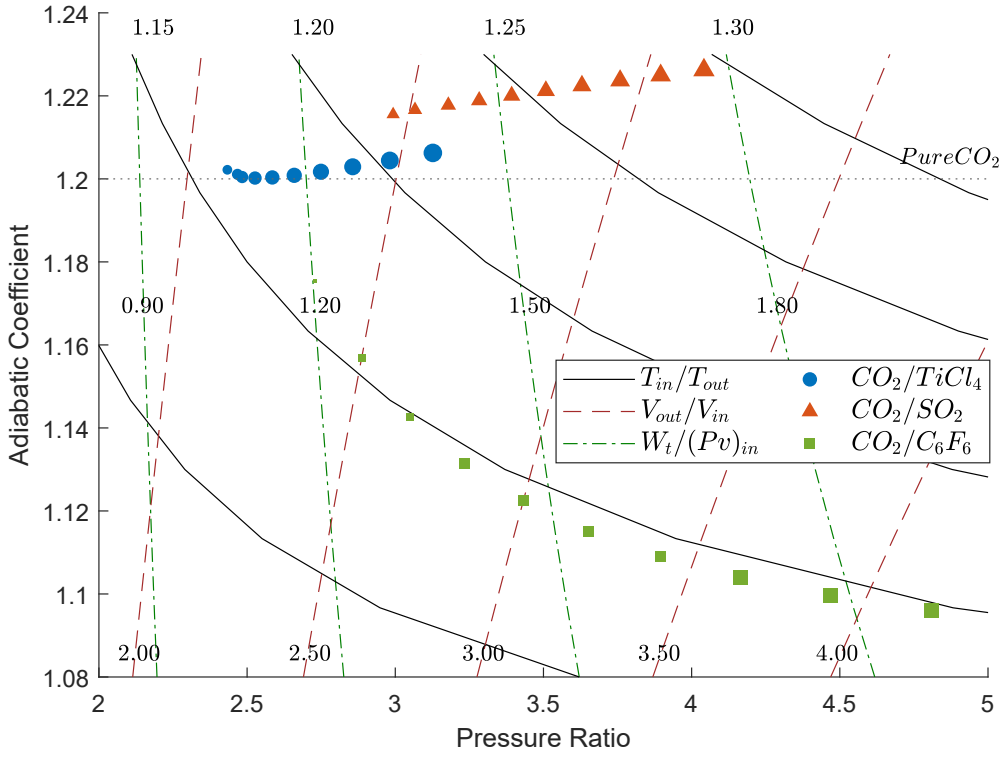

Figure 4.11: Maps the effect of dopant fraction on the turbine isentropic volume, temperature, and pressure ratios. The size of the point is proportional to the dopant fraction

that the decrease in the isentropic coefficient negates the effect of the increase in pressure ratio on the temperature drop across the turbine, thus maintaining almost the same temperature drop for all fractions. In contrast, the temperature drop increases for $CO_2/TiCl_4$ and CO_2/SO_2, suggesting a reduction in the recuperative capacity of their cycles. This finding agrees with the trends in specific recuperated heat shown in Figure 4.5.

The expansion ratio of the CO_2/C_6F_6 increases at a higher rate than the other two mixtures because of the more drastic changes in the pressure ratio and in the adiabatic coefficient. Higher expansion ratios indicate greater compressibility effects, as confirmed by Figure 4.14. Therefore, CO_2/C_6F_6 turbines may be more susceptible to supersonic flows than the other two mixtures, and are also likely to exhibit larger blade height variations in multi-stage turbines as the amount of C_6F_6 increases. This is explored in the next section.

By rearranging Eq. 4.2, the relation between specific work and adiabatic coefficient can be described through the work to pressure-volume ratio, as seen in Eq. 4.3.

$$\frac{w_{\mathrm{t}}}{(P\nu)_{\mathrm{in}}} = \left(\frac{\gamma}{\gamma - 1}\right)\left(1 - r^{\frac{1-\gamma}{\gamma}}\right) \tag{4.3}$$

The fixed density-specific work isolines in Figure 4.11 depict the relative independence of specific work from the adiabatic coefficient. At its greatest, the drop in the adiabatic coefficient of CO_2/C_6F_6 causes a mere 3% drop in specific work, whereas its effect on the specific work for the other two mixtures is less than 1%. Overall, Figure 4.11 suggests that the adiabatic coefficient becomes more significant at higher pressure ratios. Therefore, if the maximum allowable cycle pressure is increased, the variances between the expansion processes of the mixtures are expected to become more pronounced.

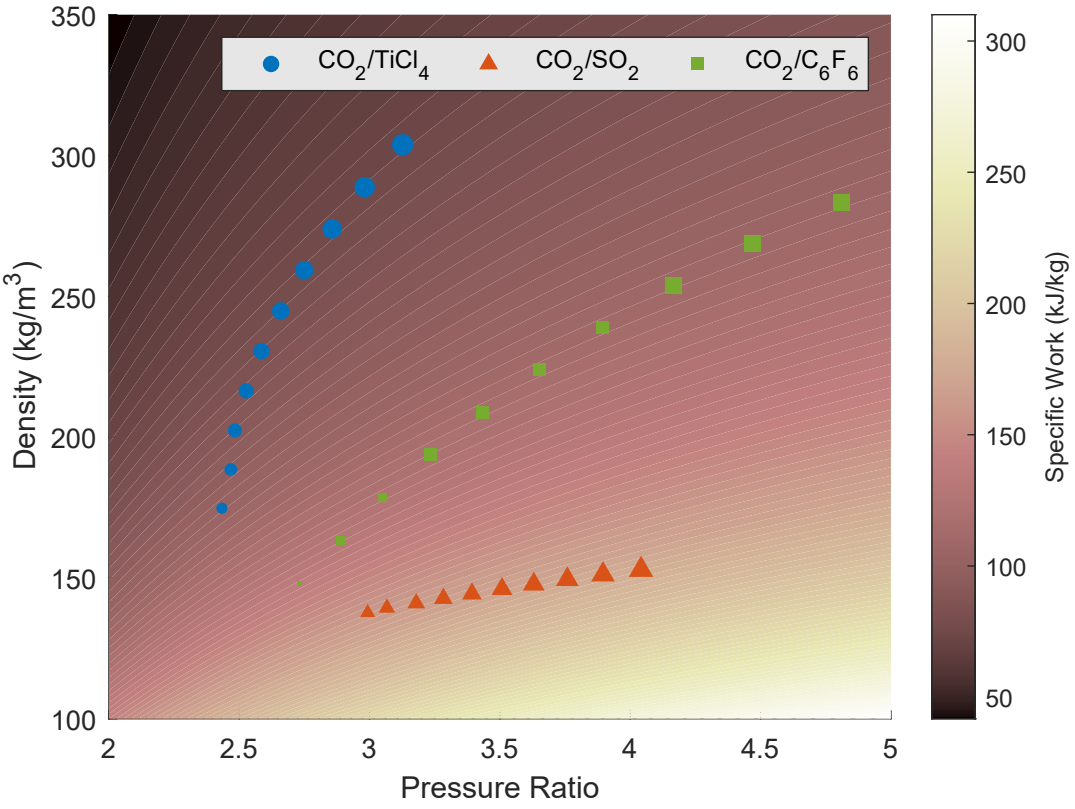

Figure 4.12: Maps the effect of dopant fraction on the working fluid's density at turbine inlet, pressure ratio, and turbine specific work. The size of the point is proportional to the dopant fraction

The effect of the density at turbine inlet is evident in Figure 4.12. Whilst ignoring

the effect of the change in the adiabatic coefficient on specific work, which has been shown to be trivial, higher densities result in lower specific work for a given pressure ratio. In the present study, both density at turbine inlet and pressure ratio increase with dopant molar fraction, but to varying degrees. For CO_2/SO_2 the increase in density is small, thus the specific work increases with the increasing pressure ratio. For $CO_2/TiCl_4$ and CO_2/C_6F_6, however, there is a significant increase in density which causes a decrease in the specific work, even though the pressure ratio increases. For comparison, the densities of $CO_2/TiCl_4$, CO_2/SO_2, and CO_2/C_6F_6 increase by 74%, 11%, and 91%, whilst the pressure ratios increase by 28%, 35%, and 76%, respectively. The outcome is a 27% and 19% decrease in specific work for $CO_2/TiCl_4$ and CO_2/C_6F_6, and an increase of 12% in specific work for CO_2/SO_2. These results demonstrate the dependence of specific work on both density and pressure ratio, which are in turn dependant on the dopant molar fraction.

The same phenomena may also be observed through the slope of the expansion isentrope in a P-h diagram and in Eq. 4.4. In Figure 4.13, the slope of the isentrope depends on the fluid density while the horizontal distance between the two ends of the expansion process indicates its specific work.

$$\mathrm{d}h = T\mathrm{d}s + \mathrm{d}P/\rho \xrightarrow{\mathrm{d}s=0} \mathrm{d}h = \mathrm{d}P/\rho \tag{4.4}$$

As the molar fraction of the dopant increases, the slope and lower end of the expansion process changes according to the turbine inlet density and pressure ratio, respectively. Since the density of all mixtures increases with blend fraction, their expansion follows a steeper isentrope. Simultaneously, the increasing pressure ratio extends the vertical length of the line. The combined movements of the two effects ultimately determines the horizontal distance (enthalpy drop). The same effect may be attained by lowering the turbine inlet temperature and moving closer to the Andrew's curve (saturation line) where densities are higher.

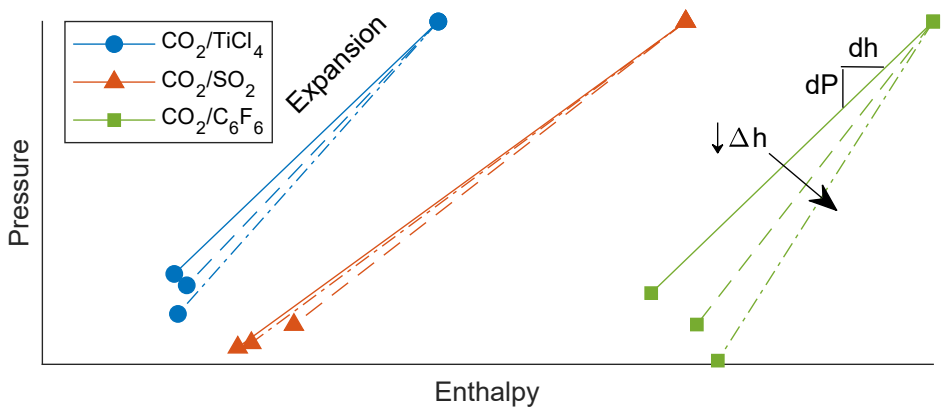

Figure 4.13: Comparison between the expansion process for three different amounts of dopant fractions. The solid line (-) indicates low dopant fraction, the dashed line (--) indicates medium dopant fraction, and the dot-dash (-.) line indicates high dopant fraction

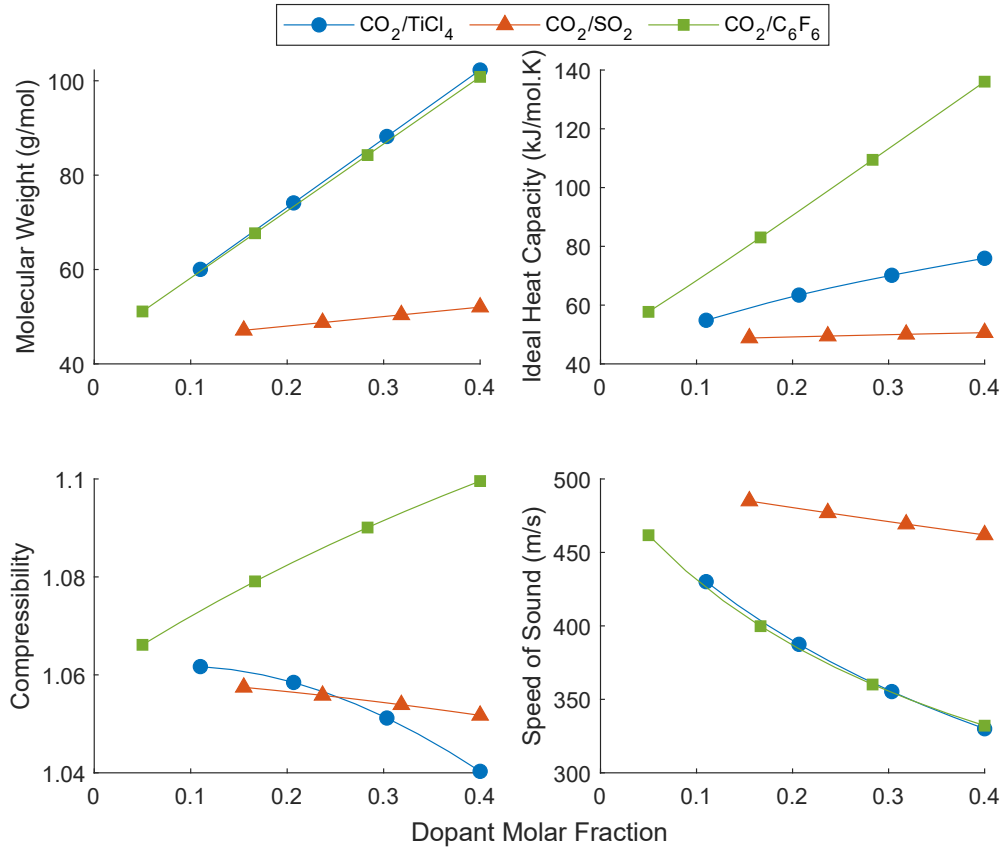

Figure 4.14: Variation of molecular weight, ideal specific heat capacity, compressibility factor at turbine inlet, and speed of sound at turbine inlet with dopant molar fraction

4.2.6 Molecular characteristics

As shown in Figure 4.14, the molecular weight of the working fluid increases significantly with the addition of C_6F_6 or $TiCl_4$, but only slightly with SO_2. Higher

molecular weights are known to decrease the heat transfer coefficient and increase the size of the heat exchangers (Lasala et al. 2018). Since the turbine inlet temperature is constant, and the effect of the isentropic coefficient is minor, the increase in molecular weight leads to an increase in density and a decrease in the speed of sound according to Eq. 4.5 and 4.6:

$$a = \sqrt{\gamma RT/M} \tag{4.5}$$

$$\rho = PM/ZRT \tag{4.6}$$

where the fluid is assumed to be an ideal gas, a is the speed of sound (m/s), γ is the adiabatic coefficient, M is the molar weight (kg/mol), Z is the compressibility factor, and R is the ideal gas constant (8.314 $J/mol.K$).

The decrease in the speed of sound is almost identical for the two heavy mixtures $CO_2/TiCl_4$ and CO_2/C_6F_6, while CO_2/SO_2 exhibits a less dramatic change in the speed of sound. As a general rule, the reduction in the speed of sound in conjunction with the increase in pressure ratio may lead to an increase in Mach numbers and the creation of supersonic flows.

Counter intuitively, $CO_2/TiCl_4$ is expected to have lower Mach numbers than CO_2/C_6F_6, although it exhibits comparable sound speeds. This contrast is attributed to the particulars of the overall cycle behaviour which limit the pressure drop of $CO_2/TiCl_4$ during expansion. Consequently, for the same number of stages, lower Mach numbers are expected in $CO_2/TiCl_4$ than the other two mixtures. However, as will be seen in the next section, subsonic flow requirements are not the determining factor for the number of turbine stages, rather it's the maximum allowable blade stress. Therefore, it is unlikely that supersonic flow conditions will present issues for any of the blends.

The ideal heat capacity, also shown in Figure 4.14, is also affected by the dopant molar fraction. It increases for mixtures of CO_2/C_6F_6 and $CO_2/TiCl_4$, but remains almost constant for CO_2/SO_2. Ideal heat capacity depends on the molecular complexity of the fluid (number of atoms per molecule and their configurations). From a molecular perspective, this trend may be attributed to the increasing complexity

of the mixture molecules with the addition of the dopants. Since SO_2 has a similar complexity to that of CO_2, there is no tangible change in the mixture's ideal heat capacity.

The ideal heat capacity has profound implications on recuperative cycles. Higher values reduce the difference between the heat capacities of the low- and high-pressure streams of the recuperator. The relative difference between the two has a direct effect on the pinch point temperature and the compatibility of the temperature profiles; i.e. the lower the difference the better the recuperation. The trend in ideal specific heat explains the T-Q profiles and irreversibilites observed in Figure 4.7 earlier.

4.2.7 Mean-line design of axial turbine

The results presented in this section are intended to compare the general trends in the turbine design with dopant molar fraction. Moving into the mean-line design of an axial turbine requires the definition of certain parameters, which are summarised in Table 4.4. The selection of these parameters was based on common design practices that yield high turbine efficiencies (Saravanamuttoo et al. 2017). No attempt has been made to modify these parameters to optimise the turbine designs. Rather, the assumptions were made with the intent of providing a common basis for comparing turbine geometries, regardless of the blend. Further turbine optimisation is required before optimal designs for specific blends are compared, which will be considered in future work. In Chapter 6 the implications of doping CO_2 on the optimal designs of radial inflow turbines is investigated in detail.

The turbine mean-line design relies on the assumption of a fixed turbine efficiency. This assumption is deemed sufficient for the objectives of the current study, which is focused more on the overall cycle and general effect of the blend the turbine design, rather than identifying optimal turbine geometries. The set of assumptions are listed in Table 4.4.

As mentioned previously, the number of axial turbine stages is governed by the mechanical integrity of the turbine blades. Both rotor blade centrifugal and gas

Table 4.4: Axial turbine design parameters

Parameter	Value	Units
Rotational speed (N)	3000	RPM
Turbine efficiency (η_t)	90	%
Loading Coefficient (ψ)	1.65	-
Flow Coefficient (ϕ)	0.23	-
Degree of Reaction (Λ)	0.5	-
Aspect ratio (b/c)	2	-
Thickness-to-chord ratio (t/c)	0.5	-
Pitch-to-chord ratio (S/c)	0.85	-

bending stresses were calculated for all possible mixture compositions. Unlike steam or gas turbines, centrifugal stress is not the dominant source of mechanical stress in CO_2 turbines. As seen in Figure 4.15, gas bending stresses are greater by an order of magnitude.

In general, the tensile centrifugal stress is determined by the turbine's rotational speed and annulus area according to Eq. 4.7:

$$\sigma_{ct} = 2\pi K N^2 \rho_{\mathrm{b}} A_{\mathrm{avg}}/3600 \tag{4.7}$$

where the coefficient K depends on the taper of the blade and is set to 2/3 assuming a tapered blade (Moustapha et al. 2003), ρ_{b} is the density of the blade (appx. 8000 kg/m^3), and A_{avg} is the average annulus area between rotor inlet and outlet.

The rotational speed was fixed to a relatively moderate value of 3000 RPM to allow direct connection to a 50 Hz synchronous electric generator, without the need for a gearbox. On the other hand, the annulus area is narrower than that of gas turbines because of the low volumetric flow rate of the working fluid. Both of these factor reduce the significance of centrifugal stresses.

Gas bending stress may be expressed as a function of the fluid density, stage enthalpy drop, flow coefficient, and stage geometric relations:

$$\sigma_{\mathrm{gb}} = \left(\frac{4\pi\varphi N}{60}\right)\left(\frac{r_{\mathrm{s/c}} {r_{\mathrm{b/c}}}^2}{z}\right)\rho\Delta h \;\rightarrow\; \sigma_{\mathrm{gb}} \propto \rho\Delta h \tag{4.8}$$

The flow coefficient (ϕ) and stage geometric relations ($r_{\mathrm{s/c}}$, $r_{\mathrm{b/c}}$) were chosen based on gas turbine best practices, thus are not the cause for the high stresses. The strong aerodynamic stresses are likely to be caused by the fluid's high density and the stage enthalpy drop. Since the density is imposed by optimal cycle conditions, the stress may otherwise be alleviated by increasing the number of stages to reduce the enthalpy drop per stage. As seen in Figure 4.15, at least 4 stages are required to remain below the maximum design stress. The figure also shows that higher dopant fractions produce greater gas bending stresses. However, the difference between the stresses for all fractions reduces with increasing number of stages. One could argue that the number of stages is no longer affected by the blend fraction for axial turbine with three or more stages. The severity of aerodynamic stresses in sCO_2 turbines have been identified in previous publications (Zhang et al. 2015, Moroz et al. 2014, Wang et al. 2004).

Although the design presented here is for a 4-stage axial turbine, according to Figure 2.31 the number of stages for CO_2-based turbines will have to be at least 12-stages to achieve total-to-static efficiencies greater than 90%. Indeed, this is confirmed by Abdeldayem et al. (2023) who presented a 14-stage axial turbine design for a CO_2/SO_2 mixture. However, the analysis of the trends presented here hold true regardless of the number of stages.

Figure 4.16 illustrates the meridonal profiles of the turbine rotors for the range of blend fractions considered and may be studied to draw a comparison between two trends: (1) the different turbine geometries of the three dopants; (2) and the varying turbine geometries of the same mixture, but with changing dopant fractions.

For a fixed loading coefficient and rotational speed, the diameter of the turbine becomes a sole function of the enthalpy drop. Therefore, CO_2/SO_2 turbines, which experience higher enthalpy drops per stage, require wider turbines than CO_2/C_6F_6 or $CO_2/TiCl_4$. On the other hand, the blade height is influenced by the volume flow rate and enthalpy drop of the turbine in accordance with Eq. 4.9:

$$b \propto \dot{V}/\Delta h \tag{4.9}$$

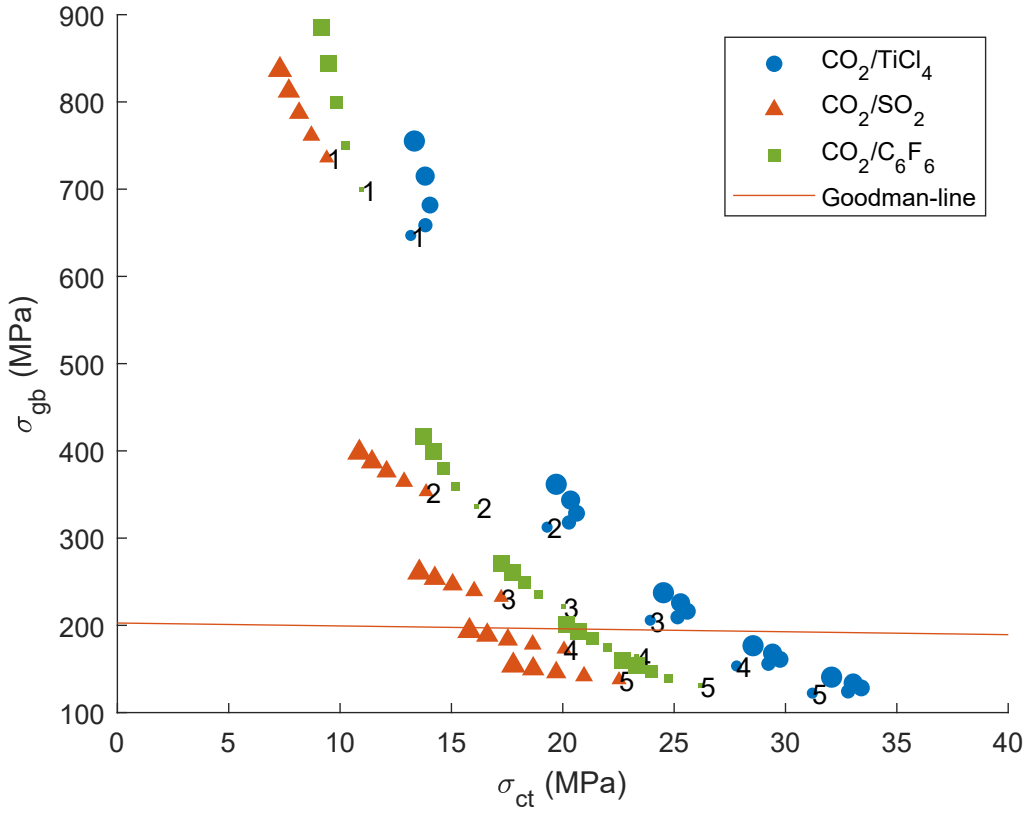

Figure 4.15: Maximum allowable blade mechanical stresses based on number of turbine stages. The numbers denote the number of turbine stages corresponding to the plotted points and the point size is proportional to the dopant fraction

As seen in Figure 4.17, $CO_2/TiCl_4$ requires the longest blades, followed by CO_2/C_6F_6 and CO_2/SO_2, which is explained by its higher volume flow rates and lower specific work. Moreover, the blade heights of $CO_2/TiCl_4$ and CO_2/C_6F_6 increase with blend fraction but decrease for CO_2/SO_2 blends.

Since the blade aspect ratio is fixed, the chord length becomes linearly proportional to the blade height. Therefore, the chord length increases with blade length, and the axial length of the turbine increases by consequence. Accordingly, in a transcritical cycle, one might expect the turbine to have a wider diameter and shorter length for mixtures that increase its specific work.

As previously noted, the expansion ratio increases with blend fraction for all mixtures. This is demonstrated in Figure 4.18, which plots the normalized heights of the turbine rotor blades, where the change in blade height is proportional to the expansion ratio across the turbine. The change in blade height with each stage

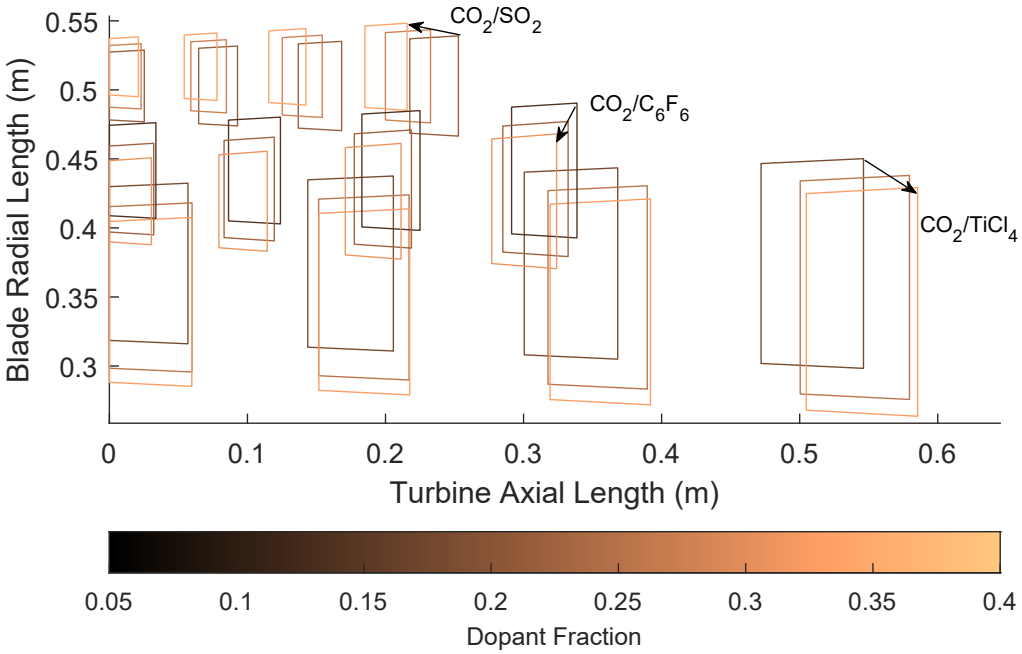

Figure 4.16: Transformation of rotor profiles based on dopant molar fraction

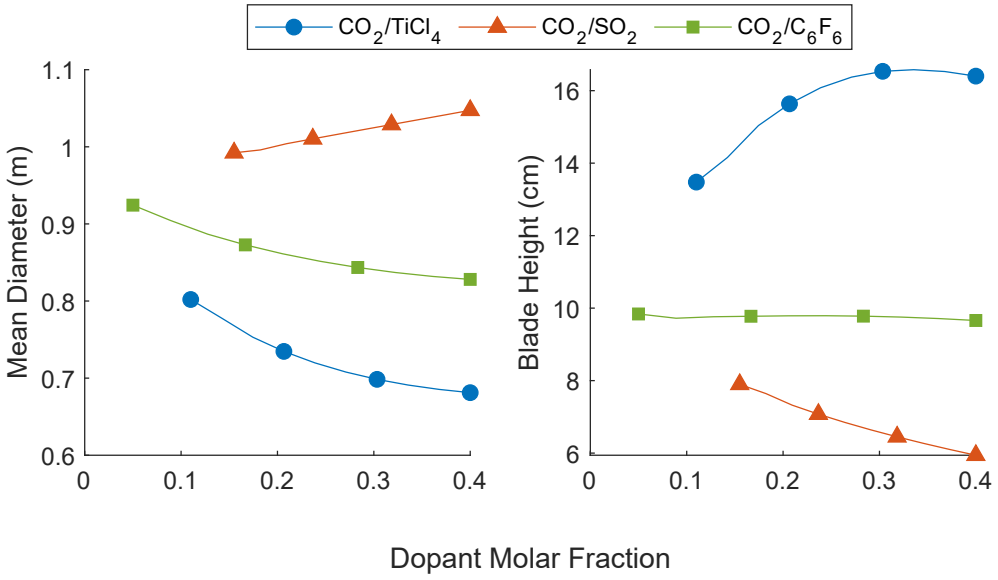

Figure 4.17: Variation of mean diameter and rotor blade height at last stage with dopant molar fraction

increases with blend fraction for all mixtures, suggesting that the turbine flare angle increases with blend fraction. However, CO_2/C_6F_6 exhibits the greatest increase.

A schematic of the T-s diagram and turbine flow paths meridional view corresponding to the optimal points are illustrated in Figure 4.19 and 4.20. The cycle

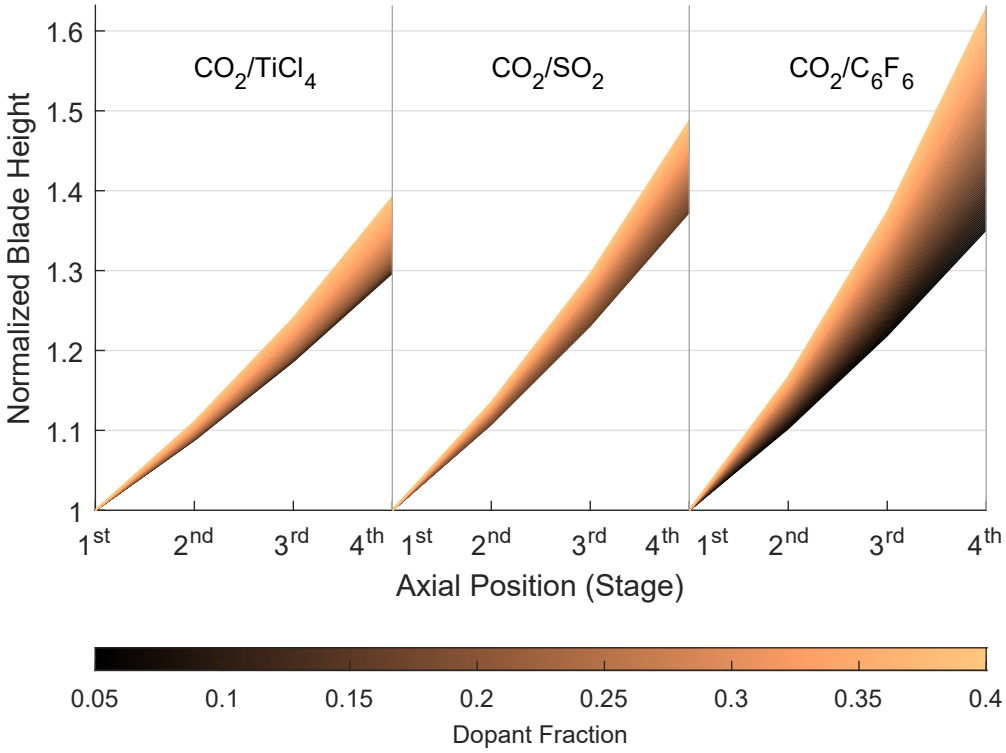

Figure 4.18: Normalised stage-wise rotor blade height for the range of dopant molar fraction

and turbine parameters corresponding to the compositions, pressure ratio, and recuperator effectiveness that yield optimal cycle efficiency are summarised in Table 4.5. Although there are notable differences between the four working fluids, they share comparably high mass-flow rates in the order of 1000 kg/s, and relatively low volumetric flow rates below 10 m^3/s. To put these number into perspective, the H-100 gas turbine manufactured by Mitsubishi has a similar capacity of around 100 MW, and exhausts about 300 kg/s of air at approximately 550 °C. Assuming ideal gas and ambient pressure conditions, this translates to 700 m^3/s. Therefore, the contrast between air and CO_2-based turbines' design space shows in both mass and volume flow rates.

Not only do blended CO_2 cycles outperform pure CO_2 in simple recuperated cycles, they also outperform pure CO_2 in recompression plants. Modelling of recompression cycle with similar boundary conditions, equipment efficiencies, 89% recompressor efficiency, and 0.79 split fraction yields an overall thermal efficiency of 43.4%.

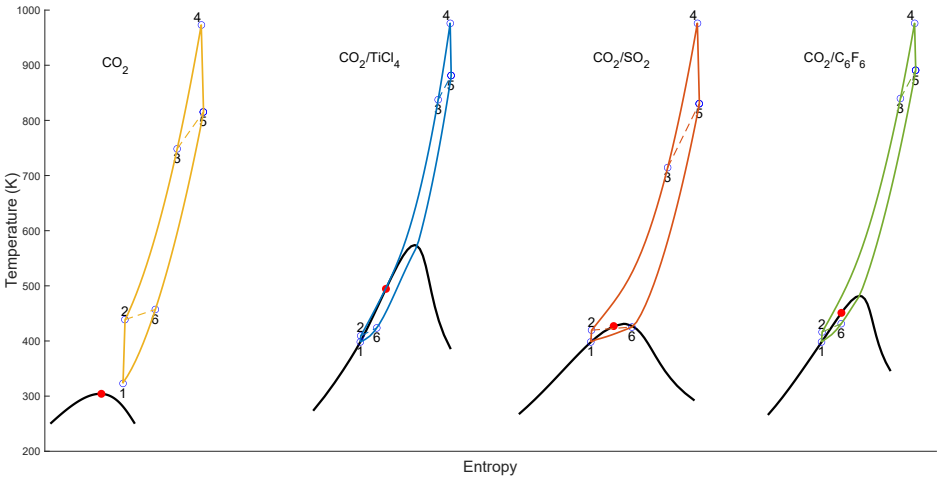

Figure 4.19: Schematic of the T-s diagram for the dopant fraction and cycle conditions that yield optimal thermal efficiency. The critical point is indicated by a red dot

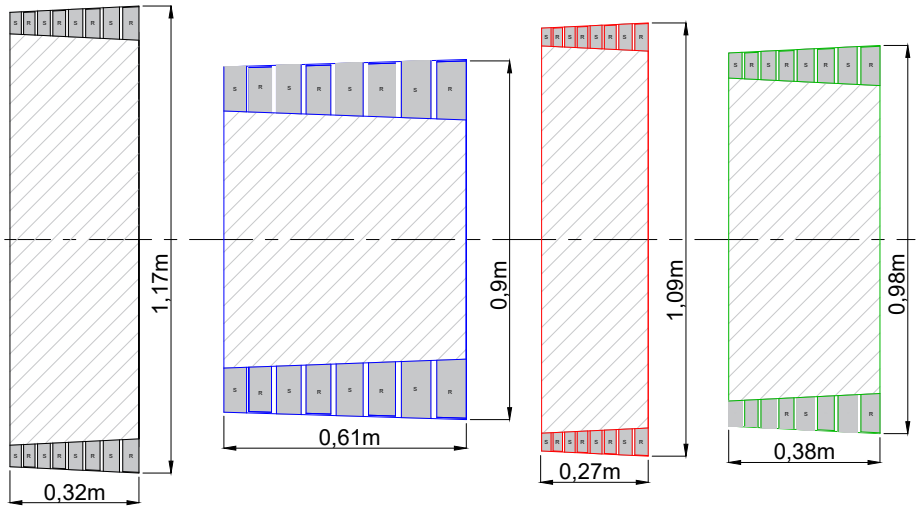

Figure 4.20: Comparison of turbine flow paths meridional view corresponding to the design point that yields optimal thermal efficiency for pure CO_2 and CO_2-based mixtures. Left to right: Pure CO_2; $CO_2/TiCl_4$; CO_2/SO_2; CO_2/C_6F_6

This comparison suggests that dopants like $TiCl_4$ and C_6F_6 achieve higher thermal efficiencies even in simpler cycle layouts. The implications of doping CO_2 on the performance of recompression cycles is explored next.

Table 4.5: Comparison of design and performance parameters of 100 MWe pure sCO_2 and tCO_2 power plants operating with different mixtures

Working Fluid	CO_2	$CO_2/TiCl_4$	CO_2/SO_2	CO_2/C_6F_6
Dopant Molar fraction	0	0.174	0.264	0.167
Thermal Efficiency (%)	41.7	49.5	42.3	46.5
Recuperator Effectiveness (%)	98.5	95.9	98	93.1
Recuperator Heat Load (MW)	398	844	389	799
PHE Inlet Temperature (K)	762	823	687	819
PHE Heat Load (MW)	242	204	239	217
Turbine				
Mass flow rate (kg/s)	902	1393	738	1054
Exhaust volume flow rate (m^3/s)	7.03	6.88	5.11	5.31
Inlet temperature (K)	973	973	973	973
Outlet temperature (K)	817	869	817	877
Enthalpy drop (MJ/kg)	186	88.8	163	120
Mean diameter (m)	1.09	0.753	1.02	0.873
Axial length (m)	0.32	0.61	0.27	0.38

4.3 Effect of dopant on cycle architecture

In Section 2.2, the reduction of recuperation irreversibilities was identified as the chief impetus for the adoption of complex cycles such as the recompression and precompression layouts. As noted earlier, the issue of irreversibility is solved through these layouts by reducing the difference in the heat flow capacity of the the high- and low-pressure streams of the recuperator. It was shown in the preceding Section 4.2.3 that recuperator irreversibility is influenced by the choice of the dopant; $CO_2/TiCl_4$ and CO_2/C_6F_6 reduced irreversibility, whilst CO_2/SO_2 did not reduce it significantly. Therefore, one may hypothesise that dopants of higher ideal specific heat capacity at constant pressure will reduce recuperation irreversibility, thus negate the advantage of complex layouts.

4.3.1 Optimisation conditions

In this Section 4.3 the problem of dry-cooling in CSP plants is departed from to investigate the influence of the dopant choice and amount on the recuperative capabilities of simple recuperated cycles. Both simple and recompression cycles are optimised for a range of dopant molar fractions and their efficiencies are compared. Because the problem of recuperation is not exclusive to CSP, the compressor inlet temperature is assumed to be 15^{o}C. This temperature was chosen so that below or near critical temperature compression is ensured for all the mixtures for the entire range of their blend fractions considered here. Therefore, all cycles are transcritical and the difference between the sub-critical and super-critical specific heat capacity at constant pressure will persist. A summary of the recompression design and optimisation assumptions is provided in Table 4.6. Note that a common dopant molar fraction range was set for all fluids.

Table 4.6: Recompression cycle design and optimisation variables

Controlled Parameters		
Parameter	**Range**	**Unit**
Dopant Molar Fraction	0.05-0.5	%
Turbine Inlet Temperature (T_4)	700	°C
Pump Inlet Temperature (T_1)	15	°C
Pump Isentropic Efficiency(η_p)	85	%
Turbine Isentropic Efficiency(η_t)	90	%
Generator Efficiency(η_g)	99	%
Minimum internal temperature approach (MITA)	5	°C
$\Delta p/p$ of Primary Heat Exchanger	0.015	-
$\Delta p/p$ of Recuperator High- and Low-pressure sides	0.01 and 0.015	-
$\Delta p/p$ of Condenser	0.02	-
Dependant Parameters		
Pump Inlet Pressure(P_1)	$P_{\mathrm{sat@(T_1+2)}}$	MPa
Turbine Inlet Pressure(P_4)	Max (25)	MPa
Optimised Parameters		
Pressure Ratio (r)	2 to Max (P_4)/P_1	-
Recuperator Effectiveness(ϵ)	80 to 98	%
Split fraction(ϵ)	0 to 1	%

4.3.2 Choice of dopants

The study of the simple and recompression transcritical cycles is extended to nine dopants. These dopants were chosen so that they produce mixtures with critical temperatures above the preset pump inlet temperature of 15^{o}C. The dopants are listed in Table 4.7, along with select properties of interest. Moreover, the aim of this study is not to find the optimal mixture, rather is is to study the effect of the molecular characteristic of the dopants on cycle performance; therefore, the selection of the dopants does not take into account the thermal stability of the dopants at elevated temperatures nor their environmental impacts.

Table 4.7: Physical and thermodynamic properties of pure compounds (collected from DIPPR database and from Poling et al. (2001))

Name	**Chemical Formula**	**Molecular Weight** (g/mol)	**Acentric Factor** (ω)	**Critical Temperature** (K)	**Critical Pressure** (MPa)
Hydrogen sulphide	$\mathbf{H_2S}$	34.01	0.081	373.2	8.94
Sulpher dioxide	$\mathbf{SO_2}$	64.06	0.245	430.8	7.88
Propane	$\mathbf{C_3H_8}$	36.46	0.133	324.7	8.31
n-butane	$\mathbf{C_4H_{10}}$	58.12	0.199	425.2	3.80
n-pentane	$\mathbf{C_5H_{12}}$	72.15	0.251	469.7	3.37
Benzene	$\mathbf{C_6H_6}$	78.11	0.212	562.1	4.89
Thiophene	$\mathbf{C_4H_4S}$	84.14	0.197	579.4	5.69
Titanium tetrachloride	$\mathbf{TiCl_4}$	189.7	0.284	639.1	4.66
Hexaflourobenzene	$\mathbf{C_6F_6}$	186.1	0.395	516.7	3.27

As explained previously, a binary interaction parameters must be defined when using the van der Waals mixing rules. Apart from CO_2/$TiCl_4$, the values of k_{ij} in Table 4.8 were obtained by fitting PR EoS to experimental data from the sources listed in the table. In Chapter 7, the affect of the uncertainty in k_{ij} is investigated further. However, the current study is qualitative in nature and its results are expected to hold true despite the k_{ij} uncertainty.

Table 4.8: Values of k_{ij} that minimise the error between PR EoS and experimental data

Mixture	k_{ij}	Δk_{ij}	**Source of data**
$\mathbf{CO_2/H_2S}$	0.0871	0.0035	Bierlein & Kay (1953)
$\mathbf{CO_2/SO_2}$	0.0243	0.0031	Coquelet et al. (2014)
$\mathbf{CO_2/C_3H_8}$	0.0954	0.0637	Kim & Kim (2005)
$\mathbf{CO_2/C_4H_{10}}$	0.1228	0.0449	Shlbata & Sandler (1989)
$\mathbf{CO_2/C_5H_{12}}$	0.1350	0.0414	Tochigi et al. (1998)
$\mathbf{CO_2/C_6H_6}$	0.0874	0.0341	Gupta et al. (1982)
$\mathbf{CO_2/C_4H_4S}$	0.0639	0.0329	Elizalde-Solis & Galicia-Luna (2005)
$\mathbf{CO_2/TiCl_4}$	0.0745	0.0456	Bonalumi et al. (2018)
$\mathbf{CO_2/C_6F_6}$	0.0312	0.0104	Dias et al. (2006)

Comparison of simple and recompression transcritical cycles

Generally, recompression cycles have thermal efficiencies that are equal to or greater than that of the simple recuperated cycle, as shown in Figure 4.21. The recompression cycle is more efficient at the lowest dopant fraction (0.05) for all mixtures. The trends in Figure 4.21 may be put into three categories based on the efficiency difference (η_{r-s}) between the two cycles: constant, gradually diminishing, and abruptly diminishing.

The subplots are arranged in order of decreasing η_{r-s} ; left to right and top to bottom. For the first mixture of CO_2/H_2S, η_{r-s} remains relatively constant and H_2S is not expected to alleviate the irreversibility in the recuperator of a simple recuperated cycle; therefore, the recompression cycle will always be more efficient than the recuperated cycle under the same operating temperatures. The addition of SO_2 slightly alleviates the recuperator irreversibility, thus the modest change in η_{r-s} . With CO_2/propane, an increase in the molar fraction of propane brings the efficiency of the recompression cycle closer to that of the simple recuperated cycle, yet the former will clearly be more advantageous than latter. The decrease in η_{r-s} becomes greater as more complex dopants are used where the the efficiencies of the two cycles converge. With mixtures of butane, pentane, and benzene, this convergence occurs at lower amounts of dopant fraction as more complex dopants are used, indicating a correlation between the molecular complexity of the dopant and the rate at which η_{r-s}

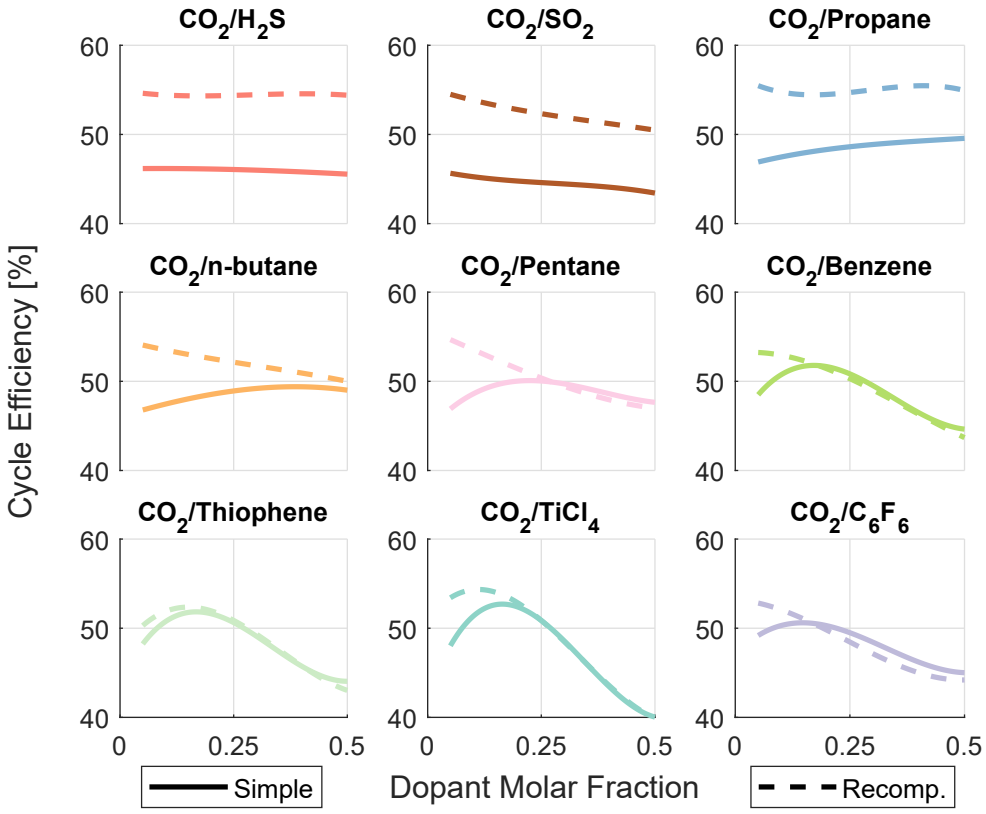

Figure 4.21: Thermal efficiency of simple recuperated (solid line) and recompression (dashed line) cycles across dopant molar fractions

diminishes with the dopant molar fraction; the more complex the dopant, the lesser fraction of it is needed to overcome recuperator irreversibility. Mixtures containing the most complex dopants, $CO_2/TiCl_4$, CO_2/thiophene, CO_2/C_6F_6, and CO_2/C_6H_6, overcome recuperator irrevesibility at relatively low dopant molar fractions below 0.2.

As suggested by Tafur-escanta et al. (2021), the recompression cycle may be thought of as two cycles operating in conjunction with each other: one that is driven by the pump which cycles through points 1 to 8, as in a simple recuperated cycle, and another that is driven by the recompressor which cycles through 3a, 4, 5, 6, 7, and 8. A schematic of this theoretical partition of the recompression cycle is shown in Figure 4.22. The amount of mass flowing in the recompressor-driven cycle depends on the irrevesibility of the heat exchange in the LTR. Therefore, the split fraction (x_s) can be thought of as a measure of the need for recuperator irreversibility alleviation; the higher the split fraction, the greater is the amount of flow diverted to the recompressor, the closer are the heat flow capacities of the low- and high-pressure streams.

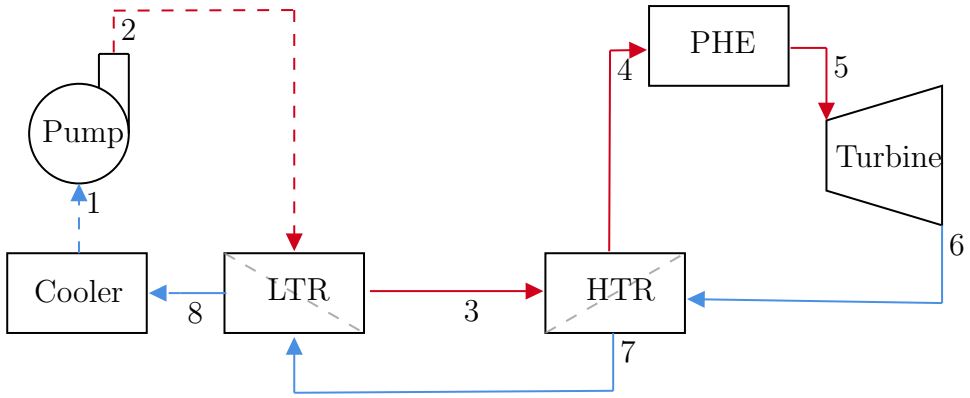

(a) Pump-driven

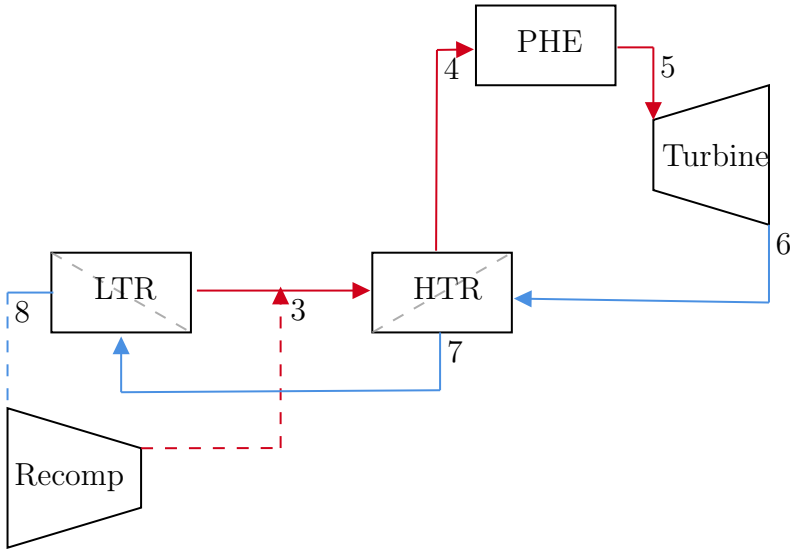

(b) Recompressor-driven

Figure 4.22: Theoretical partition of the recompression cycle into two cycles

The trend in the recompression cycle efficiency may be better understood by examining the trend in the flow split fraction, which is shown in Figure 4.23. For dopant fractions that achieve comparable efficiencies in both the recompression and simple cycles, the split fraction is zero; flow is not diverted to the recompressor. Therefore, the recompression cycle in those cases is in effect a simple recuperated cycle.

As already mentioned, the trends clearly suggest a relation between the molecular complexity of the dopants and recuperator irreversibility. To quantify this relation, molecular complexity (σ) will be defined in accordance with the definition used by

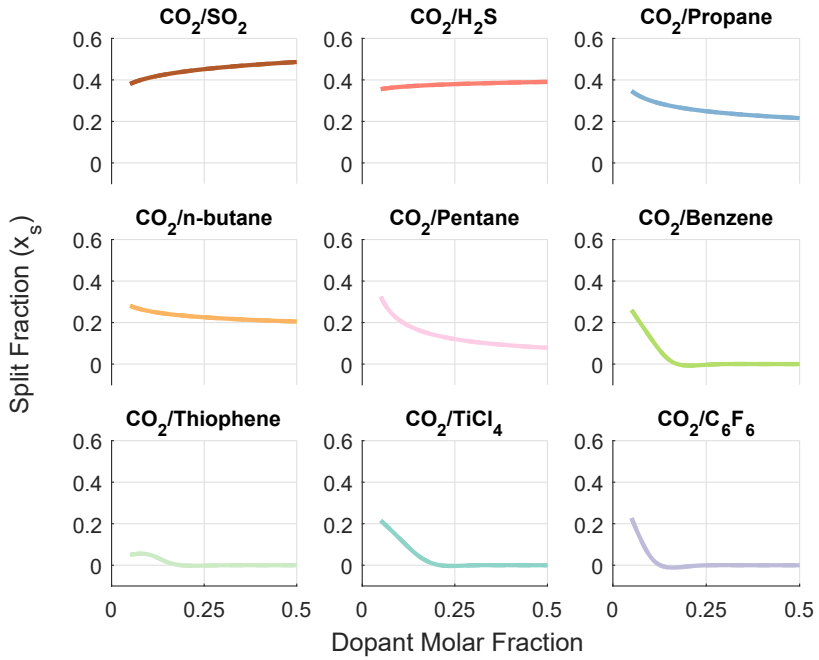

Figure 4.23: Split fraction in recompression cycles for the range of dopant molar fractions studied

Invernizzi (2013):

$$\sigma \approx \frac{C_{\mathrm{p}}^{0}}{0.7R} - \frac{\ln 10}{0.49} \times \frac{7}{3}(\omega + 1) \tag{4.10}$$

where C_{p}^{0} is the specific heat capacity at constant pressure at the dew point at a reduced temperature of 0.7, R is the specific gas constant, and ω is the acentric factor. Although originally developed for pure fluids, σ is extended to calculate the complexity of mixtures here; therefore, each mixture and dopant molar fraction combination will have a specified molecular complexity. Using this approach, the relation between σ and $\eta_{\mathrm{r-s}}$ is shown in Figure 4.24. The trend observed between the two variables agrees with the trends observed in the cycle efficiencies in Figure 4.21. Dopants that have molecular structures similar to CO_2, namely H_2S and SO_2, have an insignificant effect on the molecular complexity of the resulting mixture, thus an insignificant effect on the difference between the recompression and simple recuperated cycles. The effect of complexity is most evident with dopants that are slightly more complex than CO_2, namely propane, butane, and pentane, because the increase in complexity with dopant molar fraction is gradual, and so is the reduction in $\eta_{\mathrm{r-s}}$.

Ideally, the trend should be asymptotic to $\eta_{\mathrm{r-s}}$ =0; the recompression efficiency would not be lower than the simple recuperated cycle. However, even if the split

fraction becomes zero, at which none of the flow is diverted to the recompressor, the recompression cycle has an additional pressure drop because of the additional recuperator. Therefore, the efficiency of the recompression cycle may drop below that of the simple recuperated cycle; but in practice this would not be the case because a single recuperator would be used for a split fraction of zero. In other words, this is a modeling artifact that may be resolved by assuming a single recuperator if the split fraction is equal to zero.

A clear cut complexity threshold above which the recompression and simple recuperated cycle have the same efficiency is not discernible. This could be due to other factors that affect cycle efficiency such as the pressure ratio, pressure drop in the heat exchanger, and, as will be seen in Chapter 7, the uncertainty in the calculation of fluid properties. The complexity of the dopants relative to CO_2 may also be observed by comparing the shape of their saturation domes in the reduced temperature-entropy plane, as shown in Figure 4.25. The slope of the curve ($\frac{\partial T}{\partial s}$) indicates the complexity of the fluid; the lower the slope, the more complex the fluid.

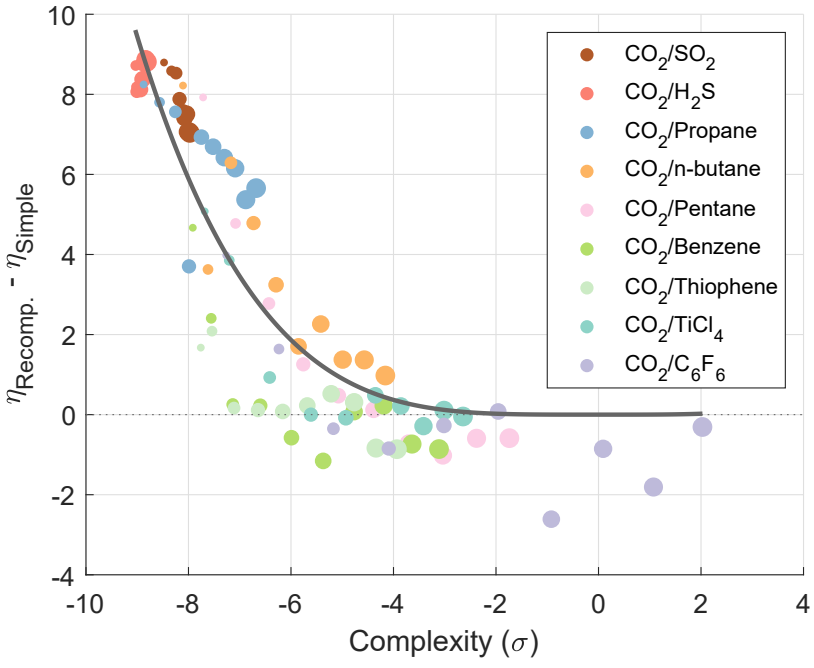

Figure 4.24: Correlation between molecular complexity and the difference between the recompression and simple recuperated cycles. The size of the points indicates the dopant molar fraction; the larger the point the greater the dopant molar fraction. A trend line has been added to show the asymptotic nature of the relation.

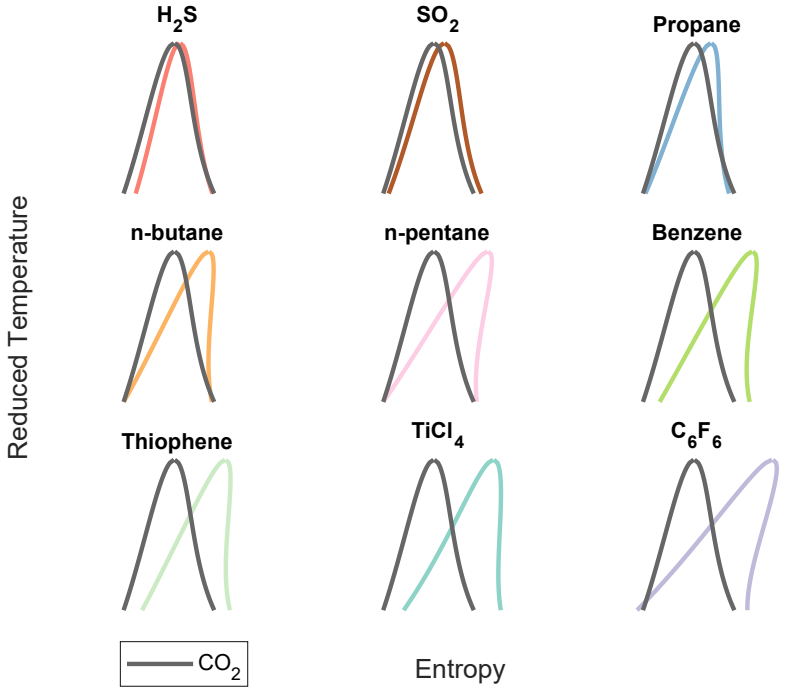

Figure 4.25: Saturation domes of the pure dopants compared to CO_2 in the reduced temperature-entropy plane.

4.4 Summary

The comparative analysis presented in Chapter 4 has investigated the effect of three dopants ($TiCl_4$, SO_2, or C_6F_6) and their amounts on the optimal thermodynamic cycle conditions and turbine design for a 100 MW CSP power plant operating with sCO_2 blends. Increasing dopant molar fraction was found to increase the pressure ratio of all blends. The maximum achievable efficiencies were found to be 48.1%, 46.5%, and 42.2% for molar fractions of 0.21 of $CO_2/TiCl_4$, 0.32 of CO_2/SO_2, and 0.17 of CO_2/C_6F_6. The adoption of molecularly complex dopants has been shown to alleviate the irreversibilites in the recuperator and enables condensing cycles to be realised with dry cooling. This could lead to higher thermal efficiencies, but at the cost of possibly larger recuperators.

In terms of turbine design, the specific work was found to decrease with $TiCl_4$ and C_6F_6, but increase with SO_2. Moreover, the addition of any of the three dopants increases the pressure, temperature, and expansion ratios across the turbine; except for C_6F_6, which exhibits an almost constant temperature ratio. The fluid's density at turbine inlet increases with all dopants as well. Conversely, the speed of sound at

turbine inlet decreases with all dopants, yet higher Mach numbers are expected in CO_2/C_6F_6 turbines.

By studying a 100 MWe power plant as an example, preliminary turbine sizing data was presented. This serves to investigate the sensitivity of the turbine design to the blend and molar fraction before moving onto a more detailed turbine design optimisation stage. Since heavier working fluids reduce the specific work, they increase the mass flow rate into the turbine, which in turn requires larger flow annuli. On the other hand, the turbine mean diameter is smaller for heavy working fluids. Therefore, they require narrower but longer turbines compared to the lighter dopant (SO_2).

Blade mechanical stresses were found to be dominated by gas bending stresses induced by aerodynamic forces. Modifying the CO_2 working fluid for condensing cycles in CSP applications necessitates dopants heavier than CO_2 to increase its critical temperature. Increasing the density of the working fluid will further exacerbate the blade mechanical stresses. Dedicated optimisation studies of turbine design should be undertaken to lower the aerodynamic stresses by adding more blades or increasing blade chord or thickness. Ultimately, a compromise between turbine size, mechanical strength, and aerodynamic efficiency can be made.

An informed decision of the most suitable dopant must account for techno-economic considerations. The effect of the relatively high temperature glides in $CO_2/TiCl_4$ and CO_2/C_6F_6 recuperators on heat exchanger design remains to be examined. Moreover, additional equipment may be needed to address the fractionation of $CO_2/TiCl_4$ and CO_2/C_6F_6 during heat rejection, which may increase the plant size and cost. Another, deciding factor pertaining to fluid selection is off-design analysis, which is increasingly important when the design of CSP plants which are subject to daily and seasonal variations.

The effect of the choice of dopant and its molar fraction on the performance of recompression cycles was also investigated. The study involved 9 dopants with different molecular complexities and properties. Additionally, the pump inlet pressure

was lowered to 15 ^{o}C, thus outside the realm of dry-cooled CSP plants. It was found that the benefit of a recompression cycle diminishes as the aggregate molecular complexity of the working fluid increases. For simple dopants, such as H_2S and SO_2, the recompression cycle will outperform the simple recuperated cycle, regardless of the dopant molar fraction. On the other hand, more complex dopants may achieve thermal efficiencies in simple recuperated cycles that are comparable to a recompression cycle. The dopant molar fraction at which both cycles achieve a similar performances depends on the molecular complexity of the dopant; the more complex the dopant, the lower the molar fraction at which this occurs.

Chapter 5

The theory and design of radial inflow turbines

5.1 Introduction

As pointed out in the literature review in Chapter 2, radial inflow turbine, hereafter may also be referred to as radial turbines, are typically used in small- to medium-sized plants. In this chapter, the theory of radial inflow turbines, their flow features, and design philosophies are introduced. Then, the mean-line design process, otherwise known as 1D design, that is used in subsequent analysis is described in detail. Finally, the 1D turbine design model is verified and confirmed using data from the literature and CFD simulations.

5.2 Theoretical background of turbomachinery

The Euler turbomachinery equation governs the work of a turbomachine and is derived by applying the conservation of momentum on a control volume of an arbitrary turbomachine, similar to that in Figure 5.1, operating under steady-state conditions. The specific work of a turbomachine $\frac{\dot{W}}{\dot{m}}$ is dependent on the blade tip

speeds U and tangential velocity of the flow C_θ at inlet and outlet.

$$\frac{\dot{W}}{\dot{m}} = U_{\text{in}} C_{\theta\text{in}} - U_{\text{out}} C_{\theta\text{out}} \tag{5.1}$$

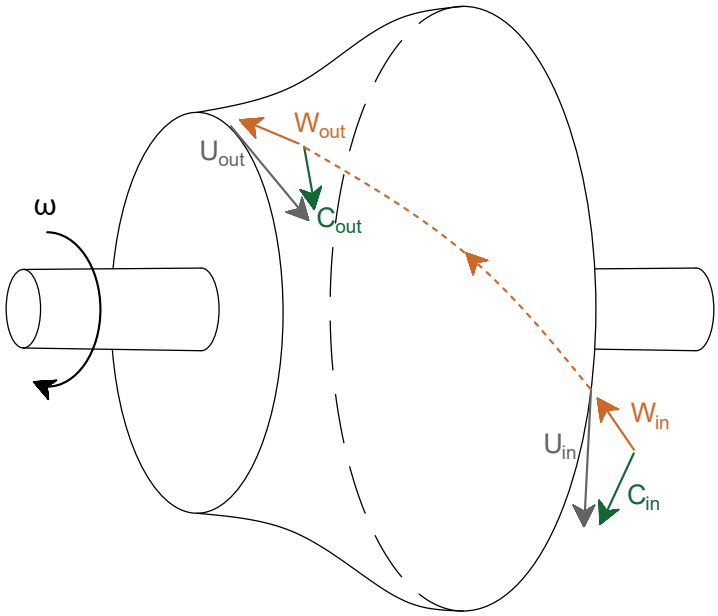

Figure 5.1: Schematic of generalised turbomachine showing the velocity triangle at inlet and outlet

Because the Euler equation is based on a control volume approach, it is universally applicable regardless of the type of turbomachine, be it a turbine or a compressor, axial flow or radial inflow/outflow; or the type of fluid, be it compressible or incompressible. Moreover, it determines the work from the difference between inlet and outlet conditions with no information on the inner workings of the machine.

According to Euler's equation, work may be increased by increasing the blade speed and swirl at the inlet, by minimizing the blade speed at outlet, or by creating negative swirl at the outlet. Therefore, machines of high specific work have high blade speeds and a large tangential component of the flow at the inlet. The inlet swirl is usually maximised by turning the fluid in turbine volutes and nozzles. Of course, neither the blade speed nor the swirl at inlet can be increased indefinitely. The blade speed is constrained by the allowable centrifugal stress on the blades, and the inlet swirl is constrained by the speed of sound, in case of subsonic turbines, and

incidence loss considerations. At the outlet, turbines are commonly designed for zero or negative exit swirl to maximise work; although practical design considerations may require positive swirl as well.

Other insights about turbine work are drawn from another form of the Euler equation:

$$\frac{\dot{W}}{\dot{m}} = \frac{1}{2}[\overbrace{U_{in}^2 - U_{out}^2}^{\text{Centrifugal}} - \overbrace{W_{in}^2 - W_{out}^2}^{\text{Relative Kinetic}} + \overbrace{C_{in}^2 - C_{out}^2}^{\text{Absolute Kinetic}}] \tag{5.2}$$

where the labels indicate the acceleration that is contributing to the energy terms. The first term is independent of the mass flow; therefore, turbines that have a relatively high centrifugal loading ($U_{in} > U_{out}$) are less sensitive to off-design mass flow rates. This is the case of low specific speed turbines, commonly in the form of radial inflow turbine. However, it is for this same reason that the specific work of radial inflow turbines is susceptible to off-design speeds. Compared to axial turbines, where the blade tip speed does not change between inlet and outlet, the centrifugal loading enables higher specific work per stage in radial turbines. Moreover, the loading coefficient (ψ) is lower for radial turbines, but the higher rotational speed enables larger work than is obtained in a single-stage axial turbine.

The second term is a consequence of the flow acceleration in the rotational frame of reference (relative to the rotor). In radial turbines, the hub streamline has a larger change in blade speed than the shroud streamline, therefore the flow decelerates more towards the hub. To increase the relative velocity, the area near the hub is reduced such that the flow channels reduce in area from inlet to outlet (Casey & Robinson 2021). Although relative acceleration of the fluid may increase specific work, it does so at the cost of efficiency. As will be shown later in this chapter, specifically in Equation 6.3 , the friction losses within the rotor passage are proportional to the square of the relative velocity of the fluid. Therefore, it is beneficial to reduce relative velocity at inlet and outlet. On the other hand, reducing the relative velocity excessively would cause flow to stagnate in the rotor. For radial turbines, the magnitude of the second term is usually greater than that of axial turbines. This is a consequence of the reduction in radius.

The third term is a direct measure of the kinetic energy of the fluid based on its absolute velocity. Here it is best to minimise the exit velocity, otherwise the total-to-static efficiency of the turbine drops considerably. Generally, the design of a radial inflow turbine is a continuous trade-off between the centrifugal and relative velocity terms; low specific speed turbines (low flow and loading coefficients) rely more on centrifugal terms, whereas higher specific speed (high flow and loading coefficients) shift more of the work to the relative velocity term.

The contribution of each term to the specific work of a turbine across the specific speed range typical for radial inflow turbines is shown in Figure 5.2. The work contribution due to the change in the absolute kinetic energy of the flow drastically decreases above $N_s > 0.5$; owing to the increase in the absolute exit velocity at higher specific speeds. On the other hand, the work owing to the change in the blade speed (centrifugal term) remains significant consistently with specific speed even as the turbine morphs into a shape similar to an axial turbine and in the process reduces the difference between the blade speed at inlet and outlet. Conversely, the work contribution to the change in the relative kinetic energy increases at higher specific speeds.

5.3 Radial inflow turbine flow features

Following the sectioning introduced by Zangeneh-Kazemi et al. (1988), the rotor may be segmented into three sections: an inlet inducer section, an axial to radial bend section, and an axial exducer section. The following description of motion in the rotor is based on descriptions from multiple sources (Zangeneh-Kazemi et al. 1988, Huntsman 1993, Kaufmann 2020).

Throughout the rotor, Coriolis forces play a role in loading and secondary flow generation, especially in the inducer. Therefore, it is useful to keep in mind that, like centrifugal forces, this is an apparent force that results from the transformation of the equation of motion into a rotating reference frame. The magnitude and direction of the Coriolis force can be calculated as $2\omega \times w$, where ω is the rotational speed of the rotor and w is the relative velocity. Therefore, Coriolis forces will appear only

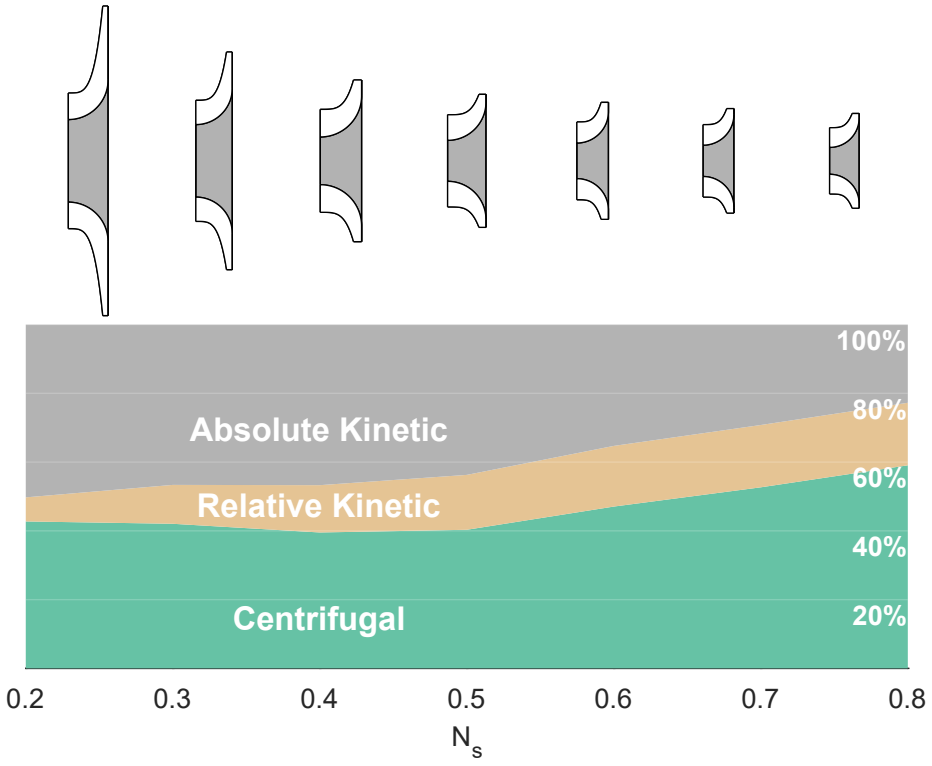

Figure 5.2: Contribution of acceleration terms to work in radial inflow turbines for a range of specific speeds. The turbine profile changes considerably along the specific speed range.

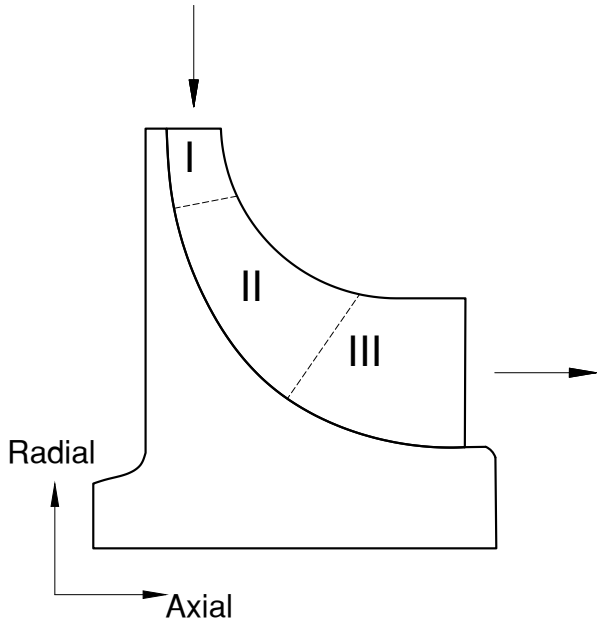

Figure 5.3: Radial inflow turbine meridional geometry.

with respect to velocity components in the radial and tangential direction, not in the axial direction, and will act in a direction that is perpendicular to both the rotational axis and to the direction of the velocity. The change in and effect of Coriolis forces

along the rotor blade is explained next.

Inducer section I

As flow enters the rotor through the radial section, the component of the apparent Coriolis forces due to the meridional component of the relative flow ($2\omega \times w_m$) is strong and pushes the fluid from the pressure to the suction surface, thus turning the flow counter-directional to the rotation of the rotor to conserve the angular momentum of the flow. The velocity profile resulting from the superposition of the radial inlet velocity and the vortex sets up a static pressure differential across the passage between the blade surfaces. This pressure differential contributes to the loading of the blade at inlet; the steeper the pressure gradient, the greater the blade loading.

Inlet incidence can either amplify or reduce the intensity of the vortex. Therefore, incidence has a direct effect on blade loading and secondary flows. At large negative incidence the counter-rotating vortex can be strong enough to stagnate, or even separate the low momentum flow near the pressure surface. On the other hand, a zero or positive incidence weakens the vortex; consequently, the cross-passage pressure gradient may become weak enough to cause flow to separate near the suction surface.

Radial to axial bend section II

As the flow moves towards the mid-section and turns in the axial direction, the meridional curvature in the bend section causes a pressure gradient in the spanwise direction that increases from shroud to hub, thus an associated secondary flow develops moving flow from the hub to the shroud where the pressure is lower. Moreover, the relative motion between the blade tip and the casing decreases because of the decrease in radius and the sharpening of the blade curvature, both of which increase tip leakage compared to the inlet section.

Exducer section III

As in the mid-section, secondary flows are induced by the blade curvature in the exducer; but here the curvature is the in tangential direction. Therefore, a cross-

passage pressure gradient is created, which induces secondary flow from the pressure to suction side.

Tip leakage

A description of the tip leakage phenomenon as described by Dambach et al. (1998) is presented here because of its significance in small-scale turbines. To clarify, the tip clearance refers to the gap measured when the rotor is standing still at ambient temperature. Differential expansion of the rotor and the casing require that a gap is maintained between the two. Fluid flow through this gap is often termed tip leakage. Two main factors affect the tip-leakage flow. The first is the pressure difference between the pressure and suction surfaces of the blade, which drives the flow over the blade tip through the clearance gap. Assuming inviscid flow, the amount of leakage and its associated losses increase as the gap becomes larger relative to the blade span. Because the leaked flow does not drive the impeller, work is lost. Moreover, leakage jets leaving the gap migrate across the rotor channel and block the primary flow, thus lowering the flow capacity of the rotor. In reality, the effect of leakage flows through the tip clearance are more complex as the flow is not inviscid.

The second factor affecting tip-leakage flow is the motion of the casing relative to the blade. Adopting the same division of the rotor as before, tip-leakage flow pattern changes along the streamline, as shown in Figure 5.4. In the inducer region, the tip-leakage is small. This is because the relatively high casing motion drags the fluid in the opposite direction of leakage flow, thus restricting the amount that passes from the pressure to the suction side. As the fluid moves streamwise towards the bend, the relative casing motion decreases but the difference in pressure and suction surfaces remains high. Consequently, the scraping effect is weakened. In the exducer, where the relative casing motion is the lowest, the tip-leakage flow grows larger still and is similar to that of an axial turbine. Dambach & Hodson (2001) showed that the amount of scraping depends on the tip gap and the blade thickness.Although the scraping effect may be of significance in relatively small gaps such as those in the inducer, it will likely reduce in significance as the clearance gap increases, including in the inducer.

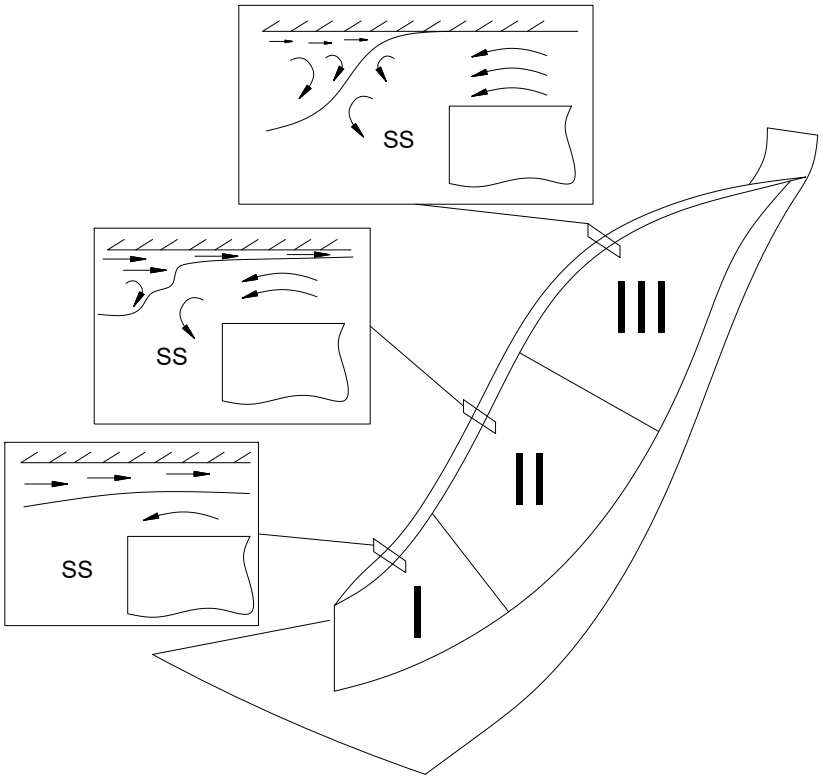

Figure 5.4: Tip flow at different streamwise locations in a radial inflow turbine (adapted from Dambach & Hodson (2000))

Two types of clearances are commonly specified in radial inflow turbines: axial in the inducer and radial in the exducer. Because the flow features within the inducer are different from the exducer, the effect of axial and radial clearances on turbine performance has been shown to be different. A comparison of these effects was summarised by Moustapha et al. (2003) where they showed that the clearance in the exducer is of greater consequence than in the axial clearance in the inducer.

Shrouds may be installed on the rotor tip to reduce tip-leakage. Unlike unshrouded blades where the driving forces is the pressure difference across the blade, the leakage in shrouded turbines is driven by the pressure difference between the leading and trailing edge of the blade in the streamwise direction on the outer surface of the shroud. Although it may improve aerodynamic performance, a shrouded rotor is subject to higher centrifugal loading from the cover mass, which limits the maximum tip speed and reduces work output.

5.4 Design philosophy

Methods for the design of radial inflow turbines have had decades to develop. Regardless of the chosen methodology, a trade-off between accuracy and run-time will persist. Therefore, a prudent choice of the design method is that which is most suitable to the design phase; early phase designs are less accurate than late phase designs, but are quicker.

5.4.1 0D design

Non-dimensional design of radial inflow turbines relies solely on the turbine boundary conditions to estimate its efficiency. The most widely used parameter for this purpose is the specific speed N_s. A well-established body of literature provides guidance on the maximum achievable efficiency for a given specific speed, the most notable of which are the maps produced by Balje (1981). The specific diameter may be added as a secondary dimension to indicate the achievable head at a given specific speed and efficiency. Alternatively, the expansion ratio and size parameter may also be used to estimate efficiency before proceeding with the detailed design (Macchi & Astolfi 2017).

Although they do not explicitly determine the turbine design, non-dimensional maps aid designers in their choice of discrete design decisions, such as the number of turbine stages that are required to maintain specific speed values within a range that yields good performance. Therefore, a 0D design requires no computational effort, and is almost instantaneous; yet it provides a reasonable estimate of the achievable efficiency. Non-dimensional maps will be treated in more detail in Chapter 6. Design optimisation is not relevant here and is limited to the choice of the non-dimensional parameters.

5.4.2 1D design

The mean-line design, otherwise known as the 1D design, is the process of solving mass, momentum, and energy continuity equations at specific stations along the flow

path; usually at the terminals of turbine components such as the inlet and outlet of the rotor. It assumes that flow is uniform at any point in the passage cross section, and that the solution at any station is representative of the average conditions at that station. Therefore, fluid properties only change in the streamwise direction, hence the name 1D design.

Because the flow structure is not resolved in a mean-line method, aerodynamic losses are estimated using loss equations, of which there are several in the literature. These equations are used to estimate losses that are caused by several mechanisms, such as friction or incidence. Although they have been shown to be accurate in estimating losses within conventional turbine design space, it is uncertain if they remain to be suitable as the geometries or the working fluids deviate from those upon which the loss models were originally defined.

Computationally inexpensive, moderately accurate, and quick – the 1D design is commonly used to provide preliminary turbine designs. These include broad component dimensions, velocity triangles, and efficiency. Subsequent refining is achieved through detailed 3D numerical simulations. In this thesis, 1D radial inflow turbine are designed according to the mean-line method, as detailed in Section 5.5.

In terms of flexibility and optimisation, the 1D approach enables the optimisation of a myriad of key design variables such as the radii, passage width, blade count, and flow angles, to name a few. Therefore, a reasonable estimate of the turbine geometry and kinematics can be obtained using this method. Arguably, although the 1D model is neither as accurate nor as precise as 3D design, its consequences are much greater because major decisions are determined at this stage of the design, such as the turbine dimensions, the angle of the blades, and the rotational speed of the rotor. Therefore, this method is deemed suitable for the purposes of the analysis conducted in this thesis.

5.4.3 2D design

Also known as *Through Flow* design, the 2D design method solves streamline curvatures across the spanwise directions. Since the flow is assumed inviscid, aerodynamic losses are calculated through loss relations. Unlike the 1D design, this approach can predict flow features in the turbine rotor such as secondary flows.

The 2D through flow method can be used to optimise the radial distribution of flow angles and axial distribution of the mean radius, in addition to the design variables available in the 1D design. However, it is mainly applied in the design of axial turbines and is reliable for use in radial inflow turbine design because of the more complicated 3D flow field.

5.4.4 Q3D design

The quasi-3D (Q3D) method combines through flow analysis with 2D analysis in the blade-to-blade planes, effectively resolving the flow field in three dimensions: spanwise, streamwise, and blade-to-blade. Although fewer than ten planes are resolved in any direction, Q3D design still allows for the optimisation of the 3D blade surface.

5.4.5 3D design

3D flow resolution is typically used at the final stages of design development. It requires the specification of additional design variables related to the 3D shape of the blade such as the camberline angle, streamwise thickness profile, and the streamwise blade metal angle. Owing to its high computational cost and long run time, 3D solvers are used to verify the turbine design and fine tune its geometry.

Numerical analysis is used to solve mass and energy conservation equations along with a set of partial differential equations, namely the Navier-Stoke equation, coupled with the equation of state of the fluid, to describe the distributed properties (fields) of the fluid; this process is referred to as computational fluid dynamics (CFD). In tur-

bomachinery design, the common method of numerical analysis is the finite volume discretisation. It involves discretising the computational domain into a finite number of control volumes (meshing) and solving for the fluid property at a predefined location relative to the cell such as in the vertex- or cell-centered schemes. Generally, the larger the number of cells (the finer the grid), the more accurate is the solution.

There are several options to describe the fluid problem, when ordered in increasing accuracy and computational cost they are: Euler equation, Reynolds-average Navier-Stokes equation (RANS), Large Eddy Simulations (LES), and Direct Numerical Solution (DNS). Euler equations do not include the viscous term of the Navier-Stokes equation, thus do not account for viscous loss. Once the stresses due to velocity fluctuations in turbulent flows are considered, the system of equations becomes underdetermined. With the RANS method, an additional set of equations is used to represent the Reynolds stresses and close the Navier-Stokes equation. This approach time averages both the primary flow and the fluctuating turbulent flow. The RANS method is the common choice when modelling turbomachinery due to is relatively low computational cost compared to LES or DNS. Instead of averaging the effect of turbulence, the LES solves for large turbulent eddies thus accounting for a large part of the turbulent kinetic energy, whilst the thermal energy dissipation is accounted for using sub-grid turbulence models. Finally, the DNS calculates both the mean flow and the turbulent velocity fluctuations to the smallest practical scale.

With the continuous increase in computational power, CFD is becoming integral to the design process, namely for blade shape optimisation. Using CFD simulations, or surrogate models, the shape of the blade may be controlled by as many as 50 decision variables to optimise specific turbine features such as performance.

5.5 Turbine design model

Conventionally, radial inflow turbines are designed by assuming a set of geometric and kinematic parameters, the values of which are based on recommendations from the literature. At first, the rotor geometry and kinematics are defined, which in turn inform the nozzle and volute designs. Most literature follow one of the five most

popular design methodologies introduced by: (1) Rohlik (1968); (2)Glassman (1976); (3) Aungier (2006); (4) Moustapha et al. (2003); and (5) Whitfield (1990). Lee & Gurgenci (2020) compared the latter three against experimental data from Kofskey & Holeski (1966) for a cold-test radial inflow turbine operating with air and found that they deviate from experimental data to various degrees, but the deviation is of the same order of magnitude. Also, they studied their consequences on the rotor design of sCO_2 turbines in high-temperature (833 K) Brayton cycles of different power scales (300 kW, 1 MW, 10 MW, and 10 MW). All three methods yielded total-to-static efficiencies within 2% of each other, with the method by Whitfield (1990) resulting in the lowest efficiency due to faster flow velocities.

In this thesis, the flow coefficient (ϕ), the loading coefficient (ψ), and the meridional velocity ratio (ζ) are used to determine the velocity triangles, following the method suggested by Moustapha et al. (2003). They are defined as:

$$\phi = \frac{C_{5m}}{U_4} \tag{5.3}$$

$$\psi = \frac{\Delta h_0}{U_4^2} \tag{5.4}$$

$$\zeta = \frac{C_{5m}}{C_{4m}} \tag{5.5}$$

where $\Delta h_0[J/kg]$ is the total-to-total enthalpy drop across the turbine, and the velocities U_4, C_{4m} and C_{5m} are indicated in Figures 5.7 and 5.9. Additionally, the hub-to-shroud ($r_{5\mathrm{h}}/r_{5\mathrm{sh}}$) and the outlet-to-inlet (r_5/r_4) radius ratios are used to control the turbine shape. In Figure 5.5, key dimensions of the turbine rotor are shown, whereas the velocity triangles and labeling convention of the tangential and merdional directions are shown in Figures 5.7 and 5.9.

In the following section, the equations calculated by the 1D mean-line model are described in the order of calculation.

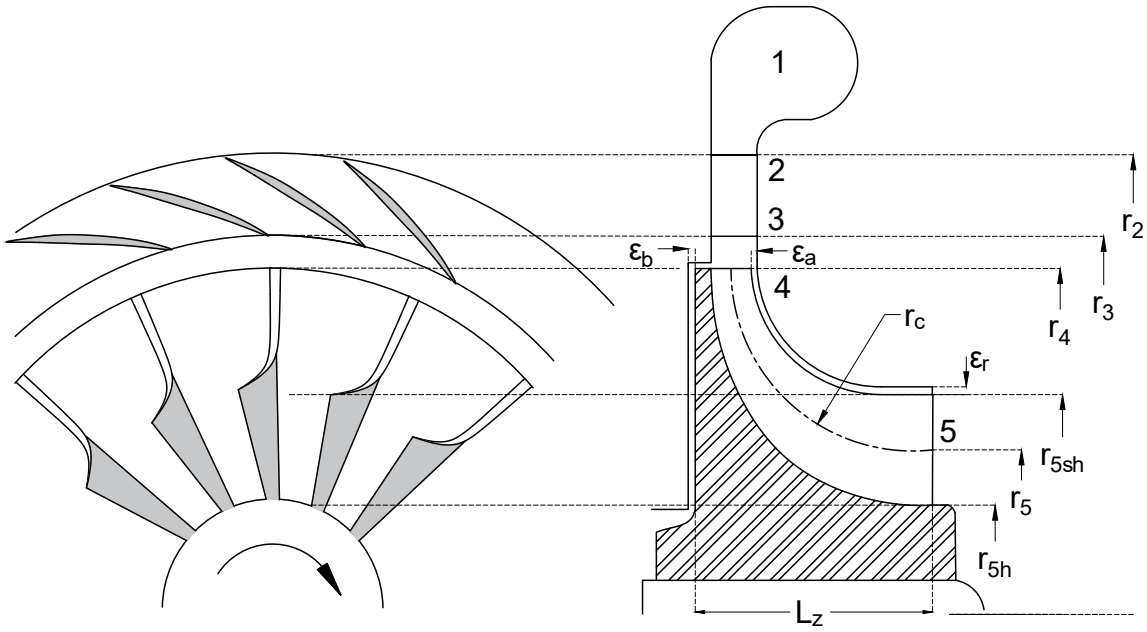

Figure 5.5: Meridional geometry of a radial inflow turbine showing key dimensions

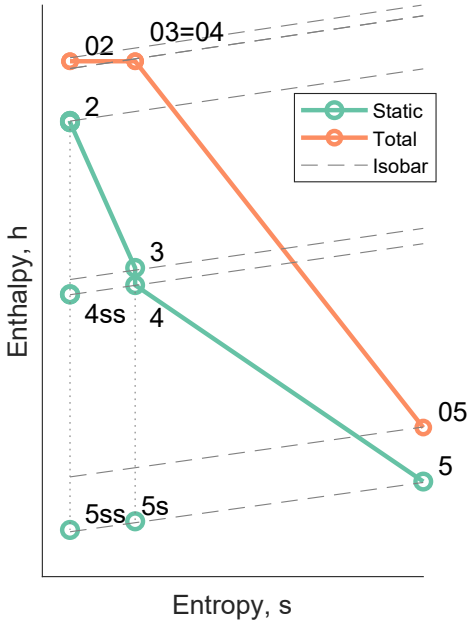

Figure 5.6: Enthalpy-entropy diagram showing the expansion process in the turbine

5.5.1 Rotor inlet

The turbine design is initiated by determining the total conditions at the rotor inlet (T_{01} and P_{01}), the static pressure at the outlet (P_5), and the total enthalpy drop (Δh_0) based on an initial assumption of total-to-static efficiency (η_{ts}).

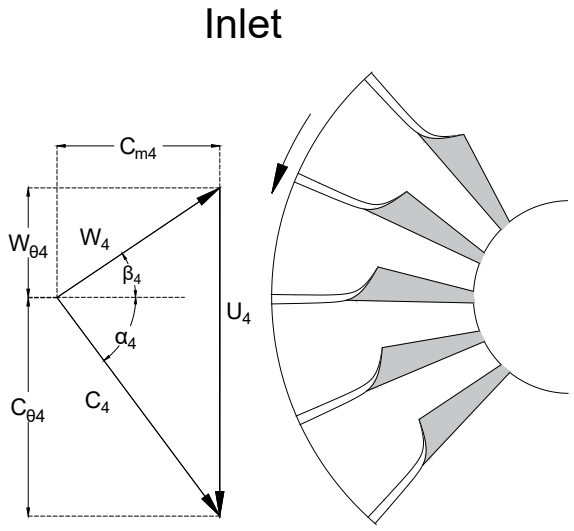

Figure 5.7: Velocity triangle at rotor inlet

$$[h_{04}, s_{04}] = f(T_{01}, P_{01}) \tag{5.6}$$

$$h_{5\mathrm{ss}} = f(P_5, s_{01}) \tag{5.7}$$

$$\Delta h_0 = \eta_{ts}(h_{01} - h_{5\mathrm{ss}}) \tag{5.8}$$

The velocity triangle at inlet is then resolved based on the coefficients prescribed in Equations 5.3 to 5.5.

$$U_4 = \sqrt{\frac{\Delta h_\mathrm{o}}{\psi}} \tag{5.9}$$

$$C_{4\mathrm{m}} = \frac{\phi U_4}{\xi} \tag{5.10}$$

$$C_{4\theta} = \psi U_4 \tag{5.11}$$

$$C_4 = \sqrt{C_{4\mathrm{m}}^2 + C_{4\theta}^2} \tag{5.12}$$

$$W_{4\theta} = C_{4\theta} U_4 \tag{5.13}$$

$$W_4 = \sqrt{W_{4\theta}^2 + C_{4\mathrm{m}}^2} \tag{5.14}$$

$$\alpha_4 = \tan^{-1}\left(\frac{C_{4\theta}}{C_{4\mathrm{m}}}\right) \tag{5.15}$$

$$\beta_4 = \tan^{-1}\left(\frac{W_{4\theta}}{C_{4\mathrm{m}}}\right) \tag{5.16}$$

The non-isentropic and isentropic static enthalpy at inlet can be calculated using the inlet absolute velocity and the enthalpy due to entropy generation in the stator row (Δh_{n}), which is carried over from the previous iteration (assumed zero in the first iteration). Then, the static state properties can be calculated using the pressure and enthalpy. Moreover, the absolute and relative Mach number (M_4 and $M_{4,\mathrm{rel}}$) are calculated to ensure subsonic flow.

$$h_4 = h_{04} - \frac{C_4^2}{2} \tag{5.17}$$

$$h_{4\mathrm{s}} = h_4 - \Delta h_{\mathrm{n}} \tag{5.18}$$

$$P_4 = f(h_{4\mathrm{s}}, s_1) \tag{5.19}$$

$$[T_4, \rho_4, a_4] = f(P_4, h_4) \tag{5.20}$$

$$M_4 = \frac{C_4}{a_4} \tag{5.21}$$

$$M_{4,\mathrm{rel}} = \frac{W_4}{a_4} \tag{5.22}$$

With the mass flow rate, static density, and meridional velocity known, the cross sectional area can be calculated. However, at this point, the blade height b_4 cannot be calculated since the inlet radius is not known. As will be described later, determination of the blade height at inlet requires a concurrent determination of the inlet and outlet radii along with the blade blockage at outlet.

$$A_4 = \frac{\dot{m}}{C_{4\mathrm{m}}\rho_4} \tag{5.23}$$

Because Coriolis forces cause a cross passage pressure gradient, the relative velocity across the passage is not uniform; it is lower at the pressure side than the suction side. The velocity gradient across the passage is a function of the arc angle between the blades. Therefore, according to Jamieson (1955), there must be a minimum number of rotor blades above which flow will not stagnate at the pressure surface. The effect of the number of rotor blades on the profile of the relative velocity across the passage is illustrated in Fig 5.8.To that end, the Equation 5.24 was developed by

Glassman (1976), which is used here.

$$Z_{\mathrm{r}} = \left\lfloor \frac{\pi(110 - \alpha_4)\tan\alpha_4}{30} \right\rfloor \tag{5.24}$$

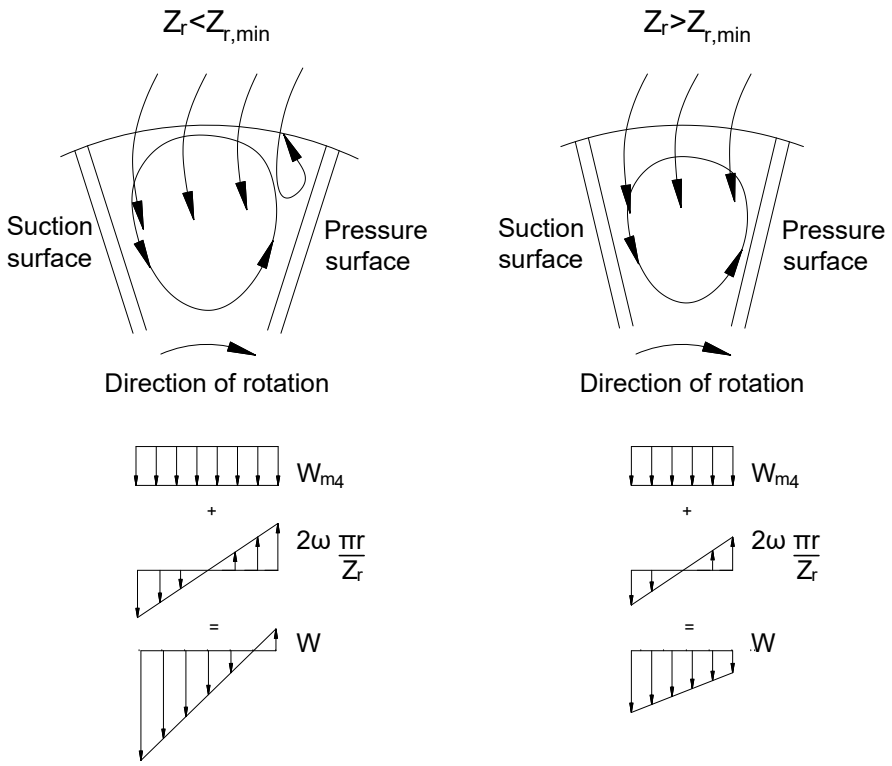

Figure 5.8: Relative velocity profile in rotor passage: too few blades cause the flow to separate on near the pressure side of the passage. The term $2\pi\omega\frac{r}{Z_{\mathrm{r}}}$ denotes the velocity due to the Coriolis acceleration.

5.5.2 Rotor outlet

The rotor outlet station is conventionally defined at the root mean square radius. Using the prescribed radius ratio r_5/r_4 the blade velocity U_5 may be calculated. Moreover, zero exit-swirl is assumed ($\alpha_5 = 0$). Therefore, the velocity triangle at outlet can be determined based on the prescribed flow coefficient ψ.

$$U_5 = \frac{r_5}{r_4}U_4 \tag{5.25}$$

$$C_{5\mathrm{m}} = \phi U_4 \tag{5.26}$$

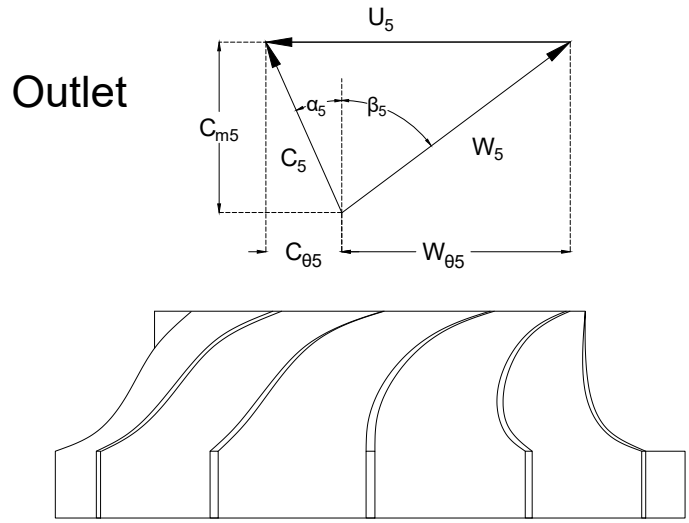

Figure 5.9: Velocity triangle at rotor outlet

$$C_5 = \frac{C_{5\mathrm{m}}}{\cos \alpha_5} \tag{5.27}$$

$$W_{5\theta} = C_{5\theta} U_5 \tag{5.28}$$

$$W_5 = \sqrt{W_{5\theta}^2 + C_{5\mathrm{m}}^2} \tag{5.29}$$

$$\beta_5 = \tan^{-1}\left(\frac{W_{5\theta}}{C_{5\mathrm{m}}}\right) \tag{5.30}$$

Static enthalpy at outlet after isentropic expansion was previously calculated using the static outlet pressure P_5 and the inlet specific entropy s_{01}. Thereafter, the static enthalpy is calculated using the enthalpy drop due to losses in the stator Δh_n and rotor Δh_r.

$$h_5 = h_{5\mathrm{ss}} + \Delta h_\mathrm{n} + \Delta h_\mathrm{r} \tag{5.31}$$

$$h_{05} = h_5 + \frac{C_5^2}{2} \tag{5.32}$$

As with the inlet, the thermodynamic state at outlet is determined, along with the absolute and relative Mach numbers.

$$P_5 = f(h_{5\mathrm{ss}}, s_1) \tag{5.33}$$

$$[T_5, \rho_5, a_5] = f(P_5, h_5) \tag{5.34}$$

$$M_5 = \frac{C_5}{a_5} \tag{5.35}$$

$$M_{5,\mathrm{rel}} = \frac{W_5}{a_5} \tag{5.36}$$

To find the blade blockage at outlet, the method originally developed by Atkinson (1998) and later applied by White (2015) is used. Basically, the process requires iterating between Equations 5.37 to 5.44 to find the values of the inlet and outlet radii that satisfies Equation 5.37 within the prescribed radius ratios r_5/r_4 and $r_{5\mathrm{h}}/r_{5\mathrm{sh}}$.

$$A_5 = \frac{\dot{m}}{C_{5\mathrm{m}}\rho_5} = \pi(r_{5\mathrm{t}}^2 - r_{5\mathrm{h}}^2)(1 - BK_5) \tag{5.37}$$

$$r_5 = \sqrt{\frac{A_5(1 + (r_{5\mathrm{h}}/r_{5\mathrm{h}})^2)}{2\pi(1 - BK_5)(1 - (r_{5\mathrm{h}}/r_{5\mathrm{h}})^2)}} \tag{5.38}$$

As shown in Figure 5.10, each blade is assumed to block a trapezium area of height $(r_{5\mathrm{t}} - r_{5\mathrm{h}})$ and of lower and upper bases t_{eh} and t_{es}, respectively.

$$A_{\mathrm{bb}} = \frac{(r_{5\mathrm{t}} - r_{5\mathrm{h}})(t_{\mathrm{et}} + t_{\mathrm{eh}})}{2} \tag{5.39}$$

$$BK_5 = \frac{Z_{\mathrm{R}} A_{\mathrm{bb}}}{\pi(r_{5\mathrm{t}}^2 - r_{5\mathrm{h}}^2)} \tag{5.40}$$

where t_{eh} and t_{et} are the projections of $t_{5\mathrm{t}}$ and $t_{5\mathrm{h}}$, respectively, on the exit plane. Because $t_{5\mathrm{t}}$ and $t_{5\mathrm{h}}$ are normal to the blade which has an angle of β with the exit plane, then:

$$t_{\mathrm{eh}} = \frac{t_{5\mathrm{h}}}{\cos\beta_{5\mathrm{h}}} \tag{5.41}$$

$$t_{\mathrm{et}} = \frac{t_{5\mathrm{t}}}{\cos\beta_{5\mathrm{t}}} \tag{5.42}$$

Assuming the blades are radially fibred, then the angle at any point along their radius is proportional to the radius:

$$\beta_{5\mathrm{h}} = \tan^{-1}\left(\frac{r_{5\mathrm{h}}\tan\beta_5}{r_5}\right) \tag{5.43}$$

$$\beta_{5\mathrm{t}} = \tan^{-1}\left(\frac{r_{5\mathrm{t}}\tan\beta_5}{r_5}\right) \tag{5.44}$$

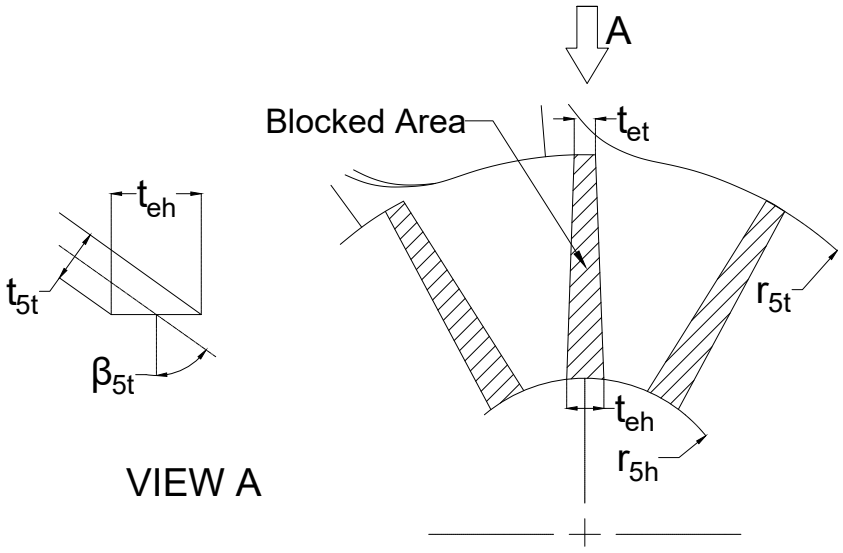

Figure 5.10: Schematic showing the geometrical area blocked by the blade at the rotor outlet (White 2015)

The blade thickness at inlet t_4 and at outlet, $t_{5\mathrm{h}}$ and $t_{5\mathrm{sh}}$, are set relative to r_4. With the outlet radius known, the rotor inlet radius r_4 follows based on the prescribed radius ratio r_4/r_5. Blades also block the inlet annulus; therefore, the blocked area must be discounted when the blade height is calculated. Moreover, to fully define the rotor dimensions the axial length is calculated based on the equation recommended by Aungier (2006).

$$t_4 = 0.04r_4 \tag{5.45}$$

$$t_{\mathrm{h}} = 0.02r_4 \tag{5.46}$$

$$t_{\mathrm{sh}} = 0.01r_4 \tag{5.47}$$

$$b_4 = \frac{A_4}{\pi d_4 - Z_{\mathrm{r}}t_4} \tag{5.48}$$

$$b_5 = r_{5\mathrm{s}} - r_{5\mathrm{h}} \tag{5.49}$$

$$L_{\mathrm{z}} = 1.5b_5 \tag{5.50}$$

Lastly, the rotational speed of the rotor is determined based on the inlet blade

tip speed U_4 and radius r_4.

$$\omega = \frac{U_4}{r_4} \tag{5.51}$$

5.5.3 Stator - rotor interspace

The annular gap between the stator trailing edge and the rotor leading edge allows the flow to intermix before entering the rotor (Moustapha et al. 2003). However, the width of the interspace is a compromise between reduced mechanical coupling, turbine size and increased pressure losses. A wider interspace distance increases fluid friction, whereas a narrower gap increases blade row interaction (Moustapha et al. 2003). Watanabe et al. (1971) proposed a correlation to estimate a suitable clearance gap between the stator exit and the rotor inlet, where the efficiency maximising value of the flow path length to blade height ratio ($\frac{S}{b_4}$) is 2.

$$r_3 = r_4 + \left(\frac{S}{b_4}\right) b_4 \cos \alpha_4 \tag{5.52}$$

According to experimentally substantiated CFD analysis conducted by Simpson et al. (2008) on air turbines, the optimal interspace ratio (r_3/r_4) is around 1.175. However, in his PhD theses, Keep (2018) found that the entropy generation in the stator and in the interspace is dominated by viscous effects, whilst mixing and stator-rotor interactions where of comparatively smaller consequence. Moreover, viscous effects due to endwalls were greater compared to those due to the stator blade profile. Therefore, he makes the case for reducing the stator-rotor interspace because of the importance of reducing the viscous effects, despite the increase in the entropy due to mixing and stator-rotor interaction.

According to Keep, the strong viscous effects are likely caused by the small hydraulic diameter in the interspace, which is to be expected in the low specific speed turbine that he had considered. Also common in low specific speed turbines is the small hydraulic diameter of the passage and the longer flow path in the interspace because of the highly tangential stator blade angles. Consequently, interspace size for low specific speed designs will be narrower than for medium or high specific speed

designs. Because the nozzle trailing edge wakes were less significant for sCO_2 than for gas turbines, the interspace ratio may be reduced to less than 1.05.

5.5.4 Stator design

The stator nozzle blades are located upstream the rotor to orient and accelerate the flow in accordance with the velocity triangle at the rotor inlet. Fundamentally, the stator is subdivided into three stations: inlet, throat, and outlet; as seen in Figure 5.11. The design of he stator involves an iterative approach whereby the state of the fluid and the nozzle geometry are resolved successionally until both converge to a stable solution that satisfies the continuity equations. The following describes this process in accordance with the method proposed by Aungier (2006) and later employed by White (2015).

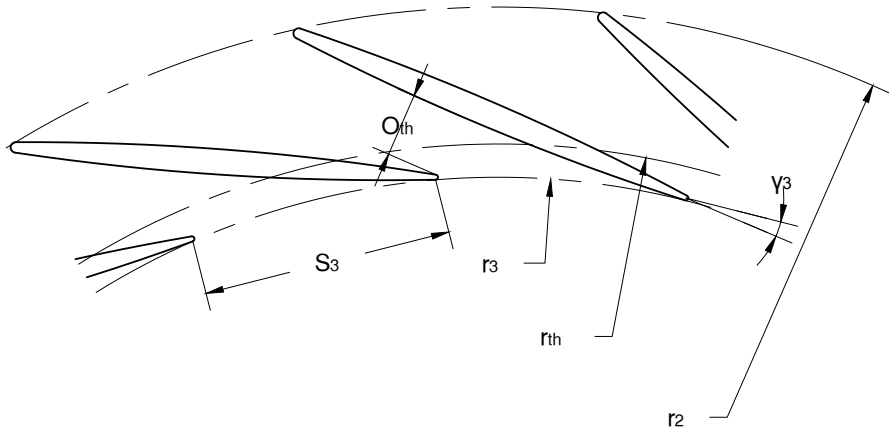

Figure 5.11: Stator row geometry based on Aungier (2006)

Because no work is done in the stator, the total enthalpy is assumed to be constant through out ($h_{02} = h_{03}$), whilst the total enthalpy at the nozzle trailing edge is equal to that at the rotor leading edge ($h_{03} = h_{04}$) because no work is done in the interspace either. Moreover, the passage width is set equal to the blade height at the rotor leading edge ($b_3 = b_4$).

Stator outlet

Solving for the nozzle design begins with determining the state at the nozzle outlet, which is initially assumed to be identical to that at the rotor inlet, but at a different radial distance. Using the conservation of momentum, the tangential velocity at the stator trailing edge $C_{3\theta}$ is obtained. At this point neither the density ρ_3 nor the absolute meridional velocity $C_{3\mathrm{m}}$ are known, in which case Equations 5.54 to 5.58 are iterated until convergence.

$$C_{3\theta} = C_{4\theta}(\frac{r_4}{r_3}) \tag{5.53}$$

$$C_{3\mathrm{m}} = \frac{\dot{m}}{2\pi r_3 b_3 \rho_3} \tag{5.54}$$

$$\alpha_3 = \tan^{-1}\left(\frac{C_{3\theta}}{C_{3\mathrm{m}}}\right) \tag{5.55}$$

$$C_3 = \sqrt{C_{3\theta}^2 + C_{3\mathrm{m}}^2} \tag{5.56}$$

$$h_3 = h_{03} - \frac{C_3^2}{2} \tag{5.57}$$

$$\rho_3 = f(h_3, s_{03}) \tag{5.58}$$

Stator throat

The throat width o_{th} is informed by the pitch S_3 and flow angle α_3 required at the outlet. To find o_{th}, the method proposed by Aungier (2006) is used whereby the cosine rule is applied between the throat and stator outlet, but which was modified to account for the variation in passage width and radius between the throat and the outlet.

Based on an initial estimation of the number of stator blades Z_{n} and setting angle γ_3, two adjacent stator nozzle blades are constructed to find the throat width o_{th} and radius r_{th} geometrically, then Equations 5.60 to 5.65 are executed to provide an updated setting angle γ_3. This process is repeated until convergence. Moreover, radial inflow turbines are prone to choked flow at the stator throat; therefore, the

Table 5.1: Stator profile design parameters

Parameter	Z_n	S_3/c	θ_n	d/c	t_2/c	t_3/c	t_max/c
Value	Z_r+3	0.6	0^o	0.4	0.012	0.025	0.06

Mach number is also calculated to ensure subsonic flow at the throat.

$$S_3 = \frac{2\pi r_3}{Z_\mathrm{n}} \tag{5.59}$$

$$\alpha_\mathrm{th} = \tan^{-1}\left(\left(\frac{r_3}{r_\mathrm{th}}\right)\left(\frac{\rho_\mathrm{th}}{\rho_3}\right)\tan\alpha_3\right) \tag{5.60}$$

$$o_\mathrm{th} = S_3\cos\alpha_\mathrm{th} \tag{5.61}$$

$$C_\mathrm{th} = \frac{\dot{m}}{\rho_\mathrm{th}A_\mathrm{th}} \tag{5.62}$$

$$h_\mathrm{th} = h_{03} - \frac{C_\mathrm{th}}{2} \tag{5.63}$$

$$[T_\mathrm{th}, P_\mathrm{th}, \rho_\mathrm{th}, a_\mathrm{th}] = f(h_\mathrm{th}, s_3) \tag{5.64}$$

$$\gamma_3 = \sin^{-1}\left(\frac{o}{o_\mathrm{th}}\sin(\gamma_3)\right) \tag{5.65}$$

$$M_\mathrm{th} = \frac{C_\mathrm{th}}{a_\mathrm{th}} \tag{5.66}$$

The geometry of the nozzle was also designed in accordance with the method presented by Aungier (2006). The method entails the specification of key parameters, which are listed in Table 5.1 and illustrated in Figure 5.12. A typical subsonic radial turbine has a camber line deflection θ_n shallower than 30^o, compared to up to 80^o for 50% reaction axial turbines. Radial turbine nozzles have a relatively small deflection because the flow is turned in the volute before entering the nozzles. If the scroll is sufficiently large, the scroll velocities are small; thus the scroll frictional losses and possibly nozzle incidence losses become small (Rodgers 1967).

Stator inlet

Having specified the stator profile, position, and orientation, the stator inlet radius r_2 may be determined geometrically. The angle at which the fluid flows into the stator

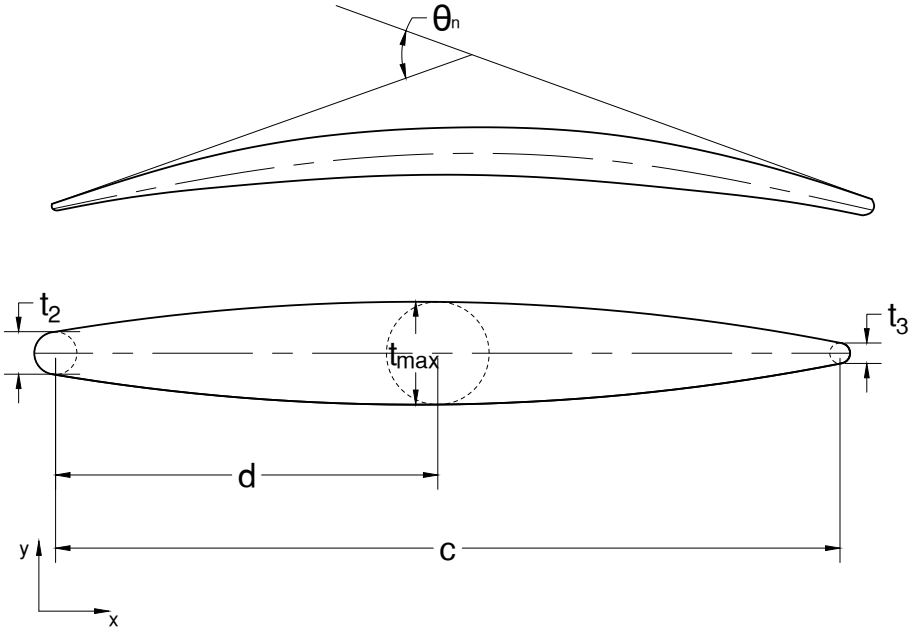

Figure 5.12: Stator blade profile based on Aungier (2006)

α_2 is assumed to be equal to the optimal angle α^* that minimises the angle of incidence i^*. Aungier (2006) suggested using Equations 5.67 and 5.68, which are based on an earlier work by Herrig et al. (1957). Where β_2 and β_3 are the blade angles at the leading and trailing edges, respectively.

$$i^* = \left(3.6\sqrt{\frac{10t_2}{c}} + \frac{|\beta_3 - \beta_2|}{3.4}\right)\sqrt{\frac{c}{S_3}} - \frac{|\beta_3 - \beta_2|}{2} \tag{5.67}$$

$$\alpha^* = \beta_2 - i^* sgn(\beta_3 - \beta_2) \tag{5.68}$$

The design of the volute is not included in the 1D mean line presented here; however, the volute is assumed to be isentropic and that the flow is aligned in volute to match the prescribed angle at the stator inlet α_2. Therefore, the state at stator inlet may be resolved by iterating Equations 5.69 to 5.71

$$C_2 = \frac{\dot{m}}{2\pi r_2 b_2 \rho_2} \tag{5.69}$$

$$h_2 = h_{01} - \frac{C_2^2}{2} \tag{5.70}$$

$$\rho_2 = f(h_2, s_{01}) \tag{5.71}$$

5.6 Turbine performance estimation

The performance of the turbine is evaluated using a set of loss models. The total enthalpy loss in the turbine is equal to the arithmetic sum of the individual aerodynamic losses:

$$\Delta h_{\mathrm{loss}} = \Delta h_{\mathrm{n}} + \overbrace{\Delta h_{\mathrm{i}} + \Delta h_{\mathrm{p}} + \Delta h_{\mathrm{c}} + \Delta h_{\mathrm{te}}}^{\Delta h_{rotor}} + \Delta h_{\mathrm{e}} \tag{5.72}$$

Total-to-static and total-to-total efficiencies are calculated as:

$$\eta_{\mathrm{ts}} = \frac{h_4 - h_5}{h_4 - h_{5\mathrm{s}}} \tag{5.73}$$

$$\eta_{\mathrm{tt}} = \frac{h_4 - h_5}{h_4 - h_{05\mathrm{s}}} \tag{5.74}$$

Unlike other losses, the enthalpy drop due to windage is subtracted from the total enthalpy drop when calculating the power:

$$W = \dot{m}(\Delta h_{\mathrm{tt}} - \Delta h_{\mathrm{w}}) \tag{5.75}$$

Therefore, it is not considered as an internal loss in the rotor and does not contribute to the entropy generation between the rotor inlet and outlet.

5.6.1 Nozzle loss

The enthalpy loss in the nozzle is calculated based on the empirical correlation formulated by Rodgers (1967) for straight nozzle blades. In this formulation, the trailing edge and shock losses are negligible provided that the Mach number is less than 1.2, which is a reasonable assumption for CO_2 turbines as they are not expected to be trans- or supersonic, and that the thickness of the trailing edge to the chord length ratio is less than 2%, which is also ensured during the design process. Moreover, this model does not account for incidence loss and assumes that the incoming flow is aligned with the nozzle and its passages. For these reasons, this formulation

was deemed suitable for CO_2 turbines.

$$\Delta h_{\mathrm{n}} = \frac{C_3^2}{2} \frac{0.05}{Re_3^{0.2}} \left(\frac{3 \tan \alpha_3}{S_3/c} + \frac{S_3 \cos \alpha_3}{b_3} \right) \tag{5.76}$$

$$Re_3 = \frac{C_3 b_3}{\nu_3} \tag{5.77}$$

where C_3 is the flow velocity, α_3 [deg] is the flow angle, b_3 [m] is the passage height, ν_3 [m^2/s] is the kinematic viscosity, Re_3 is the Reynolds number, and S_3 [m] is the pitch at the nozzle exit, and c [m] is the chord length of the nozzle blade.

5.6.2 Rotor loss

There are two types of losses in a rotor: internal and external. The internal losses, such as incidence, passage, trailing edge, and clearance loss, take place within the blade passages; the external losses, such as windage, outside.

Incidence loss

Only near the design-point operation will the fluid move smoothly into the passages of the rotor; at other operating conditions there will be an incidence angle between the relative velocity vector of the approaching fluid and the rotor blade angle. In a radial inflow turbine rotor, the operating point at which the incidence losses are a minimum does not usually coincide with a zero angle of incidence (Baines 1996). Therefore, no tangential velocity change is expected to occur at the optimum relative flow angle $\beta_{4,\mathrm{opt}}$.

The approach devised by Wasserbauer & Glassman (1975) at NASA assumes that the kinetic energy associated with the change in relative tangential velocity is converted into internal energy of the working fluid, which manifests as an increase in entropy. The purpose of the incidence loss model is to calculate both the entropy gain due to incidence and the incidence angle for which minimum loss occurs.

$$\Delta h_{\mathrm{i}} = \frac{W_4^2}{2} (\sin(\beta_4 - \beta_{4,\mathrm{opt}}))^2 \tag{5.78}$$

$$\beta_{4,\text{opt}} = \arctan\left(\frac{\tan(\alpha_4)}{1 - Z_\text{r}/1.98}\right) \tag{5.79}$$

Passage loss

Passage loss refers to losses incurred within the rotor chamber and between its blades. The model used by Moustapha et al. (2003) includes both friction and secondary flow losses:

$$\Delta h_\text{p} = m_\text{f} K_\text{p} \left[\frac{L_\text{h}}{D_\text{h}} + 0.68\left(1 - \left(\frac{r_5}{r_4}\right)^2\right)\frac{\cos\beta_5}{b_5/c}\right]\frac{W_4^2 + W_5^2}{2} \tag{5.80}$$

where the first term in the square brackets accounts friction loss while the second accounts for secondary flow loss. The hydraulic length L_h is the mean arc length of two quarter circles in the axial and radial directions and the hydraulic diameter D_h is averaged between inlet and outlet.

$$L_\text{h} = \frac{\pi}{4}\left[\left(L_\text{z} - \frac{b_4}{2}\right) + \left(r_4 - r_{5\text{s}} - \frac{b_5}{2}\right)\right] \tag{5.81}$$

$$D_\text{h} = \frac{d_{\text{h}4} + d_{\text{h}5}}{2} \tag{5.82}$$

$$D_{\text{h}4} = \frac{4\pi r_4 b_4}{2\pi r_4 + Z_\text{r} b_4} \tag{5.83}$$

$$D_{\text{h}5} = \frac{2\pi(r_{5\text{s}}^2 - r_{5\text{h}}^2)}{\pi(r_{5\text{s}} - r_{5\text{h}}) + Z_\text{r} b_5} \tag{5.84}$$

The factor c in Equation 5.81 accounts for the turning of the flow in the tangential plane.

$$c = L_\text{z}/\cos\bar{\beta} \tag{5.85}$$

$$\bar{\beta} = \arctan\left(\frac{\tan\beta_4 + \tan\beta_5}{2}\right) \tag{5.86}$$

The factor $K_\text{p} = 0.11$ is based on experimental data. Finally, m_f is a correction factor that accounts for the high secondary losses in high specific speed turbines with sharp

meridional curvature (high excuder tip to inlet radius ratio) according to:

$$m_{\mathrm{f}} = \begin{cases} 1 & (r_4 - r_{5\mathrm{s}})/b_5) > 0.2 \\ 2 & (r_4 - r_{5\mathrm{s}})/b_5) \leq 0.2 \end{cases} \tag{5.87}$$

Clearance loss

In an unshrouded impeller, a clearance gap between the blade tip and the shroud is necessary to avoid contact between the two. Due to differential thermal expansion of the rotor and shroud, the clearance gap must be wide enough to ensure separation from cold start to operation. As previously mentioned, the pressure differential between the two sides of the blade drives leakage flow between the rotor tip and shroud surfaces, in both the radial and axial directions, which gives rise to tip clearance loss. Equations 6.4 to 5.90 used here was used by Moustapha et al. (2003), where the three terms in the brackets correspond to the axial and radial clearances and the interaction between them.

$$\Delta h_{\mathrm{c}} = \frac{Z_{\mathrm{r}} U_4^3}{8\pi} (K_{\mathrm{a}} \epsilon_{\mathrm{a}} C_{\mathrm{a}} + K_{\mathrm{r}} \epsilon_{\mathrm{r}} C_{\mathrm{r}} + K_{\mathrm{ar}} \sqrt{\epsilon_{\mathrm{a}} \epsilon_{\mathrm{r}} C_{\mathrm{a}} C_{\mathrm{r}}}) \tag{5.88}$$

$$C_{\mathrm{x}} = \frac{(1 - r_{5\mathrm{s}}/r_4)}{C_{4\mathrm{m}} b_4} \tag{5.89}$$

$$C_{\mathrm{r}} = \frac{r_{5\mathrm{s}}}{r_4} \frac{(L_{\mathrm{z}} - b_4)}{C_{5\mathrm{m}} r_5 b_5} \tag{5.90}$$

The factors $K_{\mathrm{a}} = 0.4$, $K_{\mathrm{r}} = 0.75$, and $K_{\mathrm{ar}} = -0.3$ indicate that the effect of radial clearance in the exducer is greater than the effect of axial clearance in the inducer. According to Dambach et al. (1998), the reason for this was related to the blade angle and to the speed of the blade tip relative to the casing.

Trailing edge loss

The trailing edge loss is calculated assuming a sudden expansion downstream the trailing edge of the rotor blades, which decelerates the flow in the meridional direction. The model used here, which accounts for blade blockage, is a version based

on a formulation by Glassman (1995), which was then modified by Meroni (2018) using a method by Horlock (1960) to express the loss as a drop in enthalpy; instead of pressure loss as originally presented by Glassman (1995).

$$\Delta h_{\mathrm{te}} = \frac{W_5^2}{2}\left(\frac{Z_{\mathrm{r}} t_5}{\pi(r_{5\mathrm{sh}} + r_{5\mathrm{h}})\cos(\beta_5)}\right)\left[1 + \frac{\gamma_5 - 1}{2} M a_{5,\mathrm{rel}}^2)\right]^{\frac{\gamma_5}{1-\gamma_5}} \tag{5.91}$$

Exit loss

Without a diffuser, all the kinetic energy of the fluid exiting the rotor is assumed to be wasted.

$$\Delta h_{\mathrm{e}} = \frac{C_5^2}{2} \tag{5.92}$$

Windage loss

Unlike the other rotor losses, the disk friction loss, otherwise known as windage loss, is an external loss that occurs outside the rotor. Therefore, it does not contribute to entropy generation between the rotor inlet and exit; however, it does reduce the power output of the turbine due to friction between the rotor disk backface and the backplate. Here, the full form of the theoretically developed correlation by Daily & Nece (1960) is used:

$$\Delta h_{\mathrm{w}} = 0.25 C_{\mathrm{w}} \rho_4 \omega^2 r_4^5 \tag{5.93}$$

where, C_{w} is an empirical friction coefficient. According to experiments conducted by Daily & Nece (1960), the friction coefficient is dependent upon the flow regime, which is dependent on the back-face clearance to radius ratio ($\epsilon_{\mathrm{b}}/r_4$) and Reynolds

number. The flow regime is predicted based on the following:

$$C_{\mathrm{w}} = \begin{cases} \epsilon_{\mathrm{b}}/r_4 \leq 0.05 & \\ \hline \frac{3.70(\epsilon_{\mathrm{b}}/r_4)^{1/10}}{Re^{1/2}} & Re < 10^5, \\ \frac{0.08}{(\epsilon_{\mathrm{b}}/r_4)^{1/6}Re^{1/4}} & 10^5 \leq Re < 10^7 \\ \frac{0.0102(\epsilon_{\mathrm{b}}/r_4)^{1/10}}{Re^{1/5}} & 10^7 \leq Re \\ \epsilon_{\mathrm{b}}/r_4 > 0.05 & \\ \hline \frac{0.08}{(\epsilon_{\mathrm{b}}/r_4)^{1/6}Re^{1/4}} & Re < 10^5, \\ \frac{0.0102(\epsilon_{\mathrm{b}}/r_4)^{1/10}}{Re^{1/5}} & 10^5 \leq Re \end{cases} \tag{5.94}$$

Once the losses in the turbine are estimated, the total-to-total and total-to-static efficiencies are updated based on the calculated rotor and stator losses and the mean-line design is iterated following the method described in Section 5.5.

5.7 Model verification

The process of verification aims to confirm the robustness of the 1D mean-line model by demonstrating that it generates results consistent with other 1D mean-line models. This may be achieved by simulating existing 1D turbine designs and comparing the results with that of the source. Model verification is made complicated because it is uncommon to find existing works which use an identical mean-line design approach to the one used here. Alternatively, a sensible approach to verification is to tailor the mean-line model to match the assumptions of the existing models whilst maintaining core features intact.

5.7.1 Verification with 0D charts

Once a turbine architecture is chosen, a Smith-type chart is usually consulted for a preliminary estimate of aerodynamic efficiency based on the values of the flow

and the loading coefficients. Although originally created for axial turbines, Chen & Baines (1994) proved that a similar chart can be produced for radial inflow turbines using data from existing turbines, and has since been commonly used as a for the estimation of radial inflow turbine total-to-static efficiency. According to Figure 5.13, total-to-static efficiency is maximised for a flow coefficient between 0.2 and 0.3 and a loading coefficient between 0.9 and 1.0.

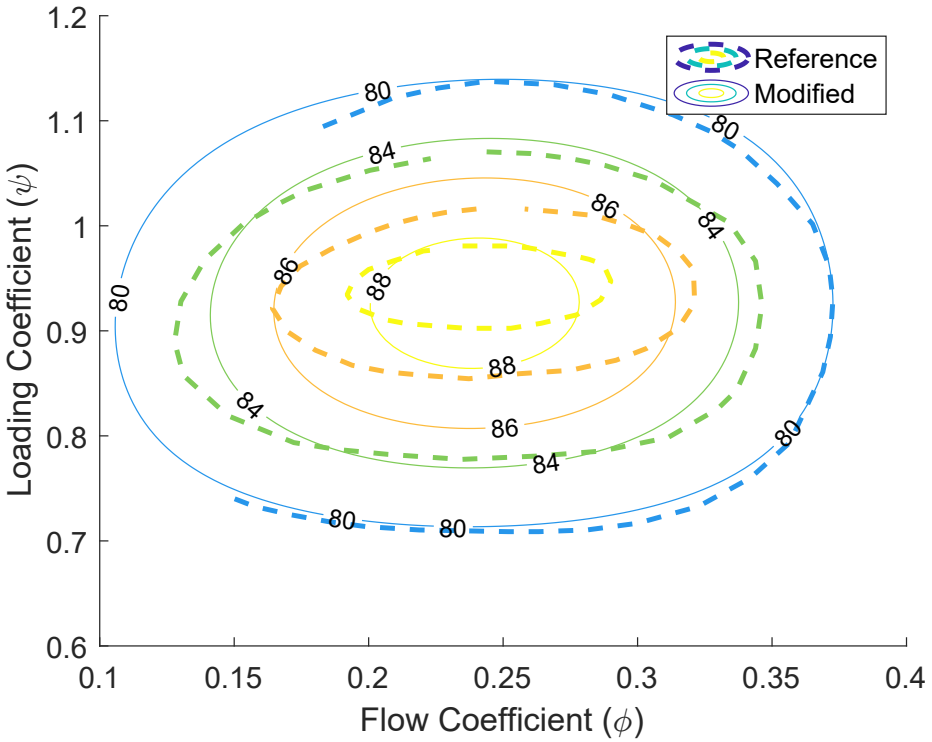

Figure 5.13: Modified flow-loading coefficients chart based on data from Chen & Baines (1994)

Supposedly, Chen and Baines shaped the contours to best fit the data from existing turbines. Unfortunately, they did not disclose the function that was used to produce the contours. A recreation of the original contours by fitting the data cited by Chen & Baines (1994) using a a second-order multivariable polynomial results in a different set of contours, which are also shown in Figure 5.13.

The root mean square error (RMSE) between the data points and the contour estimates quantifies the uncertainty of the newly created chart. Doubling the value of the RMSE produces the 95% confidence interval. Based on the comparison between the data points and the reproduced chart, the RMSE is 1.89%, thus there is confidence that 95% of the data points fall within ±3.8% of the contour values. The error bars

indicate the difference between experimental and estimated efficiency for each data point, also known as the residual. However, after some scrutiny, at least one of the points (highlighted in red) may have been mislabelled as 82 by Chen & Baines (1994), whereas the original source of the data by Kofskey & Holeski (1966) reports an efficiency of 87.2, which agrees with the contours.

By comparing the error between the contours and data points for both the original and the recreated best fit model, it was concluded that the recreated model is more accurate with an RMSE of 1.89%, whereas the original has an RMSE of 3.14% in nominal efficiency.

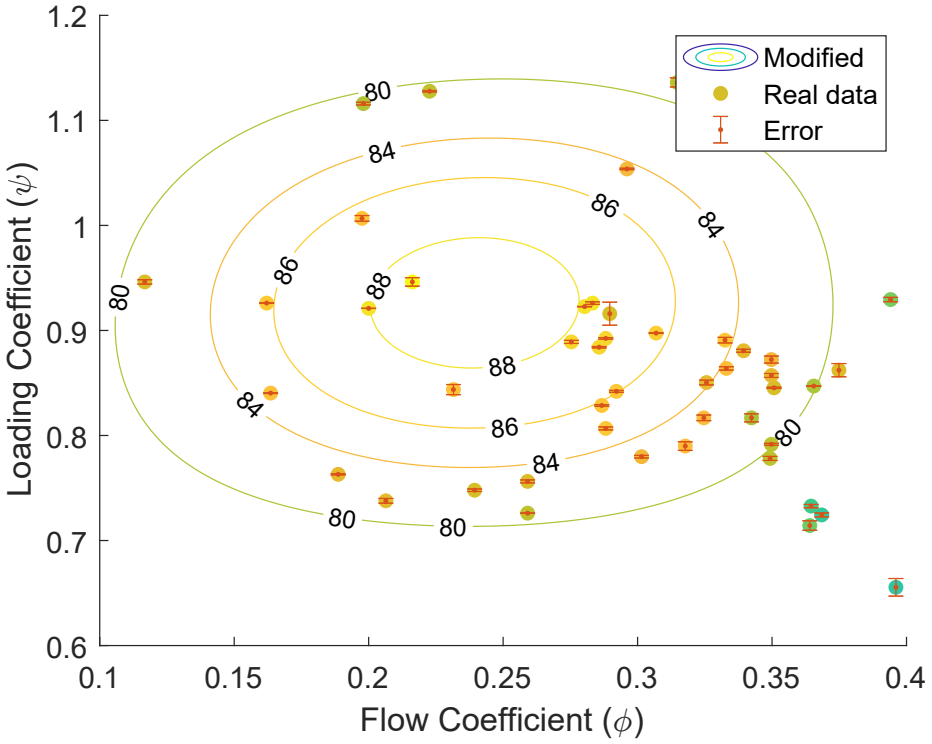

Figure 5.14: Modified Smith-type chart based on data from Chen & Baines (1994). The vertical lines indicate the error between the efficiency of the data points and the that which is calculated using the modified chart.

The modified Smith-type chart was used here to test the consistency of the mean-line design model developed in this work. An air turbine was used to generate the chart, for which the boundary conditions are listed in Table 5.2. The set of charts presented in Figure 5.15 show the difference between the efficiency estimated by the model and that of the modified chart. The highlighted areas are those where the difference between the two is less than 1%. The highlighted areas also correspond

Table 5.2: Turbine boundary conditions for which the Smith-type chart of Figure 5.14 was generated

Parameter	Fluid	$T_{04}[K]$	$P_{04}[kPa]$	P_{04}/P_5	$\dot{m}[kg/s]$
Value	Air	973	400	3.5	39.3

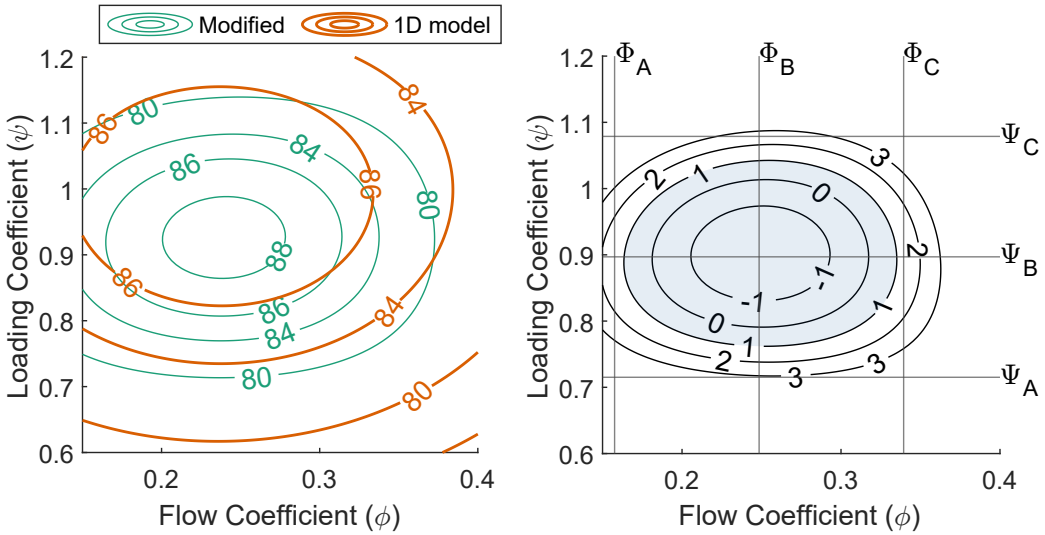

Figure 5.15: Comparison of the recreated Smith-type chart with 1D model . The shaded region in the chart on the right indicates the range of ϕ and ψ that minimises the differences.

To elaborate on the differences between the model and the recreated chart, the flow and loading coefficient isolines A-C are plotted in Figure 5.16 to visualise the differences between the contours at specific locations. The difference between the efficiency contours is minimised close to $\phi = 0.27$ and $\psi = 0.9$, but grows greater at non-optimal coefficients.

5.7.2 Verification with other 1D tools

To further verify the current model, it is compared with the mean-line model of Lv et al. (2018) which was confirmed with CFD simulations. To ensure a fair comparison, the 1D mean-line model was temporarily modified to neglect blade blockage at both the leading and trailing edges of the rotor, as was the case in the source study.

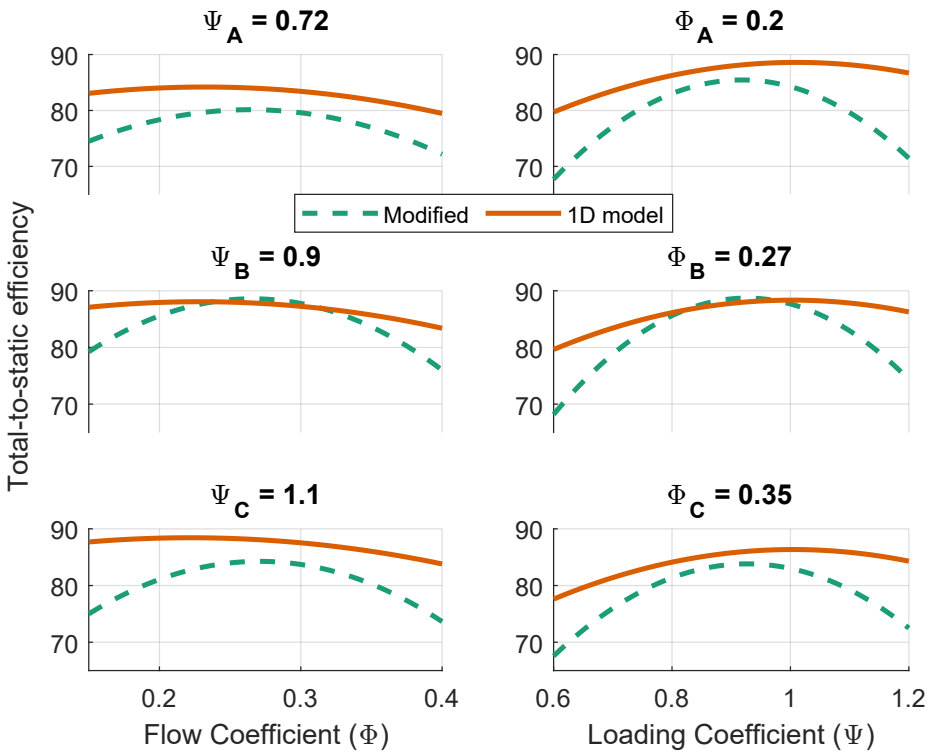

Figure 5.16: Isolines of the flow and loading coefficients based on the sections indicated in Figure 5.15

Two versions of the 1D model are compared in Table 5.3: one that neglects blade blockage in accordance with the source study; the other accounts for blockage. The former is a temporary modification to the model which is used exclusively for comparison, but is discarded otherwise.

With the regards to the modified model, although blockage is not accounted for, there are differences in most parameters, the greatest of which is in the leading edge height b_4 with a deviation of -11% from the source. This is because the modified model produces a greater inlet radius r_4, which is a consequence of the greater tip speed U_4. The higher tip speeds are attributed to the overestimation of the inlet velocity C_4. Ultimately, all these differences originate from the enthalpy loss through the stator; the model estimates lower loss compared to Lv et al. (2018).

The same may be inferred with respect to the current model which accounts for blade blockage, as listed in the last column of Table 5.3. However, the differences in the geometric parameters are greater because the passage is partly blocked by the blades, thus larger radii are required to maintain the same passage areas.

Table 5.3: Mean-line model verification against Lv et al. (2018)

Input	Lv et al. (2018)	$\text{Model}_{\text{no blockage}}$		Model	
$\dot{m}$[kg/s]	1.80	1.80		1.80	
T_{04}[K]	943	943		943	
p_{04}[bar]	106.9	106.9		106.9	
p_6[bar]	77.7	77.7		77.7	
N[kRPM]	80.0	80.0		80.0	
Z_r	14.0	14.0		14.0	
Z_n	21.0	21.0		21.0	
ϵ[mm]	0.30	0.30		0.30	
t_4[mm]	0	0		**1.24**	
t_{5s}[mm]	0	0		**0.31**	
t_{5h}[mm]	0	0		**0.62**	
ϕ	0.88	0.88		0.88	
ψ	0.28	0.28		0.28	
ξ	1.14	1.14		1.14	
r_5/r_4	0.48	0.48		0.48	
r_{5h}/r_{5s}	0.50	0.50		0.50	
α_4[°]	76.5	76.5		76.5	
Results			dev[%]		dev[%]
r_4[mm]	27.3	27.8	2	31.0	14
r_{5s}[mm]	17.5	16.9	-3	18.9	8
r_{5h}[mm]	8.69	8.38	-4	9.36	8
b_4[mm]	4.48	3.99	-11	3.93	-12
β_4[°]	28.5	-29.6	4	-29.6	4
$\beta_{5,rms}$[°]	58.7	-63.4	8	-63.4	8
U_4[m/s]	228	233	2	232	2
C_4[m/s]	208	211	1	210	1
W_4[m/s]	55.6	56.5	2	56.5	2
C_6[m/s]	55.3	56.0	1	55.9	1
W_6[m/s]	123	125	2	125	2
η_{ts}[%]	**83.1**	**84.2**	**1.1**	**84.0**	**0.9**
η_{tt}[%]	**85.4**	**86.6**	**1.2**	**86.4**	**1**

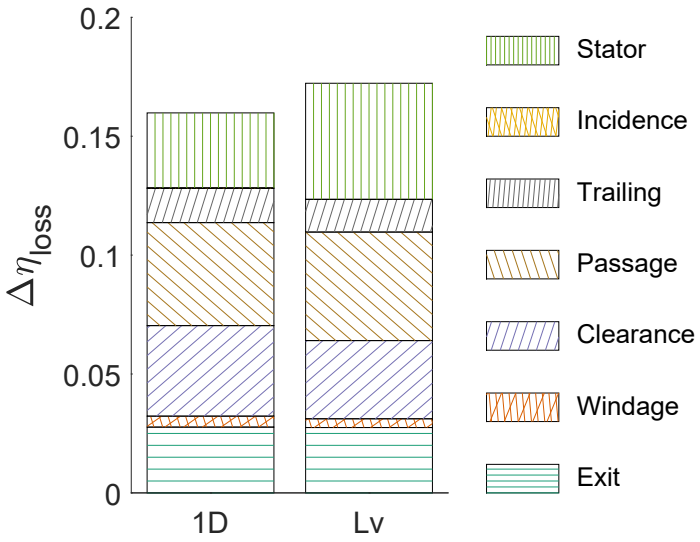

Figure 5.17: Loss comparison with Lv et al. (2018)

Overall, the discrepancies culminate in an efficiency difference of ∼1%. A loss breakdown of the current turbine design and that as reported by Lv et al. (2018) is shown in Figure 5.17. The loss profiles are well aligned apart from small differences in the passage and clearance losses, which are likely due to the deviations in velocities. The greatest difference is in the stator loss. This is expected because the source study uses a different stator loss model that only depends on the flow velocity and a loss coefficient, unlike the model used here in Equation 6.1, which also accounts for the angle of the flow and the viscosity of the fluid.

5.7.3 Model confirmation using CFD

Confirmation is necessary because the loss equations used in the mean-line design model were originally created for air turbines. Therefore, it is imperative to confirm their accuracy in the design of non-air gas turbines before interpreting the results of the mean-line model. Ideally, the mean-line model results would be bench-marked against experimental data points. However, in the absence of experimental data, a numerical model, such as CFD, is commonly used in lieu of experiments.

Although CFD is commonly used to develop and improve on the preliminary mean-line design, CFD is used exclusively for the purpose of confirmation the 1D model; the optimisation of the 3D geometry of the turbine is not within the scope of this thesis.

Conducting numerical simulations of the turbine requires the construction of the 3D profiles of the rotor and stator blades. The 3D geometry of the rotor blade was built in ANSYS BladeGen using the blade inlet and outlet geometries generated by the mean-line model. In addition to the rotor dimensions, the blade metal angle (β_{b}) and blade camberline (θ_{c}) profiles must be defined. The distribution of β_{b} and θ_{c} depends on the blade metal angle at the leading and trailing edges in conjunction with the trailing edge wrap angle (θ_{le}). The former two angles are informed by the meanline design, whereas the wrap angle, defined in Figure 5.18, is set in the range of 40^o to 60^o based on the recommendation by Sauret (2012) and Jones (1994). Moreover, the blade overlap angle, also defined in Figure 5.18 was maintained between 0^o to 5^o, where possible. Typical distribution profiles of β_{b}, θ_{c}, and thickness are shown in Figure 5.19. Radially fibred blades, with no blade lean, were used to limit the bending stress and a shallow-parabolic blade thickness distribution was used along the length of the blades.

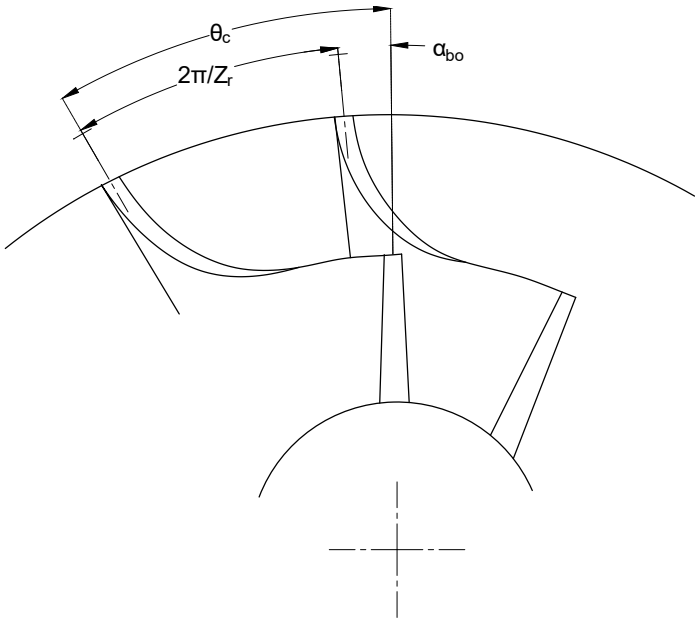

Figure 5.18: Definition of trailing edge wrap angle θ_{le} and blade overlap angle α_{bo}. Adapted from Atkinson (1998).

The stator was built in SolidWorks and then imported into ANSYS DesignModeler. The 3D rotor and stator blades and their passages were meshed using ANSYS TurboGrid. The mesh resolution was determined from mesh-dependence study for both the rotor and stator, the results of which are shown in Fig 5.20. The final mesh

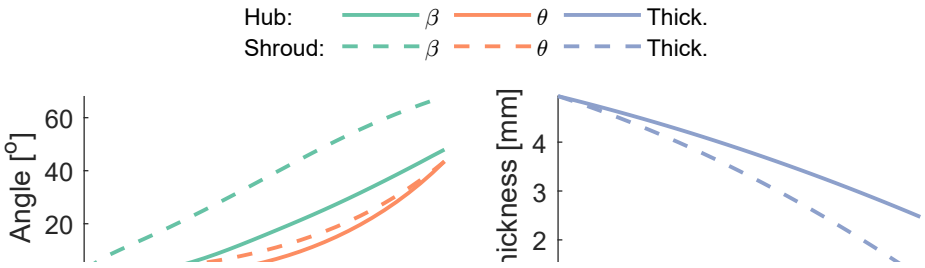

Figure lade
cambe

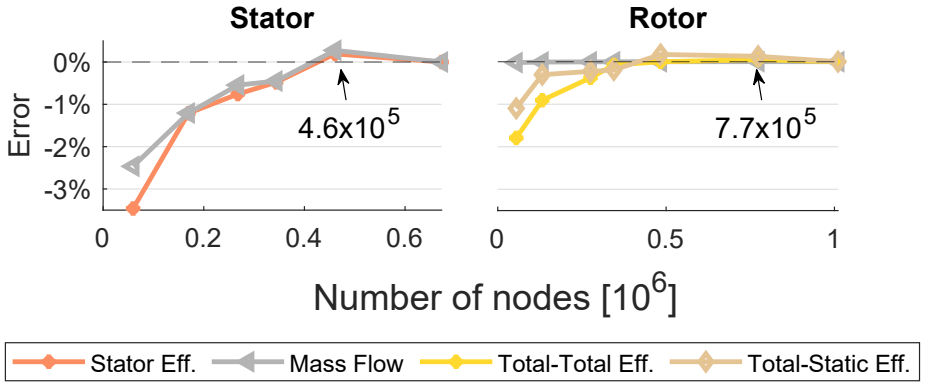

Figure 5.20: Grid independence study for rotor and stator

was composed of approximately 770 thousand nodes in the rotor, and 460 thousand nodes in the stator.

Simulations were then conducted using ANSYS CFX solver. The Reynolds-averaged Navier-Stokes (RANS) equations were closed with the $k - \epsilon$ turbulence model. Boundary conditions were imposed as total conditions at the inlet and static pressure at the exit of the domain. Solution convergence was achieved if the root mean square (RMS) residuals for mass, momentum, and turbulence had reduced to at least 10^{-5}, along with the convergence of the mass flow, and the total-to-static and the total-to-total efficiencies.

Thermodynamic and transport properties were supplied to the CFD solver by a lookup table created with properties calculated by Simulus Thermodynamics software package using the Peng-Robinson equation of state. Moreover, transport properties were calculated using the Ely-Hanley method (Ely & Hanley 1981, Ely & Hartley 1983). The size of the lookup table was 200×200, which was determined through a

sensitivity study, and spans the range of $7 < P < 30$ MPa and $700 < T < 950K$.

The meanline model was confirmed for the three CO_2-based mixtures ($CO_2/TiCl_4$, CO_2/SO_2, and CO_2/C_6F_6) and for pure CO_2 using CFD. A summary of the turbine boundary conditions are listed in Table 5.4. A comparison of key variables of the meanline and CFD simulations are listed in Table 5.5.

Table 5.4: Boundary conditions for the turbines designs confirmed with CFD

Parameter	$CO_2/TiCl_4$	CO_2/SO_2	CO_2/C_6F_6	CO_2
T_{02} [K]	973	973	973	973
P_{02} [MPa]	16.67	16.67	16.67	16.67
α_2 [°]	78	78	78	78
N [kRPM]	30.9	38.1	32.0	43.7

Table 5.5: Mean-line model verification against CFD

Fluid	Variable	Model	CFD	dev[%]
$CO_2/TiCl_4$	η_{tt}[%]	88.94	91.57	-2.63
	η_{ts}[%]	87.02	86.88	0.14
	$\dot{m}$[kg/s]	23.98	24.13	-0.63
	Power [MW]	10.003	10.086	-0.82
CO_2/SO_2	η_{tt}[%]	88.91	90.79	-1.88
	η_{ts}[%]	86.95	85.95	1.00
	$\dot{m}$[kg/s]	17.14	17.40	-1.50
	Power [MW]	10.003	10.008	0.05
CO_2/C_6F_6	η_{tt}[%]	88.87	91.55	-2.68
	η_{ts}[%]	87.12	85.66	0.16
	$\dot{m}$[kg/s]	22.82	22.96	-0.62
	Power [MW]	10.007	10.006	-0.54
CO_2	η_{tt}[%]	88.23	91.44	-2.68
	η_{ts}[%]	85.66	85.57	0.1
	$\dot{m}$[kg/s]	15.32	15.65	-2.13
	Power [MW]	10.0	10.2	2.08

5.8 Summary

In this chapter, the theory of turbomachinery that underpins the design of radial inflow turbines was introduced, along with some of their specific features. Among the possible design approaches, a 1D mean-line model was deemed to be the most suitable for the purposes of this work. The method relies on the resolution of mass, momentum, and energy conservation at the terminals of the stator and rotor to determine the velocity triangles and turbine geometry. The stator geometry largely follows that which was introduced by Aungier (2006). Moreover, aerodynamic losses were calculated by estimating the loss contributions due to several loss mechanisms using loss models found in the literature.

Since these loss models were originally developed for air turbines, it is necessary to quantify the uncertainty in the calculated efficiency by comparing the results from the mean-line model with numerical solutions using CFD. First, the mean-line model was confirmed against the Smith-type chart developed by Chen & Baines (1994). Then, the model was confirmed against an existing model that had been confirmed using CFD with CO_2 as the working fluid. Comparison of the two shows that their estimates of total-to-static efficiency are within 1% of each other. The mean-line model was further confirmed by directly comparing it with CFD for the three mixtures and pure CO_2. Although key parameters such as the mass flow rate, total-to-total efficiency, and power output may vary by up to 3% between the mean-line model and the CFD, the total-to-static efficiency remains within 1% for all the fluids considered.

Chapter 6

Radial inflow turbines for CO_2 mixtures

6.1 Introduction

In this chapter, the design space of sCO_2 radial inflow turbines is investigated using the 1D mean-line design method presented in Chapter 5. The effects of kinematic and geometric parameters on loss estimation are investigated. Within the context of CO_2-based working fluids, different design scenarios are analysed to compare the effect of dopants on the design of radial inflow turbines. The purpose of these design scenarios is to discern the differences in design that are due to inherent differences between the dopants, if any, and those that are due to practical design considerations. Finally, a conjugate optimisation model is described through which the cycle modelling is repeated not with a constant isentropic efficiency for the turbine but with an efficiency estimate informed by the performance estimates of the mean-line design.

6.2 Loss model sensitivity

The loss models presented in Section 5.6, which are summarised in Table 6.1, mainly depend on kinematic and geometric features of the turbine, which are set by

design parameters such as the flow coefficient ϕ, the loading coefficient ψ, and the meridional velocity ratio ξ, among others.

Table 6.1: Summary of loss equations used in the 1D mean-line model

Loss mechanism	Correlation	Equation
Nozzle	$\Delta h_{\mathrm{n}} = \frac{C_4^2}{2}\frac{0.05}{Re_{\mathrm{N}}^{0.2}}\left(\frac{3\tan\alpha_4}{s/c} + \frac{s\cos\alpha_4}{b_4}\right)$	(6.1)
Incidence	$\Delta h_{\mathrm{i}} = \frac{W_4^2}{2}(\sin(\beta_4 - \beta_{4,\mathrm{opt}}))^2$	(6.2)
Passage	$\Delta h_{\mathrm{p}} = m_{\mathrm{f}}\left[\frac{L_{\mathrm{h}}}{D_{\mathrm{h}}} + 0.68\left(1 - \left(\frac{r_5}{r_4}\right)^2\right)\frac{\cos\beta_5}{b_5/c}\right]\frac{W_4^2+W_5^2}{2}$	(6.3)
Clearance	$\Delta h_{\mathrm{c}} = \frac{Z_{\mathrm{r}}U_4^3}{8\pi}(K_{\mathrm{a}}\epsilon_{\mathrm{a}}C_{\mathrm{a}} + K_{\mathrm{r}}\epsilon_{\mathrm{r}}C_{\mathrm{r}} + K_{\mathrm{ar}}\sqrt{\epsilon_{\mathrm{a}}\epsilon_{\mathrm{r}}C_{\mathrm{a}}C_{\mathrm{r}}})$	(6.4)
Trailing edge	$\Delta h_{\mathrm{te}} = \left(\frac{Z_{\mathrm{r}}t_5}{\pi(r_{5\mathrm{s}}+r_{5\mathrm{h}})\cos\beta_5}\right)\frac{W_5^2Y_5}{2}$	(6.5)
Exit	$\Delta h_{\mathrm{e}} = \frac{C_5^2}{2}$	(6.6)
Windage	$\Delta h_{\mathrm{w}} = 0.25C_{\mathrm{w}}\rho_4\omega^2 r_4^5$	(6.7)

The purpose of the following analysis is to examine and explain the sensitivity of the loss models to changes in the geometric and kinematic features of the RIT, and in the viscosity of the fluid. The ranges of the input variables are set based on the expected turbine design space, and are shown in Table 6.3, in which the limits of some parameters are set as a fraction of the base value, while the limits for others are set in absolute value. The base values are taken from the 10 MW CO_2 turbine from Case-B in Section 6.3 as an example.

This analysis is purely mathematical and assumes that all terms are mutually exclusive, and thus can be changed independently of each other; which is not physically possible. However, loss models are ultimately mathematical formulas and will be treated as such for the purposes of this analysis. By understanding the effect each term has on turbine losses the optimal turbines designs presented in the preceding sections may be justified. The variables that are involved in each of the loss models are listed in Table 6.2.

In Figures 6.1 to 6.6, the change in loss is presented as the ratio of the enthalpy loss corresponding to the lower limit of the parameter range to the enthalpy loss corresponding to the upper limit ($\Delta h_{\mathrm{upper}}/\Delta h_{\mathrm{lower}}$). For example, the change in

Table 6.2: Variables that influence the loss models in 1D mean-line design

Loss model	Control variables	Equation reference
Nozzle loss	$\alpha_4, C_4, b_4, \nu_4$	6.1
Passage loss	$r_4, r_{5\mathrm{s}}, r_{5\mathrm{h}}, L_{\mathrm{z}}, Z_{\mathrm{r}}, W_4, W_5, \beta_4, \beta_5$	6.3
Clearance loss	$r_4, r_{5\mathrm{s}}, r_{5\mathrm{h}}, L_{\mathrm{z}}, Z_{\mathrm{r}}, \epsilon, U_4, C_{4\mathrm{m}}, C_{5\mathrm{m}}$	6.4
Trailing edge loss	$r_{5\mathrm{s}}, r_{5\mathrm{h}}, Z_{\mathrm{r}}, w_5, \beta_5$	6.5
Exit loss	C_5	6.6
Incidence loss	$\alpha_4, W_4, \beta_4, Z_{\mathrm{r}}$	6.2
Windage loss	$r_4, b_4, \epsilon, C_{4\mathrm{m}}, U_4, \nu_4$	6.7

nozzle loss is shown in Figure 6.1. The length of each bar is proportional to the change in nozzle loss due to the increase of the absolute inlet velocity from its lower limit to its upper limit (i.e. $C_4 = 150$ to $C_4 = 450$). Moreover, the figures are plotted on a logarithmic scale. Therefore, bars extending to the right indicate a multiplication of loss whereas bars extending to the left indicate a reduction of loss.

Table 6.3: Range of parameters for loss sensitivity study

	Lower	Upper		Lower	Upper	Unit
Fractional limits			Absolute limits			
b_4	0.75	1.25	W_4	50	250	[m/s]
r_{5s}	0.75	1.25	W_5	50	250	[m/s]
r_{5h}	0.75	1.25	C_4	150	450	[m/s]
r_4	0.75	1.25	C_{4m}	50	250	[m/s]
L_z	0.75	1.25	C_5	50	150	[m/s]
ϵ	0.5	1.5	Z_r	12	32	
ν_4	0.5	1.5	α_4	40	80	[°]
			β_4	-40	40	[°]
			β_5	45	85	[°]

6.2.1 Nozzle loss

Nozzle loss is primarily affected by the absolute inlet velocity and flow angle. An increase in the blade height will decrease the nozzle loss as the flow passages become wider, assuming a fixed pitch. The kinematic viscosity is not expected to have a great sway on the nozzle loss compared to the other parameters. Therefore, nozzle loss is a mainly a function of the rotor inlet kinematics. However, the loss model used here was developed by Rodgers (1967) under the assumption of negligible stator incidence

loss. Consequently, the stator and volute designs are assumed to be flexible to match the [illegible] incidence loss [illegible] factor in de[illegible]

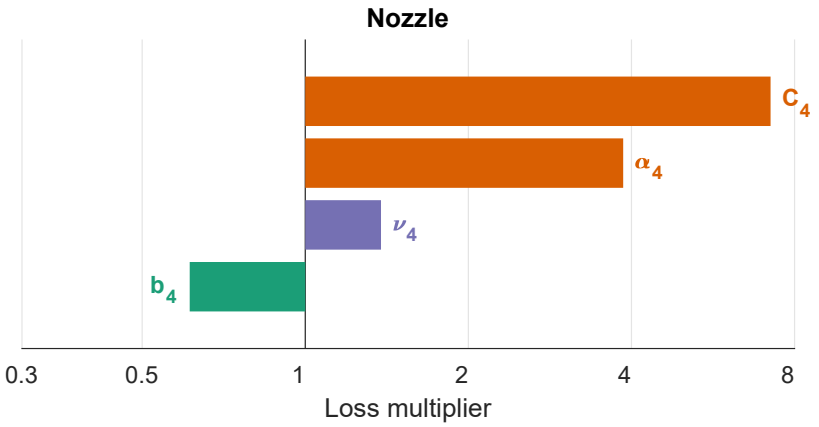

Figure 6.1: Relative sensitivity of nozzle loss to its control variables

6.2.2 Passage loss

The passage loss model used here accounts for both skin friction and secondary losses. Unlike the other parameters, an increase in the shroud radius at outlet reduces passage loss. This is likely due to the shortening of the mean flow path of the fluid, which reduces friction and secondary losses. However, the widening of the shroud radius whilst maintaining a constant inlet radius will also create a smaller radius of curvature along the blade tip, which induces greater secondary flow and possibly separation. All other parameters increase passage losses, with the relative velocities having the greatest effect as they increase both friction and secondary loss terms. The inlet radius, axial length, and number of blades lengthen the mean flow path, thus increase friction loss. The hub radius has a smaller effect on both friction and secondary losses compared to the shroud radius because the hub radius makes a smaller contribution to the mean outlet radius and mean flow path owing to its smaller value relative to the shroud radius. However, if the ratio of the exducer to inlet tip radius ratio becomes large enough (see Equation 5.87) the secondary flow loss is doubled to capture the sharper flow turning.

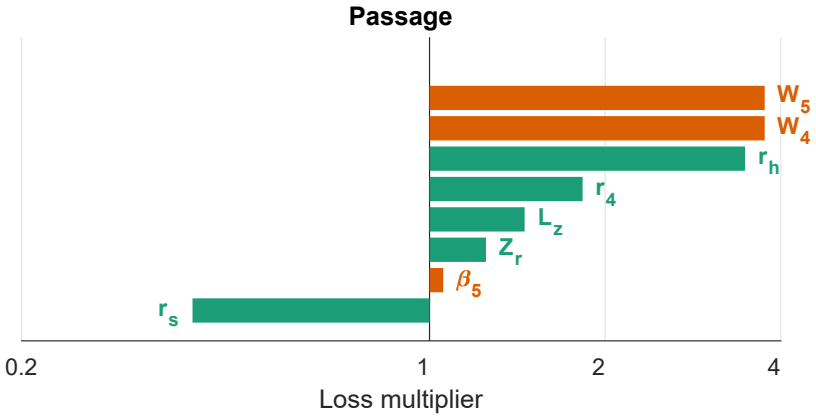

Figure 6.2: Relative sensitivity of passage loss to its control variables

6.2.3 Clearance loss

The formulation of the clearance loss in Equation 6.1 assumes that the velocity of the fluid flowing over the blade is equal to the local blade tip speed. Therefore, the leading-edge blade tip speed U_4 determines the amount of fluid leakage and its kinetic energy. Consequently, an increase in U_4 causes an appreciable increase in clearance loss. This formulation of clearance loss also accounts for the importance of the leaked mass relative to the mainstream mass flow. Consequently, an increase in either the inlet or outlet absolute meridional velocities ($C_{4\mathrm{m}}$, $C_{5\mathrm{m}}$) increases the mass flow rate, thus reducing the importance of the tip leakage flow relative to the mass flow rate of the primary flow through the turbine.

Clearance loss depends on several geometric parameters, such as the clearance gap (ϵ); the higher the gap the higher the leakage losses. Moreover, the leakage loss is a direct multiple of the number of blades ($\mathrm{Z_r}$); more blades, more gaps for the flow to leak through. Additionally, an increase in the axial length increases the blade tip length in the radial direction, thus allowing for longer tip gaps. On the other hand, increasing the tip radius at outlet shortens the blade tip length and dramatically reduces loss.

The largest increase in clearance loss is caused by the increase in the hub diameter. This is because increasing the hub diameter reduces the blade height at outlet, thus enlarging the clearance gap height relative to the blade height, which leads to larger percentage of the flow leaking through the gap.

Although increasing the inlet radius lengthens the overall blade tip length and allows for greater leakage, it also causes a lower tip speed at the outlet, which reduces the amount of leakage in the exducer. Ultimately, an increase in the inlet radius for a fixed inlet tip speed reduces clearance loss. Moreover, because the clearance gap is assumed to be proportional to the blade height at inlet, an increase in the latter will wide wever, the reduce clea

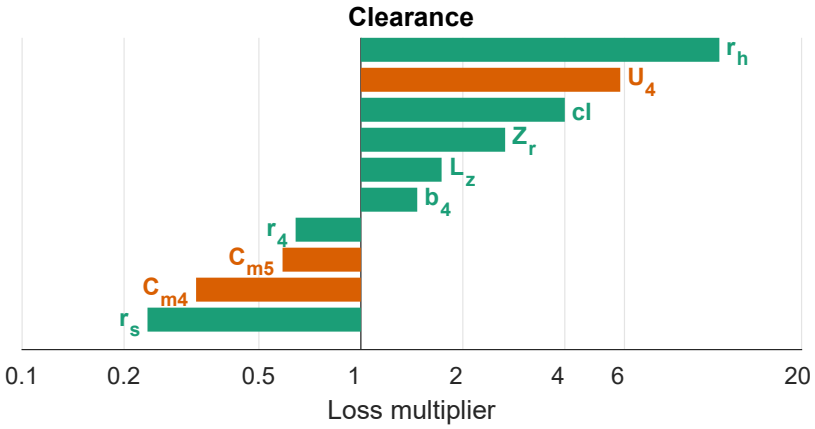

Figure 6.3: Relative sensitivity of clearance loss to its control variables

6.2.4 Trailing edge loss

The trailing edge loss is largely determined by the exit relative velocity and relative angle. A greater relative velocity will increase the sudden expansion loss at the trailing edge, whereas a sharper blade angle at the outlet increases the blade thickness projection on the exit plant, thus increases the trailing edge loss. Like clearance loss, the trailing edge loss is also a direct multiple of the number of blades. An increase in either the hub or shroud radii will decrease the trailing edge loss because the blade blocks a smaller portion of the flow.

6.2.5 Incidence loss

Incidence loss may be amplified by orders of magnitude depending on the change in inlet kinematics and blade count. An increase in the absolute inlet flow angle turns

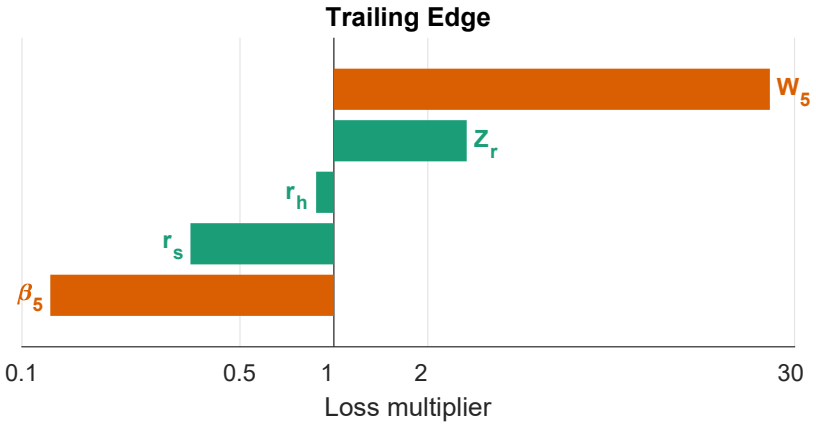

Figure 6.4: Relative sensitivity of trailing edge loss to its control variables

the flow towards the tangential direction which causes a significant increase in the incidence loss. Non-optimal relative angles are also likely to cause secondary flows in the inducer and increase incidence loss. On the other hand, increasing the number of blades reduces flow recirculation and improves incidence, even if the blade count is more than the minimum required to avoid separation. However, as we have seen in other losses, increasing the number of blades will increase passage, clearance, and traili imum. All f cause flow

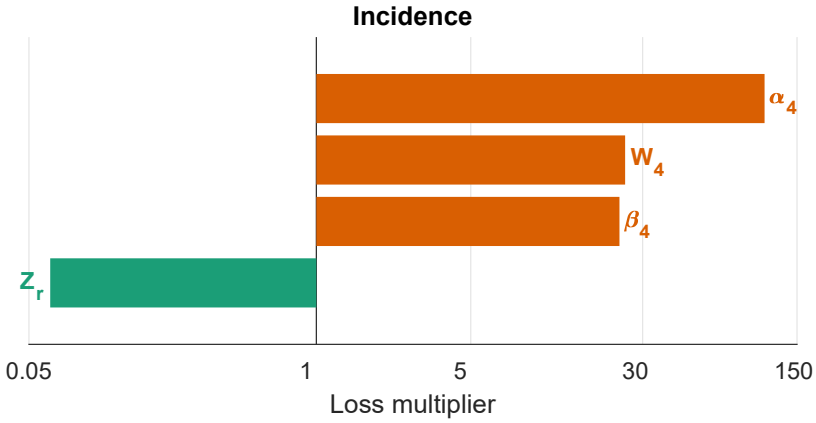

Figure 6.5: Relative sensitivity of incidence loss to its control variables

6.2.6 Exit loss

Exit loss is solely dependent on the exit merdional velocity, assuming zero exit swirl. Out of all the parameters, the exit velocity has the greatest significance on the

total-to-static efficiency of the turbine; so much so, that increasing the outlet velocity might eclipse all other losses combined, as observed in the loss breakdown presented by Rohlik (1968). No breakdown of exit loss is shown because it is reliant on a single variable (C_5).

6.2.7 Windage loss

Windage loss is primarily a function of the disc speed (blade tip speed), rotor radius, viscosity, and back face clearance gap. An increase in any of these four parameters will increase windage loss, but the blade tip speed has the greatest effect. The [illegible] only if it is higher the [illegible]

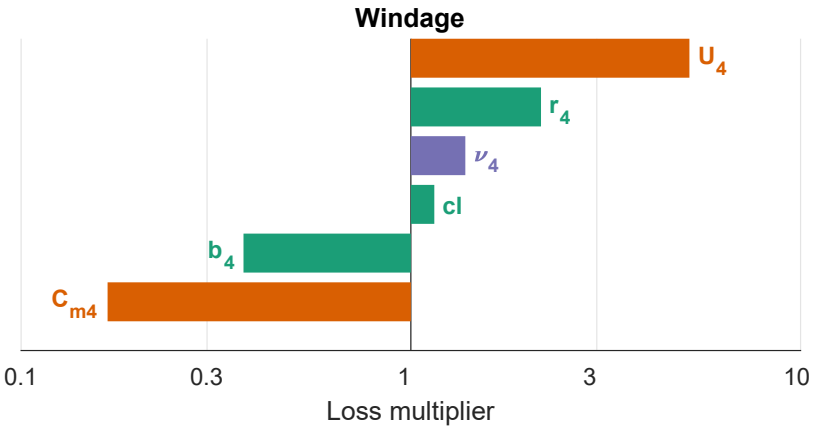

Figure 6.6: Relative sensitivity of windage loss to its control variables

The sensitivity analysis indicates that the losses estimated using the 1D model are mainly a function of the turbine geometry and kinematiecs, with a comparativly weak dependence on fluid-specific properties, namely the kinematic viscosity. Therefore, doping CO2 is expected to the affect the turbine design in so far as it affects the kinematics and geometry of the turbine; the change in kinematic viscosity, if any, will not significantly change the turbine efficiency. The loss model sensitivity analysis presented here will be used in Section 6.3 to explain key differences among the optimised radial inflow turbine designs of the the three mixtures across scales.

6.3 Turbine design optimisation methodology

In the following study, radial inflow turbines are designed for four working fluids (molar composition): $CO_2/TiCl_4$ (%16.7/%83.3), CO_2/SO_2 (%26.7/%73.3), CO_2/C_6F_6 (%17.4/%82.6), and pure CO_2 ; under three scenarios (Case-A, Case-B, and Case-C) and three power capacities (0.1 MW, 1 MW, and 10 MW). In all instances, the turbines are assumed to operate under similar inlet conditions, namely total temperature and pressure; but, the static outlet pressure and mass flow rate depend on the scenario and the power capacity, respectively. The assumptions in each scenario, along with the RIT design algorithm, are shown in Figure 6.7 and explained next.

Case-A: Fixed design and pressure ratio

In the first instance, all design parameters are selected and fixed based on common recommendations in the literature, which are listed in Table 6.5. This exercise aims to study the effectiveness of the standard approach in choosing an efficient design for each of the working fluids. Moreover, the pressure ratio are also fixed according to the cycle conditions under which each working fluid is designed to operate, as described in Chapter 4 and summarised in Table 6.4. Although these pressure ratios may not maximise turbine performance, they are the typical conditions under which the turbines are expected to operate.

Case-B: Optimised design at fixed pressure ratio

Next, the pressure ratios are maintained according to the cycle, but the input design parameters are optimised within the constraints shown in Table 6.5. The range of each of these parameters that yields good turbine performance is well-established in the literature and will be used to confine the turbine design space. This iteration represents a more thorough design approach than Case-A because more effort is required to find the optimal design rather than relying on a one-size-fits all approach.

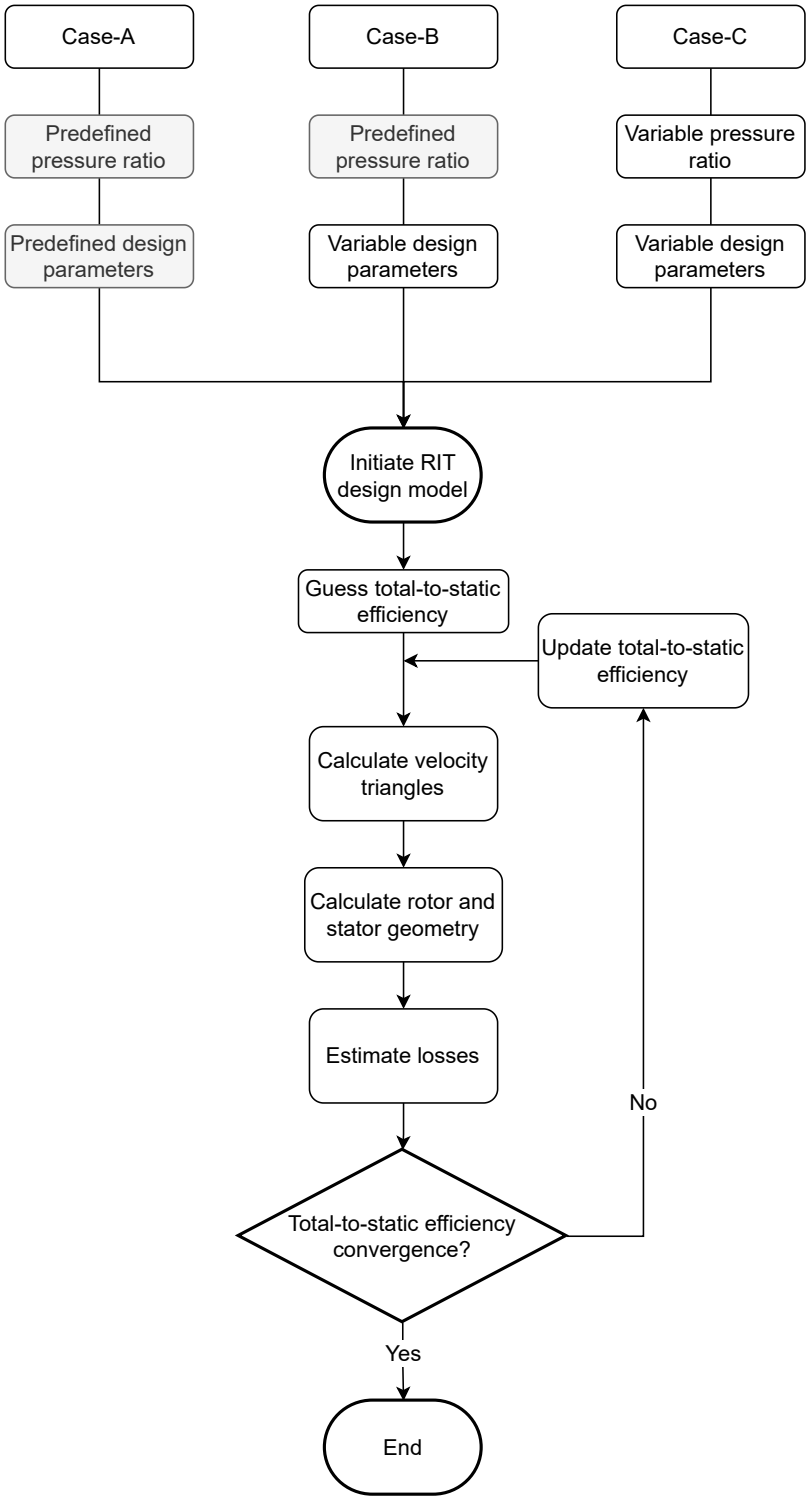

Figure 6.7: Assumption of radial inflow turbine (RIT) design process for each design case

Case-C: Optimised design and variable pressure ratio

Finally, the pressure ratios along with the input parameters of Case-B are used to optimise the turbine total-to-static efficiency. The change in pressure ratio is

Table 6.4: Turbine boundary conditions for Cases A and B

Variable	$CO_2/TiCl_4$	CO_2/SO_2	CO_2/C_6F_6	CO_2
T_{in}[°C]	700	700	700	700
P_{in} [MPa]	25	25	25	25
$P_{in,t}/P_{out,s}$	2.50	3.39	3.25	3.42

balanced by a change in mass flow rate to maintain a prescribed power output. This scenario decouples the turbine pressure ratio from that of the cycle pressure ratio with multiple aims: to determine whether the turbines will converge on a common pressure ratio, to examine whether the differences between the fluids are caused by the turbine boundary conditions rather than intrinsic differences between the fluids themselves, and to indicate the potential benefit of multi-staging in each of the working fluids.

Table 6.5: Turbine optimisation parameters

Variable	Type	Case-A	Cases B & C	Ref
ϕ	Variable	0.23	0.2 - 0.3	(Moustapha et al. 2003)
ψ	Variable	0.93	0.85 - 1.0	(Moustapha et al. 2003)
ξ	Variable	1.0	1.0 - 1.5	(White 2015)
r_5/r_4	Variable	0.5	0.3 - 0.7	(Rodgers 1967, Rohlik 1968)
r_{5h}/r_{5sh}	Variable	0.45	0.4 - 0.7	(Rohlik 1968)
α_4[°]	Constraint		68 - 78	(Korpela 2019)
β_4[°]	Constraint		-20 - -40	(Moustapha et al. 2003)
r_{5sh}/r_4	Constraint		< 0.7	(Rodgers 1967)
α_5[°]	Input	0	0	(Moustapha et al. 2003)
$\epsilon_{a,r}[mm]$	Input	0.4	0.4	(Rodgers 1967)
L_z/b_5	Input	1.50	1.50	(Aungier 2006)
t_4/r_4	Input	0.04	0.04	(White 2015)
t_{5h}/r_4	Input	0.02	0.02	(White 2015)
t_{5sh}/r_4	Input	0.01	0.01	(White 2015)

Power scaling

Large scale designs may suppress the differences among the working fluids. Therefore, the three aforementioned cases are simulated for turbines with power outputs of 0.1 MW, 1 MW, and 10 MW. Ultimately, power scaling will reveal whether certain mixtures have an inherent advantage at smaller scales.

6.4 Turbine design comparison

This section explores turbine designs for pure and mixed CO_2 working fluids under the three design approaches across power scales. Firstly, the performance of all the cases are discussed in terms of total-to-static efficiency. Secondly, the loss breakdown of Case-B against Case-C is presented to explain the observed trends. Next, particular interest is given to clearance loss owing to its importance at smaller scales. Lastly, similarities and dissimilarities between the fluids are highlighted.

6.4.1 Performance trends

The following discussion refers to the total-to-static efficiencies presented in Figure 6.8.

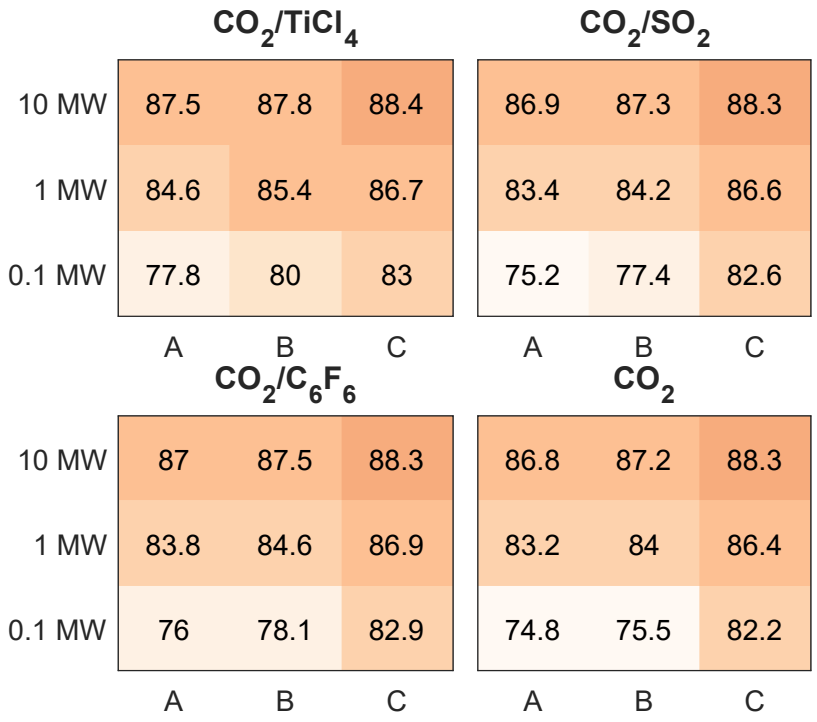

Figure 6.8: Total-to-static efficiency of the three cases at different power capacities

Power Scaling

Regardless of the working fluid, the gain in efficiency from 0.1 MW to 1 MW is always greater than the gain from 1 MW to 10 MW. Apart from a few cases, the

former is more than double the latter. Among the fluids, the increase in efficiency with power scaling is greatest for CO_2, regardless of the design approach (Case A, B, or C). At its greatest, the gain in efficiency is 12% between 0.1 MW and 10 MW for Case-A of CO_2. The smallest gains are $\sim$5.4% between 0.1 MW and 10 MW for Case-C of $CO_2/TiCl_4$ and CO_2/C_6F_6.

The power a turbine generates scales with the radius squared, but the leakage flow scales linearly with the radius (Wright et al. 2010). Therefore, avoiding leakage losses is easier in large turbines, but will be difficult in small-scale turbines. Ultimately, the clearance gap to blade height ratio is the best indicator of the loss in efficiency due to leakage.

The consequence of the clearance to blade height ratio is best understood through Figure 6.9, in which designs according to Case-A are presented. Case-A was chosen because the discrepancies between the fluids are most pronounced, whereas the differences are lessened by the optimisation in Cases-B and C. There is a direct but inverse correlation between the total-to-static efficiency and the clearance-to-height ratio; the greater the ratio, the lower the efficiency. Because $CO_2/TiCl_4$ can maintain the lowest ϵ/b_4 across scales, it has the highest turbine efficiency amongst the fluids, which is confirmed by Figure 6.8. Conversely, CO_2 has the greatest (ϵ/b_4), thus the lowest efficiency.

Although the trends in efficiency and ϵ/b_4 are observably correlated, they do not necessarily prove causation. However, causation is demonstrated in the same figure by the parallel lines of efficiency at the top of the figure. These lines were produced by running similar scenarios as in Case-A; but with a constant clearance to blade height ratio $\epsilon/b_4 = 0.02$. This assumption is for illustrative purposes and may not be feasible as the clearance gap may be as low as 22 μm in 0.1 MW turbines. Although narrower gaps have been cited in the literature (Qi et al. 2017), their feasibility was not physically demonstrated.

This hypothetical example demonstrates that if ϵ/b_4 is assumed constant, the change in efficiency across scales becomes uniform for all fluids, thus negating the

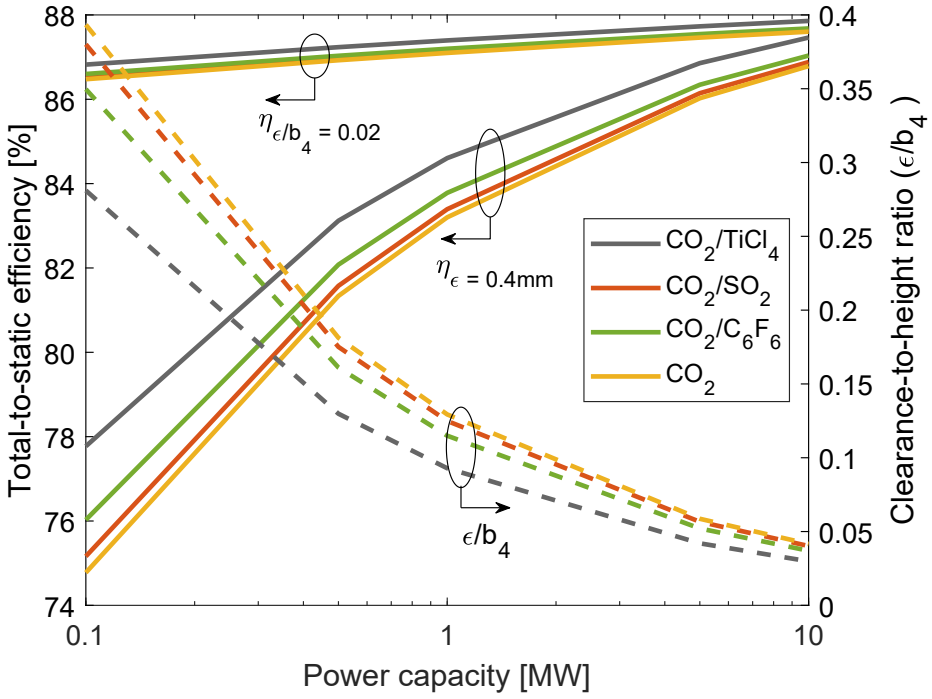

Figure 6.9: Left axis: Change in efficiency across power scales at constant $\epsilon = 0.4mm$, and at constant clearance-to-height ratio $\epsilon/b_4 = 0.02$. Right axis: the change in ϵ/b_4 when $\epsilon = 0.4mm$

positive effect wider blade heights have on efficiency. It also indicates the potentially significant gain in efficiency if shrouded rotors are used, especially at small scale. Of course, the use of shrouds will be accompanied by greater windage loss; nonetheless, the potential gains due to the reduction in clearance loss will likely outweigh the penalties of windage loss. The factors limiting the use of closed rotors are likely to be mechanical. Firstly, the structural limits placed on the blade tip speeds are more stringent when closed shrouds are used. Generally, tip speeds should be lower with closed rotors. Moreover, the manufacturability of the closed rotor passages at such small scales is a key hindrance, as well as the increased mass and the effect this might have on rotordynamics - particularly at the smaller scales.

The larger blade heights in $CO_2/TiCl_4$ turbines is a consequence of the lower specific work of the turbine, which causes higher mass flow rates to maintain the same power output. Evidently, this is due to the difference in the inlet density of the fluid and, to a lesser degree, its adiabatic coefficient, as explained in Chapter 4. Although the difference in the blade heights is exacerbated by the difference in the pressure ratio between the working fluids, it is not eliminated even if a uniform

pressure ratio is applied to all fluids, as is discussed in the following section.

Design scenarios

The merits of design optimisation are evident in all fluids and for all power capacities. As stated earlier, Case-A assumes both fixed design parameters and pressure ratios, whereas Case-B optimises the design variables but maintains the same pressure ratios. Therefore, any differences between the two approaches will be a result of the change in turbine design parameters. Overall, Case-B improves the performance of all turbines, indicating that optimisation converges on design parameters that are more suitable than those assumed in Case-A.

A greater gain in the efficiency of Case-B indicates a greater inadequacy of the assumptions of Case-A. This is most apparent at small scales where the differences between the two cases are the greatest. Therefore, small turbines require a different set of design parameters than those assumed in Case-A. For example, the smallest gain in design parameter optimisation is 0.3% for 10 MW $CO_2/TiCl_4$, and the greatest is 2.2% for 0.1 MW CO_2/SO_2. For all fluids, as the turbines are scaled up towards 10 MW, the differences between Case-A and Case-B decrease, thus indicating that the assumption of Case-A are better suited to 10 MW turbines.

The turbine is decoupled from cycle conditions in Case-C by optimising the static pressure at the outlet, thus the turbine pressure ratio is optimised. Case-C also optimises design parameters. Therefore, performances differences between Case-C and Case-B are derived from pressure ratio optimisation even if the design parameters are different.

For all working fluids, the optimisation algorithm converges on the minimum limit of the pressure ratio (1.5) by maximising the outlet pressure. This is an expected outcome because lower pressure ratios induce lower flow velocities and, consequently, lower aerodynamic losses; which is true across power capacities. Here, as in Case-B, small turbines benefit the most from pressure ratio optimisation. The greatest increase in efficiency for Case-C compared to Case-B is 6.7% with 0.1 MW CO_2 turbine, and the smallest increase is 0.6% with 10 MW CO_2.

Among the fluids, the smallest gain in pressure ratio optimisation is for $CO_2/TiCl_4$. This is because the pressure ratio set by cycle conditions, as used for Cases A & B, is lower than those of the other fluids, as listed in Table 6.4. Therefore, the change in the pressure ratio for $CO_2/TiCl_4$ is 1.0 compared to 1.75, 1.89, and 1.92 for CO_2/SO_2, CO_2/C_6F_6, and CO_2, respectively. This suggests that $CO_2/TiCl_4$ will benefit less from multi-staging compared to the other fluids when operating within pressure ratios dictated by their respective cycles.

Generally, the benefits of scaling is greatest for Case-A, followed by Case-B and the Case-C, regardless of the working fluid. Therefore, the differences in the efficiencies of the cases for a given power capacity decreases at higher power scales. For example, the efficiency of Case-C is 7.4% higher than that of Case-A for 0.1 MW CO_2/SO_2, but this difference shrinks to 1.4% at a scale of 10 MW. A similar trend is observed in all fluids, but to varying degrees. The cause of the dissimilar trends in performance across power scales is the drastic change in the height of the clearance gap at the blade with respect to the height of the blade, as was explained through Figure 6.9.

An apt comparison of fluids, cases, and power scales may be made through a classical specific speed and efficiency chart. In Fig 6.10, all turbines discussed thus far are plotted with respect to the curve produced by Baljé (1962). The benefits of optimisation are evident in Case-B and Case-C where the efficiency is higher than Case-A, especially in 0.1 MW turbines. Moreover, the higher flow coefficients result in higher specific speeds in Cases-B and C. Overall, designs fall in the range of $0.3 < N_s < 0.5$.

6.4.2 Loss analysis

The loss profiles of the optimal RIT designs according to Case-B are presented in Fig 6.11. Overall, the contributions of losses are similar for all fluids, with the rotor passage loss having the greatest weight in 10 MW turbines, clearance and passage equally contributing to losses in 1 MW turbines, and clearance as the predominate loss in 0.1 MW turbines. Among all losses, however, the clearance loss is the most salient variance across power scales. In the proceeding analysis, the similarities across

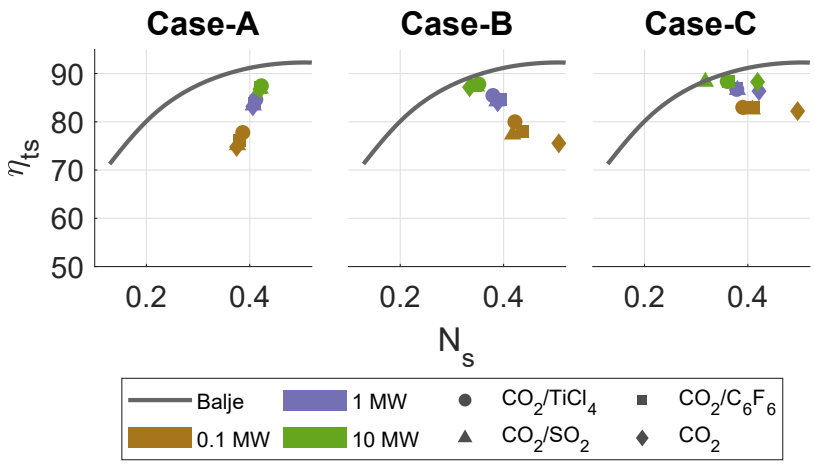

Figure 6.10: Specific speed and efficiency comparison

the working fluids are explained, followed by a discussion on the variance across power scales.

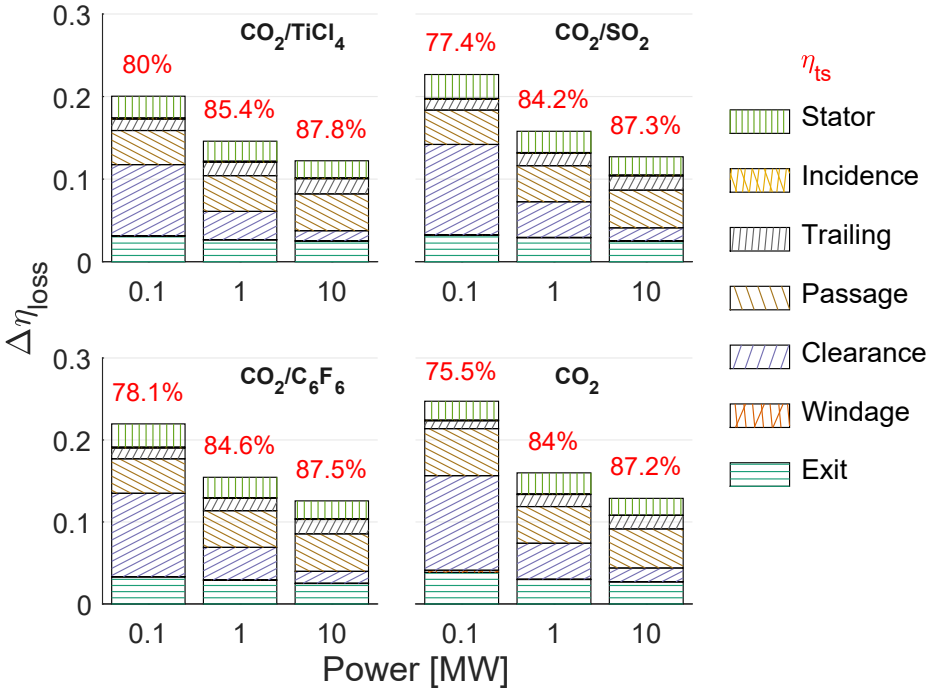

Figure 6.11: Loss contributions for Case-B

Stator and exit losses mainly depend on the absolute inlet and outlet velocities, respectively. Therefore, the stator and exit losses are almost uniform among the fluids at the same power scale owing to the similar velocity diagrams at inlet and outlet, an example of which is shown in Figure 6.12. The sizes of the triangles scale with the specific work of the turbine, but the shapes are determined by ψ, ϕ and ζ. Although stator loss is also dependent on the kinematic viscosity of the working fluid, as seen

in Equation 6.1, it will be shown in Section 6.4.3 that this dependency is weak.

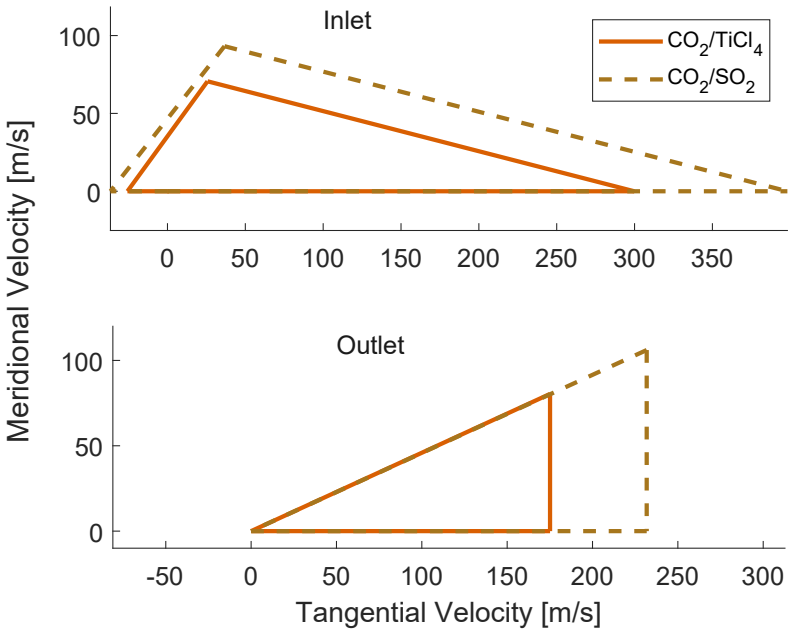

Figure 6.12: Velocity triangles for 0.1 MW $CO_2/TiCl_4$ and CO_2/SO_2 turbines from Case-B

Across power scales, however, there is an increase in the stator loss and a more notable increase in the exit loss. Velocity diagrams may also be used to explain these increases. An example is shown in Fig 6.15 for CO_2/SO_2, in which the outlet velocity is greater in small turbines, which is driven by the increase in the flow coefficient (ϕ). This trend is observed in all working fluids and is the response of the optimisation algorithm to the increasing clearance. According to the clearance loss model in Equation 6.4, losses will decrease with increasing merdional velocities C_{4m} and C_{5m}. Therefore, as the significance of clearance loss amplifies at smaller scales, optimisation favors designs that have higher flow coefficients. This is an attempt to abate the increase in clearance loss because of its increasing importance at small scale; which is not prevalent in larger turbines where the increase in the passage loss due to higher flow velocities outweighs the decrease in clearance loss, thus lower flow coefficients are preferred. Moreover, the inlet radius reduces in order to reduce the clearance/blade height, which would further increase the rotational speed at small scale; this is evident in the increase in the blade width to radius ratio (b_4/r_4) shown in Table 6.6.

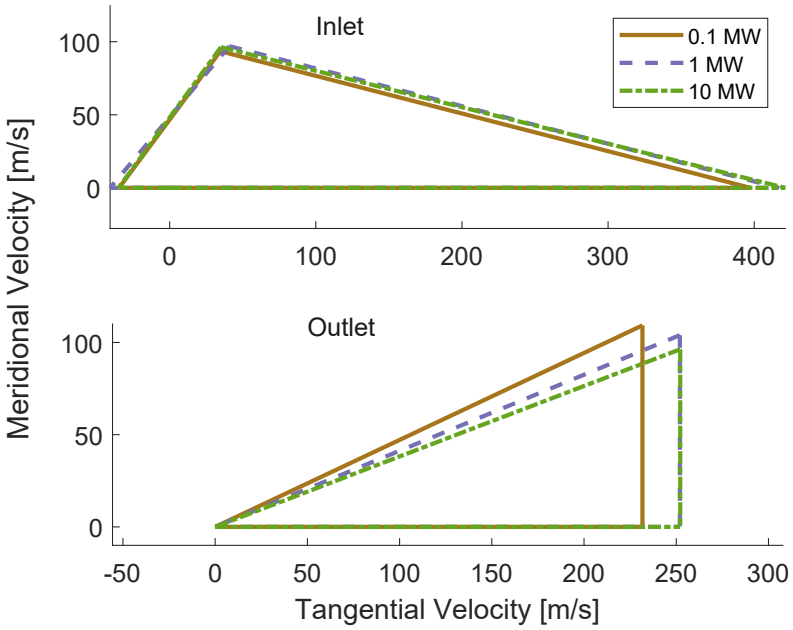

Figure 6.13: Velocity triangles across power scales for CO_2/SO_2 from Case-B

Like the exit loss, the trailing edge loss is also influenced by the velocity triangle at the outlet, namely by w_5 and β_5, and to a lesser degree, by the outlet blade dimensions and the blade count. Therefore, the similar outlet velocity triangles and proximate blade counts render the trailing edge loss contributions comparable for all fluids at the same power scale. Unlike clearance loss, the trailing edge loss is less important in small turbines compared to large turbines owing to the decrease in the relative velocity at outlet w_5 and the decrease in the blade count in some fluids like $CO_2/TiCl_4$ and CO_2. Both incidence and windage losses are negligible for all fluids. The former is suppressed by the constraint of $-40^o < \beta_4 < -20^o$ imposed on the optimisation, which maintains favourable flow angles into the rotor and keeps the loading coefficient ψ close to 0.9.

Instead of presenting an additional loss profile chart for Case-C, Figure 6.14 shows the difference in each loss contribution with respect to the baseline Case-B. Compared to Case-B, both passage and clearance losses are lower in Case-C for all turbines across all power scales, while trailing edge losses are higher. This is because the lower pressure ratios of Case-C compared to Case-B require turbines that are less loaded. According to Euler's equation, the specific work of a turbine with zero exit

swirl ($\alpha_5 = 0$) is defined as:

$$w = U_4 C_{4\theta} \tag{6.8}$$

Therefore, to decrease the specific work ('unload' the turbine), the blade tip speed and or the inlet tangential velocity must be decreased. In Case-C, both U_4 and $C_{4\theta}$ reduce in concert to maintain a favorable absolute inlet flow angle within the limits of Table 6.5.

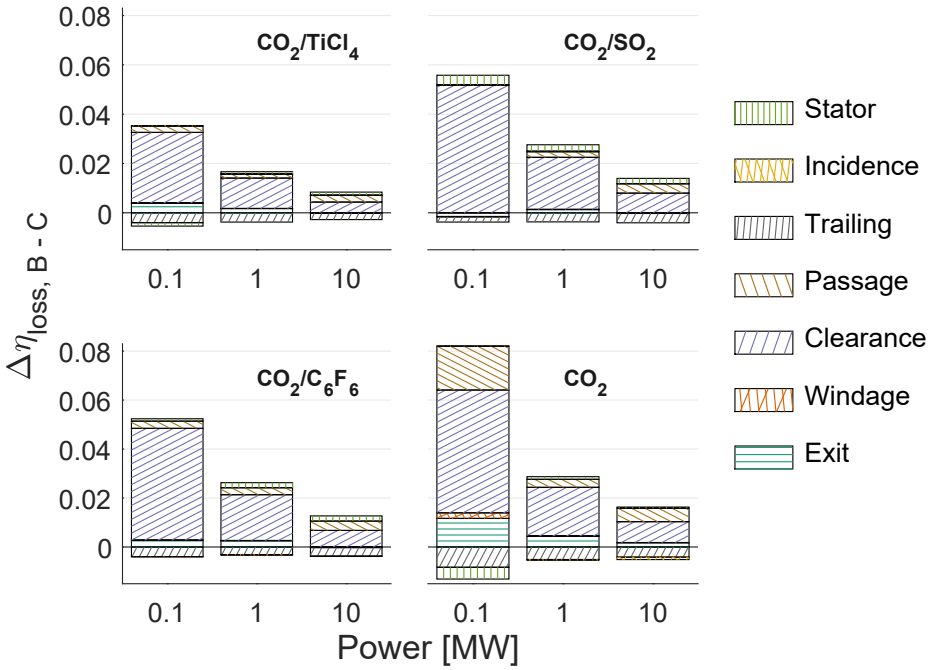

Figure 6.14: Difference in loss contributions between Case-B and Case-C

Concurrently, to maintain the prescribed power capacity at a lower specific work, the mass flow rate must increase. With slower flows and greater flow rates, the passage areas must enlarge, leading to wider blades. Ultimately, the wider blades lower clearance losses by decreasing the clearance gap to blade height ratio ϵ/b_4 in both the axial and radial direction at the inducer and exducer, respectively. Moreover, slower internal flows in the rotor decrease friction and its associated passage loss. On the other hand, the wider blades at the outlet induce higher trailing edge losses, as observed for all turbines.

6.4.3 Loss model sensitivity

In Figure 6.15, the qualitative significance of a parameter is indicated by the length of its bars, the color of the bar indicates the nature of the parameter (kinematic, geometric, or physical), and the contrast of the color indicates the power scale: dark for 10 MW; light for 0.1 MW

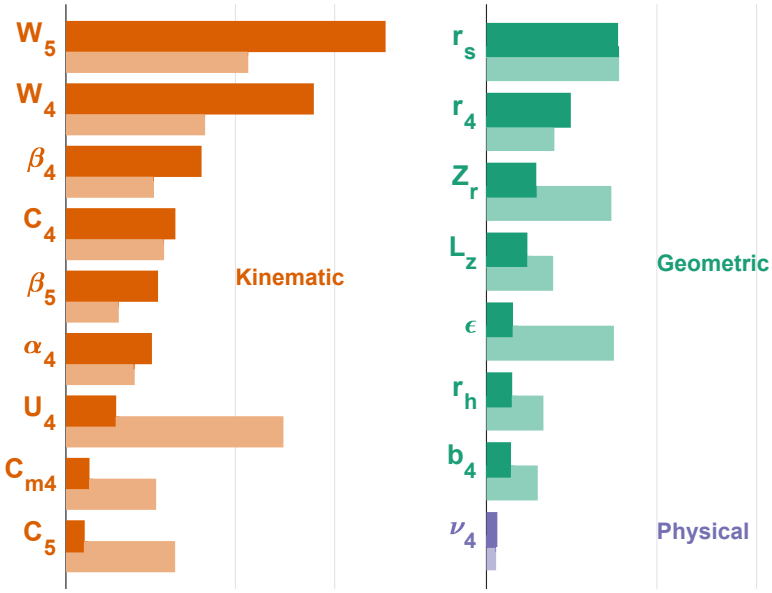

Figure 6.15: Loss sensitivity: the length of the bars indicates the qualitative effect a parameter has on the total loss. Dark bars are for 10 MW; Light for 0.1 MW

A perceptible feature of Figure 6.15 is the uneven influence of parameters, which is dependent on the significance of the losses to which it contributes. For example, the most influential parameters at the 10 MW scale are those which affect passage loss because, as seen earlier in Figure 6.11, the passage loss is predominant in large turbines. Among the kinematic parameters, the relative flow velocities w_4 and w_5 have the greatest effect. The relative outlet velocity w_5 is more significant because, in addition to passage loss, it affects the trailing edge loss as well. On the other hand, small-scale turbines are penalised more by clearance loss. Therefore, the efficiency is expected to become increasingly sensitive to parameters that contribute to clearance loss as the turbine is scaled down to 0.1 MW. This is confirmed by Figure 6.15, in which the significance of terms that appear in Equation6.4, such as ϵ, U_4, and, Z_r, is amplified in the 0.1 MW turbine. Overall, geometric parameters become more important in 0.1 MW turbines, as observed in the general trend in right side plot of

Figure 6.15.

The effect of the physical properties of the fluid, represented by the kinematic viscosity, is the smallest at both scales. Therefore, the differences in the viscosity of the fluids has little sway on turbine performance; in other words, the loss models are fluid-agnostic. It must be emphasised that this conclusion is strictly based on the mathematical nature of the loss models used here, and may not accurately represent the effect that each of these parameters has on the physical flow in the rotor. Indeed, Keep & Jahn (2019) conducted a numerical loss investigation of a 300 kW low-specific speed RIT operating with CO_2 and concluded that endwall viscous losses in the stator are more significant than predicted using gas turbine derived preliminary design methods. Moreover, viscous stresses are stronger at low Reynolds number. Accordingly, losses are likely to have increased sensitivity to the viscosity of the fluid at low Reynolds number, which is not the case here as $\mathrm{Re} >> 10^6$. However, the trends shown in Figure 6.15 justify the convergence of the 1D model on a similar turbine design regardless of the fluid. Ultimately, it's the flow and shape characteristics of a turbine that determine its performance, not the characteristics of the working fluid.

6.4.4 Similarities and dissimilarities

The designs of the turbines from Case-B are compared in Tables 6.6 and 6.7 and Figure 6.17. For a given power capacity, the turbines have similar shapes, which may be attributed to the consistency in the design parameters $(N_s, \phi, \psi, \xi, r_5/r_4, r_{5h}/r_{5s}, L_z/b_5)$. Therefore, a consistent rotor shape optimises aerodynamic performance regardless of the working fluid. There are a few likely reasons for this. First, all working fluids behave very close to ideal gases throughout the expansion process; they have compressibility factors close to unity. This is confirmed in Figure 6.16 where the expansion process with respect to compressibility contours on reduced pressure-temperature axes are depicted. All the working fluids studied here have compressibility values in the range of 0.97 to 1.04 throughout the expansion process. The process shown in Figure 6.16 is for 10 MW Case-B turbines; however, the compressibility factors are within the same range in all cases at all power-scales.

Table 6.6: Design data for optimal 0.1 MW Case-B RIT

Parameter	$CO_2/TiCl_4$	CO_2/SO_2	CO_2/C_6F_6	CO_2
ψ	0.9	0.91	0.91	0.88
ϕ	0.26	0.27	0.28	0.3
ξ	1	1.17	1.18	1
r_5/r_4	0.6	0.58	0.58	0.47
r_h/r_s	0.69	0.62	0.62	0.32
N_s	0.4	0.42	0.43	0.49
$b_4/r_4[\%]$	8.0	9.1	9.2	9.0
$\eta_{tt}[\%]$	80	77.4	78.1	75.5
$\eta_{ts}[\%]$	82.6	79.9	80.7	78.6
p_{06}/p_5	2.5	3.39	3.25	3.42
Δh_{tt} [kJ/kg]	103	186	138	212
N [kRPM]	192.7	314.1	252.7	396.3
α_4 [°]	73.7	75.6	75.6	71.2
β_4 [°]	-20	-20.3	-20.8	-22.6
β_5 [°]	-66.2	-64.8	-64.6	-57.6
U [m/s]	302	397	344	427

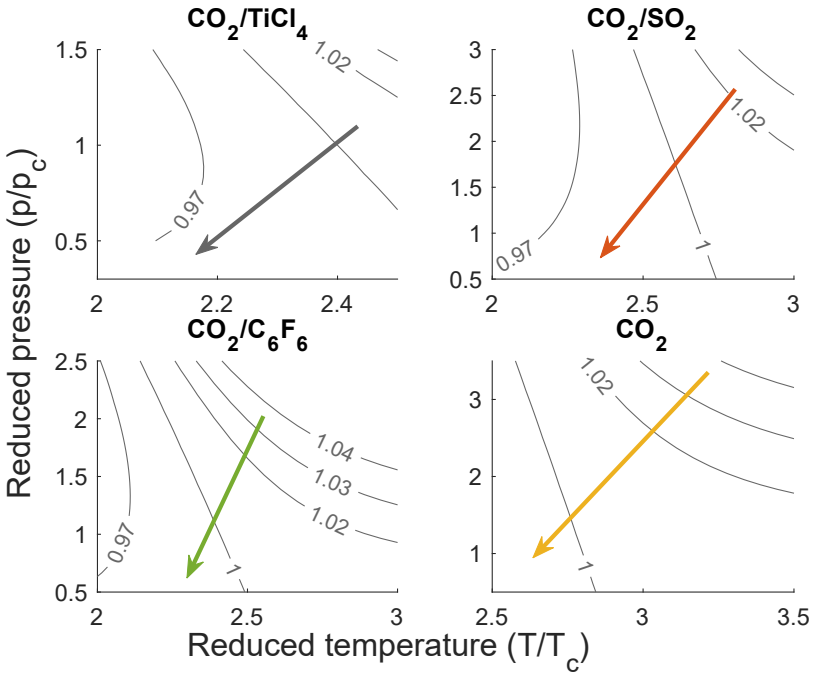

Figure 6.16: Expansion process with respect to compressibility contours for 10 MW Case-B

Second, the loss models presented in Section 5.6, which are summarised in Table 6.1 mainly depend on kinematic and geometric features of the turbine, which are set by the aforementioned design parameters, and not on the thermophysical

Table 6.7: Design data for optimal 10 MW Case-B RIT

Parameter	$CO_2/TiCl_4$	CO_2/SO_2	CO_2/C_6F_6	CO_2
ψ	0.92	0.92	0.92	0.86
ϕ	0.23	0.23	0.23	0.23
ξ	1	1	1	1.04
r_5/r_4	0.6	0.6	0.6	0.59
r_h/r_s	0.67	0.68	0.68	0.67
N_s	0.39	0.38	0.38	0.41
b_4/r_4[%]	8.1	6.8	6.7	6.9
η_{tt}[%]	87.8	87.3	87.5	87.2
η_{ts}[%]	90.1	89.5	89.7	89.6
p_{06}/p_5	2.5	3.39	3.25	3.42
Δh_{tt} [kJ/kg]	103	186	138	212
N [kRPM]	20	30.6	24.2	35.8
α_4 [°]	76	76	76	75.6
β_4 [°]	-20	-20	-20	-31.3
β_5 [°]	-69	-69.1	-69.1	-68.8
U [m/s]	314	421	363	462

properties of the fluid, as explained in Section 6.4.3.

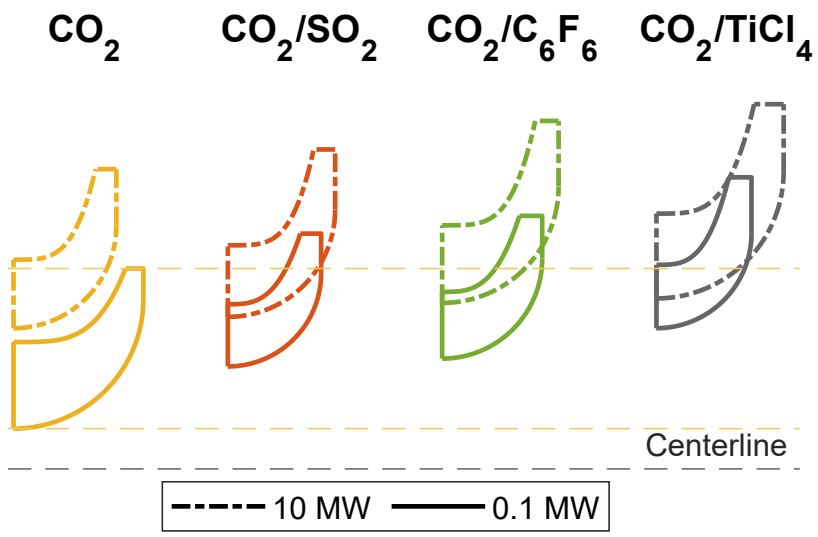

Figure 6.17: Rotor meridional profile. Dimensions of 10 MW turbines have been scaled down

Based on the analysis presented thus far, the differences in turbine performance are attributed to two main aspects: pressure ratio and clearance-to-height ratio. Fluids which operate in cycles with lower pressure ratios are able to achieve higher turbine efficiencies. Moreover, fluids that have turbines with shorter blades are penalised

more by clearance loss. However, as seen in Figure 6.15, kinematic viscosity may contribute to the performance differences of the turbines, although slightly. This may have implications in the context of CO_2-based power cycles, where pressure ratio, turbine blade height, and fluid viscosity are determined by the dopant choice and dopant fraction.

In the following analysis, Case-A designs of 0.1 MW $CO_2/TiCl_4$ and CO_2 turbines are revisited to understand the dissimilarities between the fluids by quantifying the influence of pressure ratio, clearance-to-height ratio, and kinematic viscosity. Five sub-cases are devised with a combination of fixed parameters as marked in Figure 6.18a. To eliminate the effect of viscosity, a fixed viscosity of $4mm^2/s$ was assumed for both fluids in Case-A5.

According to the results in Figure 6.18b, the clearance-to-height ratio is the biggest contributor to the difference in performance, followed by the pressure ratio; however, the clearance-to-height ratio will be less important in larger turbines. On the other hand, a common viscosity reduces the difference by a mere 0.4%. If pressure ratio, clearance-to-height, and viscosity are all assumed equal, then the difference between the efficiency of the two fluids will be 0.1%, mainly due to windage loss differences. A similar analysis at the 10 MW scale yields a difference of 0.05%. Therefore, the uneven performance metrics of the fluids stem from the pressure ratio imposed by the cycle, and by the minimum allowable clearance gap; otherwise, there is no intrinsic aerodynamic advantage of any single mixture over the others.

Doping CO_2 will produce working fluids that are inherently different, despite their ideal gas behaviour in the vicinity of the turbine. Although the thermophysical differences do not manifest in different aerodynamic designs, they affect extensive features of the turbine such as size, thrust, torque, and rotational speed.

For a given power capacity and pressure ratio, the level of specific work possible depends on the fluid. Therefore, the mass flow required by the fluids will differ; and so will the size of their respective turbines. Additionally, doping CO_2 changes its density. In the case of the dopants studied here, which were selected to increase the

Case	p_{04}/p_5	ϵ/b_4
A1		
A2	X	
A3		X
A4	X	X
A5	X	X

(a)

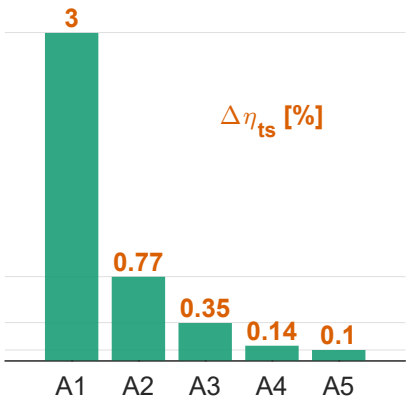

(b)

Figure 6.18: (a) Parameters assumed fixed in each sub-case. (b) Difference in efficiency between $CO_2/TiCl_4$ and CO_2 0.1 MW turbines for each sub-case

critical temperature, the resulting mixtures have densities that are higher than pure CO_2.

What has been shown thus far is that optimisation produces similar turbine designs, in terms of the shape of the rotor and the shape of the velocity diagrams; but the sizes of the turbines will be different, and so will the sizes of their velocity diagrams. For example, owing to its high specific work CO_2/SO_2 turbines have considerably higher tip speeds than the other two mixtures. Likewise, pure CO_2 turbines may have double the rotational speed of $CO_2/TiCl_4$ turbines. Although the consequences on aerodynamic performance is minute, increased rotational speeds entail more demanding mechanical design features including rotordynamics, blade root stresses and hence thickness, disc design as well as material selection and bearing selection requirements. Moreover, axial thrust is expected to be greater in turbines with heavier working fluids such as $CO_2/TiCl_4$ or CO_2/C_6F_6, which may alter the thrust balancing requirements depending on the dopant. Axial force in a radial inflow turbine consists of pressure and momentum forces, which are proportional to the turbine back pressure and mass flow rate. For example, the axial thrust for 10 MW turbines from Case-B is shown in Figure 6.19 which shows that the axial thrust is greater in the $CO_2/TiCl_4$ turbine.

Although this study is focused on the aerodynamic characteristics of radial inflow turbines for CO_2-based mixtures, it would be good to discuss some of the mechanical implications of these designs, most potent of which is the rotational speed. An

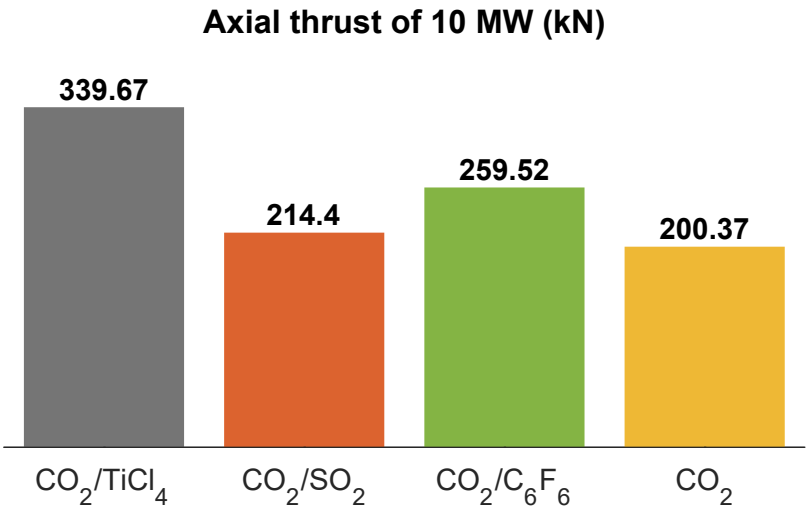

Figure 6.19: Axial thrust for 10 MW

overview of the practical limits of designing CO_2 was presented by Mcclung et al. (2018), in which an empirical chart was used to determine the practical rotational speed limit of a generator for a given power output. According to that study, the rotational speed limits for 0.1 MW, 1 MW, and 10 MW turbines are 151 kRPM, 46.4 kRPM, and 14.3 kRPM, respectively. Compared to these limits, the rotational speeds quoted in Table 6.6 are impractical; for all fluids. The turbines that are the furthest from the practical rotational speed limits are those of CO_2 with rotational speeds about 270% of the speed limit. It is expected that applying the rotational speed limit would penalise the efficiency of all turbines; but to what degree? To answer this question, the optimisation in Case-B is repeated under the aforementioned rotational speed constraints.

Predictably, limiting the rotational speed had a significant influence on the total-to-static efficiency and the specific speeds of the turbines, which are shown in Figure 6.20.

The greatest drop in efficiency is 15% for the 0.1 MW CO_2 turbine; the lowest is 1% for the 10 MW $CO_2/TiCl_4$ turbine. Not only does the efficiency drop, but the differences between the turbine designs of the fluids are exacerbated by the practical speed limit, which is notable in the reduction in the specific speed of all designs. The range of specific speeds reduces from $0.3 < N_s < 0.5$ to about $0.15 < N_s < 0.3$. The restriction of sCO_2 radial inflow turbines to low specific speeds was already noted by

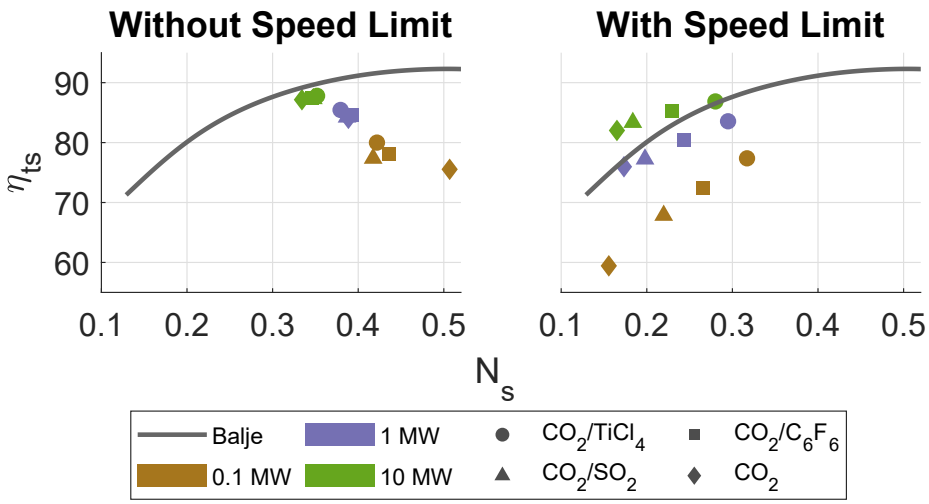

Figure 6.20: Specific speed and efficiency comparison of Case-B with and without a limit of rotational speed

Keep (2018), and it seems that the same applies to CO_2 mixtures; however, higher specific speeds are possible in mixtures owing to the lower specific work imposed by their cycles. To maintain favourable specific speeds, and thus good efficiency, multi-staging will be required; more so for sCO_2 and SO_2 than for $TiCl_4$ and C_6F_6.

Ultimately, the rotational speed limit is yet another practical limit on turbine design which causes the turbine designs of the fluids to diverge. It is expected that the designs will diverge even further as more design limits are imposed (as was seen with the clearance gap and rotational speed).

6.5 Conjugate cycle and turbine optimisation

The analysis presented in Section 6.4.1 through Cases B and C suggests that the pressure ratio affects the achievable total-to-static efficiency of turbines differently, depending on the fluid. As explained previously, a decrease in the pressure ratio is beneficial because of the decrease in the relative flow velocities within the turbine passages, thus lower friction losses and higher efficiency. Simultaneously, because a constant power output must be maintained, then a drop in the pressure ratio, which leads to a drop in the specific work of the turbine, requires an increase in the mass flow rate of the fluid throughout the cycle. Moreover, lower fluid densities are to be expected at lower inlet pressures. Therefore, higher mass flow rates combined

with lower inlet densities result in higher volume flow rates at inlet, which increases the size of the turbine: an effect which is most pertinent in small scale turbines. In Fi ıd vc

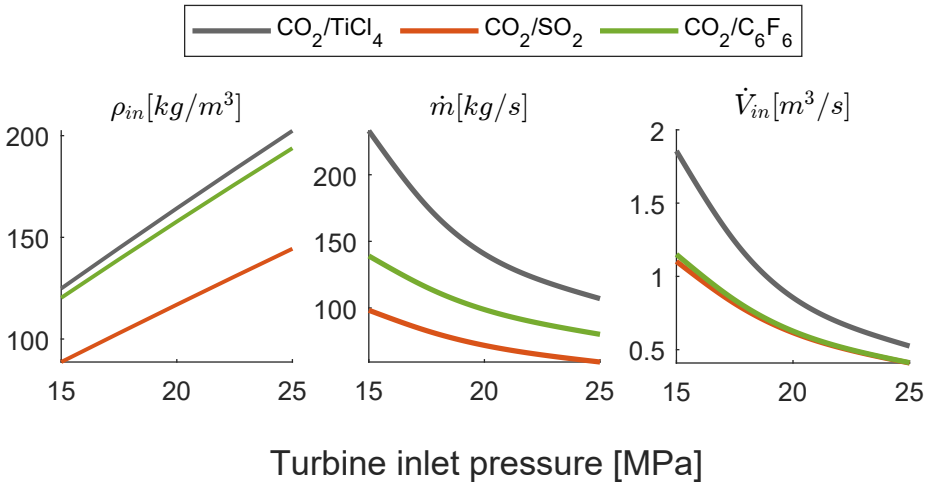

Figure 6.21: Effect of turbine inlet pressure on the density, mass flow, and volume flow rate in a 10 MW turbine

In Figure 6.22, the dependence of the efficiency on the pressure ratio of the fluid is presented. Here, the pressure ratio is increased by increasing the turbine inlet press of sm to th

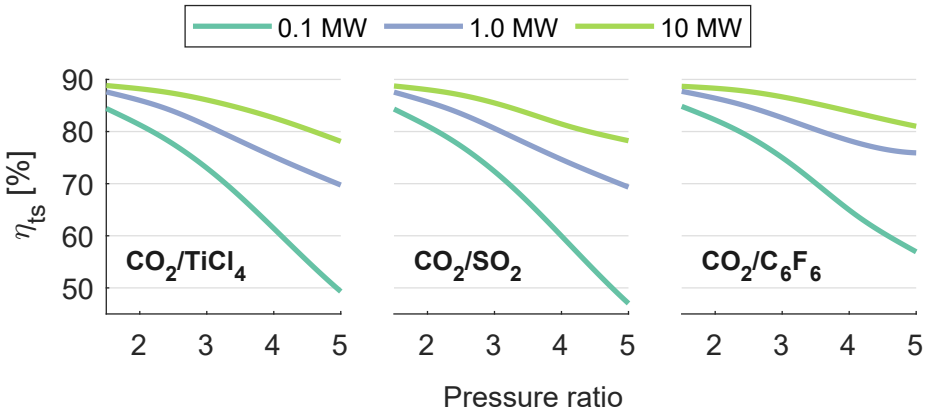

Figure 6.22: Effect of turbine pressure ratio on the total-to-static efficiency of radial inflow turbines

Feher (1968) acknowledged early on the benefit of increasing the pressure ratio to at least 2.0 on the thermal efficiency of a supercritical cycle. He also showed the

expected reduction in thermal efficiency with the reduction in the turbine and pump efficie ect of the tu

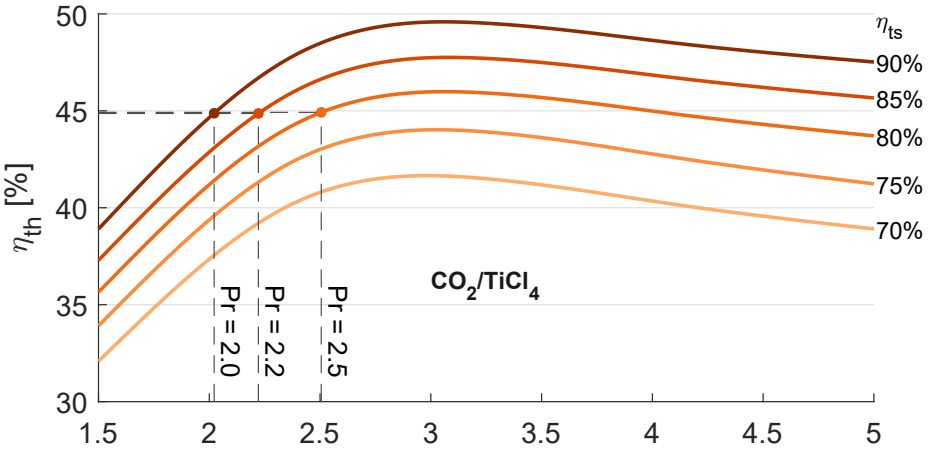

Figure cy of CO_2/T

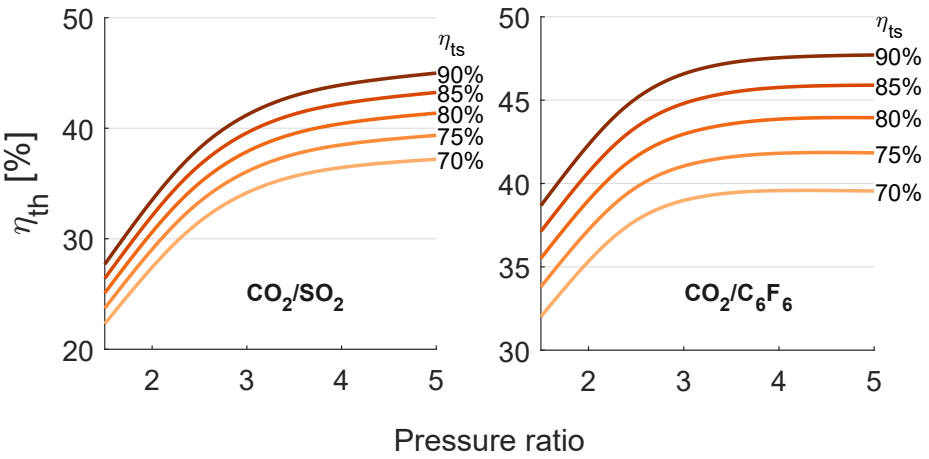

Figure 6.24: Effect of pressure ratio and turbine efficiency on cycle efficiency of CO_2/SO_2 (left) and CO_2/C_6F_6 (right)

What's the importance of this? It shows that improving turbine efficiency enables the same thermal efficiency at lower pressure ratios. An example is indicated in Figure 6.23 whereby a cycle efficiency of 45% for $CO_2/TiCl_4$ mixture may be achieved in multiple ways: at a pressure ratio of 2.0 with a turbine efficiency of 90%, at a pressure ratio of 2.2 with turbine efficiency of 85%, or at a pressure ratio of 2.5 with a turbine efficiency of 80%. Preferably, the lowest pressure ratio that achieves a given efficiency should be chosen, as this maximises turbine efficiency and reduces the cost

of greater pressure containment in piping and equipment.

For all mixtures, the dependency of thermal efficiency on pressure ratio does not change with the turbine efficiency; the same trend is maintained, but with a shift to higher or lower efficiencies depending on the turbine efficiency. However, pressure ratios have an unequal effect on the mixtures. With CO_2/SO_2 , the cycle thermal efficiency continues to increase up to a pressure ratio of 5, although at a diminishing rate. For CO_2/C_6F_6 the thermal efficiency almost plateaus at pressure ratios above 3. On the other hand, the thermal efficiency of $CO_2/TiCl_4$ decreases above a pressure ratio of 3.

The dissimilar trends are explained by the relative change in the net-work w_n from the cycle and the heat input q_h to the cycle. As seen from Figure 6.25, although w_n increases with pressure ratio, it does at a decreasing rate. Similarly, q_n increases at a decreasing rate, but the rate of decrease is lower than that of w_n, which explains the trends exhibited by the cycle thermal efficiency. The trend in w_n is similar for all fluids, but the trend q_h is different; the rate of increase of q_h is much lower in CO_2/SO_2 than in $CO_2/TiCl_4$. The difference in q_h is attributed to the relative

c een

i ted

a red

t

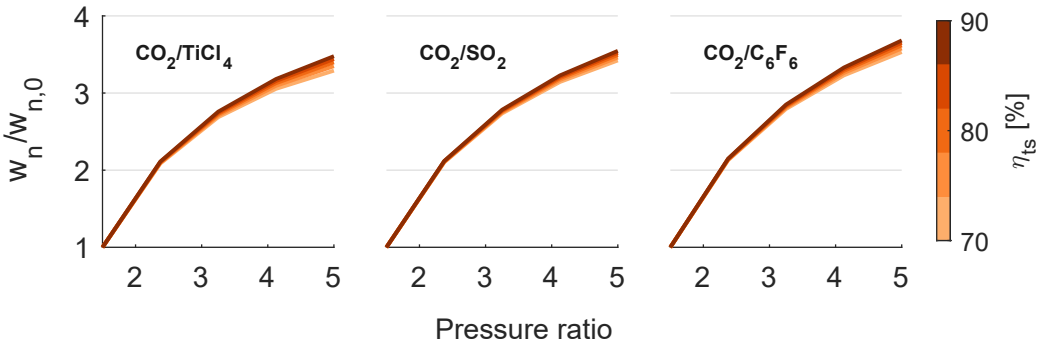

Figure 6.25: Effect of pressure ratio and turbine efficiency on specific net-work. The value of w_n has been normalised by the value corresponding to the value at the lower pressure ratio of 1.5

The dependence of cycle thermal efficiency on the pressure ratio combined with

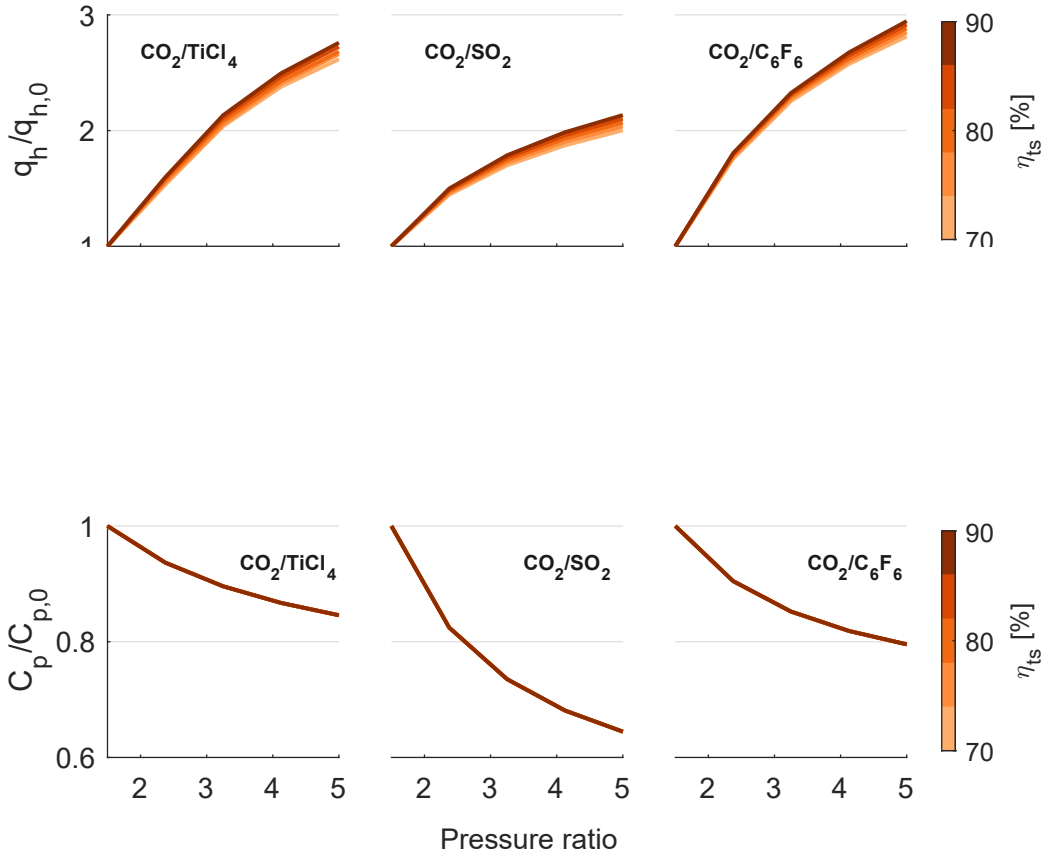

Figure 6.27: Effect of pressure ratio and turbine efficiency on the specific heat capacity at pump outlet. The value of C_{p2} has been normalised by the value corresponding to the value at the lower pressure ratio of 1.5

the dependence of the turbine performance on pressure ratio, indicates that the power scale may influence the optimal cycle pressure ratio. Then, several questions may be formulated: at what pressure ratio is the cycle efficiency maximised whilst considering the dependence of turbine efficiency on pressure ratio and its consequence on cycle efficiency? Does the choice of the pressure ratio depend on the power scale, or on the choice of dopant, or on the dopant molar fraction, or does it depend on a combination of these factors?

In this section, previous work that investigated the trade-off between pressure ratio and turbine efficiency and its consequence on cycle efficiency is first presented. Then, the models presented in the Chapters 3 and 5 are developed into a conjugate cycle-turbine design model. In this manner, the turbine designs are optimized simultaneously with the overall system in order to achieve the best overall cycle performance, thus replacing the conventional approach of using constant turbine isentropic

efficiency values in cycle calculations. With a fixed isentropic turbine efficiency, the power capacity of the power plant and the mass flow rate of the working fluid will not have any affect on cycle thermal efficiency, nor on the choice of the optimal dopant fraction. The aim of the exercise is to determine whether turbine efficiency will advantage certain blend fractions, thus influencing the choice of optimal dopant fraction as was determined with a fixed turbine efficiency.

Romei et al. (2019) emphasised the importance of using variable turbomachinery efficiencies when modelling a recompression sCO_2 cycle rather than assuming constant efficiencies. Different trends in the relation between cycle efficiency and parameters such as the pressure ratio or turbine inlet temperature are produced when the achievable turbomachinery performance is considered. Therefore, a proper modelling of turbomachinery is crucial to get reliable sCO_2 cycle optimisation, where failing to do so produced up to 4% efficiency difference in the worst-case scenario. They also quantified the benefits of using multi-stage turbomachinery, which may increase cycle efficiency by up to 1.8%. Additionally, a correlation for estimating the efficiency of centrifugal compressors and radial turbines based on the size parameter and pressure ratio was presented.

The importance of turbomachinery performance prediction was further investigated by Alfani et al. (2022) through a techno-economic study of a recompression cycle with intercooling in a CSP plant. The two main indicators used were the specific cost ($/kW) and solar-to-electricity efficiency of the plant. Two cases were compared: (1) with constant turbomachinery efficiency, and (2) with variable turbomachinery efficiency estimated using the correlation presented by Romei et al. (2019). The reduction of the turbomachinery efficiency led to a decrease in the solar-to-electricity efficiency from 23.8% to 22.3% (-6.3%) and an increase of the specific cost from 6629.3 to 7145.6 $/kW (+7.8%) for the optimal case (minimum plant specific cost).

Song et al. (2020) coupled transcritical (tCO_2) cycle calculations with a model for the preliminary design of radial-inflow turbines. Results indicate that the use of a constant turbine efficiency can lead to a significant underestimation or overestimation of the system thermo-economic performance and to sub-optimal operating conditions.

At its highest, the difference between the two approaches was 14% and 22% for thermodynamic and economic performance, respectively.

By simulating a recompression cycle fitted with a radial inflow turbine, Zhou, song Li, dong Ren, Song & wei Gu (2020) calculated the uncertainty in assuming a constant turbine efficiency of 87% compared to an efficiency estimated using a preliminary turbine design. The cycle was simulated for a range of conditions: turbine inlet temperature (600-975 K) and pressure (18-25 MPa); compressor inlet temperature (305-325 K) and pressure (7.5-9.0 MPa); and split ratio (0.65-0.90). Most parameters resulted in turbine efficiencies within 0.4% of 87%, thus had little effect on cycle efficiency; except for the turbine inlet temperature which resulted in a 1.5% change in turbine efficiency and a consequent 0.23% change in cycle efficiency.

Another effort to integrate cycle and radial inflow turbine designs was made by Saeed & Kim (2018). By simulating a recompression cycle with a fixed turbine efficiency of 90% and comparing it with that estimated using a 1D model, they concluded that the difference in cycle efficiency could be as high as 4%. This difference was based on simulations of a range of main compressor inlet temperatures from 305 to 350 K, where the highest difference was 4% and an almost zero difference at a compressor inlet temperature of 317 K. Although they did not explain this trend, it is likely because of the change in the working fluid mass flow rate in response to the increase in compression work, and the change in turbine performance in response to that. In their treatment of the turbine design, they illustrated the trends in turbine performance, power output, and losses such as passage exit and clearance, for a range of design parameters that include the velocity ratio (ν_0) and the hub- and shroud-to-inlet radius ratio. Regrettably, they only described the trends without discussing their causes.

6.5.1 Model description

An algorithm for the concurrent optimisation of the cycle and the turbine chiefly relies on the cycle and radial inflow turbine optimisation algorithms presented in Chapters 3 and 5, respectively. Here, the two algorithms are coupled into an iterative

loop whereby an updated estimate of the total-to-static efficiency based on the mean-line design is used to update the cycle design. This process is repeated until the turbine efficiency converges to a solution, thus so does the cycle thermal efficiency. The objective function is the overall thermal efficiency of the cycle; therefore, the algorithm may converge on non-optimal turbine designs as long as the overall cycle efficiency is maximised.

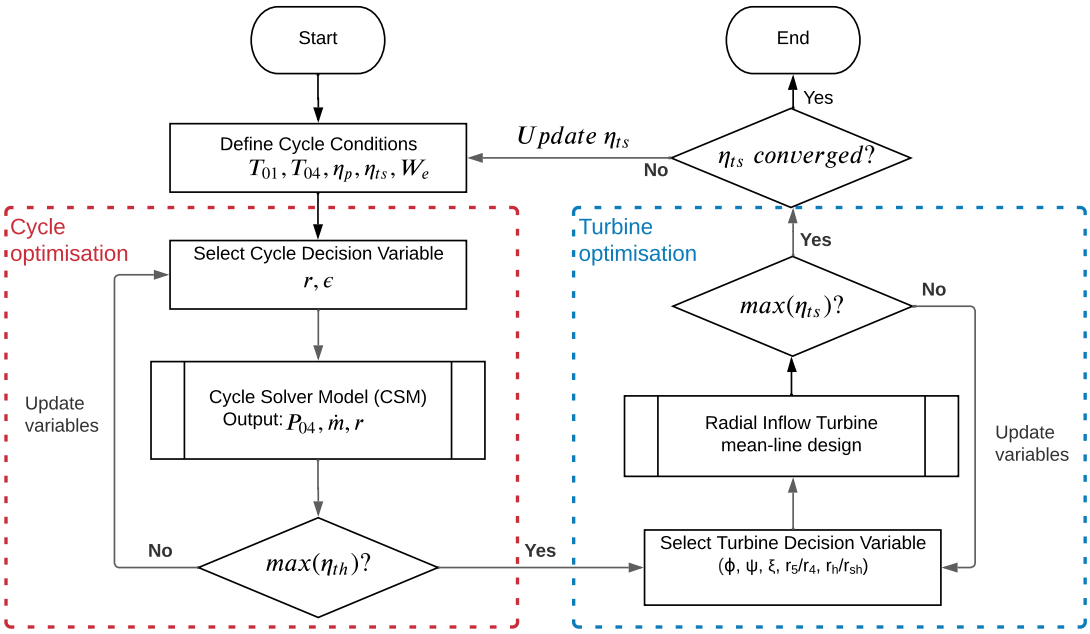

Figure 6.28: Combined cycle and turbine optimisation algorithm

6.5.2 Discussion of results

A conjugate optimisation was conducted for the three mixtures with the optimal dopant fractions used thus far. The cycle optimisation conditions are similar to those used in Chapter 4, which are repeated here in Table 6.8; however, the turbine efficiency is not set to a fixed value, instead it is estimated using the 1D mean line model.

Before analysing the results of the conjugate optimisation, one may predict the effect of considering a turbine efficiency based on preliminary turbine designs. Since cycle optimisation will naturally favour higher pressure ratios, whilst turbine optimisation prefers the opposite, then a conjugate optimisation may either converge on a

Table 6.8: Inputs required for cycle solution

Controlled Parameters		
Parameter	**Range**	**Unit**
Turbine Inlet Temperature (T_4)	700	°C
Pump Inlet Temperature (T_1)	50	°C
Pump Isentropic Efficiency(η_p)	85	%
Generator Efficiency(η_g)	99	%
Minimum internal temperature approach (MITA)	5	°C
$\Delta p/p$ of Primary Heat Exchanger	0.015	-
$\Delta p/p$ of Recuperator High- and Low-pressure sides	0.01 and 0.015	-
$\Delta p/p$ of Condenser	0.02	-
Dependant Parameters		
Pump Inlet Pressure(P_1)	$P_{sat@(T_1+2)}$	MPa
Turbine Inlet Pressure(P_4)	Max (25)	MPa
Optimised Parameters		
Pressure Ratio (r)	1.5 to 5	-
Recuperator Effectiveness(ϵ)	80 to 98	%

smaller pressure ratio to maintain favourable turbine efficiencies, or, in case the turbine efficiency is not penalised enough, maintain the highest possible inlet pressure of 25 MPa.

A parametric analysis is first conducted to compare the modified cycle efficiency for a range of pressure ratios, the results of which are presented in Figures 6.29 through 6.31. For reference, a curve has been superimposed to represent the calculated cycle thermal efficiency assuming a turbine total-to-static efficiency of 85%. For all the working fluids, the pressure ratio at which cycle efficiency is maximised is lower than that of the constant turbine efficiency line, as previously hypothesised.

These results are telling of the differences between the mixtures and the power scales. Compared to CO_2/SO_2, the efficiency of $CO_2/TiCl_4$ and CO_2/C_6F_6 starts to drop, or in the case of 10 MW CO_2/C_6F_6 turbines plateau, at lower pressure ratios of between 2.0 to 2.5; whereas for CO_2/SO_2 thermal efficiency starts to drop/plateau between 2.5 and 3.0. The optimal pressure ratio is the same regardless of the power scale because the difference in the deterioration in turbine efficiency amongst the

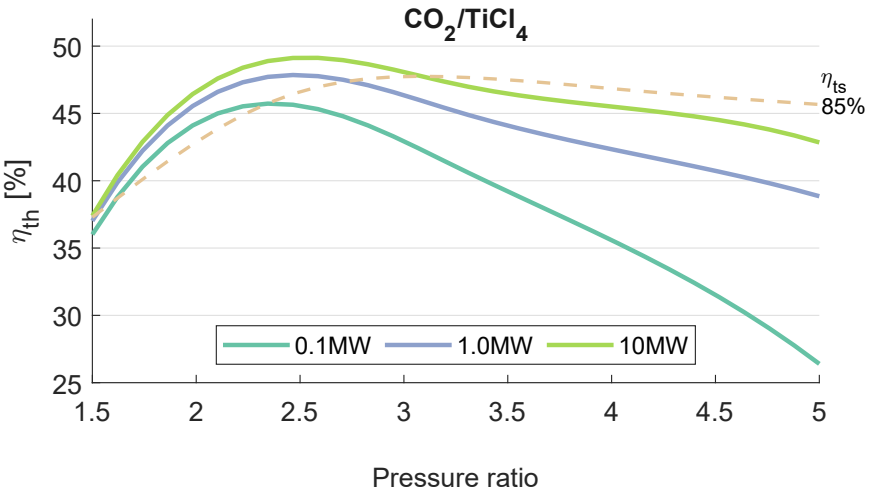

Figure 6 ... across power sc

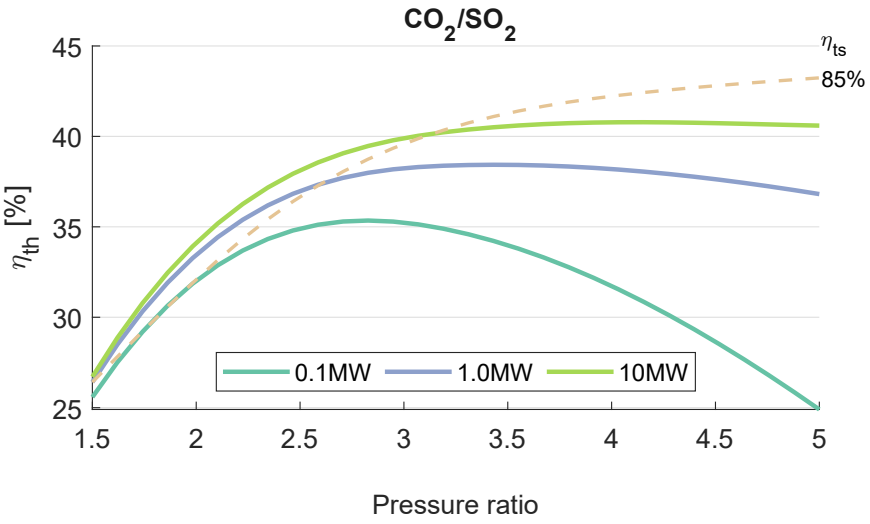

Figure 6.30: Cycle thermal efficiency based on achievable turbine efficiencies across power scales for CO_2/SO_2

power scales is not significant enough to shift the optimal cycle pressure ratio with scale. This trend was hinted at in Figures 6.23 and 6.24 which show the degradation of thermal efficiency in $CO_2/TiCl_4$ cycles at higher pressure ratios; the plateau in cycles of CO_2/C_6F_6; and the continual increase of efficiency in CO_2/SO_2 cycles, even at higher pressure ratios. Accounting for the achievable turbine efficiency accentuates these trends; especially in smaller turbines.

As explained previously, small scale turbines are penalised the most by an increase in the turbine inlet pressure and pressure ratio. This is also evident in Figures 6.29 through 6.31 since the deterioration in cycle efficiency is most significant in small

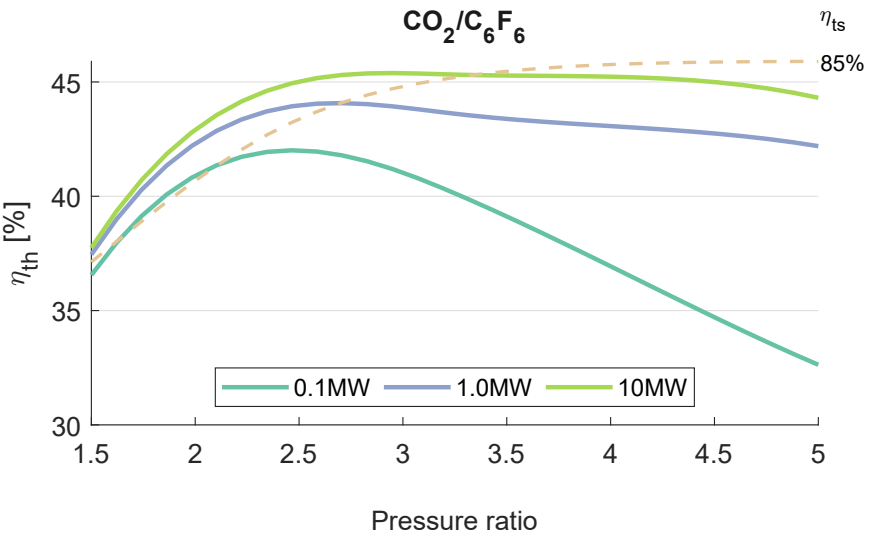

Figure 6.31: Cycle thermal efficiency based on achievable turbine efficiencies across power scales for CO_2/C_6F_6

scale power plants. However, $CO_2/TiCl_4$ will still have higher thermal efficiencies than CO_2/C_6F_6 and CO_2/SO_2, and CO_2/C_6F_6 higher than CO_2/SO_2, regardless of the pressure ratio or power scale. This is because of two reasons. The first is that the differences in cycle efficiency are chiefly due to the irreversibility of the recuperation process. As already explained in Chapter 4, the recuperation in simple transcritical cycles of $CO_2/TiCl_4$ is the least irreversible, followed by CO_2/C_6F_6 , and then CO_2/SO_2. The second reason is that the differences in turbine efficiencies between the mixtures are small. Therefore, unless the differences in turbine efficiency are great enough to negate the advantage of lower recuperator irreversibility, the relative difference in cycle efficiencies will persist.

How great should the differences in turbine efficiency be to yield a noticeable difference in cycle efficiency? As an example, at a pressure ratio of 2.3, which is favourable to both $CO_2/TiCl_4$ and CO_2/C_6F_6, the total-to-static efficiency of the $CO_2/TiCl_4$ turbine would have to be 70% compared to 88% of CO_2/C_6F_6 for the latter to have a higher cycle thermal efficiency; a 18% difference in turbine efficiency.

As previously demonstrated in Section 6.4, the differences between the mixtures of different dopants grow greater at smaller scale; therefore, it is expected that the differences between mixtures of the same dopant will also grow greater at smaller scale. Indeed, according to Figure 6.32, the difference between mixtures of the same

dopant but with different molar fractions grows greater as the turbine size decreases. The change in the total-to-static efficiency with dopant fraction of 10 MW turbines is much smaller than that of 0.1 MW and grows greater at higher pressure ratios. This happens because, mainly, increasing the dopant fraction reduces the specific work of the turbine, thus increases the mass flow rate to maintain the same power capacity. This is true for the dopants studied here but other dopants may reduce the specific work and have the opposite effect.

Moreover, as explained previously, the turbine back pressure is determined by the saturation pressure of the working fluid at 52°C, therefore working fluids with lower back pressures will have lower inlet pressure for a given pressure ratio. With all dopants, increasing their molar fraction decreases the turbine back pressure; see Figure 4.4 in Chapter 4. The increase in mass flow rate and reduction in inlet pressure lead to an increase in the volume flow rate, which benefits small turbines more than large turbines, as stated previously.

It is that for that same reason that the effect of the dopant fraction is not the same among the three mixtures. The addition of more SO_2 has little effect on η_{ts}

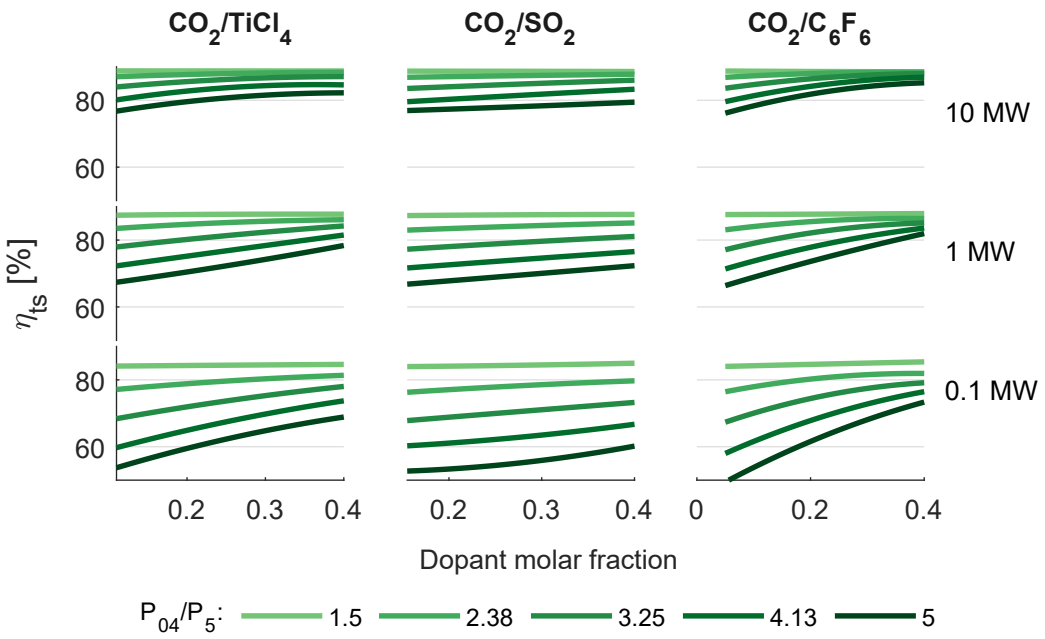

Figure 6.32: Total-to-static efficiency of a combination of mixtures, power scales, and pressures ratios for a range of dopant fractions

In Chapter 4, the dopant fraction was chosen to maximise cycle efficiency. According, to Figures 6.33, the choice of the optimal molar fractions will remain the same across power scales, further reaffirming that the dopant molar fraction is predominantly determined by the recuperator irreversibility. Only at medium-scale power plants of 10 MW are turbine efficiencies close to 85% achievable by mix-

t

b

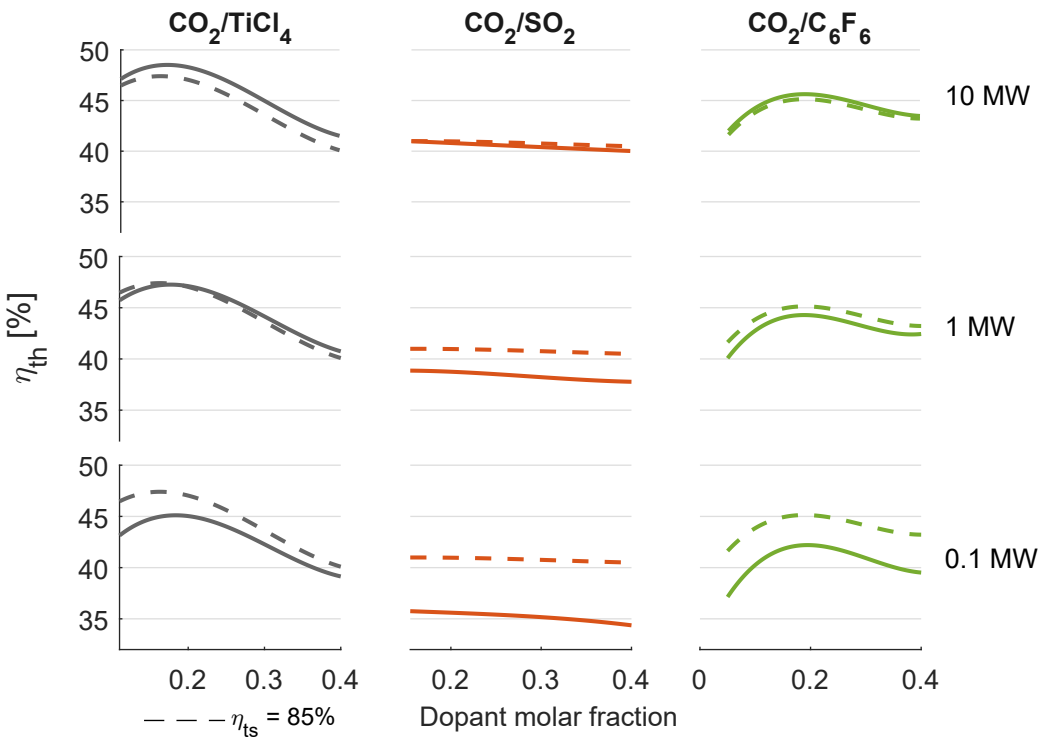

Figure 6.33: Cycle thermal efficiency for a range of dopant fractions based on turbine efficiency estimated by 1D model (solid lines) and constant turbine efficiency (dashed lines)

It seems that the turbine efficiency is dependent on the dopant molar fraction, with the highest turbine efficiencies being achieved by the highest fraction of $TiCl_4$, the lowest fraction of SO_2, and a medium fraction of C_6F_6. These trends may be explained by referring to Figures 6.29 to 6.31 in which the efficiency of $CO_2/TiCl_4$ cycles decreases at higher pressure ratios, CO_2/SO_2 cycles show an increase in the efficiency even at high pressure ratios, and CO_2/C_6F_6 show a diminishing benefit with the increase in pressure ratio.

Indeed, in Figure 6.34 a moderate pressure ratio is maintained in $CO_2/TiCl_4$

mixtures, which, when combined with the decrease in turbine inlet pressure, allows for higher turbine efficiencies at higher dopant fractions. On the other hand, the turbine inlet pressure is maximised with CO_2/SO_2 mixtures to maintain a favourable cycle efficiency at the cost of lower turbine efficiency; however, the inlet pressure is reduced in the small-scale plant 0.1 MW as the degradation in turbine efficiency is signi
effici
dopa
max

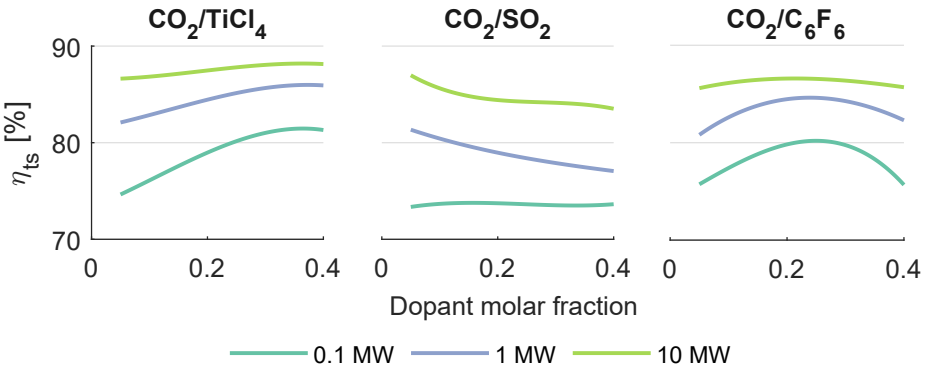

Figure 6.34: Turbine total-to-static efficiency for a range of dopant fractions as estimated by the 1D model for the cycle conditions that yield maximum thermal efficiency

6.6 Summary

In this chapter, the designs of small- to medium-scale radial inflow turbines under multiple design assumptions were analysed with the aim of discerning the effects of doping CO_2. Results indicate that the aerodynamic behaviour of the working fluids is similar. Therefore, turbine designs for all working fluids converge on similar rotor shapes and velocity diagrams. However, not all turbines achieve the same efficiency.

Among the mixtures studied, $CO_2/TiCl_4$ achieved the highest performance, followed by CO_2/C_6F_6, and then CO_2/SO_2. For example, 100 kW turbines for $CO_2/TiCl_4$, CO_2/C_6F_6, CO_2/SO_2, and CO_2 achieve total-to-static efficiencies of 80.0%, 77.4%, 78.1%, and 75.5% respectively. Whereas, the efficiencies for 10 MW turbines are 87.8%, 87.3%, 87.5%, and 87.2%, in the same order.

Variations in the achievable efficiency amongst the fluids stem from variations in their clearance-to-blade height ratio, their pressure ratios, rotational speed limits, and, to a lesser degree, differences in their viscosity.

In conclusion, apart from viscosity, the fluid mechanics of the fluid are not expected to change. Even the change in viscosity is not expected to change the flow features of the fluid within the turbine, assuming similar velocity triangles and rotor shape. Ultimately, although doping CO_2 has little effect on the aerodynamic performance of the turbine, it is the consequence of the change in cycle conditions along with the design limitations of radial inflow turbines that lead to differences in the performance of the turbines amongst the fluids.

The differences in performance amongst the fluids are greatest in small scale turbines; with fluids that produce turbines of greater blade heights having the highest efficiency. The effect of clearance loss is attenuated with design optimisation by allowing greater flow coefficients, which increase velocities and reduce tip clearance loss. Consequently, the specific speed of the turbines increases at smaller power scales.

The study reveals that loss models are not sensitive to the working fluid. Moreover, the influence of geometric and kinematic parameters changes with power scale. Multi-staging of CO_2, CO_2/SO_2, and CO_2/C_6F_6 turbines is more beneficial than for $CO_2/TiCl_4$ because of the high pressure ratio cycle within which they operate. Additionally, the size of the rotor and the magnitude of the velocities depends on the working fluid, which may entail different mechanical requirements, such as bearing selection and rotordynamics.

Based on the parametric analysis studying the effect of pressure ratio and turbine efficiency on the thermal efficiency of a simple recuperated transcritical cycle, differences between the mixtures are to be expected. Indeed, it was shown through the conjugate optimisation of the cycle turbine designs that the turbine efficiency plays a greater role in determining the optimal pressure ratio in small-scale power plants. However, the optimal dopant fraction is not expected to change, regardless of the turbine efficiency.

It is recommended that future work builds on the findings of this chapter by completing a comprehensive mechanical design of the turbines, including bearing selection, rotordynamics, and structural analysis, to ascertain the consequences of doping CO_2 on the full design of the turbine.

Chapter 7

Sensitivity of CO_2 mixture modelling to fluid properties calculations

7.1 Introduction

In this chapter, the effects of the choice of the fluid model parameters, namely the equation of state (EoS) and the binary interaction parameter (k_{ij}), are studied. The analysis presented here aims to highlight the uncertainty associated with the modelling of CO_2 mixtures using equations of state, and to quantify the effect of the uncertainty on the consistency of cycle and turbine modelling efforts.

7.2 Overview

Regardless of the working fluid, cycle performance prediction and equipment sizing are affected by the equation of state that is used to describe the thermophysical properties of the fluid. Specifically, the thermodynamic properties determine both the cycle thermal efficiency and equipment sizing, while the transport properties affect equipment sizing. Note that the choice of the fluid model does not alter the physical behavior of the fluid or the cycle, but only effects our ability to model their

behavior. The influence of the fluid model on the estimated cycle performance and equipment sizing has been investigated in the past, a summary of which is presented in Table 7.1 and discussed here.

Most literature that is concerned with the effect of the uncertainty in modelling CO_2 can be categorised based on whether or not they considered CO_2 mixtures, confined the study to the prediction of thermophysical properites or expanded it to the effect on cycle modelling, and if they considered the uncertainty in k_{ij}. This categorisation was used to label sources listed in Table 7.1.

Table 7.1: Literature review of working fluids and thermodynamic references used for CO_2 power cycle analysis

Author and Year	Dopants	EoS	Type of study
Manikantachari et al. (2017)	CO_2/CH_4/O_2/CO /C_2H_6/H_2O/H_2	PR (Peng-Robinson), SRK (Soave-Redlich-Kwong), Ideal gas, NIST data	Properties
Bertini et al. (2021)	CO_2/R1234yf, CO_2/R1234ze(E), CO_2/n-butane, CO_2/n-hexane, CO_2/n-pentane, CO_2/propane	PR, PR-Twu (PR modified by Twu), LKP (Lee-Kesler-Plocker), Coolprop	Properties and cycle modelling
White & Weiland (2018)	CO_2/H_2O	PR-BM (Peng-Robinson modified by Boston-Mathias), SRK, BWRS (Benedict-Webb-Rubin modified by Starling and Nishiumi), LKP, PC-SAFT (Perturbed Chain Statistical Associating Fluid Theory)	Properties and cycle modelling
Zhao et al. (2017)	CO_2	PR, PR-BM, SRK, LKP, BWRS, SW (Span-Wagner)	Properties and cycle modelling
Marcoberardino et al. (2022)	CO_2/C_6F_6	PR, PR-BM, SRK, LKP, BWRS	Properties, cycle modelling, and effect of Δk_{ij}

Zhao et al. (2017) conducted a selection procedure which compared six EoS to identify the best option for the modelling of a pure CO_2 working fluid in a recompression cycle. It was concluded that the Span-Wagner (SW) EoS provided the most accurate predictions of pure CO_2 properties in the near-critical and supercritical regions. The Mean Absolute Percentage Error (MAPE) in the constant-pressure specific heat in the supercritical region calculated using the SW EoS was 0.5% compared to

experimental data. Other EoS resulted in MAPE values of about 2% in the calculated constant-pressure specific heat values near the supercritical region; however, they did not mention the uncertainty in the measured quantities. At most the variation in thermal efficiency was within 2% depending on the EoS. In terms of equipment sizing, they noted that a deviation of 10% in recuperator size (indicated by the product of the overall heat transfer coefficient and heat exchange area) and compressor diameter is possible depending on the choice of EoS. The variation in the compressor size was attributed to its operation near the critical point where evaluation of the constant-pressure specific heat capacity by an EoS is not precise. Conversely, the influence on turbine diameter was found to be more limited (from 0.2% to 3.0%), which is expected since equations of state converge on to the ideal gas law at high temperatures above the critical dense-gas region.

The study of mixtures adds another uncertainty in thermodynamic property predictions because of the use of the Binary Interaction Parameter (BIP or k_{ij}), which is a correction factor applied to an EoS to account for intermolecular interactions between mixture components, as described in Section 3.2.1. A value for k_{ij} may be obtained by regressions based on experimental Vapor-Liquid Equilibrium (VLE) data, where k_{ij} is calibrated to fit the EoS predictions with empirical results. It is also possible to predict the value of k_{ij} using models such as the Predictive Peng-Robinson or the Enhanced Predictive Peng-Robinson-78 equation of state (Lasala et al. 2020). However, predictive models will not be used in this study since experimental data are available for all the mixtures involved.

The effect of the fluid model on CO_2 mixtures has also been previously studied. Marcoberardino et al. (2022) compared the cycle performance of a CO_2/C_6F_6 mixture using five equations of state. The parameters that were compared include the specific enthalpy at stations within the cycle, gross specific work, and the cycle thermal efficiency. The choice of EoS resulted in an inconsistent cycle thermal efficiency which ranged from 40.5% to 42.5%. They also noted that the choice of the EoS slightly effects the identification of the optimal dopant molar fraction. In the same study, they varied k_{ij} by $\pm 50\%$ and found that it had a limited effect on the cycle efficiency ($\pm 0.2\%$). However, they did not study the effect of k_{ij} on equipment sizing,

nor did they investigate its influence on mixtures other than CO_2/C_6F_6.

Bertini et al. (2021) studied the effect of the choice of the EoS on cycle modelling for six CO_2-mixtures and five EoS. They concluded that the EoS vary in accuracy depending on the thermophysical region it is applied to (liquid or gas), on the mixture, and the molar fraction of the dopant. For example, the PR was most accurate for CO_2-pentane with dopant fractions above 0.3, while the modified PR is more suitable for molar fractions below 0.3. Therefore, the choice of the EoS may have to be tailored accordingly. Moreover, EoS were more consistent at low dopant molar fractions.

In their study of CO_2/H_2O direct-fired sCO_2 cycles, White & Weiland (2018) compared the relative differences between the SW EoS used in REFPROP and six other EoS in 12 key performance variables. The difference in these variables depended on the EoS used; for example, there was a significant change in the pumping power requirements when SRK was used, but not when LKP was used, indicating that the latter was better suited for the calculation of liquid phase properties. However, in all of the six EoS, the highest change was in the recuperator minimum internal approach temperature.

Previous studies have indicated that thermodynamic property prediction is most consistent near the turbine operating conditions (Zhao et al. 2017, Marcoberardino et al. 2022). Therefore, it follows that the turbine should be the component least affected by the fluid model, which is to be expected. However, it has not yet been shown to what extent any small variation will impact the final turbine geometry or performance predictions. Answering this question will help design efforts by guiding the most suitable choice for the EoS to be used during the mean-line design and numerical CFD simulations of the turbine; a critical component of the cycle.

The aim of the current chapter, Chapter 7, is to present an investigation of the sensitivity of key cycle and turbine design parameters to the choice of EoS and k_{ij} uncertainty within a simple recuperated transcritical cycle layout using CO_2-based mixtures as working fluids. Ultimately, the aim is to quantify the effect of EoS and k_{ij} on turbine design. For the most part, the results pertaining to the cycle parameters

do not depend on the power capacity; however, a power capacity is specified before investigating the turbine mean line design. Based on the selection criteria presented in Section 3.2.1, the chosen dopants are: H_2S, SO_2, and C_6F_6. The range of dopant fractions studied in this chapter is set based on the minimum composition for which the critical temperature is greater than 343 K, and is limited to 0.65. The main dopant thermophysical parameters of interest are shown in Table 7.2.

Table 7.2: Select properties of CO_2 and dopants

Compound	**Molar Mass [g/mol]**	T_C **[K]**	P_C **[MPa]**	**Dopant fraction**
$\mathbf{CO_2}$	44.01	304.2	7.382	
$\mathbf{H_2S}$	34.08	100.4	8.963	0.55-0.65
$\mathbf{SO_2}$	64.07	430.4	7.884	0.2-0.65
$\mathbf{C_6F_6}$	186.1	516.7	3.273	0.1-0.65

The four candidate EoS that were selected for the study are shown in Table 7.3. The EoS were chosen so as to cover three different types: Cubic, Virial, and SAFT. Among these, the cubic types are the most popular owing to their accuracy in the estimation of VLE properties for most fluids. They also require little computational overhead because of their simplicity. However, the accuracy of cubic EoS are limited with highly polar compounds. Although they have the ability to describe mixtures accurately, the application of Virial type EoS is limited to low and moderate density fluids. SAFT equations of state are known to produce accurate property estimations away from the critical point and are suitable for systems in which the strength of association varies from weak hydrogen bonds to strong covalent bonds. However, their accuracy comes at a high computational cost.

Table 7.3: Equations of State used to model the mixtures

Equation of State	**Type**	**Reference**
Peng-Robinson (PR)	Cubic	(Peng & Robinson 1979)
Benedict-Webb-Rubbin modified Starling-Nishiumi (BWRS)	Virial	(Nishiumi & Saito 1975)
Soave-Redlich-Kwong (SRK)	Cubic	(Soave 1972*b*)
Peturbed Chain Statistical Associating Fluid Theory (PC-SAFT)	SAFT	(Gross & Sadowski 2001)

The cubic EoS requires the definition of the following fluid-specific parameters:

acentric factor, critical temperature, and critical pressure. In addition to the parameters required to solve a cubic EoS, the PC-SAFT model requires the following parameters for each pure component of the mixture: (i) the characteristic segment number m, (ii) the characteristic segment size parameter σ, and (iii) the characteristic segment energy parameter ϵ/k. These parameters are listed in Table 7.4.

Table 7.4: Select properties of CO_2 and dopants

Compound	m	σ	ϵ/k	**Reference**
$\mathbf{CO_2}$	1.846	2.984	140	Simulis preset
$\mathbf{H_2S}$	1.669	3.035	229	(Yazdi et al. 2020)
$\mathbf{SO_2}$	2.861	2.683	205	(Diamantonis et al. 2013)
$\mathbf{C_6F_6}$	3.779	3.396	221.65	(Marcoberardino et al. 2022)

The mean absolute percentage error (MAPE) is used to measure the accuracy of the thermodynamic model by comparing the calculated properties with experimental properties available from the literature. The lower it is, the more accurate the model. Therefore, it is used here to compare the results from the range of EoS and k_{ij} options to determine their suitability for each of the mixtures. The MAPE is calculated as follows:

$$\mathrm{MAPE} = \frac{100\%}{n_{\mathrm{e}}} \sum_{\mathrm{i}=1}^{n_{\mathrm{e}}} \left| \frac{\widetilde{U}_{\mathrm{i}} - \hat{U}_{\mathrm{i}}}{\widetilde{U}_{\mathrm{i}}} \right| \tag{7.1}$$

where U corresponds to either the temperature or pressure, n_{e} is the number of data points, and the accents ($\wedge$) and ($\sim$) indicate experimental and calculated properties. Table 7.5 presents the values of k_{ij} for each EoS and mixture combination, and includes the MAPE associated with each combination. Based on the MAPE values presented in Table 7.5, the two cubic equations of state (PR and SRK) are more suitable than the virial equation of state (BWRS) for all mixtures, whilst PC-SAFT is most accurate for CO_2/H_2S and CO_2/C_6F_6.

The suitability of the EoS depends on the mixture. Among the three mixtures, CO_2/H_2S has the lowest MAPE in property estimation for all equations of state. Moreover, BWRS is more suitable for CO_2/SO_2 than for CO_2/C_6F_6 , whereas the opposite is true of the suitability of PC-SAFT.

Table 7.5: Binary interaction coefficient and its associated MAPE for each CO_2-based mixture and EoS combination

Binary Interaction Parameter (k_{ij})				
	PR	**BWRS**	**SRK**	**PC-SAFT**
CO_2/H_2S	0.0871	0.0453	0.0871	-0.0393
CO_2/SO_2	0.0214	0.0182	0.0249	-0.0939
CO_2/C_6F_6	0.0332	0.0626	0.0394	-0.0571
Density Mean Absolute Percentage Error (MAPE%)				
	PR	**BWRS**	**SRK**	**PC-SAFT**
CO_2/H_2S	0.3862	0.4901	0.4025	0.275
CO_2/SO_2	2.089	1.938	2.068	4.722
CO_2/C_6F_6	2.619	5.028	2.374	2.227
	No. data points		**Reference**	
CO_2/H_2S	122		(Bierlein & Kay 1953)	
CO_2/SO_2	48		(Coquelet et al. 2014)	
CO_2/C_6F_6	64		(Dias et al. 2006)	

On the other hand the fidelity in k_{ij} depends on on a few factors such as the number of data, the range of blend fractions covered, the experimental uncertainty, and the fitness of the EoS for the mixture. As an example, a MonteCarlo simulation was conducted with 1000 trials to determine the value of k_{ij} and its Δk_{ij} based on four sets of experimental data. These data sets originate from a single source, however, some of the sets were intentionally altered to show the effect of the experimental data quality on k_{ij} and Δk_{ij}. A summary of the alterations is listed in Table 7.6.

Table 7.6: Description of alterations made on the CO_2/SO_2 VLE data sets from Coquelet et al. (2014)

Data Set	Alteration
Set-1	None
Set-2	The uncertainty in the measurements is doubled
Set-3	Only half of the data is considered
Set-4	Only one isotherm is considered

The resulting Δk_{ij} uncertainty is indicated by the probability distribution in Figure 7.1, where k_{ij} has been normalised based on the mean value of the original data

(Set-1). The quality of the experimental data affects both the mean k_{ij} and its uncertainty Δk_{ij}. Doubling the uncertainty in the measured quantities, as in Set-2, increases Δk_{ij} from 5% to around 18%, increases the probability of higher values of Δk_{ij}, thus creating a non-symmetric distribution. Halving the amount of data points, as in Set-3, also increases Δk_{ij}; an even greater increase in Δk_{ij} is to be expected if the amount of data points is reduced further. The data from Coquelet et al. (2014) is based on two isotherms (263 K and 333 K). Excluding one of the isotherms, as in

depend on

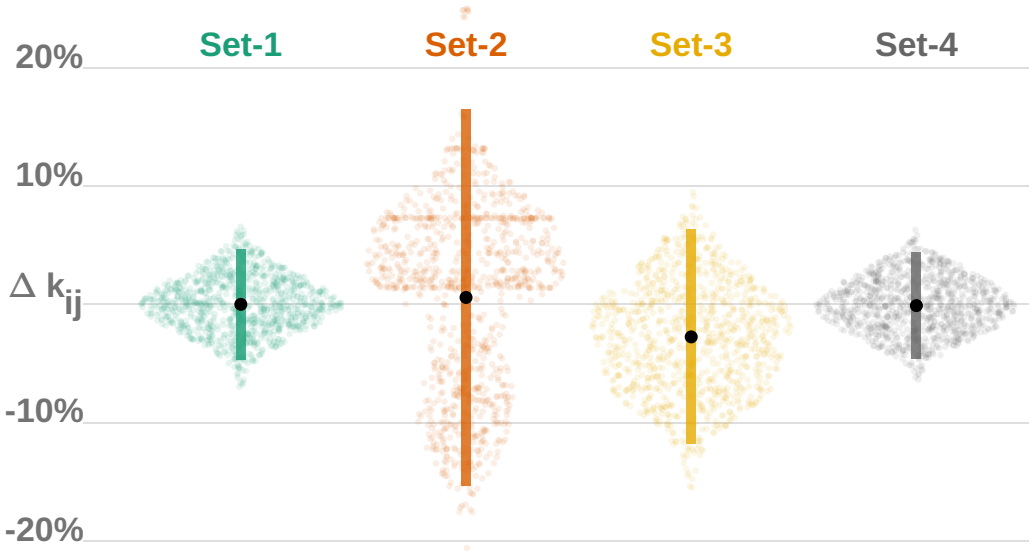

Figure 7.1: Monte-Carlo results showing the distribution of k_{ij} for the sets of data. Values have been normalised based on the mean value of Set-1. The vertical bars indicate the 95% confidence interval of k_{ij}; whereas the black dots indicate the mean value of k_{ij}. Variations in the x-direction indicate the probability of density of the k_{ij}.

Therefore, to properly compare the influence of k_{ij} uncertainty in each mixture, the effect of VLE data availability, which may be collected through experiments to narrow the uncertainty margins and improve model fidelity, must be negated when comparing mixtures. The basis for this comparison is described in Section 7.3.

7.3 Methodology

As with any experimentally derived quantity, the value of k_{ij} has an uncertainty associated with it. The degree of this uncertainty depends on a few factors, such as the uncertainty in the measured quantities, the number of data points (sample size), and their spread. As described in Section 4.2.2, a MonteCarlo simulation may be

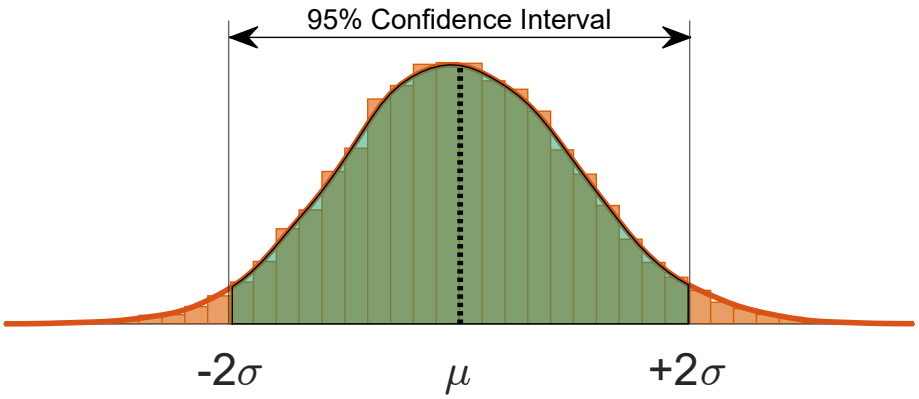

Figure 7.2: Normal probability distribution, where μ is the mean and the σ is the standard deviation

In the following analysis, the effect of the uncertainty in k_{ij} on modeling is investigated by assuming a maximum variation in k_{ij}. There are two possible ways of choosing this uncertainty: a fixed nominal value, or a fixed percentage value. Each approach serves a different purpose; the results of a nominal Δk_{ij} indicate the sensitivity of the fluid-EoS combination to nominal changes in k_{ij}; whereas the results of a relative Δk_{ij} indicate the sensitivity to a percentage change in k_{ij}. The following is an elaboration on these differences.

Assessing the uncertainty based on a fixed nominal value for Δk_{ij} would make intuitive sense to ensure that equal variations are imposed on all EoS-mixture combinations, thus an equal basis for comparing the effect on each fluid model. The advantage of this method is that it provides an estimate of the error with increments in k_{ij}. However, this method does not reflect the probabilistic nature of the error, and

may overestimate, or underestimate, the uncertainty depending on the fluid model.

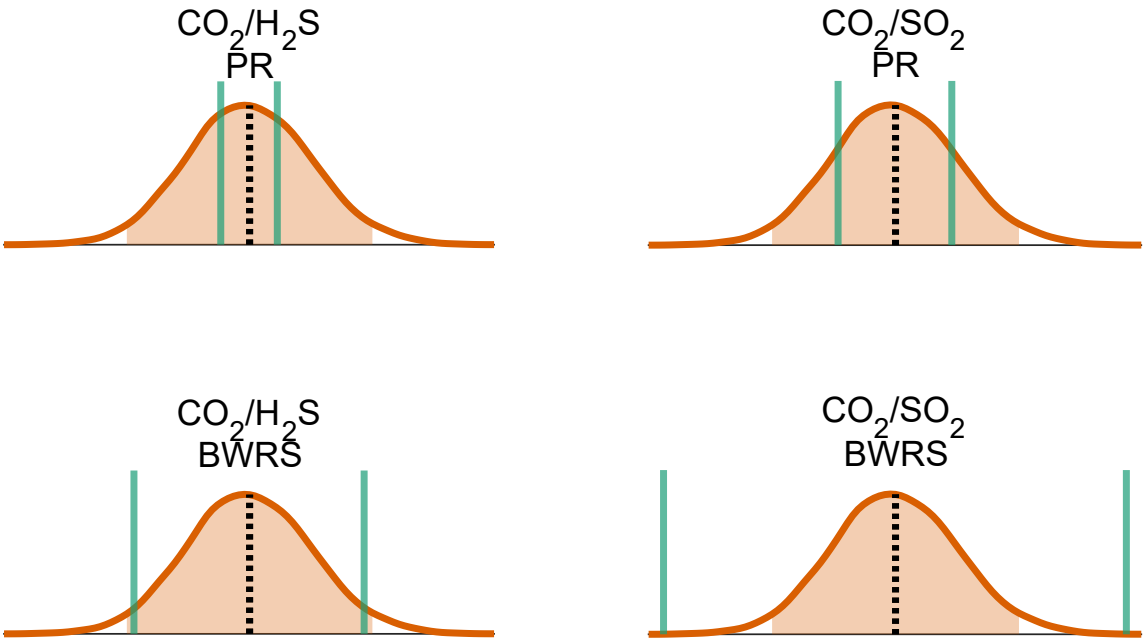

Figure 7.3: Hypothetical PDFs assuming normal distriubtution of k_{ij}. Shaded area: 95% confidence interval. Green bars: error margins assuming Δk_{ij}=0.01 and using the values of k_{ij} listed in Table 7.5

As seen in the figure, the imposition of a nominally equal Δk_{ij} translates to non-equal margins of error. Only in CO_2/H_2S with BWRS does the margin of error coincide with the 95% confidence interval; for the other fluid models, the same Δk_{ij} can cover confidence intervals ranging from 40% to 99.9%. As stated previously, the objective of this analysis is to negate the advantage of any of the fluids that is due to the current availability of experimental data. Therefore, a standardised deviation, represented by a common confidence interval is necessary.

Alternatively, a fixed relative variation imposes a uniform confidence interval; assuming a similar probability distribution profile of k_{ij} in all fluid models. Figure 7.4 shows a uniform variation for all fluid models with $\Delta k_{ij} = 50\%$. The intervals coincide with the 95% confidence interval; however, this is coincidental because the confidence interval that corresponds to a 50% variation from the mean will generally depend on the probability distribution function. Nevertheless, as long as the probability distribution function is similar across fluids, then a uniform relative marginal error

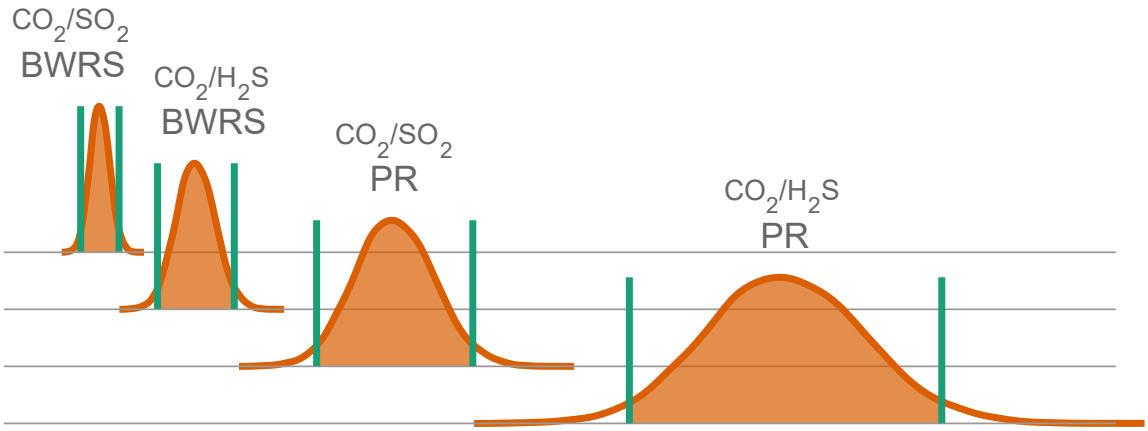

Figure 7.4: Hypothetical PDFs assuming normal distribution of k_{ij}. Shaded area: 95% confidence interval. Green bars: error margins assuming Δk_{ij}=50% and using the values of k_{ij} listed in Table 7.5

The advantage of a relative Δk_{ij} is that it reflects the experimental uncertainty well, because, for a given experimental apparatus, the uncertainty in the measured VLE data is fixed regardless of the fluid measured or the EoS fitted to the data. Therefore, assuming a uniform probability distribution for all models and fluids, the relative marginal error in k_{ij} should be similar for all fluid models for a given experimental setup. Accordingly, the range of Δk_{ij} for each EoS and fluid combination are visualised in Figure 7.5 and detailed in Table 7.7.

Table 7.7: Imposed binary interaction coefficient uncertainty for each CO_2-based mixture and EoS combination

	PR		**BWRS**		**SRK**		**PC-SAFT**	
	$-\Delta k_{ij}$	$+\Delta k_{ij}$	$-\Delta k_{ij}$	$+\Delta k_{ij}$	$-\Delta k_{ij}$	$+\Delta k_{ij}$	$-\Delta k_{ij}$	$+\Delta k_{ij}$
CO_2/H_2S	0.0435	0.131	0.0227	0.0680	0.0435	0.131	-0.0569	-0.0197
CO_2/SO_2	0.0107	0.0428	0.0091	0.0273	0.0125	0.0374	-0.141	-0.0470
CO_2/C_6F_6	0.0166	0.0498	0.0313	0.0939	0.0197	0.0591	-0.0857	-0.0286

Having established the consistency of a relative Δk_{ij}, it should be noted that this approach does not guarantee equality of outcome; higher mean k_{ij} will result in higher nominal marginal errors. As an example, although CO_2/H_2S and CO_2/SO_2 with BWRS have the same relative marginal error in Figure 7.4, the nominal Δk_{ij} is 0.01 and 0.0218, respectively. It is expected that the results of the fluid models which

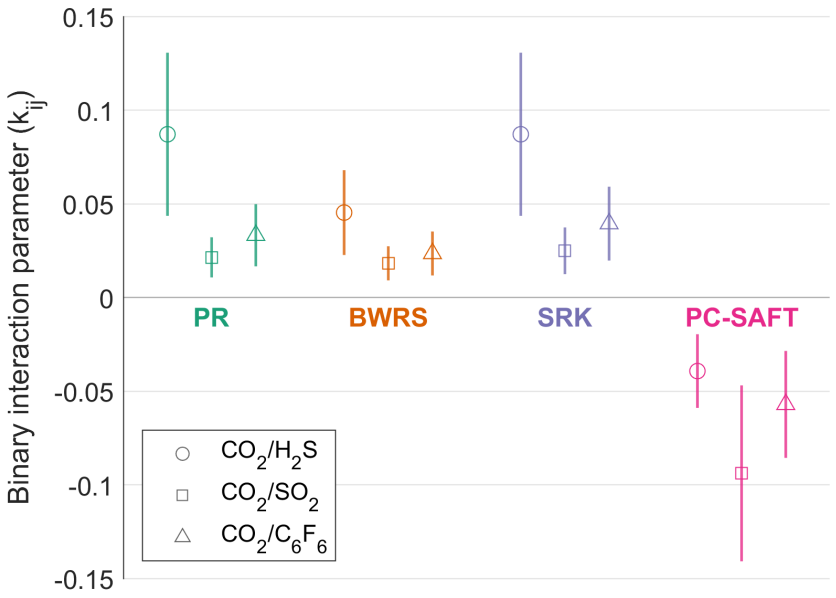

Figure 7.5: Imposed binary interaction coefficient uncertainty for each CO_2-based mixture and EoS combination. The markers indicate the original value of k_{ij} and the vertical bars indicate the minimum and maximum imposed values of Δk_{ij}

have higher k_{ij} will be affected more by the 95% margin of error.

Therefore, the following analysis includes both the error due to Δk_{ij} within the 95% confidence interval, and the sensitivity due to nominal Δk_{ij}. The results are obtained by assuming a 50% Δk_{ij}, which provides the MAPE corresponding to the marginal error. Then, the errors are normalised by the values of k_{ij} to provide the sensitivity due to nominal Δk_{ij}, as will be explained next.

The MAPE will be extensively used in this chapter to indicate the deviation in the results of the fluid models from specified baseline values. For the EoS comparison, the values of the baseline of each EoS (with Δk_{ij}=0) are compared; the difference is defined as:

$$\mathrm{MAPE}^0_{1,2} = \frac{100\%}{n_x} \sum_{i=1}^{n_x} \left| \frac{\mathrm{U}^0_1 - \mathrm{U}^0_2}{\mathrm{U}^0_1} \right|_i \tag{7.2}$$

where U^0_1 and U^0_2 are the baseline values for two arbitrary equations of state (EoS_1, EoS_2), and n_x is the total number of blend fractions considered, which is equal to 10 for all cases. This number was determined through a sensitivity analysis which indicated that a greater segmentation has no effect on the consistency of the results.

Whereas, for Δk_{ij} comparison, the values corresponding to $\pm\Delta k_{ij}$ are compared with the baseline of k_{ij} of the same EoS. Note that there will always be two values (MAPE^{+}, MAPE^{-}) corresponding to the $\pm$ variations in k_{ij}; the resulting MAPE$^{\pm}$ is the average of the two:

$$\mathrm{MAPE}_1^{+} = \frac{100\%}{n_x}\sum_{i=1}^{n_x}\left|\frac{\mathrm{U}_1^0 - \mathrm{U}_1^{+}}{\mathrm{U}_1^0}\right|_i \tag{7.3}$$

$$\mathrm{MAPE}_1^{-} = \frac{100\%}{n_x}\sum_{i=1}^{n_x}\left|\frac{\mathrm{U}_1^0 - \mathrm{E}_1^{-}}{\mathrm{U}_1^0}\right|_i \tag{7.4}$$

$$\mathrm{MAPE}_1^{\pm} = 0.5(\mathrm{MAPE}_1^{+} + \mathrm{MAPE}_1^{-}) \tag{7.5}$$

where the superscripts 0, +, and − indicate values corresponding to k_{ij}, k_{ij} + Δk_{ij}, k_{ij} - Δk_{ij}, respectively.

Finally, to estimate the maximum average variation between fluid models due to the combined effect of the EoS and Δk_{ij}, the following equation is used:

$$\mathrm{MAPE}_{1,2}^{\pm} = \mathrm{MAPE}_{1,2}^{0} + \mathrm{MAPE}_1^{\pm} + \mathrm{MAPE}_2^{\pm} \tag{7.6}$$

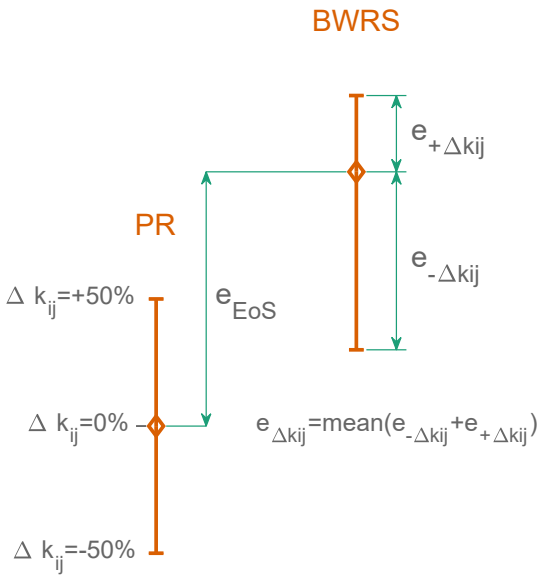

Figure 7.6: Illustrative example of error calculation for BWRS. The error (e) in the EoS is the difference between the baseline values of the two EoS being compared. The error in k_{ij} is the mean difference between the baseline and $\pm\Delta k_{ij}$

The approach to the aforementioned MAPE calculations is illustrated in Figure 7.6. Additionally, sensitivity to nominal changes in k_{ij} is indicated by the normalised variation (nMAPE), which is defined as:

$$\text{nMAPE} = \frac{\text{MAPE}^{\pm}}{k_{ij}} \tag{7.7}$$

Note that this normalisation is only relevant when comparing variations due to k_{ij} amongst the fluid models. To clarify the significance of this factor, assuming that two hypothetical EoS have the same k_{ij}, the one with the higher nMAPE will be more susceptible to a nominal change in k_{ij}.

Finally, the results pertaining to efficiency are not represented by MAPE; instead the mean absolute error (MAE) is used. This is because it is easier to understand the variation in efficiency in the native percentage unit of efficiency. The MAE is calculated as follows:

$$\text{MAE} = \frac{1}{n_e} \sum_{i=1}^{n_e} \left| \widetilde{U}_i - \hat{U}_i \right| \tag{7.8}$$

A MATLAB program was developed to study the effect of the EoS and k_{ij} on optimal cycle and turbine design. The flowchart in Figure 7.7 illustrates the calculation processes for a single CO_2 mixture. The flowchart shows four layers, three of which are parametric studies which change the EoS, k_{ij}, and dopant molar fraction. The inner most layer identifies the optimal cycle condition for the given EoS, k_{ij}, and dopant molar fraction combination. Once optimum cycle conditions are found, the program then produces a turbine geometry using the turbine boundary conditions resulting from the optimal cycle. The optimisation objective and cycle boundary conditions are similar to those of the transcritical cycle previously detailed in Chapter 3.

The cycle operational conditions are similar to those used in Chapter 3, which are repeated here. The pump inlet temperature (T_1) is set to 50 °C. It was chosen to be compatible with dry cooling temperatures in hot arid regions, assuming an ambient dry-bulb temperature of 40 °C and a minimum temperature difference of 10 °C in the condenser. Whereas an internal mininum internal temperature approach of 5 °C is assumed in line with previous work on CO_2-based cycles (Manzolini et al.

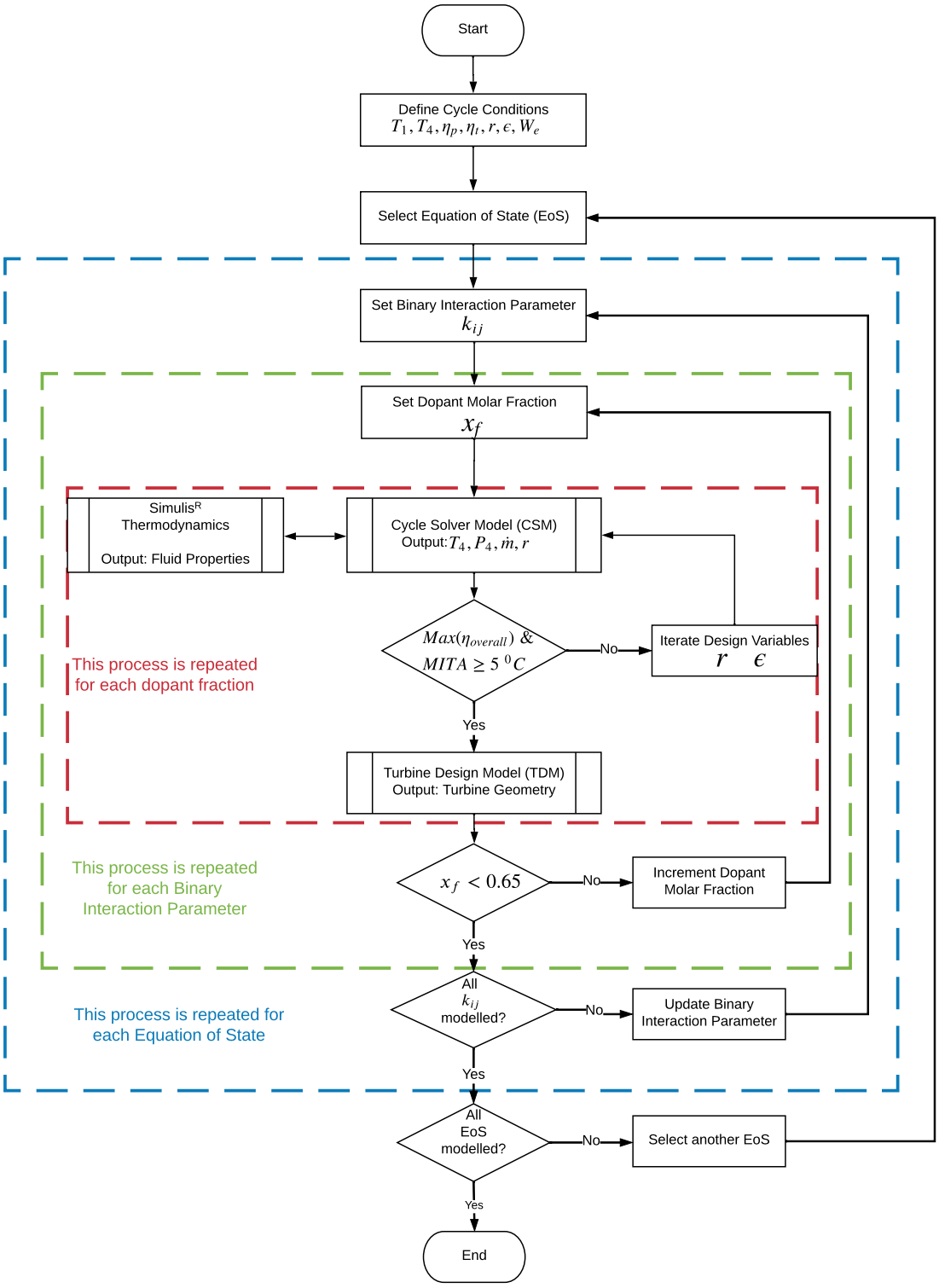

Figure 7.7: Flowchart of the thermofluid model sensitivity study for a single CO_2 mixture. The increments in the blend fraction depend on the range considered.

2022, Rodríguez-deArriba et al. 2022, Morosini et al. 2022, Crespi et al. 2022). The pump inlet was assumed to be subcooled by 2 °C below the saturation pressure.

Consequently, the pump inlet pressure (P_1) is equal to the saturation pressure of the fluid at 52 °C. The turbine inlet temperature (T_4) was set to 700 °C, which is expected from an advanced CSP receiver employing sodium salt as its Heat Transfer Medium. Additionally, the turbine inlet pressure (P_4) was restricted to 25 MPa as recommended by Dostal et al. (2004).

The maximum molar fraction of the dopant was extended to 0.65 instead of 0.4 to accommodate CO_2/H_2S , which has a minimum fraction of 0.55. The minimum dopant blend fraction depended on the critical temperature of the mixture. Heat rejection in a transcritical cycle must occur at saturation pressures below the critical pressure of the working fluid where condensation is possible. Consequently, the critical temperature of the working fluid mixture must be equal to or greater than 57 °C to allow for the formation of liquid before pump inlet. Therefore, the minimum dopant molar fraction was assumed to be the value at which the critical temperature of the mixture is equal to or slightly exceeds 57 °C. The range of dopant molar fractions is shown in Table 7.2, and a summary of the cycle assumptions is provided in Table 7.8.

The main subject of this study is the simple recuperated transcritical cycle; this is the same cycle layout that has been studied thus far. However, results for a simple non-recuperated transcritical cycle will also be used to explain the differences between the fluid models. The layouts of both cycles are shown in Figure 7.8.

7.4 Results

The following section is divided into two parts: cycle and turbine design. In the first part, the effect of the fluid model on the cycle design is discussed. In the second part, the effect on the turbine design and performance, specifically that of a radial inflow turbine is discussed.

Table 7.8: Inputs required for cycle solution

Controlled Parameters		
Parameter	**Range**	**Unit**
Dopant Molar Fraction	Max(0.4)	%
Turbine Inlet Temperature (T_4)	700	°C
Pump Inlet Temperature (T_1)	50	°C
Pump Isentropic Efficiency(η_p)	85	%
Turbine Isentropic Efficiency(η_t)	90	%
Minimum internal temperature approach (MITA)	5	°C
$\Delta p/p$ of Primary Heat Exchanger	0.015	-
$\Delta p/p$ of Recuperator High- and Low-pressure sides	0.01 and 0.015	-
$\Delta p/p$ of Condenser	0.02	-
Dependant Parameters		
Pump Inlet Pressure(P_1)	$P_{sat@(T_1+2)}$	MPa
Turbine Inlet Pressure(P_4)	Max (25)	MPa
Optimised Parameters		
Pressure Ratio (r)	2 to Max (P_4)/P_1	-
Recuperator Effectiveness(ϵ)	80 to 98	%

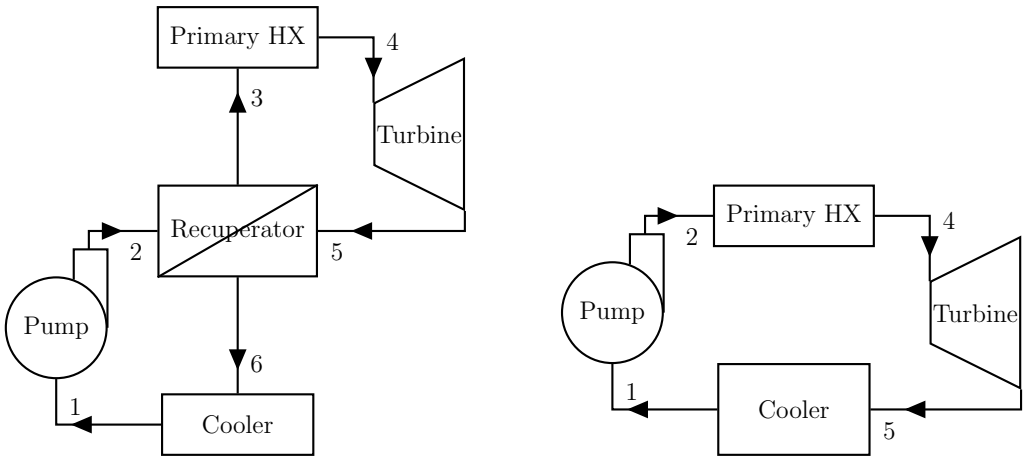

(a) Simple recuperated (b) Simple non-recuperated

Figure 7.8: Cycle layouts

7.4.1 Cycle design

Attention is first given to the choice of the optimal dopant molar fraction. This is important because it defines all subsequent fluid properties. In essence, a variation

in the dopant molar fraction of a mixture produces different fluids. Normally, the dopant fraction that produces the mixture with the optimal thermal efficiency is chosen. As seen in Figure 7.9, the thermal efficiency of the cycle is affected by the dopant molar fraction, the EoS, and the value of k_{ij}, to various degrees according to

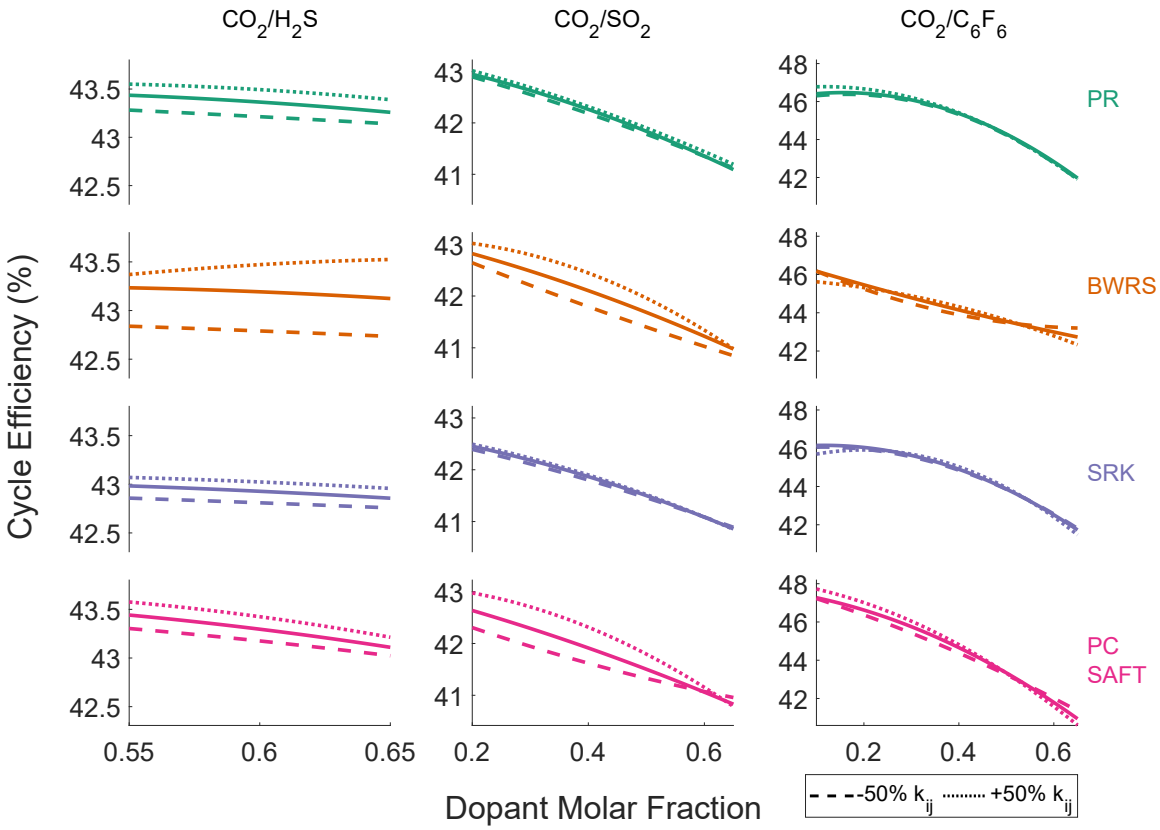

Figure 7.9: Trends in cycle thermal efficiency across blend fractions for fluid-EoS-k_{ij} combinations. Note that the vertical axis is different for each fluid

The cycle thermal efficiency for all mixtures and EoS shows a positive correlation with k_{ij}; higher values of k_{ij} produce cycles of higher thermal efficiencies. The reason for this positive correlation will become clear once other cycle parameters, such as the pump work, turbine work and the recuperated heat, are analysed. Also common among mixtures is that the thermal efficiency exhibits the same trend with dopant fraction regardless of the EoS or k_{ij}, which suggests that the dopant fraction that yields the highest thermal efficiency is independent of the fluid model used.

The differences in efficiency due to Δk_{ij} are shown in Table 7.9. The bottom row contains the average difference for each fluid, and the right-most column shows the

average difference for each EoS. The same format is used in all subsequent tables listing the differences due to Δk_{ij}.

Based on Table 7.9, the thermal efficiency fluctuates around 0.04% to 0.34% of the baseline value for variations in k_{ij}. The largest variation is 0.34%, which is observed in BWRS when used with CO_2/H_2S; the lowest is 0.04% SRK when used with CO_2/SO_2. Moreover, the average variation due to Δk_{ij} is not similar across EoS. As explained previously, the extent to which results change with Δk_{ij} is expected to be proportional to the baseline value of k_{ij}. This is confirmed by the similarity in the trend in $MAE^{\pm}$ (Table 7.9) and the trend in k_{ij} values listed in Table 7.5. For example, k_{ij} equals 0.0332 for PR and 0.0626 for BWRS when modelling CO_2/C_6F_6; the $MAE^{\pm}$ in the former is 0.12 compared to 0.24 in the latter. Nevertheless, the values in Table 7.9 indicate the extent of change in cycle thermal efficiency corresponding to a change in k_{ij} within its 95% confidence interval. In other words, there is a 95% certainty that the efficiency will be within the error margins shown in the table.

Table 7.9: $MAE^{\pm}$ [%] in cycle thermal efficiency due to Δk_{ij}

	CO_2/H_2S	CO_2/SO_2	CO_2/C_6F_6	$\mathbf{MAE^{\pm}}_{avg}$
PR	0.14	0.06	0.12	**0.1**
BWRS	0.34	0.24	0.24	**0.27**
SRK	0.11	0.04	0.11	**0.09**
PC-SAFT	0.12	0.27	0.27	**0.22**
$\mathbf{MAE^{\pm}}_{avg}$	**0.17**	**0.15**	**0.18**	**0.17**

The normalised differences in efficiency due to Δk_{ij} ($nMAE^{\pm}$) for each fluid-EoS combination are listed in Table 7.10. Among the four EoS, SRK, PR, and PC-SAFT have approximately the same sensitivity to k_{ij}, with SRK having the least. On the other hand, the sensitivity of BWRS is a few multiple higher than any of the other EoS. This suggests that, assuming an equal k_{ij}, the variation in the results due to nominal Δk_{ij} using the BWRS will be multiple times more than any of the other EoS. For example, even though BWRS has a k_{ij} value that is double that of PR when modelling CO_2/C_6F_6, a nominal change in k_{ij} will have almost five times the effect compared to PR. This heightened sensitivity of BWRS was masked in the non-normalised MAPE analysis because the nominal change in k_{ij} corresponding to a 95%

confidence interval was much smaller.

Therefore, although the nominal change indicates that certain EoS, namely BWRS, are more sensitive to k_{ij}, the imposition of a relative Δk_{ij} that corresponds to a 95% confidence interval reveals that the sensitivity will be alleviated by the lower k_{ij} values which produce narrower error margins.

Table 7.10: nMAE$^{\pm}$ [%] in cycle thermal efficiency due to Δk_{ij}

	CO_2/H_2S	CO_2/SO_2	CO_2/C_6F_6	**nMAE$^{\pm}_{avg}$**
PR	1.56	2.88	3.52	**2.65**
BWRS	7.43	13.28	10.05	**10.25**
SRK	1.21	1.76	2.72	**1.9**
PC-SAFT	3.08	2.89	4.68	**3.55**
nMAE$^{\pm}_{avg}$	**3.32**	**5.2**	**5.24**	**4.59**

The uncertainty in the choice of the EoS is quantified in the correlation matrix of Figure 7.10. Generally, the all EoS predict thermal efficiencies within 1% of each

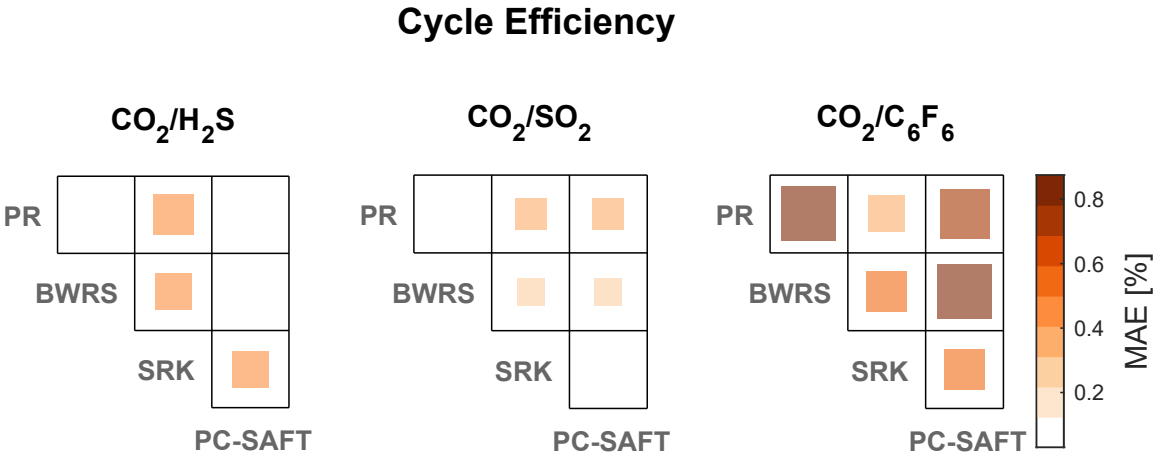

Figure 7.10: The variation in the cycle thermal efficiency based on the EoS. The size and color map indicate the MAE [%]

Finally, the combined effect of the choice of the EoS and the variation due to Δk_{ij}, as calculated in Eq. 7.6, is mapped in Figure 7.11. The results indicate that the maximum uncertainty in the thermal efficiency will be below 1.4%, regardless of the EoS and considering the variation of k_{ij} within its 95% confidence interval. Generally,

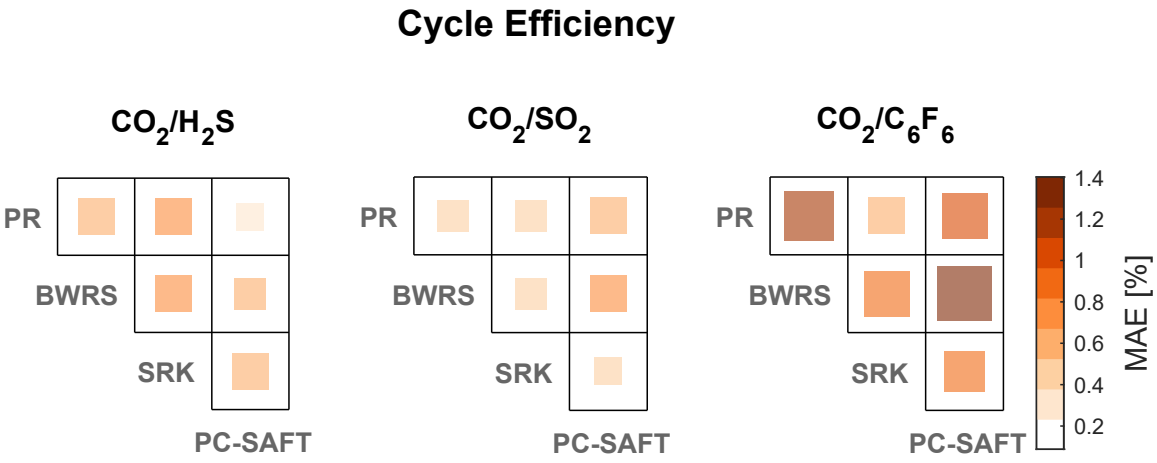

Figure 7.11: The variation in the cycle thermal efficiency based on the combined effect of EoS and Δk_{ij}. The size and color map indicate the MAE [%]

To understand what causes the change in thermal efficiency, an examination of the pump is required. As seen from Figure 7.12, the pump inlet pressure is not consistent in all fluid models, which contributes to the differences between them. Depending on the fluid and the EoS, the difference in the pump inlet pressure ranges from 1.75% to 11.9% for variations in k_{ij}; note that the trends match those observed in the variation in cycle efficiency.

Table 7.11: MAPE$^{\pm}$ [%] in pump inlet pressure due to Δk_{ij}

	CO_2/H_2S	CO_2/SO_2	CO_2/C_6F_6	**MAPE$^{\pm}_{avg}$**
PR	7.2	1.75	3.83	**4.26**
BWRS	10.17	4.22	8.57	**7.65**
SRK	6.68	1.89	4.84	**4.47**
PC-SAFT	4.94	11.9	10.04	**8.96**
MAPE$^{\pm}_{avg}$	**7.25**	**4.94**	**6.82**	**6.34**

The combined effect of Δk_{ij} and EoS, as shown in Figure 7.13, indicates that the pump inlet pressure for CO_2/C_6F_6 calculated with BWRS is inconsistent with other EoS. This inconsistency occurs for dopant molar fraction above 0.4, as evident in Figure 7.12.

The trends in the pump inlet pressure suggest that it may be the cause of the changes in the cycle thermal efficiency. Therefore, the analysis is repeated, but with

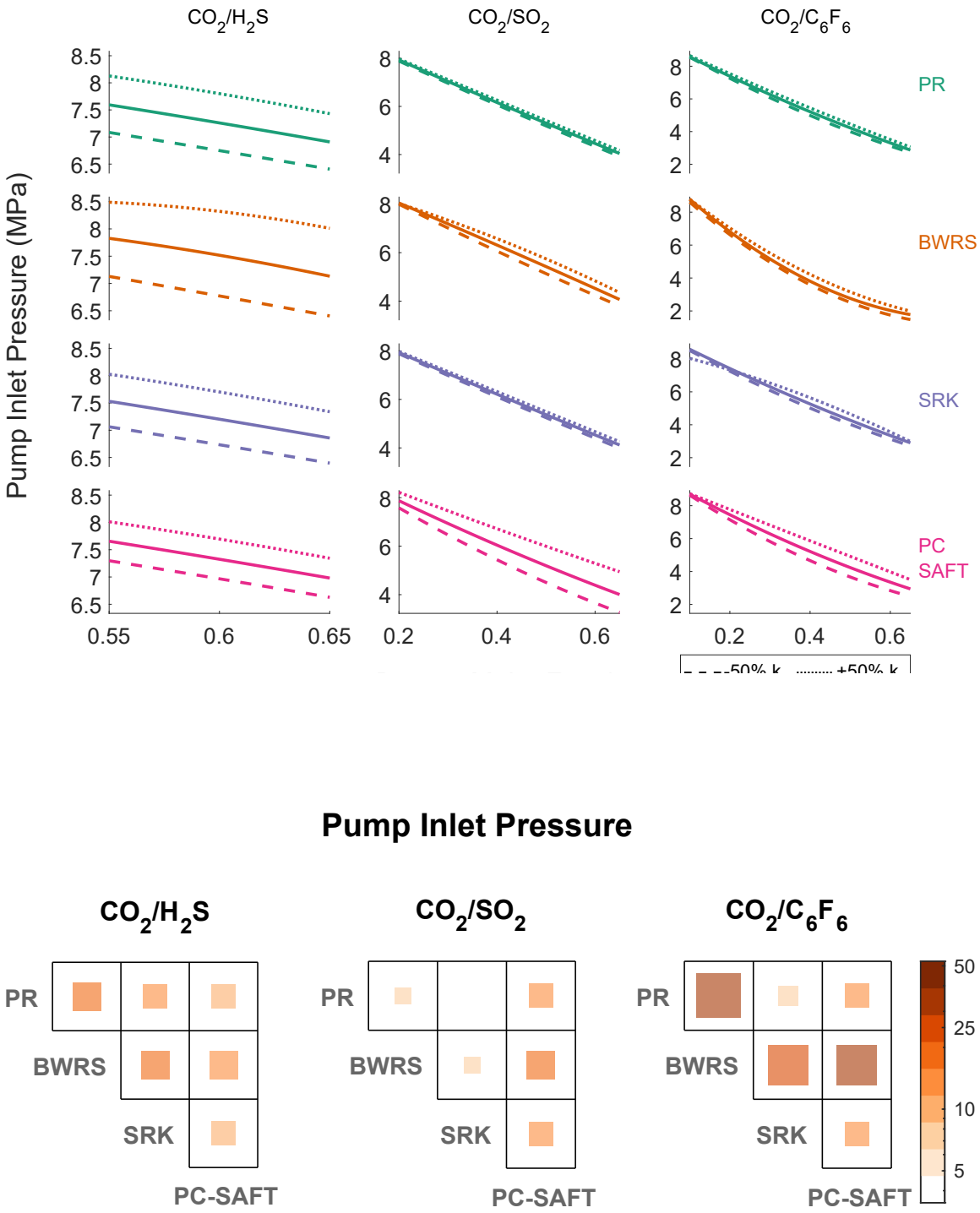

Figure 7.13: The variation in the pump inlet pressure based on the combined effect of EoS and Δk_{ij}. The size and color map are logarithmic and indicate the MAPE [%]

the pump inlet pressure for all fluid models assumed to be equal to that which is calculated by the baseline PR EoS. According to Figure 7.14, even with a common pump inlet pressure, thermal efficiency will still vary depending on the fluid model. The variation is even higher than with a model-dependent pump inlet pressure, suggesting that there must be another cause for the change in the thermal efficiency.

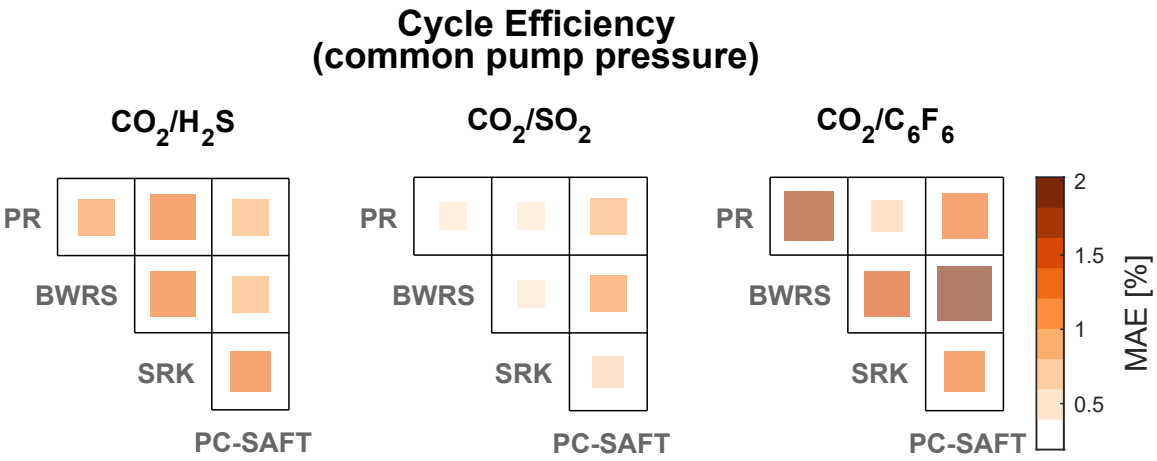

Figure 7.14: The variation in the cycle efficiency based on the combined effect of EoS and Δk_{ij} assuming a common pump inlet pressure for all fluid models for each mixture. The size and color map indicate the MAE [%]

Ultimately, the cycle efficiency depends on the net specific work and specific heat input in the primary heat exchanger:

$$\eta_{th} = \frac{w_n}{q_H} \tag{7.9}$$

therefore η_{th} is directly proportional to w_n and inversely proportional to q_H. Fluid models that underestimate q_H compared to w_n have higher thermal efficiencies. In a simple recuperated cycle, multiple variables, including q_h, w_p, w_t, and q_r, may act in concert to influence cycle thermal efficiency. Attempting to account for the trends in all of these parameters all at once is difficult. Therefore, to reveal the causes of each of these trends, a new set of assumptions must be made to separate the effects of pressure variance and recuperation. Here, the four cycles listed in Table 7.12 are considered. The following reasoning is valid for all fluid model; therefore, only the cases of 0.59/0.41 CO_2/H_2S modelled using PR with Δk_{ij}=0 and Δk_{ij}=+0.5 are compared as an example.

Table 7.12: Cycles used to investigate the change in thermal efficiency

Cycle label	Recuperated	Pump inlet pressure
NF	No	Fixed
NV	No	Variable
RF	Yes	Fixed
RV	Yes	Variable

In the simple non-recuperated cycle, the difference in w_t is negligible. This is likely due to the similarity in the pressure ratio across the turbine. Moreover, as demonstrated in Figure 7.15, the specific heat capacity at constant pressure (C_p) calculated in the vicinity of the expansion process is consistent among the fluid models. Consequently, there is a negligible difference in the expansion work.

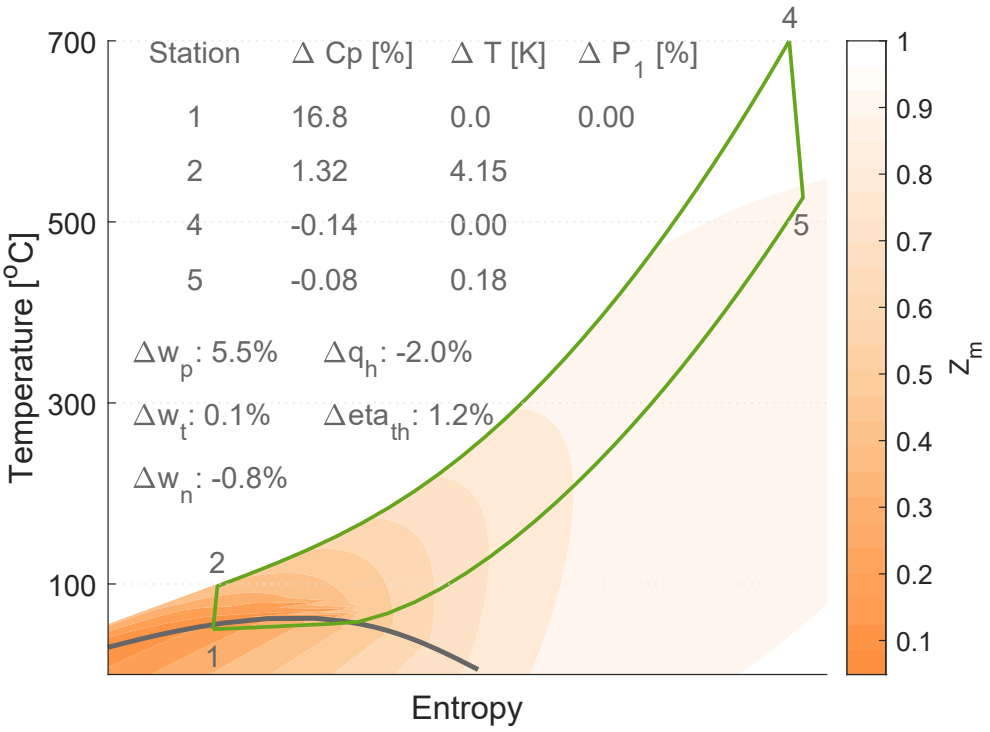

Figure 7.15: Temperature-Entropy diagram of NF cycle with compressibility contours (Z_m). The change in the parameters is based on the difference between Δk_{ij}=0 relative to Δk_{ij}=+0.5k_{ij} for the example quoted here (0.59/0.41 CO_2/H_2S modelled using PR)

On the other hand, although the pressure ratio is similar across the pump, the variation in the pump specific work is significant (5.5%). The change in w_p is a direct consequence of the variance in the calculated properties in the vicinity of the compression process, such as C_p. This is also evident in Figure 7.15, where the differences in the calculated C_p are significant close to the saturation curve, where compression occurs. Generally, the higher constant-pressure specific heat capacity the greater the amount of compression work required. Therefore, in the example shown here, an increase of 16.8% in the constant-pressure specific heat capacity at the pump inlet translates into a 5.5% increase in the pump work.

Seemingly, an increase in compression work would decrease cycle efficiency since the turbine work has not changed, but the increase in pump work is counteracted by a decrease in the heat required by the cycle. Coincidentally, C_{p} has a direct and positive relation with the pump outlet temperature; the higher C_{p}, the higher the outlet temperature. Downstream of the pump, the amount of heat provided in the primary heat exchanger depends on the temperature at the heater inlet; the higher the temperature, the smaller the amount of heat required to raise the temperature to the prescribed turbine inlet temperature. This explains the decrease in the specific heat input q_{h} which increases thermal efficiency.

Next, a simple recuperated cycle is considered, but with a fixed pump inlet pressure as in the previous case, the results of which are shown in Figure 7.16. As with the non-recuperated cycle, the turbine specific work is unaffected by the fluid model because the pressure ratio is unchanged. Moreover, the effect of C_{p} variation is similar to a non-recuperated cycle. Therefore, the addition of a recuperator does not change the cycle's sensitivity to the fluid model. What small differences there are between the recuperated and non-recuperated cycles is due to the additional pressure drop in the recuperator.

The two cases examined thus far assume a similar pump inlet pressure. However, according to Figure 7.12, the pump inlet pressure may vary depending on the fluid model. Therefore, the non-recuperated and recuperated cycles are simulated once more, but based on the pump inlet pressure estimated by the each fluid model.

To understand the effect of the pump inlet pressure, a non-recuperated cycle is considered in Figure 7.17. Although the pump inlet pressure is overestimated by 2.44%, the pump specific work is still higher because C_{p} is overestimated, which increases pump work more than the reduction caused by the change in the pressure ratio.

The opposing effects of the pressure ratio and C_{p} exist in all the fluid model variations, but to varying degrees; in some instances, the effects of the two are more equatable which translate to smaller differences in the pump specific work. As es-

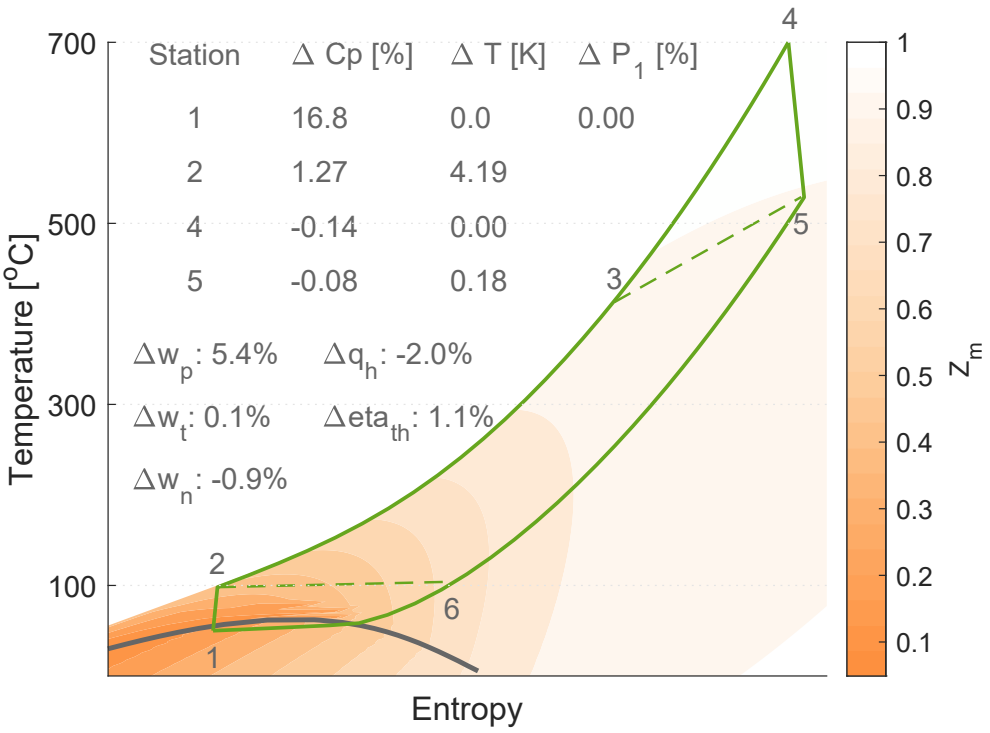

Figure 7.16: Temperature-Entropy diagram of RF cycle with compressibility contours (Z_m). The change in the parameters is based on the difference between Δk_{ij}=0 relative to Δk_{ij}=+0.5k_{ij} for the example quoted here (0.59/0.41 CO_2/H_2S modelled using PR)

tablished previously, the choice of the fluid model does not affect the turbine specific work when the pressure ratio is constant among the fluid models. However, as seen in Figure 7.17, the decrease in the pressure ratio causes a decrease in the turbine specific work w_t that is considerable relative to the constant pressure ratio cases. Ultimately, the efficiency of the non-recuperated cycle decreases because the decrease in the net specific work w_t is greater than the reduction of the heat input. This is contrary to the constant pressure case, but is intuitive because the pressure ratio of the cycle has decreased.

Lastly, the results of the original simulation are shown in Figure 7.18, which is a recuperated cycle with variable pump inlet pressure, to assess the aggregate effect of the change in the fluid model. The changes in the pump, turbine, and net specific works are similar to those in the non-recuperated cycle; however, the decrease in the heat input is greater. With higher turbine outlet temperatures, the amount of heat that is available to be internally recuperated is increased, leading to lower heat load demands in the primary heat exchanger. The end effect: a higher thermal efficiency

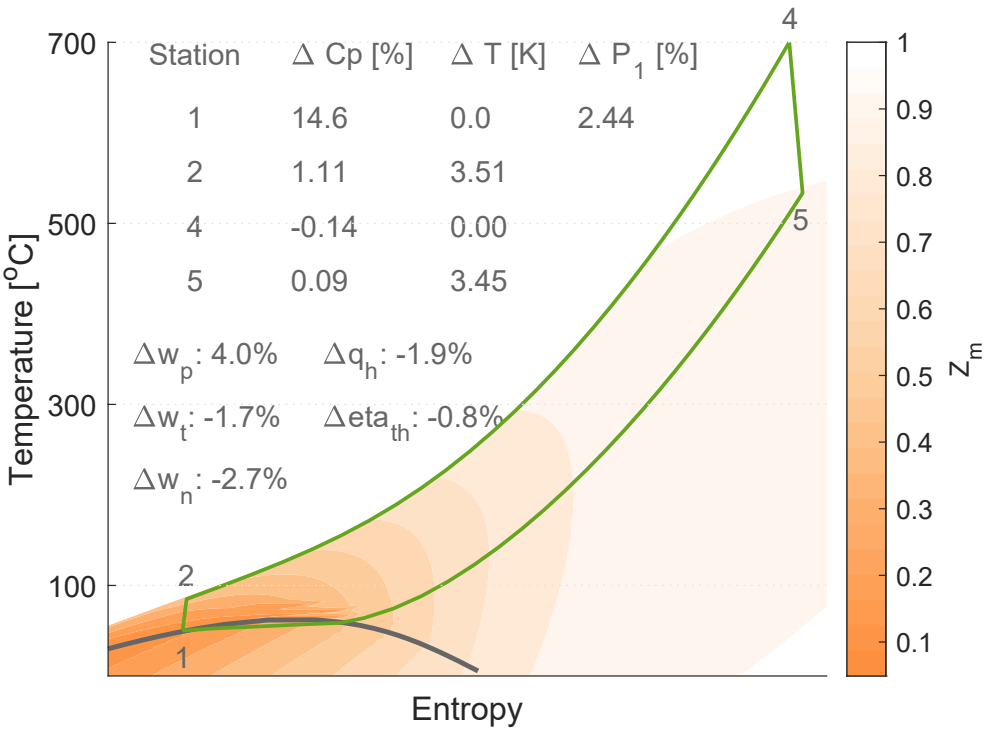

Figure 7.17: Temperature-Entropy diagram of NV cycle with compressibility contours (Z_m). The change in the parameters is based on the difference between Δk_{ij}=0 relative to Δk_{ij}=+0.5k_{ij} for the example quoted here (0.59/0.41 CO_2/H_2S modelled using PR)

is predicted for the recuperated cycle.

To conclude, the Δk_{ij} has the same effect on recuperated and non-recuperated cycle if the pump inlet pressure is assumed constant. However, adopting the pump inlet pressure that was calculated by the fluid model changes the net specific work of the cycle and its efficiency. Moreover, with a variable pump inlet pressure, the Δk_{ij} has a greater effect on the recuperated cycle.

The forgoing analysis shows that the changes in cycle efficiency are a culmination of the differential change in the specific heat capacity at constant pressure across the cycle, which leads to changes in the pump work and the heat input to the cycle, and the variation in the pump inlet pressure which affects the turbine work and recuperated heat. An illustration of this process is shown in Figure 7.19. The influence of the specific heat capacity is further demonstrated in Figure 7.20, which shows a strong positive correlation between C_p at pump inlet and η_{th} for all fluids.

Having explained the reason for the change in thermal efficiency, attention is now

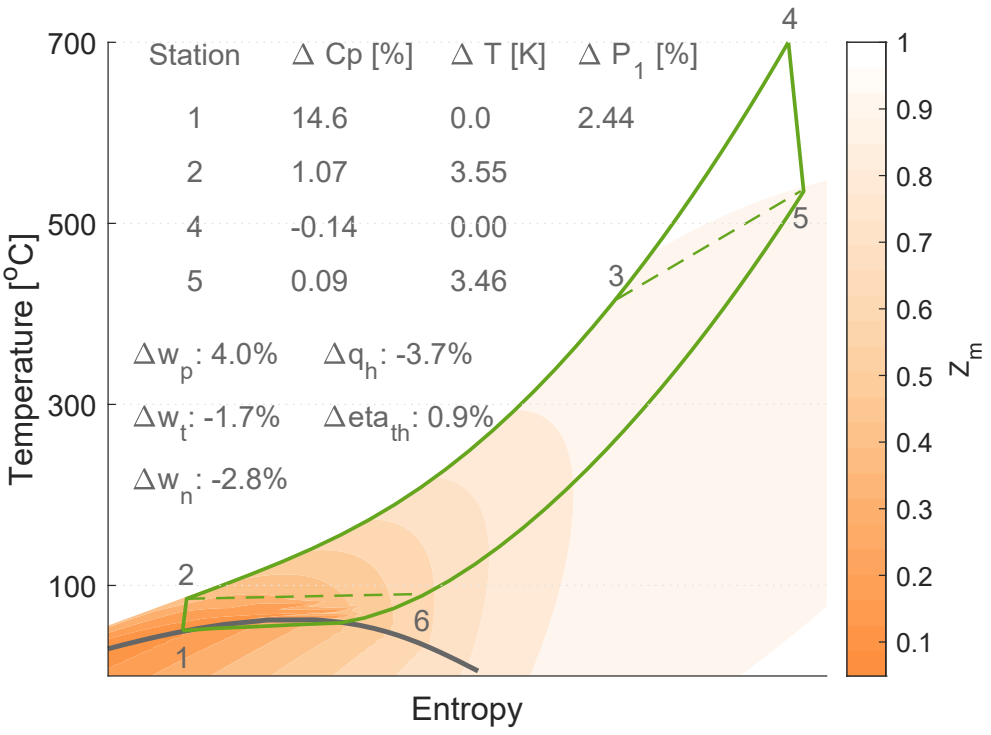

Figure 7.18: Temperature-Entropy diagram of RV cycle with compressibility contours (Z_m). The change in the parameters is based on the difference between Δk_{ij}=0 relative to Δk_{ij}=+0.5k_{ij} for the example quoted here (0.59/0.41 CO_2/H_2S modelled using PR)

turned to the disproportionate effects the fluid model variation has on the mixtures. The changes in C_p and the pump inlet pressure, which is set equal to the saturation pressure at the prescribed cooling temperature, can be linked to the difference in the shapes of the saturation curves between CO_2 and the dopants. According to White & Sayma (2018*b*), the ideal specific heat capacity at constant pressure indicates the slope of the saturation curve; whether it's wet, dry, or isentropic; whilst the acentric factor indicates the width of the saturation curve; the closer the acentric factor is to one, the wider the curve. Generally, the more similar the ideal specific heat capacities of the mixture components, the smaller is the deviation in C_p with the change in the fluid model. The ideal specific heat capacities of the fluids are shown in Table 7.13. The ideal specific heat capacities of both H_2S and SO_2 are similar to CO_2; therefore, changes in the fluid model will have a lesser effect on CO_2/H_2S and CO_2/SO_2 mixtures relative to the effect on CO_2/C_6F_6 . This can be seen in Figure 7.20, where the variations in C_p are greatest in CO_2/C_6F_6. On the other hand, the more similar the acentric factors, also shown in Table 7.13, the more consistent the saturation

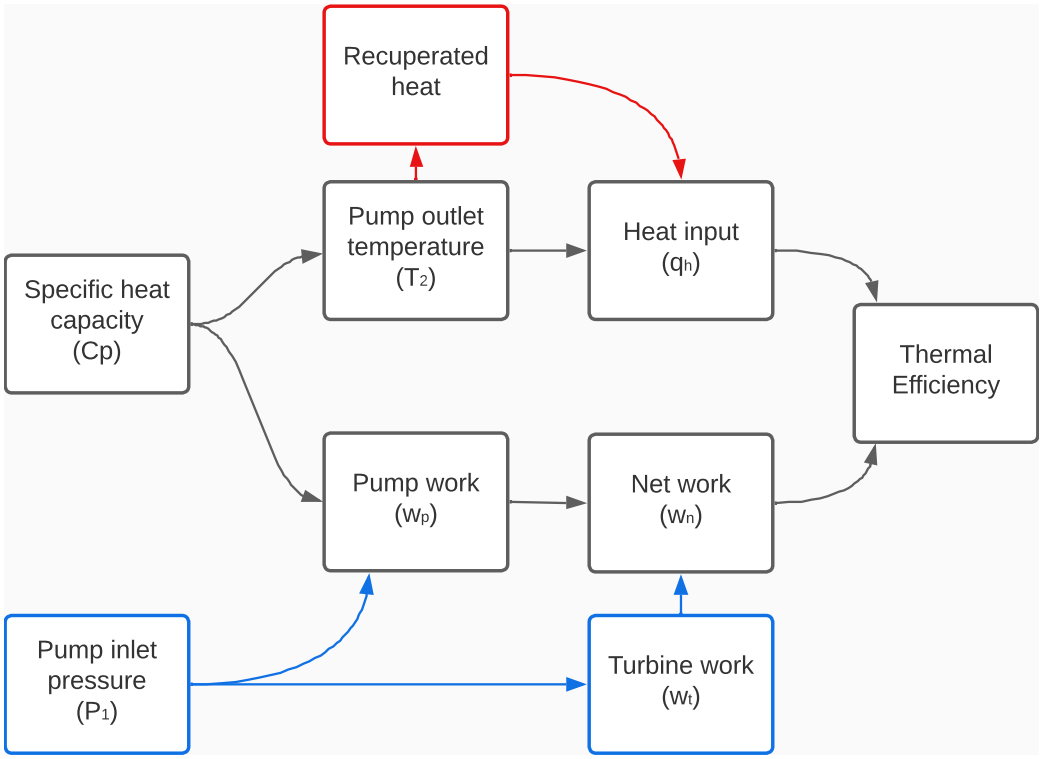

Figure 7.19: Process by which a change in the fluid model affects the efficiency of a simple recuperated transcritcal cycle

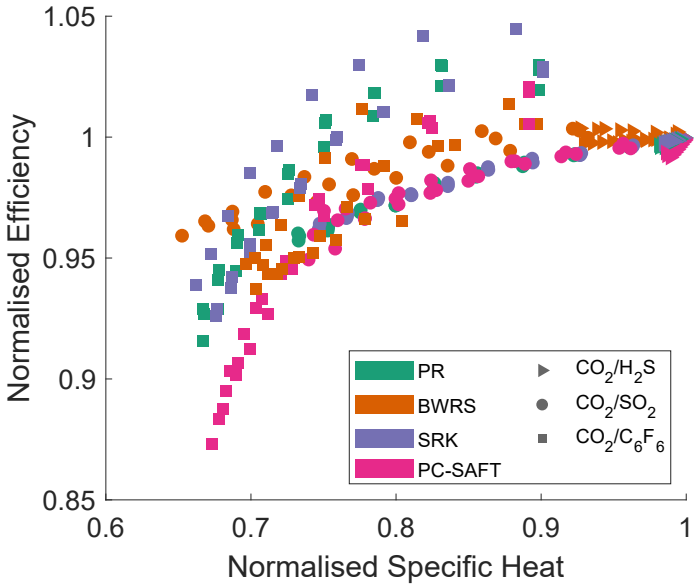

Figure 7.20: Correlation between C_p and η_{th}. Both have been normalised relative to the values produced by the lower limit of dopant fractions for each mixture

pressure. This is evident in Figures 7.12 and 7.13 and in Table 7.11, which show the inconsistency in the saturation pressure for CO_2/H_2S and CO_2/C_6F_6 , whereas CO_2/SO_2 is the most consistent. The saturation curves of the pure fluids are also compared in Figure 7.21.

Table 7.13: Ideal gas specific heat capacity of mixture components

Compound	CO_2	H_2S	SO_2	C_6F_6
C_p^o **[J/mol.K]**	41.67	47.34	53.20	272.1
Acentric factor	0.2236	0.081	0.2454	0.3953

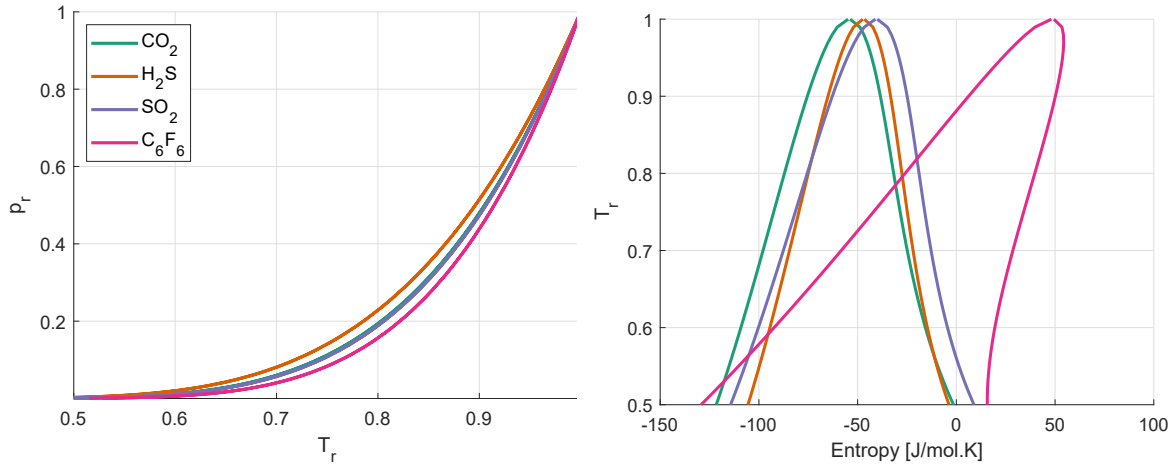

Figure 7.21: Comparison of saturation domes of pure fluids. The difference in the width of the saturation curves is best seen through the figure on the left. The difference in the shape of the curves is clear in the figure on the right

Turbine Design

As established previously, the fluid properties in the vicinity of the expansion process are not expected to change with the change in the fluid model; however, turbine design may change due to the change in the pressure ratio. In the following section a power cycle with a net output of 10 MWe is considered; based on which the turbine output is expected to be in the range of 11-12 MW. A mean line design is generated for this cycle based on the model previously outlined in Chapter 5.

Before delving into the mean line design, key turbine design parameters such as the adiabatic expansion coefficient (γ) and the speed of sound are examined. In Figure 7.22, the overall change in the adiabatic expansion coefficient at the turbine

inlet is less than 2%. To put this change into perspective, if γ is in the order of 1.2, then the maximum deviation is less than 0.024, which is unlikely to affect the expansion process. The trivial effect of γ is confirmed by both the turbine specific

t

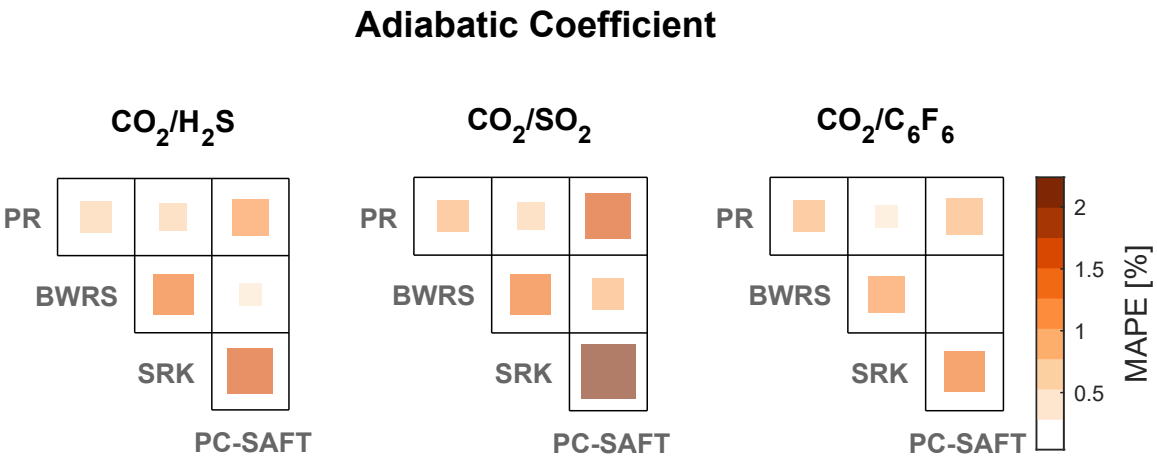

Figure 7.22: The variation in the adiabatic expansion coefficient based on the combined effect of EoS and Δk_{ij}. The size and color map indicate the MAPE [%]

Likewise, the speed of sound, which indicates the possibility of supersonic flow in the turbine, thus choking, is not affected by the fluid model. Therefore, the ability of to predict supersonic flow during expansion will not be affected by the choice of the EoS nor by the uncertainty in k_{ij}. As shown in Figure 7.23, the maximum possible change in the calculated speed of sound is less than 4%. Assuming that supersonic flow occurs at a Mach number of 1, then the uncertainty in the Mach number is 0.96-1.04, which is still considered supersonic flow. Therefore, the uncertainty in the speed of sound is not high enough to affect design decisions

Moving on to the turbine specific work, any change in w_t is a consequence of the change in the pressure ratio, as explained previously. The trends in Figure 7.24 are similar to those of Figure 7.13, which shows the change in the pump inlet pressure, thus the change in the pressure ratio. In line with the trends observed previously, the greatest variation is in CO_2/C_6F_6 when modelled with BWRS. The variation is 10-17% in CO_2/H_2S ; 2-10% in CO_2/SO_2 ; and 6-25% in CO_2/C_6F_6 . Such substantial variations in the turbine specific work are bound to affect the kinematics of the turbine, including rotational speed, and possibly lead to the prediction of supersonic

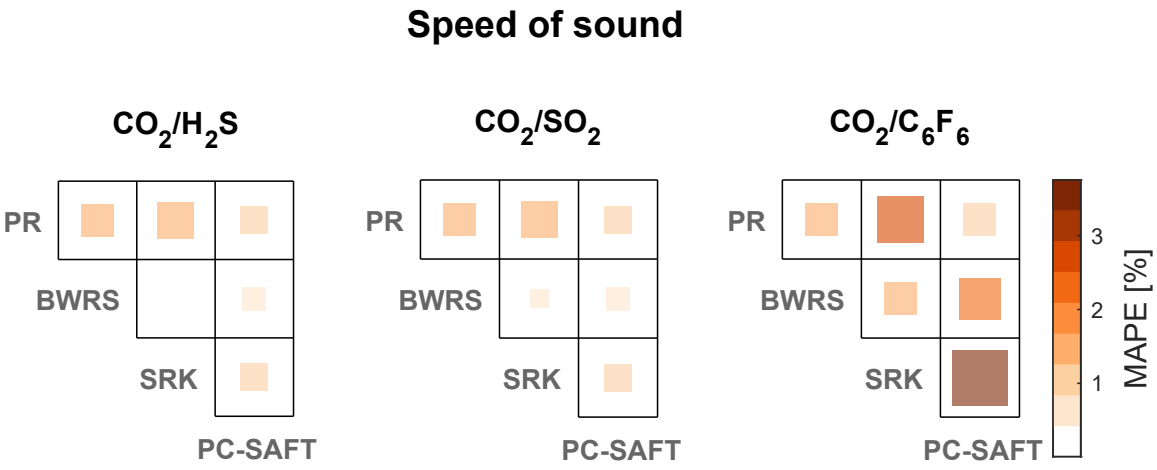

Figure 7.23: The variation in the speed of sound at turbine inlet based on the com-

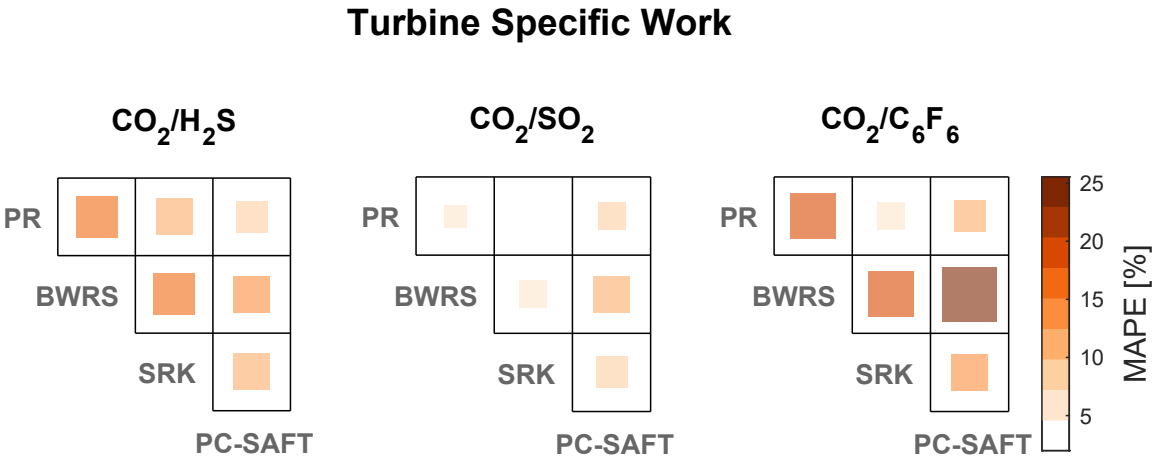

Figure 7.24: The variation in the speed of sound at turbine inlet based on the combined effect of EoS and Δk_{ij}. The size and color map indicate the MAPE [%]

With the power plant output assumed to be fixed, a change in the turbine specific work will cause an opposing change in the mass flow rate of the working fluid. As shown in Figure 7.25, the change in the mass flow rate may be as high as 26%. Consequently, the change in the mass flow rate will likely cause a proportional change in the turbine size. Seemingly, the variation in w_t and mass flow rate are substantial and warrant a closer look at the consequent differences in the turbine design.

To further examine the possible changes in turbine design, the dopant fraction is assumed to be 0.6, 0.4, and 0.34 for CO_2/H_2S , CO_2/SO_2 , CO_2/C_6F_6 , which are the median values of the blend fraction ranges covered in this study, thus are

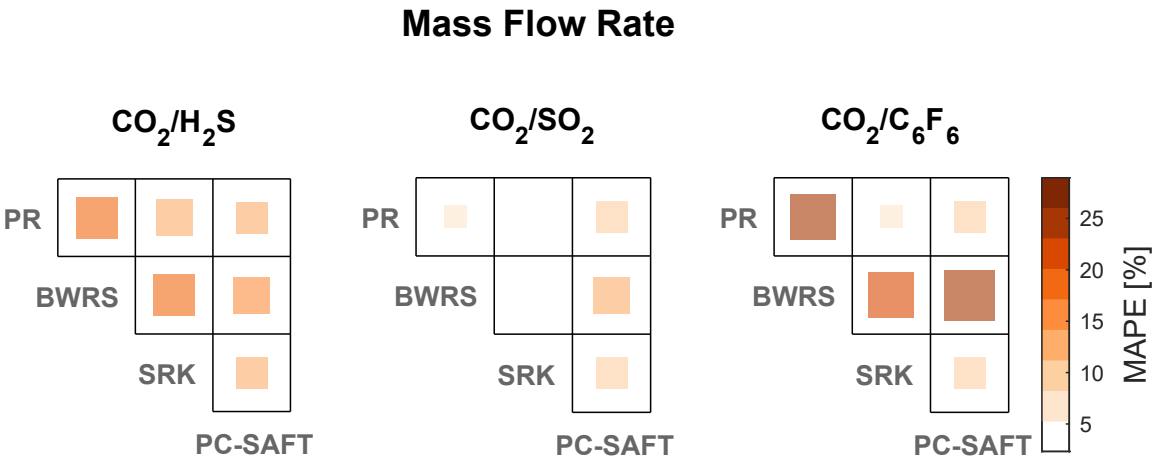

Figure 7.25: The variation in the mass flow rate based on the combined effect of EoS and Δk_{ij}. The size and color map indicate the MAPE [%]

representative of the calculated MAPE. A common set of design parameters, as listed in Table 7.14, is imposed on all the fluids, for all fluid model variations. A fixed set is chosen to provide a common basis for the comparison because the aim is to investigate the change in turbine design; whereas an attempt to optimise the designs contradicts this purpose.

Table 7.14: Parameters imposed on RIT mean line design. A description of these parameters may be found in Chapter 5

Variable	ϕ	ψ	ξ	r_5/r_4	r_{5h}/r_{5sh}
Value	0.23	0.86	1.25	0.50	0.45

The key design parameters studied here are: total-to-static efficiency, rotational speed, and rotor dimensions. In terms of the total-to-static efficiency, the difference in efficiency ranges from 0.05% to 0.35%, as shown in Figure 7.26. However, in the extreme case of CO_2/C_6F_6 with BWRS, the absolute difference in the estimated efficiency can be as high as 0.7%. This conclusion was reached under the assumption that the turbine design was not optimised to match the pressure ratio corresponding to the fluid model. In case the designs are optimised, then fluid models that predict a lower pressure ratio will produce slightly more efficient turbines.

The rotational speed is also affected by the turbine specific work. According to Figure 7.27, the difference in the rotational speed could be as high as 14%. Notice that the trends are identical to those observed in Figure 7.24. Rotor dimensions, indicated

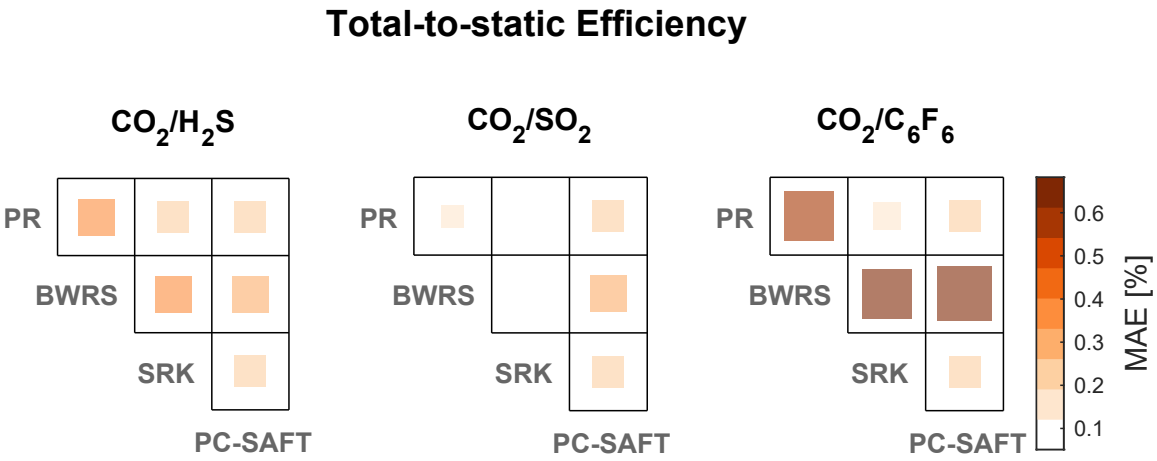

Figure 7.26: The variation in the total-to-static efficiency of the turbine based on the combined effect of EoS and Δk_{ij}. The size and color map indicate the MAE [%]

by the rotor inlet radius in Figure 7.28, are fairly constant, with a maximum deviation of 5%. Although the specific work, rotational speed, and mass flow rate of CO_2/C_6F_6 vary considerably, the rotor dimensions do not. This is likely because the dimensions

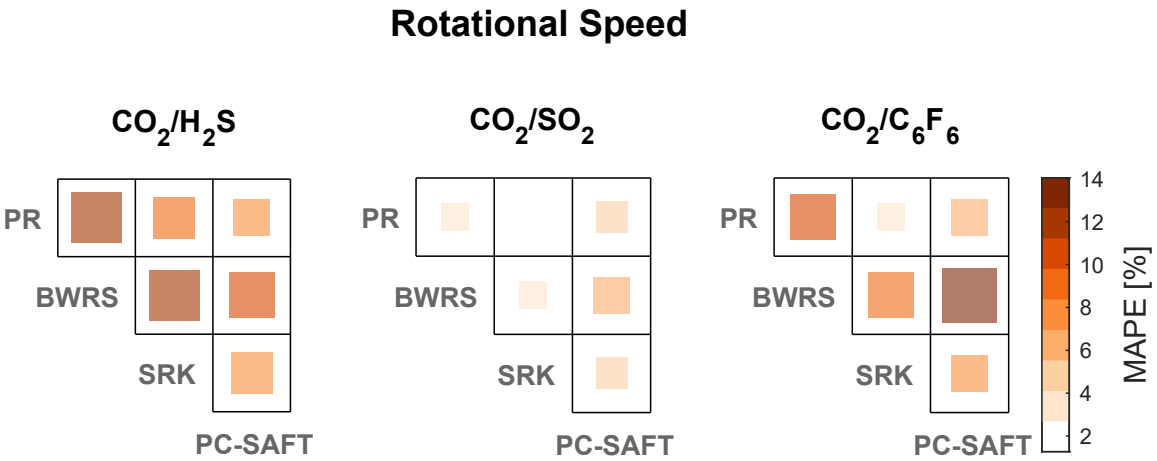

Figure 7.27: The variation in the rotational speed of the turbine based on the combined effect of EoS and Δk_{ij}. The size and color map indicate the MAPE [%]

The trends in total-to-static efficiency indicate the relative change in the losses within the turbine. Naturally, an increase in the specific work will produce a proportional increase in the specific enthalpy loss, which may or may not change the efficiency depending on the relative change between them. Out of the seven loss mechanisms considered in the mean line model, passage and clearance loss are the two most substantial causes of enthalpy loss. Figures 7.29 and 7.30 show that the

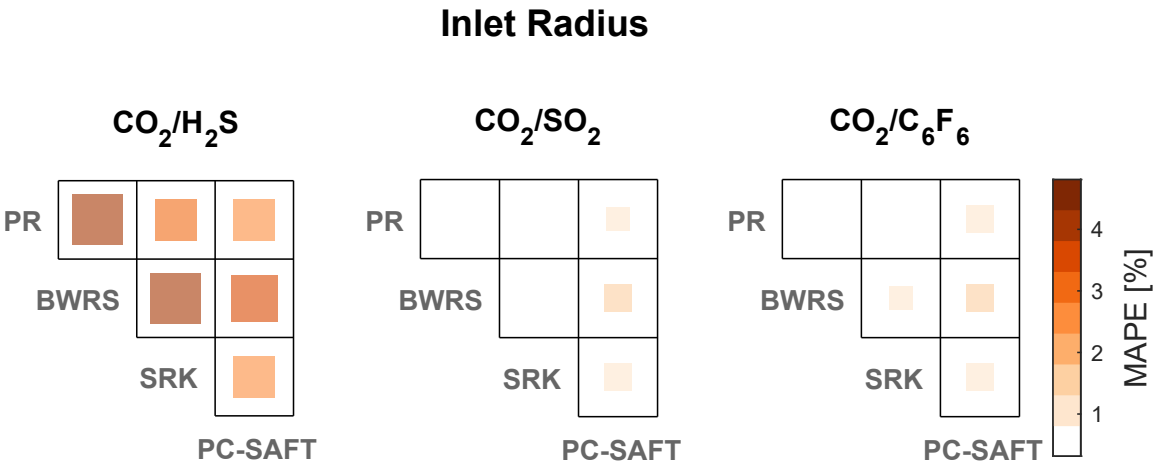

Figure 7.28: The variation in the inlet radius of the turbine based on the combined effect of EoS and Δk_{ij}. The size and color map indicate the MAPE [%]

deviations in passage and clearance loss follow the same trend as the specific work. However, the change in the clearance loss is greater than the change in the passage

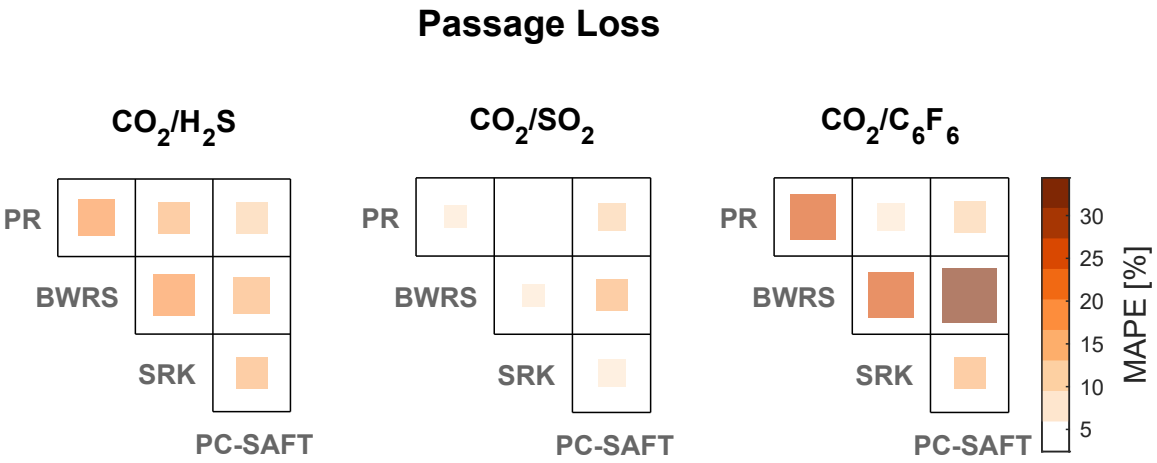

Figure 7.29: The variation in the passage loss based on the combined effect of EoS and Δk_{ij}. The size and color map indicate the MAPE [%]

To test this hypothesis, the simulation is repeated, but for a 100 kWe power plant. All trends in the thermodynamic cycle will not change because the cycle is scale-independent; however, the turbine is not. As seen in Figure 7.31, the change in total-to-static efficiency is 0.3% to 3.0%, compared to the 0.05% to 0.7% range observed in the 10 MWe power plant. This scale-dependence is caused by the increased importance of the variation in the inlet blade height at small scale, and by the rotational speed limitations imposed by the generator.

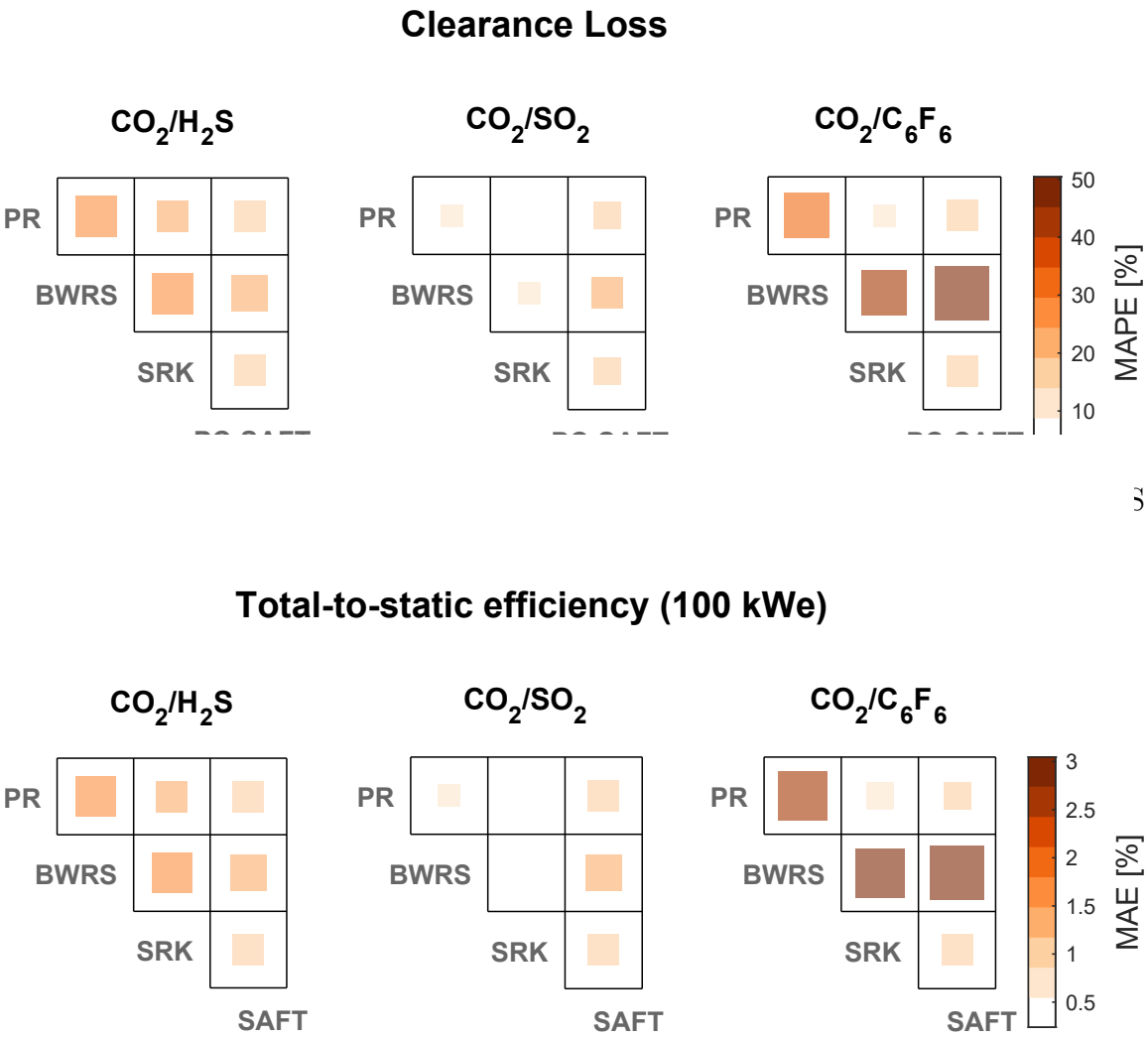

Figure 7.31: The variation in the total-to-static efficiency of the turbine corresponding to the 100 kWe power plant based on the combined effect of EoS and Δk_{ij}. The size and color map indicate the MAE [%]

How does this feedback into the cycle efficiency? An iterative solution of the cycle efficiency using the turbine performance estimate is conducted for both the 10 MWe and 100 kWe. When the variation in the turbine efficiency is accounted for during cycle optimisation, the variation in the cycle efficiency grows in significance. As seen in Figure 7.32, the change in the fluid property model may result in cycle thermal efficiency variations in the order of 0.23% to 3% for 100 kWe transcritical CO_2 -based cycle; a variation in the range of 0.2% to 2.0% for 10 MWe cycles, which is not shown here. Conversely, the change in efficiency that was calculated on the presumption that turbine performance is constant yielded a variation of 0.08% to 1.4%, as already observed in Figure 7.11 Therefore, the variations in cycle efficiency are exacerbated once the change in turbine performance is accounted for.

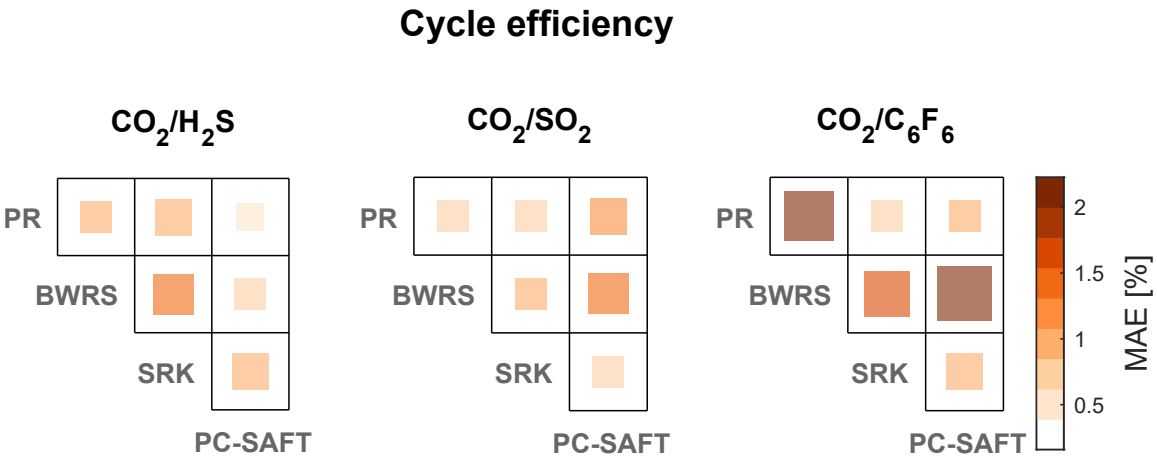

Figure 7.32: The variation in the total-to-static efficiency of the turbine corresponding to the 100 kWe power plant based on the combined effect of EoS and Δk_{ij}. The size and color map indicate the MAE [%]

7.4.2 Decoupled turbine design

The forgoing analysis showed a marked difference among the fluid models in both cycle and turbine designs. The changes in turbine designs are chiefly caused by the change in the pressure ratio.

To ascertain the change in turbine design solely due to the fluid model, the mean line design is repeated, but for a uniform turbine back pressure equal to that of the baseline PR. Consequently, the fluid models are compared only based on their ability to calculate state properties within the vicinity of the turbine boundary temperature and pressure. Decoupling the cycle from the turbine model reduces the variations in the mass flow rate, but it does not eliminate it. This is because, as explained previously, variations in the pump work will persist even with a fixed pressure ratio. Therefore, to decouple the turbine from the cycle, both the pressure ratio and the mass flow rate must be held equal for a given mixture, regardless of the fluid model. In the following analysis, the PR with no k_{ij} variation is taken as the baseline for both the back pressure and mass flow rate.

According to Figures 7.33 and 7.34, turbine performance estimation does not change substantially once the turbine boundary conditions are fixed; in other words, fluid property models converge on similar solutions. This confirms that the variations in turbine design amongst the fluid models are chiefly a consequence of the changes in

ls

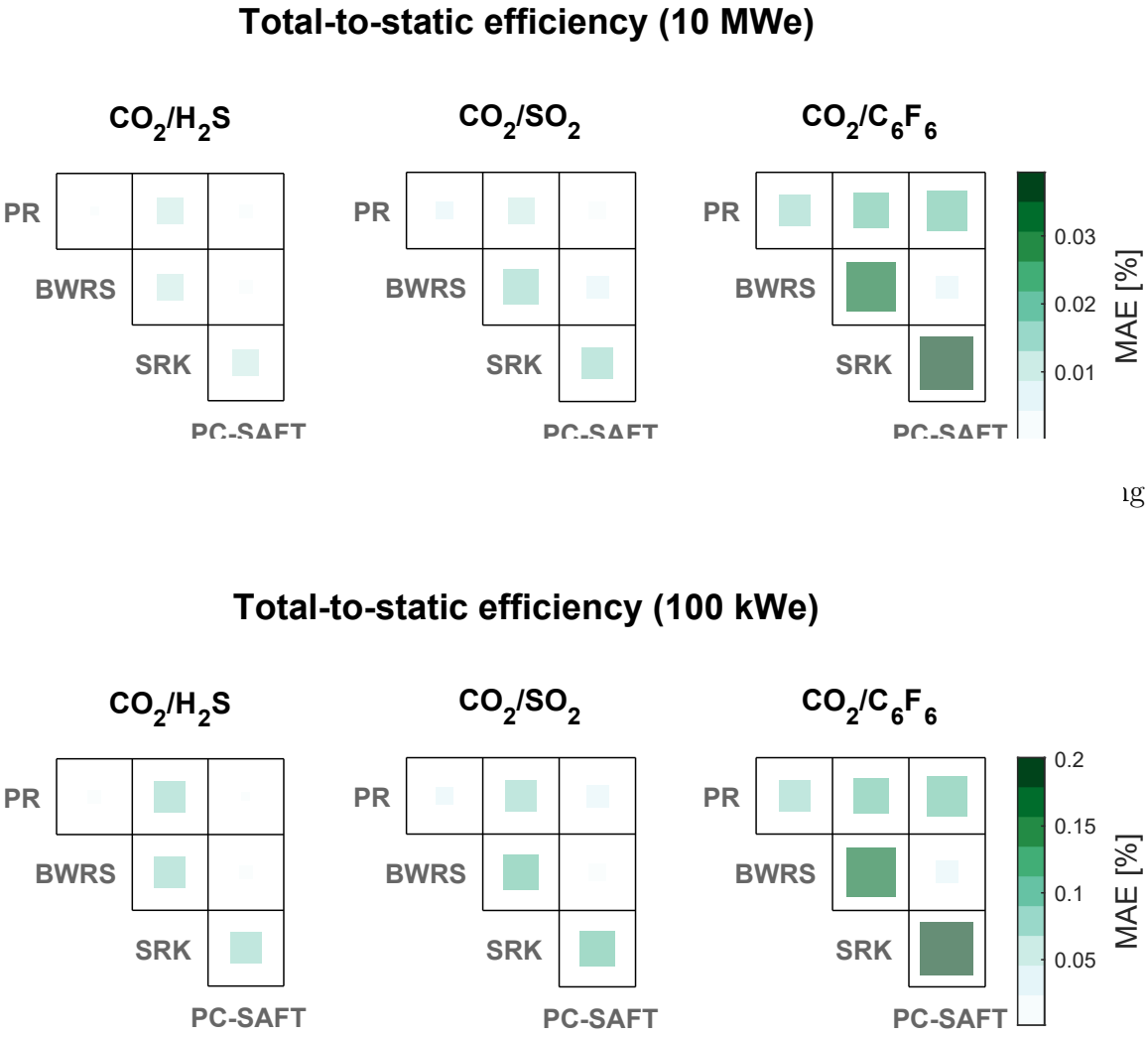

ıg

Figure 7.34: The variation in the total-to-static efficiency of the turbine corresponding to the 100 kWe power plant for common pressure ratio and mass flow rate

Finally, the effect of the fluid model on the turbine design point operation was tested by comparing the CFD simulation results of a CO_2/C_6F_6 radial inflow turbine corresponding to a 10 MWe plant using SRK $+0.5\Delta k_{ij}$ with the results of BWRS $-0.5\Delta k_{ij}$, which according to Figure 7.33 would produce total-to-static efficiencies within 0.015% of each other. The CFD simulations are setup in the same manner described in Section 5.7.3, whereby look-up tables of size 200×200 were generated using Simulus Thermodynamics software for both SRK $+0.5\Delta k_{ij}$ and BWRS $-0.5\Delta k_{ij}$. In both cases, total inlet temperature and pressure and static outlet pressure are set equal to that of the baseline PR, as shown in Table 7.15. Having fixed the turbine

geometry, boundary conditions, and inlet angles, the flow velocities, entropy generation (enthalpy loss), efficiency, mass flow rate, and power output become dependent on the numerical solution.

Table 7.15: Main parameters of the turbine used in the CFD analysis

Variable	**Value**	**Variable**	**Value**	**Variable**	**Value**
T_{04}[°C]	973	r_2[cm]	15.9	b_4 [cm]	1.39
p_{04} [MPa]	25	r_4[cm]	14.5	L_{z} [cm]	7.7
p_5 [MPa]	8.92	$r_{5\mathrm{h}}$ [cm]	4.2	$\epsilon_{a,r}[mm]$	0.4
N[kRPM]	30.0	$r_{5\mathrm{s}}$ [cm]	9.4	Z_{r}	16
Z_{n}	19	α_2[°]	59	$\beta_{5\mathrm{h}}$[°]	51

The difference in some of the key parameters are listed in Table 7.16. The difference in the predicted performance is inline with that estimated by the mean line model. There is a higher difference in the mass flow rates required by the two fluid models, which also leads to a comparable difference in the power output from the turbine. A likely cause for the difference in the mass flow rate is the difference in the inlet density. Therefore, there is an inherent discrepancy between the predictive capabilities of the fluid models, which could lead to incompatible turbine designs even though though the fluid models are most consistent in the vicinity of the expansion process. Such dissimilarities will feedback into the cycle design and exacerbate the effect of the fluid model selection and calibration.

Table 7.16: Percentage change in key turbine parameters between SRK and BWRS for common turbine design and boundary conditions based on the results of the CFD analysis

Variable	η_{ts}	$\dot{m}$	Power	ρ_4	ρ_5
Difference [%]	0.10	1.0	1.6	2.6	2.2

Apart from the variables compared in Table 7.16, the blade loading, static density, and absolute velocity patterns within the passages of the turbine may also be compared. These are shown in Figures 7.35 to 7.37, where the profiles for both models are closely matched. Moreover, the entropy along the streamwise direction shown in Figure 7.38 indicates a similar pattern between the two models. This is confirmed

Appar-

ences.

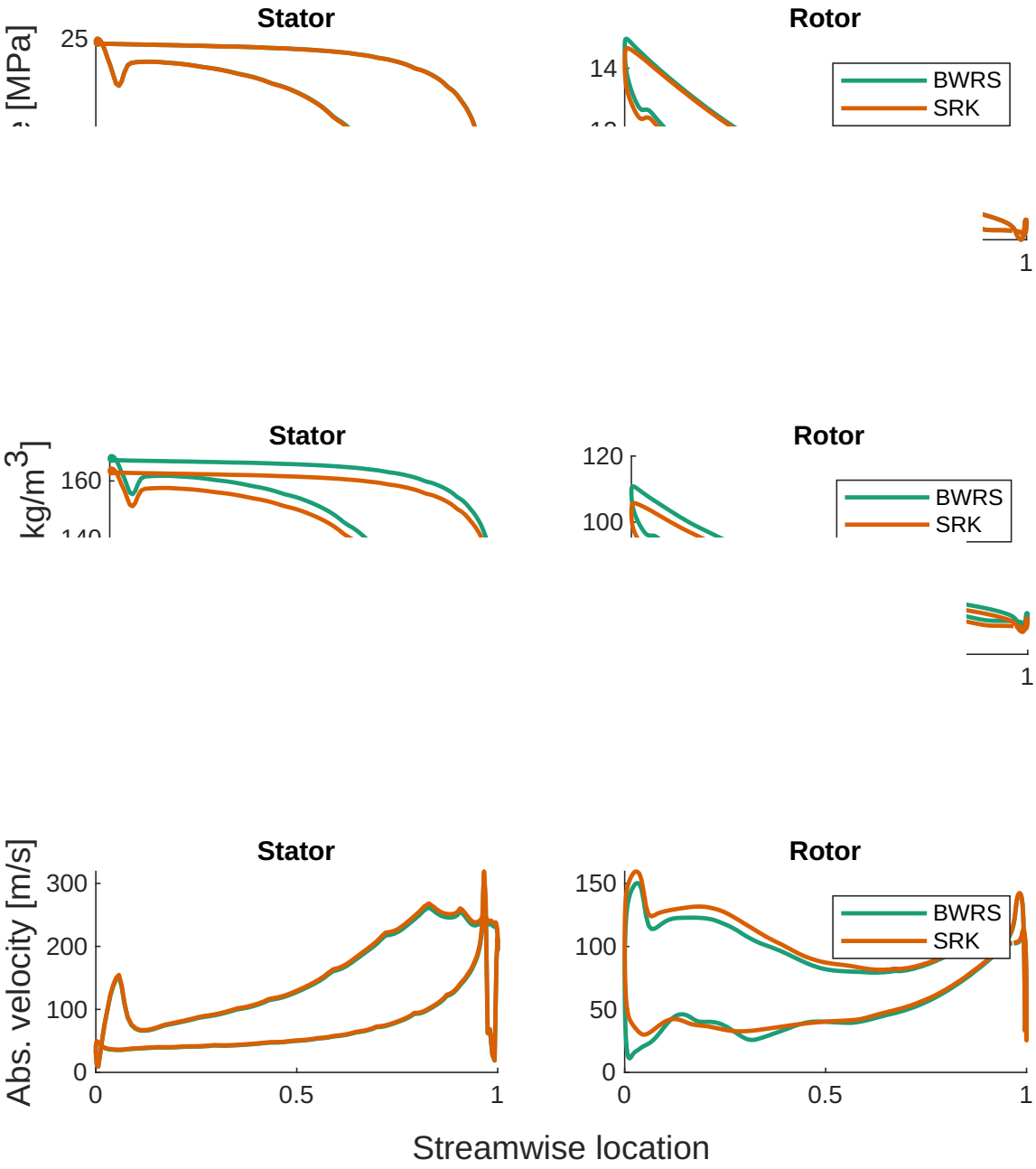

Figure 7.37: Absolute velocity in the streamwise direction.

7.5 Summary

In this chapter, the sensitivity of cycle and turbine design to the fluid property model was investigated. The study included three CO_2-based mixtures: CO_2/H_2S , CO_2/SO_2 , and CO_2/C_6F_6 ; in combination with four equations of state: PR, BWRS,

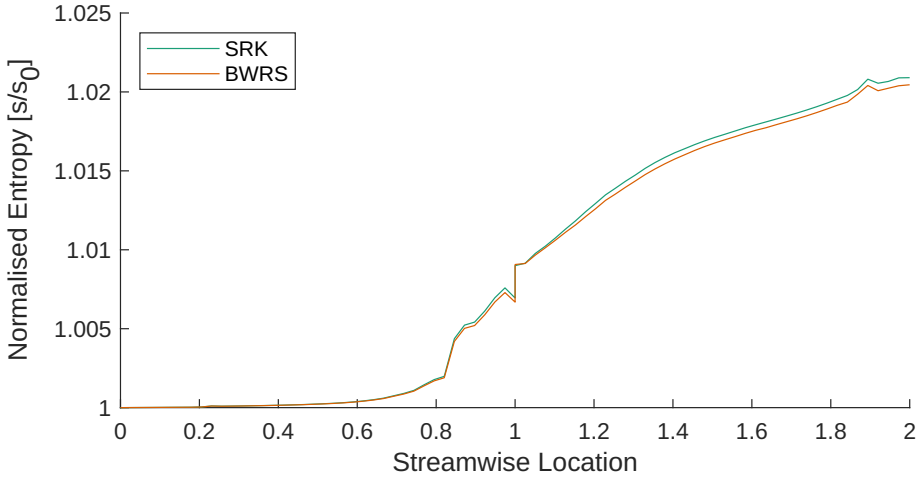

Figure 7.38: Normalised entropy in the streamwise direction.

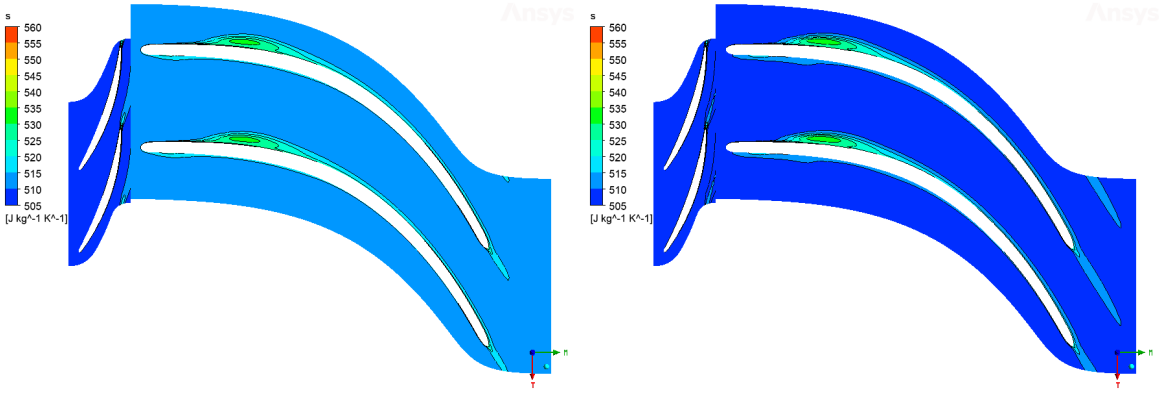

(a) SRK (b) BWRS

Figure 7.39: Contours of entropy at 20% span

SRK, and PC-SAFT; each modelled under scenarios of k_{ij} uncertainty ($\pm 50\% \Delta k_{ij}$). It was found that the choice of the dopant fraction which yields maximum cycle thermal efficiency for each mixture is independent of the fluid model used; at least within the dopant fraction ranges considered here. However, the predicted optimal thermal efficiency of the mixtures is reliant on the fluid model.

Based on cycle thermal efficiency calculations, the sensitivity of the equations of state to Δk_{ij}, in descending order, is: BWRS, PC-SAFT, PR, and SRK. The two cubic equations of state, PR and SRK, are generally less sensitive to k_{ij} variation than BWRS or PC-SAFT. This suggests that they offer more robust property prediction in the absence of quality experimental data. On the other hand, the BWRS EoS is especially sensitive to k_{ij} uncertainty, thus requires precise model calibration before it can be used reliably. Whereas, the order of sensitivity of the mixtures, in descending

order, is: CO_2/C_6F_6 ,CO_2/H_2S , and CO_2/SO_2 . The maximum uncertainty due to Δk_{ij} was found to be 0.34% when modelling CO_2/H_2S with BWRS. Generally, it is expected that fluid models with lower k_{ij} values are more likely to be affect by nominal Δk_{ij}. Moreover, cycle thermal efficiency was observed to have a positive correlation with the Δk_{ij} value for all mixture and EoS combinations. On the other hand, thermal efficiency may vary by a maximum of 1% due to the choice of the EoS assuming no variation in k_{ij}, with CO_2/C_6F_6 being the least consistent among the mixtures. If both the choice of the EoS and Δk_{ij} are considered, then the combined difference is in the range of 0.08% to 1.4%, depending on the mixture and EoS.

To determine the cause of these differences in the cycle thermal efficiency, four cycles with a combination of simple-recuperated/simple-non-recuperated and constant/varying pressure ratios were compared. The cause of the variation in cycle thermal efficiency was attributed to the change in the isobaric specific heat capacity in the vicinity of the pump, which changes pump work and the required heat input. The change in the pump inlet pressure, which affects the net work of the cycle, the heat input, and the internally recuperated heat, also contributes to the dissimilarities among the fluid models. Ultimately, the divergence of the isobaric specific heat and pump inlet pressure may be attributed to the divergence in the saturation curve shape between CO_2 and the dopants; the greater the difference, the greater is the effect of the uncertainty in the fluid model.

In terms of turbine design, all fluid models converged on similar property calculations in the vicinity of the turbine. However, turbine designs differed because the pressure ratios were inconsistent and depended on the fluid model. To quantify the turbine design dependence on the fluid model, a mean line model was used to generate radial inflow turbine designs. According to designs of 12 MW turbines, the total-to-static efficiency may vary by 0.05% to 0.7% points. The variation is even greater for smaller turbines, which is 0.3% to 3.0% for a 120 kW radial inflow turbine. Therefore, fluid model dependency is scale dependent.

The investigation was extended to an iterative design process by which the new turbine efficiency estimate was used to update the cycle optimisation. Once turbine

performance estimates were accounted for, the variation in the cycle efficiency increased to a range of 0.2% to 2.0% for a 10 MWe power plant, 0.23% to 3.0% for a 100 kWe power plant.

Finally, since most of the disagreements in turbine design may be caused by the pressure ratio and the mass flow rate, the expansion process was decoupled from the cycle by assuming a common mass flow rate and common boundary conditions among the fluid models for the same mixture. Indeed, variations in the total-to-static efficiency of the turbines diminished considerably. This was also confirmed using CFD simulations of two EoS-k_{ij} combination as an example.

In conclusion, the choice and calibration of the fluid model may have implications on efforts of modelling of CO_2 mixtures; incorrect calibration of k_{ij} may lead to considerable deviations in the turbine design, especially for small scale power plants. Fortunately, the overall uncertainty may be alleviated if a high fidelity model is used to calculate the properties near the saturation dome, where most of the discrepancies are expected to occur. Based on the findings of this analysis, modelling of CO_2-based working fluids requires good quality experimental data to minimise the uncertainty in the calibration of k_{ij}; the greater the difference between the shapes of the saturation curves between CO_2 and the candidate dopant, the greater is the uncertainty, thus the greater the need for good data. Cubic equations of state showed the most consistency against the uncertainty in the choice and calibration of the fluid model, thus are recommended for when using thermodynamic models to compare CO_2-based mixtures.

This page is left intentionally blank.

Chapter 8

Conclusion and recommendations for future work

8.1 Conclusion

In the introduction to this thesis, the potential for electricity generation using CSP plants was outlined. To maximise the thermal efficiency of a CSP plant, the concentration ratio should be maximised, which in turn helps to reduce the levelised cost of electricity (LCoE) of the plant. Therefore, a power block that can efficiently operate at high temperatures is preferable. One such cycle is the sCO_2 Brayton cycle, which outperforms the state-of-the-art steam Rankine cycle at temperatures above 550 ^oC. Because compression occurs near the critical point in a sCO_2 cycles, the thermal efficiency of the cycle degrades if the cooling temperatures exceed the critical temperature of CO_2 (31.1 ^oC) due to the increase in the compression work required. Consequently, the use of ambient air for dry-cooling in a CSP power plant penalises the overall efficiency of the plant and increases the LCoE.

One possible solution to this problem is to raise the critical temperature of the CO_2 by doping it to produce a mixture with a higher critical temperature. The choice and amount of the dopant are informed by the expected ambient air temperature; the higher the ambient air temperature, the higher the critical temperature required.

The resultant mixture is expected to have a critical temperature that is high enough to ensure liquid-phase compression after cooling, thus lower compression work and reducing the sensitivity of the cycle performance to cooling temperatures.

This thesis is part of the SCARABUES project which investigates the benefit of power cycles operating with CO_2-based mixtures as a possible pathway to improve the efficiency of CSP plants and reduce LCoE. Amongst the dopants identified by the SCARABUES project are $TiCl_4$, SO_2, C_6F_6 which are used as examples to study the effect of doping CO_2 on the cycle performance and architecture, on the expansion process, and on the design of radial inflow turbines across power scales.

Chapter 1 begins by introducing the theory underlying heat engines (power cycles), specifically those employing CO_2 as a working fluid. Then, the potential of solar power and the benefit of CSP plants were outlined before highlighting the challenges facing the implementation of CO_2 cycles in CSP plant. Subsequently, the objectives of this thesis were formulated:

- **Identify the dopant molar fractions which yield the highest efficiency in a transcritical cycle whilst considering the achievable turbine efficiencies across power scales;**
- **Determine the effect of dopant molecular complexity on the choice between simple recuperated and recompression cycles;**
- **Determine the effect of doping CO_2 on the design of radial inflow turbines and on their feasible design space when adapted to a small- to medium-scale power plants;**
- **Quantify the uncertainty in the optimisation of the cycle and turbine design due to the method of thermophysical property calculation.**

In Chapter 2, a review of the literature pertaining to CO_2 cycles with a focus on their implementation in CSP plants was presented. Moreover, considerations of working fluid behaviour and selection were also contextualised with respect to the potential doping of CO_2. A review of the literature on the design of turbines of

CO_2 applications shows that turbine performance is expected to greatly influence the performance of the power block; therefore, ensuring high turbine efficiencies is a crucial part of the design process. Research into sCO_2 turbines has shown its compactness and high-performance potential. High rotational speeds, aerodynamic losses, and mechanical integrity are amongst the possible design restrictions that must be heeded in the turbine design process, especially in small scale power plants.

Effect of dopant on cycle design

A methodology for modelling CO_2 power cycles was presented in Chapter 3 to study the effect of doping on cycle behaviour and on the characteristics of the expansion process. The simulation results in Chapter 4 for a 100 MWe CSP plant show the effect of the three dopants ($TiCl_4$, SO_2, and C_6F_6) and their molar fractions on the optimal thermodynamic cycle conditions and turbine design. Increasing dopant molar fraction was found to increase the pressure ratio of the cycle for all blends. The maximum achievable cycle efficiencies were found to be 48.1%, 46.5%, and 42.2% for molar fractions of 0.17 of $CO_2/TiCl_4$, 0.21 of CO_2/SO_2, and 0.17 of CO_2/C_6F_6.

By studying a 100 MWe power plant as an example, preliminary turbine sizing data was presented. For a utility-scale power plant, an axial turbine is expected to be the turbine type that achieves the highest efficiency. Therefore, a four-stage axial turbine was studied as an example. This serves to investigate the sensitivity of the turbine design to the blend and molar fraction before moving onto a more detailed turbine design optimisation stage. Since heavier working fluids reduce the specific work, they increase the mass flow rate into the turbine, which in turn requires larger flow annuli. On the other hand, the turbine mean diameter is smaller for heavy dopants ($TiCl_4$ and C_6F_6). Therefore, they require narrower but longer turbines compared to the lighter dopant (SO_2) with the same number of stages.

The effect of the choice of dopant and its molar fraction on the performance of recompression cycles was also investigated. The study involved nine dopants with different molecular complexities and properties. Additionally, the pump inlet temperature was lowered to 15 ^oC to ensure liquid phase compression with all nine dopants,

thus the study was outside the realm of dry-cooled CSP plants with such a low cooling temperature. It was found that the benefit of a recompression cycle diminishes as the aggregate molecular complexity of the working fluid increases. For simple dopants, such as H_2S and SO_2, the recompression cycle will outperform the simple recuperated cycle, regardless of the dopant molar fraction. On the other hand, more complex dopants may achieve thermal efficiencies in simple recuperated cycles that are comparable to a recompression cycle. The dopant molar fraction at which both cycles achieve a similar performances depends on the molecular complexity of the dopant; the more complex the dopant, the lower the molar fraction at which this occurs.

Effect of dopant on the design of radial inflow turbines

Moving to smaller power plants (0.1 MW to 10 MW) will likely require the use of radial inflow turbines. In Chapter 5, the theory underpinning radial inflow turbines was introduced along with the phases of design development. A mean-line model was chosen for the purpose of comparing turbine designs of CO_2-mixtures because it is quick to execute but provides main design features and performance estimates. The mean-line model was described in detail, verified with another model from the literature, and validated using CFD for three dopants and pure CO_2.

The design of small- to medium-scale radial inflow turbines under multiple design assumptions were analysed in Chapter 6 with the aim of discerning the effects of doping CO_2 under different design scenarios and across power scales. Initially, the rotational speeds of the turbines were not limited. With similar turbine inlet conditions but with pressure ratios imposed by their respective cycles (design scenario 'Case-B'), $CO_2/TiCl_4$ achieved the highest performance, followed by CO_2/C_6F_6, and then CO_2/SO_2. For example, 100 kW turbines for $CO_2/TiCl_4$, CO_2/C_6F_6, CO_2/SO_2, and CO_2 achieve total-to-static efficiencies of 80.0%, 77.4%, 78.1%, and 75.5% respectively. Whereas, the efficiencies for 10 MW turbines are 87.8%, 87.3%, 87.5%, and 87.2%, in the same order. Moreover, multi-staging of CO_2, CO_2/SO_2, and CO_2/C_6F_6 turbines is more beneficial than for $CO_2/TiCl_4$ because of the high pressure ratios

required by the cycle within which they are used. On the other hand, with the same inlet conditions and pressure ratio, the aerodynamic behaviour of the working fluids was similar; therefore, turbine designs for all working fluids converged on similar rotor shapes and velocity diagrams. Indeed, the total-to-static efficiency of all turbines were within ±1% of each other, at all power scales.

The differences between the turbine designs of the mixtures grew as practical limitations on the rotational speed were imposed. The rotational speed for 0.1 MW, 1 MW, and 10 MW turbines were limited to 151 kRPM, 46.4 kRPM, and 14.3 kRPM, respectively. At it's greatest, the difference between the total-to-static efficiency of the $CO_2/TiCl_4$ turbine and the CO_2 turbine was approximately 19% at a power scale of 100 kW for design scenario 'Case-B'.

Variations in the achievable total-to-static efficiency amongst the fluids stem from variations in their clearance-to-blade height ratio, their pressure ratios, rotational speed limits, and, to a lesser degree, differences in their viscosity. Although doping CO_2 has little effect on the aerodynamic behaviour of CO_2, it is the consequence of the change in cycle conditions along with the design limitations of radial inflow turbines that lead to differences in the performance of the turbines amongst the fluids. These differences are greatest in small scale turbines (<100 kW); with fluids that produce turbines of greater blade heights having the highest efficiency. The effect of clearance loss is attenuated with design optimisation by allowing greater flow coefficients, which increase velocities and reduce tip clearance loss. Consequently, the optimal design has a higher specific speed; however, the implementation of a limit on the rotational speed of the turbine induces the opposite effect.

Conjugate optimisation of the cycle and turbine designs, wherein the turbine efficiency is estimated using the 1D meanline model rather than assuming a constant isentropic efficiency, revealed that the influence of the turbine design on cycle design and performance increases at smaller scales. Moreover, the achievable performance of radial inflow turbines due to practical restrictions does not affect the choice of the dopant molar fraction; the same dopant molar fraction will maximise cycle efficiency regardless of the turbine efficiency or scale of the power plant. Therefore, the choice

of the dopant molar fraction is dependant on the irreversibility within the recuperator of a simple transcritical cycle.

Effect of fluid properties calculation on modelling results

Finally, apart from the choice of the equation of state (EoS), modelling binary mixtures adds an additional uncertainty to the fluid property calculation model due to the binary interaction parameter k_{ij}. Therefore, the sensitivity of cycle and turbine design to the fluid property model was investigated in Chapter 7. The study included three CO_2-based mixtures: CO_2/H_2S , CO_2/SO_2 , and CO_2/C_6F_6 ; in combination with four equations of state: Peng-Robinson (PR), Benedict- Webb-Rubin modified by Starling and Nishiumi (BWRS), Soave-Redlich-Kwong (SRK), and Perturbed Chain Statistical Associating Fluid Theory (PC-SAFT); each modelled under scenarios of k_{ij} uncertainty ($\pm 50\% \Delta k_{ij}$).

Generally, it is expected that fluid models with lower k_{ij} values are more likely to be affected by nominal Δk_{ij}. If both the choice of the EoS and Δk_{ij} are considered, then the combined difference in the cycle thermal efficiency will be in the range of 0.08% to 1.4%, depending on the mixture and EoS. To determine the cause of these differences in the cycle thermal efficiency, four cycles with a combination of simple-recuperated/simple-non-recuperated and constant/varying pressure ratios were compared. The cause of the variation in cycle thermal efficiency was attributed to the change in the isobaric specific heat capacity in the vicinity of the pump, which changes pump work and the required heat input.

In terms of turbine design, all fluid models converged on similar property calculations in the vicinity of the turbine. However, turbine designs differed because the pressure ratios were inconsistent and depended on the fluid model. To quantify the turbine design dependence on the fluid model, a mean line model was used to generate radial inflow turbine designs. According to designs of 12 MW turbines, the total-to-static efficiency may vary by 0.05% to 0.7% points. The variation is even greater for smaller turbines, which is 0.3% to 3.0% for a 120 kW radial inflow turbine. Therefore, fluid model dependency is scale dependent. The investigation was

extended to an iterative design process by which the new turbine efficiency estimate was used to update the cycle optimisation. Once turbine performance estimates were accounted for, the variation in the cycle efficiency increased to a range of 0.2% to 2.0% for a 10 MWe power plant, 0.23% to 3.0% for a 100 kWe power plant.

In conclusion, the choice and calibration of the fluid model may have implications on efforts of modelling of CO_2 mixtures; incorrect calibration of k_{ij} may lead to considerable deviations in the turbine design, especially for small scale power plants. Fortunately, the overall uncertainty may be alleviated if a high fidelity model is used to calculate the properties near the saturation dome, where most of the discrepancies are expected to occur. Cubic equations of state showed the most consistency in thermodynamic model results considering the choice and calibration of the fluid model, thus they are recommended for when using thermodynamic models to compare CO_2-based mixtures.

8.2 Future work

Techno-economic assessment of small-scale CSP plants

Although the performance of small-scale CSP plants operating with CO_2-based mixtures has been investigated in this thesis, the economic feasibility of such installations has not been assessed. A complete techno-economic assessment that considers both the capital and operational costs of these plants is necessary to determine the most economic choice of dopant, dopant fraction, cycle layout, and operating conditions. Such a cost analysis would account for all component costs including the heat exchangers, turbomachinery, and auxiliary equipment that comprise the power block, as well as the costs of other CSP components including the thermal energy storage and heliostat field. Crucially, off-design performance models for all equipment will need to be developed considering the seasonal variation in solar irradiance and the variable operation of CSP plants.

Depending on the power capacity, the power plant should be compared against competing technologies. For the 0.1-10 MW scale, CSP plant would be compared

with PV with batteries. Common knowledge would show that PV plants are most likely to be cheaper. However, a comprehensive comparison should also consider life cycle assessment, including environmental impact.

Choice of dopants

Although several dopants have been considered in this work, there are thousands more that may be used to adapt sCO_2 cycles to different applications. Working fluids engineering extends beyond CSP applications, indeed there is an established body of literature that investigates working fluid selection based on cycle operating conditions which are informed by the application, such as those of Organic Rankine Cycles or heat pumps. The search for CO_2 dopants may be extended to mixtures of more than two components (possibly tertiary mixtures) and reactive working fluids as studies have shown their potential to advance power cycles(Lasala et al. 2021, Barakat et al. 2022).However, the choice of the working fluid is not solely based on its thermodynamic properties, but also other criteria must be considered such as the environmental impact, toxicity, thermal stability, cost, and safety of the fluid.

Working fluid modelling accuracy

The effect of experimental data quantity and quality on model precision was demonstrated in Chapter 7. Therefore, in terms of working fluid property estimation, it is recommended to obtain good quality vapour-liquid equilibrium experimental data of CO_2-based mixtures for the calibration of the equations of state before proceeding with thermodynamic modelling. Otherwise, an uncertainty as high as 1.4% should be added to the estimates of the cycle thermal efficiency.

Experimental validation of loss models for sCO_2 turbines

In recent years, the growing interest in CO_2 power cycles and it's maturity has advanced into the design of its components. Seeing that turbine design holds great sway over the cycle efficiency it is recommended to develop loss models that are based

on kW-scale stationary cascade tests conducted with CO_2 as the working fluid, or loss models that are informed from high-fidelity CFD simulations. This would allow greater confidence in the mean-line design results in the future. Although the same is applicable to loss models for CO_2 mixtures, the need for such models is difficult to justify at the present. Why is that? Because as has been explained in this thesis, the choice of dopant and its amount will depend on the application and cycle conditions; therefore, it is impractical to develop loss models for specific dopants. Whereas loss models for CO_2 may likely me extended to CO_2-based mixtures as well seeing that the fluid behaviour is close to ideal and therefore the aerodynamic performance of CO_2 or CO_2 mixture would be very similar for a given volume ratio and flow rate.

Radial inflow turbine design considerations

Based on the findings of this thesis, tip gap clearance penalises the efficiency of small-scale radial inflow turbines and may advantage some dopants over others. Seeing that blade tip speeds, thus centrifugal stresses, are not a major limitation in turbines for CO_2-based mixtures, shrouded turbines should be considered to improve turbine performance. However, shrouded turbines add mass to the shaft which affects rotordynamic stability and should be considered at small scale because of high rotational speeds. This points to the need to consider rotordynamics as well as mechanical stress considerations.

Moreover, since the turbine pressure ratio is informed by the cooling temperature in a transcritical cycle, it was found that some dopants would require higher pressure ratios, therefore, two-stage designs should be considered to avoid choked flow. Multi-stage also has the benefit of potentially having back-to-back arrangements whereby axial thrust forces can be reduced, but here the turbines needs to be optimised for the same rotational speed. Alternatively, gearboxes or separate generators may be used.

List of References

Abdeldayem, A., Salah, S., Aqel, O., White, M., Ruggiero, M. & Sayma, A. (2023), Design of a 130 MW axial turbine operating with a supercritical carbon dioxide mixture for the SCARABEUS project, *in* 'Proceedings of 15th European Conference on Turbomachinery Fluid dynamics Thermodynamics', pp. 1–15.

Ahn, Y., Bae, S. J., Kim, M., Cho, S. K., Baik, S., Lee, J. I. & Cha, J. E. (2015), 'Review of supercritical CO2 power cycle technology and current status of research and development'.

Ahn, Y., Lee, J. J. I., Kim, S. G., Lee, J. J. I., Cha, J. E. & Lee, S. W. (2015), 'Design consideration of supercritical CO2 power cycle integral experiment loop', *Energy* **86**, 115–127.
URL: *http://dx.doi.org/10.1016/j.energy.2015.03.066*

Al-Sulaiman, F. A. & Atif, M. (2015), 'Performance comparison of different supercritical carbon dioxide Brayton cycles integrated with a solar power tower', *Energy* **82**, 61–71.

Albrecht, K. J. & Ho, C. K. (2019), 'Design and operating considerations for a shell-and-plate, moving packed-bed, particle-to-sCO2 heat exchanger', *Solar Energy* **178**(September 2018), 331–340.
URL: *https://doi.org/10.1016/j.solener.2018.11.065*

Alfani, D., Neises, T., Astolfi, M., Binotti, M. & Silva, P. (2022), 'Techno-economic analysis of CSP incorporating sCO2brayton power cycles: Trade-off between cost and performance', *AIP Conference Proceedings* **2445**(May).

Allison, T. C., Jeffrey Moore, J., Hofer, D., Towler, M. D. & Thorp, J. (2019), 'Planning for successful transients and trips in a 1 MW e -Scale High-Temperature sCO 2 test loop', *Journal of Engineering for Gas Turbines and Power* **141**(6), 1–12.

Allison, T. C., Moore, J., Pelton, R., Wilkes, J. & Ertas, B. (2017), Turbomachinery, *in* 'Fundamentals and Applications of Supercritical Carbon Dioxide (SCO2) Based Power Cycles', Elsevier Inc., pp. 147–215.

Alsagri, A. S., Chiasson, A. & Gadalla, M. (2019), 'Viability assessment of a concentrated solar power tower with a supercritical CO2 Brayton cycle power plant', *Journal of Solar Energy Engineering, Transactions of the ASME* **141**(5).

Alvin F. Hildebrandt, L. L. V.-H. (1977), 'Power with heliostats', *Science* **197**(4309), 1139–1146.

Angelino, G. (1967), 'Perspectives for the liquid phase compression gas turbine', *Journal of Engineering for Gas Turbines and Power* .

Angelino, G. (1968), 'Carbon dioxide condensation cycles for power production', *Journal of Engineering for Gas Turbines and Power* .

Angelino, G. (1969), Real gas effects in carbon dioxide cycles, *in* 'International Gas Turbine Conference Products Show'.

Angelino, G. & Colonna Di Paliano, P. (1998), 'Multicomponent working fluids for organic Rankine cycles (ORCs)', *Energy* **23**(6), 449–463.

Anselmi, E., Johnston, M. & Bunce, I. (2018), 'An Overview of the Rolls-Royce sCO 2 -Test Rig Project at Cranfield', *The 6th International Symposium - Supercritical CO2 Power Cycles* .

Arora, J. (2017), *Introduction to Optimum Design*, Elsevier.
URL: *https://linkinghub.elsevier.com/retrieve/pii/C20130153445*

Atkinson, M. J. (1998), The Design of Efficient Radial Turbines for Low Power Applications, PhD thesis, University of Sussex.

Aungier, R. H. (2006), *Turbine Aerodynamics: Axial Flow and Radial-Inflow Turbine Design and Analysis*, ASME PRESS.

Bai, W., Li, H., Zhang, X., Qiao, Y., Zhang, C., Gao, W. & Yao, M. (2022), 'Thermodynamic analysis of CO2SF6 mixture working fluid supercritical Brayton cycle used for solar power plants', *Energy* **261**(PB), 124780.
URL: *https://doi.org/10.1016/j.energy.2022.124780*

Baines, N. (1998), A meanline prediction method for radial turbine efficiency, *in* 'Sixth international conference on turbocharging and air management systems'.

Baines, N. (2005), Radial turbines: An integrated design approach, *in* '6th conference on turbomachinery: fluid dynamics and thermodynamics'.

Baines, N. C. (1996), 'Flow development in radial turbine rotors', *ASME 1996 International Gas Turbine and Aeroengine Congress and Exhibition, GT 1996* **1**.

Baljé, O. E. (1962), 'A study on design criteria and matching of turbomachines: Part A-similarity relations and design criteria of turbines', *Journal of Engineering for Gas Turbines and Power* **84**(1), 83–102.

Balje, O. E. (1981), *Turbomachines - A Guide to Design Selection and Theory*, Wiley-Interscience.

Banuti, D., Ihme, M. & Raju, M. (2018), On the characterization of transcritical fluid states, Technical report, Stanford University.

Banuti, D. T., Raju, M., Ma, P. C., Ihme, M. & Hickey, J. P. (2017), 'Seven questions about supercritical fluids towards a new fluid state diagram', *AIAA SciTech Forum - 55th AIAA Aerospace Sciences Meeting* (January).

Barakat, A., Lasala, S., Arpentinier, P. & Jaubert, J. N. (2022), 'The original and impactful exploitation of chemical energy in heat pumps', *Chemical Engineering Journal Advances* **12**(September).

Bertini, M., Fiaschi, D., Manfrida, G., Niknam, P. H. & Talluri, L. (2021), 'Evaluation of the property methods for pure and mixture of CO 2 for power cycles analysis', *Energy Conversion and Management* **245**, 114568.
URL: *https://doi.org/10.1016/j.enconman.2021.114568*

Besarati, S. M. & Goswami, D. Y. (2016), Supercritical CO2 and other advanced power cycles for concentrating solar thermal (CST) systems, *in* 'Advances in Concentrating Solar Thermal Research and Technology', Elsevier Inc., pp. 157–178.

Besarati, S. M. & Yogi Goswami, D. (2014), 'Analysis of Advanced Supercritical Carbon Dioxide Power Cycles With a Bottoming Cycle for Concentrating Solar Power Applications', *Journal of Solar Energy Engineering* **136**(1), 1–7.

Bhatia, S. C. (2014), *Advanced Renewable Energy Systems, (Part 1 and 2)*, WPI Publishing.
URL: *https://www.taylorfrancis.com/books/9781782422730*

Bianchi, G., Bianchi, G., Saravi, S. S., Loeb, R., Andri, I. & Le, O. (2019), Design of a heat to conversion facility for on power Design of a high-temperature heat

to power conversion facility for testing supercritical CO2 equipment and packaged power units, *in* 'Energy Procedia', Vol. 161, Elsevier B.V., pp. 421–428.
URL: *https://doi.org/10.1016/j.egypro.2019.02.109*

Bidkar, R. A., Mann, A., Singh, R., Sevincer, E., Cich, S., Day, M., Kulhanek, C. D., Thatte, A. M., Peter, A. M., Hofer, D. & Moore, J. (2016), Supercritical CO2 Power Cycles Conceptual Designs of 50MW e and 450MW e Supercritical CO2 Turbomachinery Trains for Power Generation from Coal. Part 1: Cycle and Turbine, *in* 'The 5th International Symposium - Supercritical CO2 Power Cycles Symposium'.

Bierlein, J. A. & Kay, W. B. (1953), 'Phase-Equilibrium Properties of System Carbon Dioxide-Hydrogen Sulfide', *Industrial Engineering Chemistry* **45**(3), 618–624.

Bonalumi, D., Lasala, S. & Macchi, E. (2018), 'CO2-TiCl4 working fluid for high-temperature heat source power cycles and solar application', *Renewable Energy* .

Bruno, L. (2019), 'Performance Evaluation of a Supercritical CO2 Power Cycle Coal Gasification Plant', *Journal of Chemical Information and Modeling* **53**(9), 1689–1699.

Casey, M. & Robinson, C. (2021), *Radial Flow Turbocompressors: Design, Analysis, and Applications*, Cambridge University Press.

Cayer, E., Galanis, N., Desilets, M., Nesreddine, H. & Roy, P. (2009), 'Analysis of a carbon dioxide transcritical power cycle using a low temperature source', *Applied Energy* **86**(7-8), 1055–1063.
URL: *https://linkinghub.elsevier.com/retrieve/pii/S0306261908002444*

Cerio Vera, M. (2015), S-CO2 for efficient power generation with energy storage, PhD thesis, Cranfield University.

Chacartegui, R., Muñoz De Escalona, J. M., Sánchez, D., Monje, B. & Sánchez, T. (2011), 'Alternative cycles based on carbon dioxide for central receiver solar power plants', *Applied Thermal Engineering* **31**(5), 872–879.
URL: *http://dx.doi.org/10.1016/j.applthermaleng.2010.11.008*

Chen, H. & Baines, N. C. (1994), 'The aerodynamic loading of radial and mixed-flow mixed-flow turbines', *Inernation Journal of Mechanical Science* **36**(1), 63–79.

Cho, J., Shin, H., Cho, J., Baik, Y. J., Choi, B., Roh, C., Ra, H. S., Kang, Y. & Huh, J. (2018), 'Design, flow simulation, and performance test for a partialadmission

axial turbine under supercritical CO2 condition', *Proceedings of the ASME Turbo Expo* **9**, 1–9.

Cho, J., Shin, H., Ra, H. S., Lee, G., Lee, B. & Baik, Y. J. (2016), 'Research on the Development of a Small-scale Supercritical Carbon Dioxide Power Cycle Experimental Test Loop', *The 5th International Symposium - Supercritical CO2 Power Cycles Symposium* pp. 1–18.

Cho, S. K., Lee, J., Lee, J. I. & Cha, J. E. (2016), S-CO2 Turbine Design for Decay Heat Removal System of Sodium Cooled Fast Reactor, *in* 'ASME Turbo Expo 2016: Turbomachinery Technical Conference and Exposition', pp. 1–11.

Chu, W. X., hui Li, X., Ma, T., tung Chen, Y. & wang Wang, Q. (2017), 'Experimental investigation on SCO2-water heat transfer characteristics in a printed circuit heat exchanger with straight channels', *International Journal of Heat and Mass Transfer* **113**, 184–194.
URL: *http://dx.doi.org/10.1016/j.ijheatmasstransfer.2017.05.059*

Clementoni, E. M., Cox, T. L. & Sprague, C. P. (2014), 'Startup and operation of a supercritical carbon dioxide brayton cycle', *Journal of Engineering for Gas Turbines and Power* **136**(7).

Clementoni, E. M., Held, T., Pasch, J. & Moore, J. (2017), Test facilities, *in* 'Fundamentals and Applications of Supercritical Carbon Dioxide (SCO2) Based Power Cycles', Elsevier Inc., pp. 393–414.

Coquelet, C., Valtz, A. & Arpentinier, P. (2014), 'Thermodynamic study of binary and ternary systems containing CO2+impurities in the context of CO2 transportation', *Fluid Phase Equilibria* **382**, 205–211.
URL: *http://dx.doi.org/10.1016/j.fluid.2014.08.031*

Crespi, F., Arriba, P. R.-d., Sánchez, D., Ayub, A., Marcoberardino, G. D., Invernizzi, C., Martínez, G., Iora, P., Bona, D. D., Binotti, M. & Manzolini, G. (2021), Thermal efficiency gains enabled by using supercritical CO2 mixtures in concentrated solar power applications, *in* 'The 4th European sCO2 Conference for Energy Systems'.

Crespi, F., Gavagnin, G., Sánchez, D. & Martínez, G. S. (2017), 'Supercritical carbon dioxide cycles for power generation: A review', *Applied Energy* **195**, 152–183.

Crespi, F., Rodríguez de Arriba, P., Sánchez, D. & Muñoz, A. (2022), 'Preliminary investigation on the adoption of CO2-SO2 working mixtures in a transcritical Recompression cycle', *Applied Thermal Engineering* **211**(September 2021).

Crespi, F., Sánchez, D., Rodríguez, J. M. & Gavagnin, G. (2018), 'A thermo-economic methodology to select sCO2 power cycles for CSP applications', *Renewable Energy* pp. 1–8.

Daily, J. W. & Nece, R. E. (1960), 'Chamber Dimension Effects on Induced Flow and Frictional Resistance of Enclosed Rotating Disks', *Journal of Basic Engineering* .

Dambach, R. & Hodson, H. (2000), 'Tip Leakage Flow: A Comparison between Small Axial and Radial Turbines', *IMechE* .

Dambach, R. & Hodson, H. P. (2001), 'Tip leakage flow in a radial inflow turbine with varying gap height', *Journal of Propulsion and Power* **17**(3), 644–650.

Dambach, R., Hodson, H. P. & Huntsman, I. (1998), An Experimental Study of Tip Clearance Flow in a Radial Inflow Turbine, *in* 'Transactions of the ASME', Vol. 121.

Deiters, U. K. & Kraska, T. (2012), Equations of State for Pure Fluids, pp. 177–210.
URL: *https://linkinghub.elsevier.com/retrieve/pii/B9780444563477000074*

Dekhtiarev, V. L. (1962), 'On designing a large, highly economical carbon dioxide power installation', *Elecrtichenskie Stantskii* **5**.

Diamantonis, N. I., Boulougouris, G. C., Mansoor, E., Tsangaris, D. M. & Economou, I. G. (2013), 'Evaluation of cubic, SAFT, and PC-SAFT equations of state for the vapor-liquid equilibrium modeling of CO2 mixtures with other gases', *Industrial and Engineering Chemistry Research* **52**(10), 3933–3942.

Dias, A. M., Carrier, H., Daridon, J. L., Pàmies, J. C., Vega, L. F., Coutinho, J. A. & Marrucho, I. M. (2006), 'Vapor - Liquid equilibrium of carbon dioxide - Perfluoroalkane mixtures: Experimental data and SAFT modeling', *Industrial and Engineering Chemistry Research* **45**(7), 2341–2350.

Dostal, V., Driscoll, M. J. & Hejzlar, P. (2004), A Supercritical Carbon Dioxide Cycle for Next Generation Nuclear Reactors, PhD thesis, MIT.
URL: *http://web.mit.edu/canes/*

Du, Y., Tian, G. & Pekris, M. (2022), 'A comprehensive review of micro-scale expanders for carbon dioxide related power and refrigeration cycles', *Applied Thermal Engineering* **201**(PA), 117722.
URL: *https://doi.org/10.1016/j.applthermaleng.2021.117722*

El Samad, T., Teixeira, J. A. & Oakey, J. (2020), 'Investigation of a Radial Turbine Design for a Utility-Scale Supercritical CO2 Power Cycle', *Applied Sciences (Switzerland)* .

Elizalde-Solis, O. & Galicia-Luna, L. A. (2005), 'Solubility of thiophene in carbon dioxide and carbon dioxide + 1-propanol mixtures at temperatures from 313 to 363 K', *Fluid Phase Equilibria* **230**(1-2), 51–57.

Ely, J. F. & Hanley, H. J. (1981), 'Prediction of Transport Properties. 1. Viscosity of Fluids and Mixtures', *Industrial and Engineering Chemistry Fundamentals* **20**(4), 323–332.

Ely, J. F. & Hartley, H. J. (1983), 'Prediction of Transport Properties. 2. Thermal Conductivity of Pure Fluids and Mixtures', *Industrial and Engineering Chemistry Fundamentals* **22**(1), 90–97.

Feher, E. G. (1968), 'The Supercritical Thermodynamic Power Cycle', *Energy Conversion* **8**, 85–90.

Fuller, R., Preuss, J. & Noall, J. (2012), Turbomachinery for supercritical CO2 power cycles, *in* 'Proceedings of ASME Turbo Expo 2012'.

Garg, P., Srinivasan, K., Dutta, P. & Kumar, P. (2014), Comparison of CO2 and steam in transcritical Rankine cycles for concentrated solar power, *in* 'Energy Procedia', Vol. 49, Elsevier Ltd, pp. 1138–1146.

Glassman, A. J. (1976), 'Computer program for design analysis of radial-inflow turbines', *NASA Technical Note* (February), 66.

Glassman, A. J. (1995), 'Enhanced analysis and users manual for radial-inflow turbine conceptual design code RTD', *NASA Contractor Report 195454* (Lewis Research Center).

Gray, C. G., Gubbins, K. E. & Joslin, C. G. (2011), *Theory of Molecular Fluids: Volume 2: Applications*, OUP Oxford.

Gross, J. & Sadowski, G. (2001), 'Perturbed-Chain SAFT: An Equation of State Based on a Perturbation Theory for Chain Molecules', *Industrial Engineering Chemistry Research* **40**(4), 1244–1260.
URL: *https://pubs.acs.org/doi/10.1021/ie0003887*

Guo, J. Q., Li, M. J., Xu, J. L., Yan, J. J. & Wang, K. (2019), 'Thermodynamic performance analysis of different supercritical Brayton cycles using CO 2 -based binary mixtures in the molten salt solar power tower systems', *Energy* pp. 785–798.

Gupta, M. K., Li, Y. H., Hulsey, B. J. & Robinson, R. L. (1982), 'Phase Equilibrium for Carbon Dioxide-Benzene at 313.2, 353.2, and 393.2 K', *Journal of Chemical and Engineering Data* **27**(1), 55–57.

Hacks, A., Schuster, S., Dohmen, H. J., Benra, F. K. & Brillert, D. (2018), 'Turbomachine Design for Supercritical Carbon Dioxide Within the sCO2-HeRo.eu Project', *Journal of Engineering for Gas Turbines and Power* **140**(12), 1–8.

Hajipour, S., Satyro, M. A. & Foley, M. W. (2014), 'Uncertainty analysis applied to thermodynamic models and process design-2. Binary mixtures', *Fluid Phase Equilibria* **364**, 15–30.
URL: *http://dx.doi.org/10.1016/j.fluid.2013.12.004*

Held, T. (2014), Initial test results of a MegaWatt-class supercritical CO2 heat engine, *in* 'The 4th International Symposium - Supercritical CO2 Power Cycles'.

Herrig, L. J., Emery, J. C. & Erwin, J. R. (1957), Systematic Two-Dimensional Cascade Tests of NACA 65-Series Compressor Blades at Low Speeds, Technical report, NACA, Washington, DC.

Ho, C. K., Carlson, M., Garg, P. & Kumar, P. (2015), 'Cost and performance tradeoffs of alternative solar-driven s-CO2 Brayton cycle configurations', *ASME 2015 9th International Conference on Energy Sustainability* **1**, 1–10.

Ho, C. K., Conboy, T., Ortega, J., Afrin, S., Gray, A., Christian, J. M., Bandyopadyay, S., Kedare, S. B., Singh, S. & Wani, P. (2014), 'High-temperature receiver designs for supercritical CO2 closed-loop Brayton cycles', *ASME 2014 8th International Conference on Energy Sustainability* **1**, 1–7.

Horlock, J. H. (1960), 'Losses and efficiencies in axial-flow turbines', *International Journal of Mechanical Sciences* **2**(1-2), 48–75.

Hu, L., Chen, D., Huang, Y., Li, L., Cao, Y., Yuan, D., Wang, J. & Pan, L. (2015), 'Investigation on the performance of the supercritical Brayton cycle with CO2-based binary mixture as working fluid for an energy transportation system of a nuclear reactor', *Energy* **89**, 874–886.

Huntsman, I. (1993), Investigation of radial inflow turbine aerodynamics, PhD thesis, University of Cambridge.

I. Sandier, S. & Orbey, H. (2000), '9 Mixing and combining rules', *Experimental Thermodynamics* **5**(C), 321–357.

IEA (2022), International Energy Agency (IEA) World Energy Outlook 2022, Technical report.

Imre, A. R., Ramboz, C., Deiters, U. K. & Kraska, T. (2015), 'Anomalous fluid properties of carbon dioxide in the supercritical region: application to geological CO2 storage and related hazards', *Environmental Earth Sciences* **73**(8), 4373–4384.

Invernizzi, C. M. (2013), *Closed Power Cycles*, Vol. 11 of *Lecture Notes in Energy*, Springer London, London.

Invernizzi, C. M. & Van Der Stelt, T. (2012), 'Supercritical and real gas Brayton cycles operating with mixtures of carbon dioxide and hydrocarbons', *Proceedings of the Institution of Mechanical Engineers, Part A: Journal of Power and Energy* **226**(5), 682–693.

IRENA (2022), World energy transitions outlook 2022, Technical report.

J. Richard Elliott, C. T. L. (2012), *Introductory Chemical Engineering Thermodynamics*, second edn, Prentice Hall.

Jamieson, A. W. H. (1955), The Radial Turbine, *in* 'Gas Turbine Principles and Practice', D. Van Nostrand Co., Inc.

Jankowski, M., Klonowicz, P. & Borsukiewicz, A. (2021), 'Multi-objective optimization of an ORC power plant using one- dimensional design of a radial-in fl ow turbine with backswept rotor blades', *Energy* **237**, 121506.
URL: *https://doi.org/10.1016/j.energy.2021.121506*

Jeong, W. S. & Jeong, Y. H. (2013), 'Performance of supercritical Brayton cycle using CO2-based binary mixture at varying critical points for SFR applications', *Nuclear Engineering and Design* **262**, 12–20.
URL: *http://dx.doi.org/10.1016/j.nucengdes.2013.04.006*

Jeong, W. S., Lee, J. I. & Jeong, Y. H. (2011), 'Potential improvements of supercritical recompression CO2 Brayton cycle by mixing other gases for power conversion system of a SFR', *Nuclear Engineering and Design* **241**(6), 2128–2137.
URL: *http://dx.doi.org/10.1016/j.nucengdes.2011.03.043*

Jones, A. C. (1994), Design and test of a small, high pressure ratio radial turbine, *in* 'International Gas Turbine and Aeroengine Congress and Exposition'.

Kalogirou, S. (2003), 'The potential of solar industrial process heat applications', *Applied Energy* **76**(4), 337–361.

Kalogirou, S. A. (2013), *Solar Energy Engineering*, 2nd edn, Academic Press.

Kalra, C., Sevincer, E., Brun, K., Director, P., Hofer, D. & Moore, J. (2014), Supercritical CO2 power cycles development of high efficiency hot gas turbo-expander for optimized CSP supercritical CO2 power block operation, *in* 'The 4th International Symposium'.

Kaufmann, S. M. (2020), A Unified Turbine Preliminary Design Study, PhD thesis, University of Cambridge.

Keep, J. (2018), On the design of small to medium scale radial inflow turbines for the supercritical CO2 Brayton cycle, PhD thesis, University of Queensland.

Keep, J. A. & Jahn, I. H. J. (2019), 'Numerical Loss Investigation of a Small Scale , Low Specific Speed Supercritical CO2 Radial Inflow Turbine', *Journal of Engineering for Gas Turbines and Power* **141**(September), 1–10.

Khatoon, S. & Kim, M.-H. (2019), 'Potential improvement and comparative assessment of supercritical Brayton cycles for arid climate', *Energy Conversion and Management* **200**(September), 112082.
URL: *https://doi.org/10.1016/j.enconman.2019.112082*

Kim, J. H. & Kim, M. S. (2005), 'Vapor-liquid equilibria for the carbon dioxide + propane system over a temperature range from 253.15 to 323.15 K', *Fluid Phase Equilibria* **238**(1), 13–19.

Kim, M. S., Ahn, Y., Kim, B. & Lee, J. I. (2016), 'Study on the supercritical CO2 power cycles for landfill gas firing gas turbine bottoming cycle', *Energy* **111**, 893–909.

Kim, Y. M., Kim, C. G. & Favrat, D. (2012), 'Transcritical or supercritical CO2 cycles using both low- and high-temperature heat sources', *Energy* **43**(1), 402–415.

Kofskey, G. & Nusbaum, W. J. (1972), Effects of specific speed on experimental performance of a radial-inflow turbine, Technical report, NASA.

Kofskey, M. G. & Holeski, D. (1966), 'Cold performance evaluation of a 6.02 inch radial inflow turbine designed for a 10kW shaft output brayton cycle space power generation system', *National Aeronautics and Space Administration* (February).

Kontogeorgis, G. M. & Folas, G. K. (2010), *Thermodynamic Models for Industrial Applications*, Wiley.

Korpela, S. A. (2019), *Principles of Turbomachinery*, John Wiley Sons.

Lasala, S. (2016), Advanced cubic equations of state for accurate modelling of fluid mixtures. Application to CO2 capture systems, PhD thesis, Politecnico di Milano.

Lasala, S., Martinez, A.-P. & Jaubert, J.-N. (2020), A Predictive Equation of State to Perform an Extending Screening of Working Fluids for Power and Refrigeration Cycles, *in* 'Organic Rankine Cycles for Waste Heat Recovery - Analysis and Applications', IntechOpen.

Lasala, S., Privat, R., Herbinet, O., Arpentinier, P., Bonalumi, D. & Jaubert, J. N. (2021), 'Thermo-chemical engines: Unexploited high-potential energy converters', *Energy Conversion and Management* **229**.

Lasala, S., Privat, R. & Jaubert, J.-N. (2018), 'Inert and Reactive Working Fluids for Closed Power Cycles: Present Knowledge, Applications and Open Researches', *Organic Rankine Cycle Technology for Heat Recovery* pp. 3–18.

Lee, S. & Gurgenci, H. (2020), 'A comparison of three methodological approaches for meanline design of supercritical CO2 radial inflow turbines', *Energy Conversion and Management* **206**(January), 112500.
URL: *https://doi.org/10.1016/j.enconman.2020.112500*

Lee, S., Yaganegi, G., Mee, D. J., Guan, Z. & Gurgenci, H. (2021), 'Part-load performance prediction model for supercritical CO2 radial inflow turbines', *Energy Conversion and Management* **235**(December 2020), 113964.
URL: *https://doi.org/10.1016/j.enconman.2021.113964*

Lewis, T. G., Conboy, T. M. & Wright, S. A. (2011), Supercritical CO2 Mixture Behavior for Advanced Power Cycles and Applications, *in* 'sCO2 Power Cycle Symposium'.

Li, J., Gurgenci, H., Li, J., Li, L., Guan, Z. & Yang, F. (2021), 'Optimal design to control rotor shaft vibrations and thermal management on a supercritical CO2 microturbine', *Mechanics and Industry* **22**.

Li, X., Huang, H. & Zhao, W. (2014), 'A supercritical or transcritical Rankine cycle with ejector using low-grade heat', *Energy Conversion and Management* **78**, 551–558.
URL: *http://dx.doi.org/10.1016/j.enconman.2013.11.020*

Li, X. & Zhang, X. (2011), 'Component exergy analysis of solar powered transcritical CO2 rankine cycle system', *Journal of Thermal Science* **20**(3), 195–200.

Liu, Y., Wang, Y. & Huang, D. (2019), 'Supercritical CO2 Brayton cycle: A state-of-the-art review', *Energy* **189**, 115900.
URL: *https://doi.org/10.1016/j.energy.2019.115900*

Lv, G., Yang, J., Shao, W. & Wang, X. (2018), 'Aerodynamic design optimization of radial-inflow turbine in supercritical CO2 cycles using a one-dimensional model', *Energy Conversion and Management* **165**(May), 827–839.
URL: *https://doi.org/10.1016/j.enconman.2018.03.005*

Ma, Y. N., Hu, P., Jia, C. Q., Wu, Z. R. & Chen, Q. (2023), 'Thermo-economic analysis and multi-objective optimization of supercritical Brayton cycles with CO2-based mixtures', *Applied Thermal Engineering* **219**(PA), 119492.
URL: *https://doi.org/10.1016/j.applthermaleng.2022.119492*

Macchi, E. & Astolfi, M. (2017), 'Axial flow turbines for Organic Rankine Cycle applications', *Organic Rankine Cycle (ORC) Power Systems: Technologies and Applications* pp. 299–319.

Manikantachari, K. R., Martin, S., Bobren-Diaz, J. O. & Vasu, S. (2017), 'Thermal and Transport Properties for the Simulation of Direct-Fired sCO2 Combustor', *Journal of Engineering for Gas Turbines and Power* **139**(12), 1–14.

Manzolini, G., Binotti, M., Bonalumi, D., Invernizzi, C. & Iora, P. (2019), 'CO2 mixtures as innovative working fluid in power cycles applied to solar plants. Techno-economic assessment', *Solar Energy* **181**(June 2018), 530–544.
URL: *https://doi.org/10.1016/j.solener.2019.01.015*

Manzolini, G., Binotti, M., Morosini, E., Sanchez, D., Crespi, F., Marcoberdino, G. D., Iora, P. & Invernizzi, C. (2022), Adoption of CO2 blended with C6F6 as working fluid in CSP plants, *in* 'AIP Conference Proceedings'.
URL: *http://aip.scitation.org/doi/abs/10.1063/5.0086520*

Marcoberardino, G. D., Morosini, E. & Manzolini, G. (2022), 'Preliminary investigation of the influence of equations of state on the performance of CO2+ C6F6 as innovative working fluid in transcritical cycles', *Energy* **238**, 121815.
URL: *https://doi.org/10.1016/j.energy.2021.121815*

Mcclung, A., Smith, N., Allison, T. & Tom, B. (2018), 'Practical considerations for the conceptual design of an sCO2 cycle', *The 6th International Symposium - Supercritical CO2 Power Cycles* pp. 1–21.

Mendez, C. & Rochau, G. (2018), sCO2 Brayton cycle: Roadmap to sCO2 power cycles NE commercial applications, Technical report.

Meroni, A. (2018), Design and Optimization of Turbomachinery for Thermodynamic Cycles Utilizing Low-Temperature Heat Sources, PhD thesis, Technical University Of Denmark.

Meroni, A., Robertson, M., Martinez-Botas, R. & Haglind, F. (2018), 'A methodology for the preliminary design and performance prediction of high-pressure ratio radial-inflow turbines', *Energy* **164**, 1062–1078.
URL: *https://doi.org/10.1016/j.energy.2018.09.045*

Moisseytsev, A. & Sienicki, J. J. (2009), 'Investigation of alternative layouts for the supercritical carbon dioxide Brayton cycle for a sodium-cooled fast reactor', *Nuclear Engineering and Design* **239**(7), 1362–1371.

Morosini, E., Ayub, A., di Marcoberardino, G., Invernizzi, C. M., Iora, P. & Manzolini, G. (2022), 'Adoption of the CO2 + SO2 mixture as working fluid for transcritical cycles: A thermodynamic assessment with optimized equation of state', *Energy Conversion and Management* **255**, 115263.
URL: *https://doi.org/10.1016/j.enconman.2022.115263*

Moroz, L., Frolov, B., Burlaka, M. & Guriev, O. (2014), Turbomachinery Flowpath Design and Performance Analysis for, *in* 'Proceedings of ASME Turbo Expo', pp. 1–8.

Moustapha, H., Zelesky, M. F., Baines, C. N. & Japikse, D. (2003), *Axial and Radial Turbines*, Concepts ETI, Inc.

Musgrove, G., Shiferaw, D., Sullivan, S., Chordia, L. & Portnoff, M. (2016), 'Tutorial: Heat Exchanger for Supercritical CO2 Power Cycle Applications', *Supercritical CO2 Power Cycle Symposium* .

Musgrove, G. & Wright, S. (2017), Introduction and background, *in* 'Fundamentals and Applications of Supercritical Carbon Dioxide (SCO2) Based Power Cycles', Elsevier, pp. 1–22.
URL: *https://linkinghub.elsevier.com/retrieve/pii/B9780081008041000013*

Neises, T. & Turchi, C. (2014), A comparison of supercritical carbon dioxide power cycle configurations with an emphasis on CSP applications, *in* 'Energy Procedia', Vol. 49, Elsevier Ltd, pp. 1187–1196.

Neises, T. & Turchi, C. (2019), 'Supercritical carbon dioxide power cycle design and configuration optimization to minimize levelized cost of energy of molten salt power towers operating at 650C', *Solar Energy* pp. 27–36.

Nishiumi, H. & Saito, S. (1975), 'An improved generalized BWR equation of state applicable to low reduced temperatures', *Journal of Chemical Engineering of Japan* **8**(5), 356–360.

Niu, X., Ma, N., Bu, Z., Hong, W. & Li, H. (2022), 'Thermodynamic analysis of supercritical Brayton cycles using CO2-based binary mixtures for solar power tower system application', *Energy* **254**, 124286.
URL: *https://doi.org/10.1016/j.energy.2022.124286*

Noriega Sanchez, C. J., Afanador García, N. & Guerrero Gómez, G. (2019), 'Carbon dioxide mixtures for organic power cycles using waste heat sources', *Journal of Physics: Conference Series* **1409**(1).

Novales, D., Erkoreka, A., De la Peña, V. & Herrazti, B. (2019), 'Sensitivity analysis of supercritical CO 2 power cycle energy and exergy efficiencies regarding cycle component efficiencies for concentrating solar power', *Energy Conversion and Management* **182**, 430–450.
URL: *https://doi.org/10.1016/j.enconman.2018.12.016*

Odabaee, M., Sauret, E. & Hooman, K. (2016), 'CFD Simulation of a Supercritical Carbon Dioxide Radial-Inflow Turbine , Comparing the Results of Using Real Gas Equation of Estate and Real Gas Property File', *Applied Mechanics and Materials* **846**, 85–90.

Osorio, J. D., Hovsapian, R. & Ordonez, J. C. (2016), 'Effect of multi-tank thermal energy storage, recuperator effectiveness, and solar receiver conductance on the performance of a concentrated solar supercritical CO2 -based power plant operating under different seasonal conditions', *Energy* **115**, 353–368.

Padilla, R. V., Too, Y. C. S., Benito, R., McNaughton, R. & Stein, W. (2016), 'Thermodynamic feasibility of alternative supercritical CO2 Brayton cycles integrated with an ejector', *Applied Energy* **169**, 49–62.
URL: *http://dx.doi.org/10.1016/j.apenergy.2016.02.029*

Pasch, J., Conboy, T., Fleming, D. & Rochau, G. (2012), Supercritical CO2 Recompression Brayton Cycle: Completed Assembly Description, Technical report, Sandia National Laboratories.
URL: *http://www.ntis.gov/help/ordermethods.asp?loc=7-4-0online*

Pasch, J. & Stapp, D. (2018), 'Testing of a new turbocompressor for supercritical carbon dioxide closed brayton cycles', *Proceedings of the ASME Turbo Expo* **9**, 1–10.

Peng, D.-Y. & Robinson, D. B. (1979), 'A new two-constant equation of state', *Industrial Engineering Chemistry Fundamentals* pp. 163–184.

Persky, R. & Sauret, E. (2019), 'Loss models for on and off -design performance of radial inflow turbomachinery', *Applied Thermal Engineering* **150**, 1066–1077.
URL: *https://doi.org/10.1016/j.applthermaleng.2019.01.042*

Persky, R., Sauret, E. & Beath, A. (2015), 'Robust Design and Optimisation of a Radial Turbine Within a Supercritical CO2 Solar Brayton Cycle', pp. 1–6.

Pitzer, K. S. (1955), 'The Volumetric and Thermodynamic Properties of Fluids. I. Theoretical Basis and Virial Coefficients', *Journal of the American Chemical Society* **77**(13), 3427–3433.

Polimeni, S., Binotti, M., Moretti, L. & Manzolini, G. (2018), 'Comparison of sodium and KCl-MgCl2 as heat transfer fluids in CSP solar tower with sCO2 power cycles', *Solar Energy* **162**, 510–524.

Poling, B. E., Prausnitz, J. M. & O'Connell, J. P. (2001), *The Properties of Gases and Liquids*, 5th edn, McGraw-Hill.

Privat, R. & Jaubert, J. N. (2013), 'Classification of global fluid-phase equilibrium behaviors in binary systems', *Chemical Engineering Research and Design* **91**(10), 1807–1839.
URL: *http://dx.doi.org/10.1016/j.cherd.2013.06.026*

Purjam, M., Goudarzi, K. & Keshtgar, M. (2017), 'A New Supercritical Carbon Dioxide Brayton Cycle with High Efficiency', *Heat Transfer - Asian Research* **46**(5), 465–482.

Qi, J., Reddell, T., Qin, K., Hooman, K. & Jahn, I. H. (2017), 'Supercritical CO2 radial turbine design performance as a function of turbine size parameters', *Journal of Turbomachinery* **139**(8).

Radermacher, R. & Hwang, Y. (2005), *Vapor Compression Heat Pumps with Refrigerant Mixtures*, Taylor and Francis Ltd.

Raju, M., Banuti, D. T., Ma, P. C. & Ihme, M. (2017), 'Widom lines in binary mixtures of supercritical fluids', *Scientific Reports* **7**(1), 1–10.

Rodgers, C. (1967), 'Efficiency and performance characteristics of radial turbines', *SAE Technical Papers* **75**(1967), 681–692.

Rodgers, C. (1987), Mainline performance prediction for radial inflow turbines, *in* 'Von Karman Inst. for Fluid Dynamics, Small High Pressure Ratio Turbines', p. 29.

Rodríguez-deArriba, P., Crespi, F., Sánchez, D., Muñoz, A. & Sánchez, T. (2022), 'The potential of transcritical cycles based on CO2 mixtures: An exergy-based analysis', *Renewable Energy* **199**(February), 1606–1628.

Rohlik, H. E. (1968), Analytical Determination of Radial Inflow Turbine Design, Technical report, NASA.

Romei, A., Gaetani, P., Giostri, A. & Persico, G. (2019), 'The role of turbomachinery performance in the optimization of supercritical carbon dioxide power systems', *Proceedings of the ASME Turbo Expo* **9**(January).

Romei, A., Gaetani, P., Giostri, A. & Persico, G. (2020), 'The role of turbomachinery performance in the optimization of supercritical carbon dioxide power systems', *Journal of Turbomachinery* pp. 1–39.
URL: *https://doi.org/10.1115/1.4046182*

Saeed, M. & Kim, M. H. (2018), 'Analysis of a recompression supercritical carbon dioxide power cycle with an integrated turbine design/optimization algorithm', *Energy* **165**, 93–111.

Saravanamuttoo, H. I. H., Rogers, G. F. C., Cohen, H., Straznicky, P. V., Nix, A. C., Saravanamuttoo, H. & Straznicky, P. V. (2017), *Gas Turbine Theory*, seventh edn, Pearson Education Limited.

Sauret, E. (2012), Open design of high pressure ratio radial-inflow turbine for academic validation, *in* 'ASME 2012 International Mechanical Engineering Congress Exposition', pp. 1–15.

Seshadri, L., Kumar, P., Nassar, A. & Giri, G. (2022), 'Analysis of Turbomachinery Losses in sCO2Brayton Power Blocks', *Journal of Energy Resources Technology, Transactions of the ASME* **144**(11), 1–9.

Shi, D., Zhang, L., Xie, Y. & Zhang, D. (2019), 'Aerodynamic design and off-design performance analysis of a multi-stage S-CO 2 axial turbine based on solar power generation system', *Applied Sciences (Switzerland)* **9**(4).

Shin, H., Cho, J., Baik, Y. J., Cho, J., Roh, C., Ra, H. S., Kang, Y. & Huh, J. (2017), 'Partial admission, axial impulse type turbine design and partial admission radial turbine test for SCO2 cycle', *Proceedings of the ASME Turbo Expo* **9**, 1–5.

Shlbata, S. K. & Sandler, S. I. (1989), 'High-Pressure Vapor-Liquid Equilibria Involving Mixtures of Nitrogen, Carbon Dioxide, and n-Butane', *Journal of Chemical and Engineering Data* **34**(3), 291–298.

Sienicki, J. J., Moisseytsev, A., Fuller, R. L., Wright, S. A. & Pickard, P. S. (2011), Scale Dependencies of Supercritical Carbon Dioxide Brayton Cycle Technologies and the Optimal Size for a Next-Step Supercritical CO2 Cycle Demonstration, *in* 'SCO2 Power Cycle Symposium'.

Silva-Pérez, M. A. (2016), Solar power towers using supercritical CO2 and supercritical steam cycles, and decoupled combined cycles, *in* 'Advances in Concentrating Solar Thermal Research and Technology', Elsevier Inc., pp. 383–402.

Simpson, A., Spence, S. & Watterson, J. (2008), 'Numerical and experimental study of the performance effects of varying vaneless space and vane solidity in radial inflow turbine stators', *Proceedings of the ASME Turbo Expo* **6**(PART B), 1–11.

Smith, R., Inomata, H. & Peters, C. (2013), Historical Background and Applications, *in* 'Introduction to Supercritical Fluids', Elsevier, chapter 4, pp. 175–273.
URL: *https://linkinghub.elsevier.com/retrieve/pii/B9780444522153000040*

Soave, G. (1972*a*), 'Equilibrium constants from a modified Redlich-Kwong equation of state', *Chemical Engineering Science* **27**(6), 1197–1203.

Soave, G. (1972*b*), 'Equilibrium constants from a modified Redlich-Kwong equation of state', *Chemical Engineering Science* **27**(6), 1197–1203.
URL: *https://linkinghub.elsevier.com/retrieve/pii/0009250972800964*

Song, J., Li, X., Ren, X., Tian, H., Shu, G., Gu, C. & Markides, C. N. (2020), 'Thermodynamic and economic investigations of transcritical CO2-cycle systems with integrated radial-inflow turbine performance predictions', *Applied Thermal Engineering* **165**, 114604.
URL: *https://doi.org/10.1016/j.applthermaleng.2019.114604*

Sorbet, F. J., de Mendoza, M. H. & García-Barberena, J. (2019), 'Performance evaluation of CSP power tower plants schemes using supercritical carbon dioxide Brayton power block', *SOLARPACES 2018: International Conference on Concentrating Solar Power and Chemical Energy Systems* **2126**(July), 030056.

Sorensen, B. (2017), Individual renewable energy sources, *in* 'Renewable Energy', Elsevier, pp. 219–353.
URL: *https://linkinghub.elsevier.com/retrieve/pii/B9780128045671000037*

Stein, K. L. & Wes, eds (2012), *Concentrating solar power technology: Principles, developments and applications*, Woodhead Publishing Limited.

Steven, W., Conboy, T. M. & Gary, R. (2011), Break-even Power Transients for two Simple Recuperated S-CO2 Brayton Cycle Test Configurations, *in* 'SCO2 Power Cycle Symposium'.

Sun, L., Wang, D. & Xie, Y. (2021), 'Thermodynamic and exergoeconomic analysis of combined supercritical CO2 cycle and organic Rankine cycle using CO2-based binary mixtures for gas turbine waste heat recovery', *Energy Conversion and Management* **243**, 114400.
URL: *https://doi.org/10.1016/j.enconman.2021.114400*

Tafur-escanta, P., Valencia-chapi, R., Ignacio, L., Coco-enr, L. & Muñoz-ant, J. (2021), 'Supercritical CO2 Binary Mixtures for Recompression Brayton s-CO2 Power Cycles Coupled to Solar Thermal Energy Plants', *Energies* .

Tang, B., Sun, L. & Xie, Y. (2022), 'Design and performance evaluation of an energy storage system using CO2-based binary mixtures for thermal power plant under dry conditions', *Energy Conversion and Management* **268**(July), 116043.
URL: *https://doi.org/10.1016/j.enconman.2022.116043*

Tocci, L., Pal, T., Pesmazoglou, I. & Franchetti, B. (2017), 'Small scale Organic Rankine Cycle (ORC): A techno-economic review', *Energies* **10**(4), 1–26.

Tochigi, K., Hasegawa, K., Asano, N. & Kojima, K. (1998), 'Vapor-liquid equilibria for the carbon dioxide + pentane and carbon dioxide + toluene systems', *Journal of Chemical and Engineering Data* **43**(6), 954–956.

Uddin, M., Gurgenci, H., Guan, Z., Klimenko, A., Li, J., Li, J. & Li, L. (2021), 'Design a cooling pillow to support a high-speed supercritical CO2 turbine shaft', *Applied Thermal Engineering* **196**(July), 117345.
URL: *https://doi.org/10.1016/j.applthermaleng.2021.117345*

Unglaube, T. & Chiang, H.-W. D. (2018), Small Scale Supercritical CO2 Radial Inflow Turbine Meanline Design Considerations, *in* 'American Society of Mechanical Engineers', Vol. 142, American Society of Mechanical Engineers, pp. 1–10.

Unglaube, T. & Chiang, H.-W. D. (2020), 'Preliminary Design of Small-Scale Supercritical CO2 Radial Inflow Turbines', *Journal of Engineering for Gas Turbines and Power* **142**(2).

Utamura, M., Hasuike, H., Ogawa, K., Yamamoto, T., Fukushima, T., Watanabe, T. & Himeno, T. (2012), 'Demonstration of supercritical CO2 closed regenerative brayton cycle in a bench scale experiment', pp. 1–10.

Uusitalo, A. & Grönman, A. (2021), 'Analysis of Radial Inflow Turbine Losses Operating with Supercritical Carbon Dioxide', *Energies* .

Uusitalo, A. & Turunen-saaresti, T. (2021), 'Design and loss analysis of radial turbines for supercritical CO 2 Brayton cycles', *Energies* **230**.

Valencia-Chapi, R., Coco-Enríquez, L. & Muñoz-Antón, J. (2020*a*), 'Comparing line-focusing and central tower solar power plants with S-CO2 binary mixture Brayton power cycles', *AIP Conference Proceedings* **2303**(December).

Valencia-Chapi, R., Coco-Enríquez, L. & Muñoz-Antón, J. (2020*b*), 'Supercritical CO2 mixtures for advanced brayton power cycles in line-focusing solar power plants', *Applied Sciences (Switzerland)* **10**(1).

Valencia-Chapi, R., Tafur-Escanta, P., Coco-Enríquez, L. & Muñoz-Antón, J. (2022), 'Supercritical CO2 mixtures for Brayton power cycles complex configurations with concentrating solar power', *AIP Conference Proceedings* **2445**(May).

van Konyneneburg, H. & Scott, R. (1980), 'Critical lines and phase equilibria in binary van der Waals mixtures', *Philosophical Transactions Of The Royal Society Of London* p. 6.

Vane, S., Schmitt, J., Willis, R., Amos, D., Kapat, J. & Custer, C. (2014), 'Study of a Supercritical CO2 Turbine with TIT of 1350 K for Brayton Cycle with 100 MW Class Output: Aerodynamic Analysis of Stage 1 Vane', pp. 1–11.

Ventura, C. A., Jacobs, P. A., Rowlands, A. S., Petrie-Repar, P. & Sauret, E. (2012), 'Preliminary design and performance estimation of radial inflow turbines: An automated approach', *Journal of Fluids Engineering, Transactions of the ASME* **134**(3), 1–13.

Vilim, R. B. (2011), Development and Validation of a Radial Inflow Turbine Model for Simulation of the SNL S-CO2 Split-Flow Loop, Technical report, Argonne National Laboratory.

Vojacek, A., Hacks, A., Frybort, O., Hajek, P. & Melichar, T. (2018), First Operational Experience From The Supercritical CO2 Experimental Loop CVR projects, *in* '2nd European Supercritical CO2 Conference'.

Wang, K., He, Y. L. & Zhu, H. H. (2017), 'Integration between supercritical CO2 Brayton cycles and molten salt solar power towers: A review and a comprehensive comparison of different cycle layouts', *Applied Energy* **195**, 819–836.
URL: *http://dx.doi.org/10.1016/j.apenergy.2017.03.099*

Wang, L., ming Pan, L., Wang, J., Chen, D., Huang, Y., Sun, W. & Hu, L. (2022), 'Investigation on the effect of mixtures physical properties on cycle efficiency in the CO2-based binary mixtures Brayton cycle', *Progress in Nuclear Energy* **143**(October 2021), 104049.
URL: *https://doi.org/10.1016/j.pnucene.2021.104049*

Wang, M., Zhao, P., Wang, J., Li, H. & Dai, Y. (2016), 'Conceptual design and parametric study of combined carbon dioxide/organic Rankine cycles', *Applied Thermal Engineering* **103**, 759–772.
URL: *http://dx.doi.org/10.1016/j.applthermaleng.2016.04.046*

Wang, X., Wang, J., Zhao, P. & Dai, Y. (2016), 'Thermodynamic Comparison and Optimization of Supercritical CO2 Brayton Cycles with a Bottoming Transcritical CO2 Cycle', *Journal of Energy Engineering* **142**(3), 1–11.

Wang, Y., Guenette, G., Hejzlar, P. & Driscoll, M. (2004), 'Compressor design for the supercritical CO 2 brayton cycle', *Collection of Technical Papers - 2nd International Energy Conversion Engineering Conference* **3**(August), 1599–1611.

Wasserbauer, C. A. & Glassman, A. J. (1975), Fortran program for predicting off-design performance of radial-inflow turbines, Technical Report September 1975.

Watanabe, I., Ariga, I. & Mashimo, T. (1971), 'Effect of Dimensional Parameters of Impellers on Performance Characteristics of a Radial-Inflow Turbine', *Journal of Engineering for Power* .

Wei, Z. (2014), Meanline analysis of radial inflow turbines at design and off-design conditions, PhD thesis, Ottawa-Carleton Institute for Mechanical Aerospace Engineering.

White, C. W. & Weiland, N. T. (2018), 'Evaluation of Property Methods for Modeling Direct-Supercritical CO2 Power Cycles', *Journal of Engineering for Gas Turbines and Power* **140**(1).

White, M. T. (2015), The design and analysis of radial inflow turbines implemented within low temperature organic Rankine cycles, PhD thesis.
URL: *http://openaccess.city.ac.uk/1189/*

White, M. T., Bianchi, G., Chai, L., Tassou, S. A. & Sayma, A. I. (2021), 'Review of supercritical CO 2 technologies and systems for power generation', **185**(December 2020).

White, M. T. & Sayma, A. (2018*a*), A preliminary comparison of different turbine architectures for a 100 kW supercritical CO 2 Rankine cycle turbine, *in* 'The 6th International Supercritical CO2 Power Cycles Symposium', pp. 1–11.

White, M. T. & Sayma, A. I. (2018*b*), 'A generalised assessment of working fluids and radial turbines for non-recuperated subcritical organic rankine cycles', *Energies* **11**(4).

Whitfield, A. (1990), Preliminary design and performance prediction techniques for centrifugal compressors, *in* 'Developments in industrial compressors', Vol. 2.

William Emrich, J. (2016), *Principles of Nuclear Rocket Propulsion*, Elsevier.
URL: *https://linkinghub.elsevier.com/retrieve/pii/C20150022201*

Wood, H. J. (1963), 'Current technology of radial-inflow turbines for compressible fluids', *Journal of Engineering for Gas Turbines and Power* **85**(1), 72–83.

Wright, S. A., Radel, R. F., Vernon, M. E., Rochau, G. E. & Pickard, P. S. (2010), Operation and Analysis of a Supercritical CO2 Brayton Cycle, Technical report, Sandia National Laboratories.
URL: *http://www.ntis.gov/help/ordermethods.asp?loc=7-4-0online*

Xia, J., Wang, J., Zhang, G., Lou, J., Zhao, P. & Dai, Y. (2018), 'Thermo-economic analysis and comparative study of transcritical power cycles using CO2-based mixtures as working fluids', *Applied Thermal Engineering* **144**, 31–44.

Yamaguchi, H., Zhang, X. R., Fujima, K., Enomoto, M. & Sawada, N. (2006), 'Solar energy powered Rankine cycle using supercritical CO2', *Applied Thermal Engineering* **26**(17-18), 2345–2354.

Yazdi, A., Najafloo, A. & Sakhaeinia, H. (2020), 'A method for thermodynamic modeling of H2S solubility using PC-SAFT equation of state based on a ternary solution of water, methyldiethanolamine and hydrogen sulfide', *Journal of Molecular Liquids* **299**.

Zangeneh-Kazemi, M., Dawes, W. N. & Hawthorne, W. R. (1988), 'Three dimensional flow in radial-inflow turbines', *Proceedings of the ASME Turbo Expo* **1**.

Zhang, H., Zhao, H., Deng, Q. & Feng, Z. (2015), 'Aerothermodynamic design and numerical investigation of supercritical carbon dioxide turbine', *Proceedings of the ASME Turbo Expo* **9**, 1–9.

Zhao, Q., Mecheri, M., Neveux, T., Privat, R. & Jaubert, J. N. (2017), 'Selection of a Proper Equation of State for the Modeling of a Supercritical CO2 Brayton Cycle: Consequences on the Process Design', *Industrial and Engineering Chemistry Research* **56**(23), 6841–6853.

Zhou, A., song Li, X., dong Ren, X., Song, J. & wei Gu, C. (2020), 'Thermodynamic and economic analysis of a supercritical carbon dioxide (SCO2) recompression cycle with the radial-inflow turbine efficiency prediction', *Energy* **191**, 116566.
URL: *https://doi.org/10.1016/j.energy.2019.116566*

Zhou, K., Wang, J., Xia, J., Guo, Y., Zhao, P. & Dai, Y. (2020), 'Design and performance analysis of a supercritical CO2 radial inflow turbine', *Applied Thermal Engineering* **167**(April 2019), 114757.
URL: *https://doi.org/10.1016/j.applthermaleng.2019.114757*

Appendices

Appendix A

Table A.1: Summary of turbomachinery parameters of existing sCO_2 cycle experimental facilities

Location	Facility	Layout	Type	Rated Power (kW)	$\dot{m}(kg/s)$	TIT (C)	Pressure Ratio	Speed (kRPM)	Turbine eff. (%)	Specific Speed	Bearings	Diameter (mm)
USA	SNL [31,32]	TAC (x2)	Radial	200	3.5	537	1.8	75	87	0.67	Gas foil journal	68.1
USA	KAPL [31,[32]	TAC (x1) TG (x1)	Radial	100	5.35	300	1.8	75	80	0.5	Gas foil journal	50.8
Japan	TIT (IAS) [31]	TAC (x1)	Radial	10	1.1	277	1.4	69	65	0.38	Gas foil journal	35
South Korea	KAIST (SCIEL) [31,32]	TAC (x1) TG (x1)	Radial	250	6.4	500	2.67	68 75	85	0.42 0.55	Magnetic bearings	n/a
South Korea	KIER [31,32]	TAC (x1)	Radial	12	3.04	180	1.64	70	84	0.51	Gas journal	48.6
		TG (x1)	Radial	1.0	0.07	200	2.28	200	n/a	n/a	Angular contact ball	22.6
		TAC (x1) TG (x1)	Axial	80	8	392	1.75	45	86.1	n/a	Tilting pad	73
USA	SwRI [32]	TG (x1)	Axial	1,000	8.4	715	2.9	27	>85	n/a	Tilting pad	n/a
USA	Echogen [1,12]	TAC (x1) TG (x1)	Radial	10,000	65-75	485	n/a	30	80	n/a	Tilting pad	n/a
Czech Republic	CVR [6]	TAC (x1)	Radial	7	0.65	200	1.5	50	74.8	0.20	Angular ball bearings	66

Table A.1 was based on information disclosed in the following references: Hacks et al. (2018), Liu et al. (2019), Cho et al. (2018), Clementoni et al. (2017).

Appendix B

The vapor-liquid-equilibrium curves presented here are those which were produced with the Peng-Robinson equation of state. The CO_2-based mixture corresponding to the experimental data in each figure, along with the binary interaction parameter

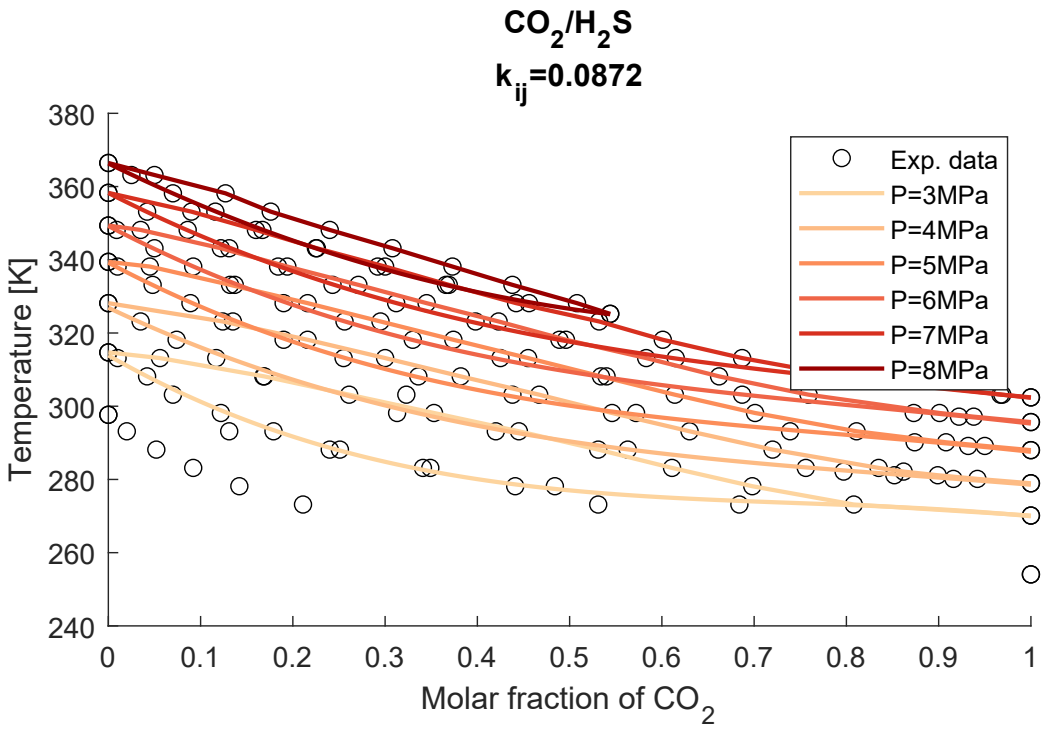

Figure B.1: Phase diagrams for the mixture CO_2/H_2S. Solid lines represent the results of PR EoS.

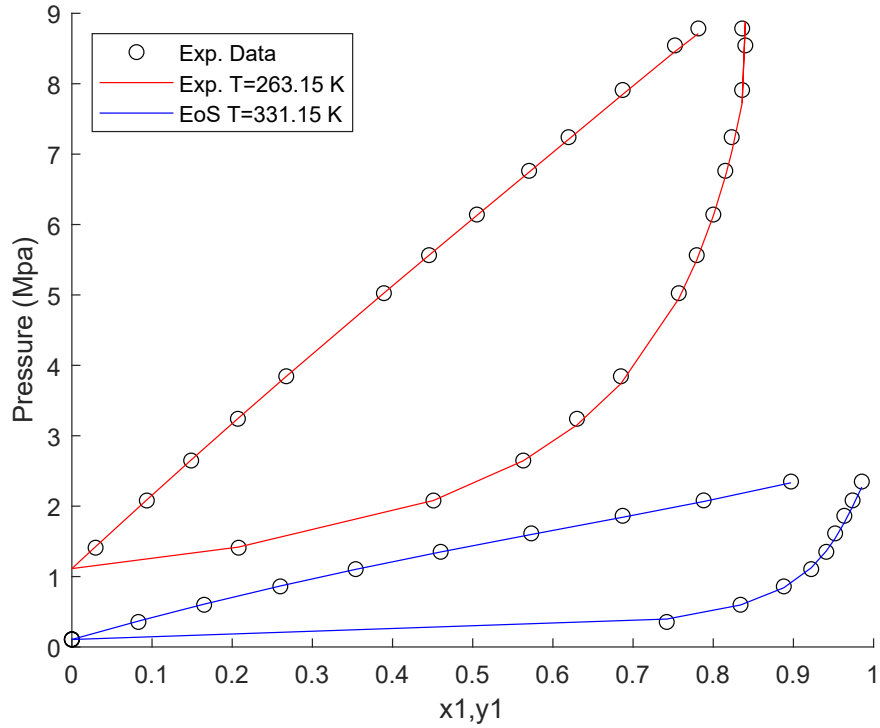

Figure B.2: Phase diagrams for the mixture CO_2/SO_2. Solid lines represent the results of PR EoS.

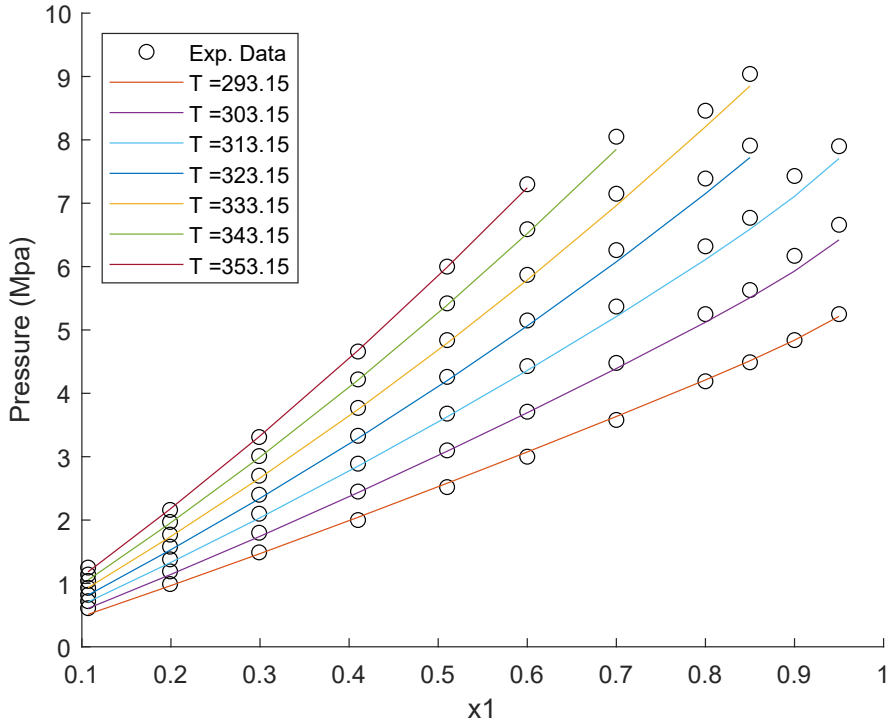

Figure B.3: Phase diagrams for the mixture CO_2/C_6F_6. Solid lines represent the results of PR EoS.

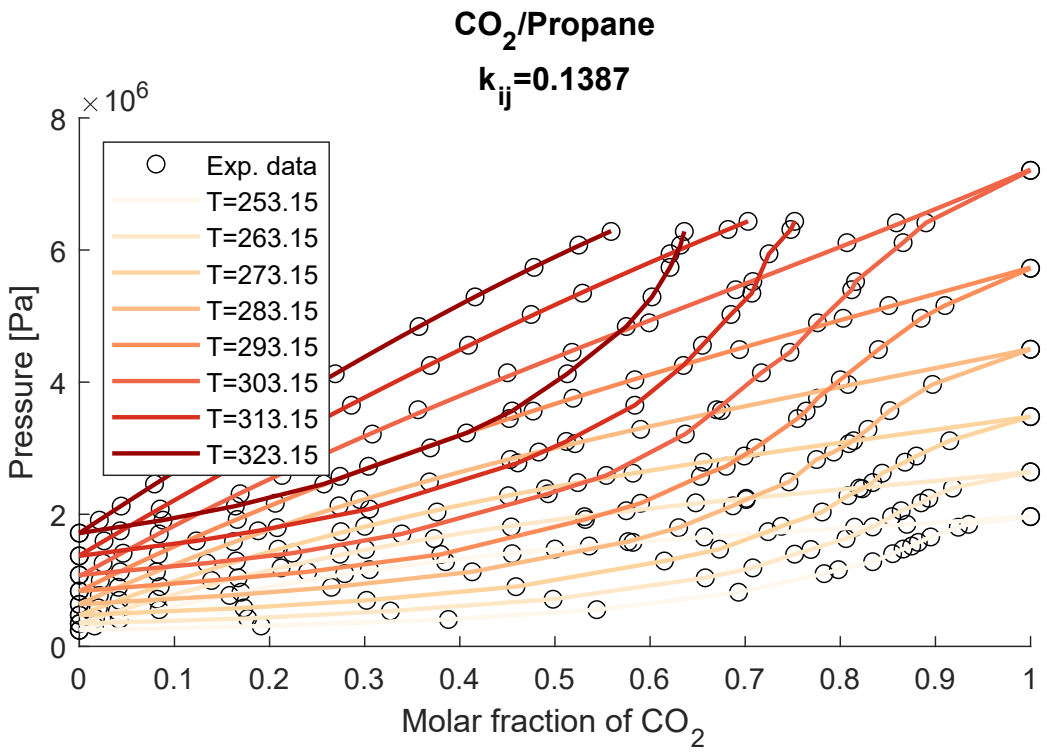

Figure B.4: Phase diagrams for the mixture CO_2/Propane. Solid lines represent the results of PR EoS

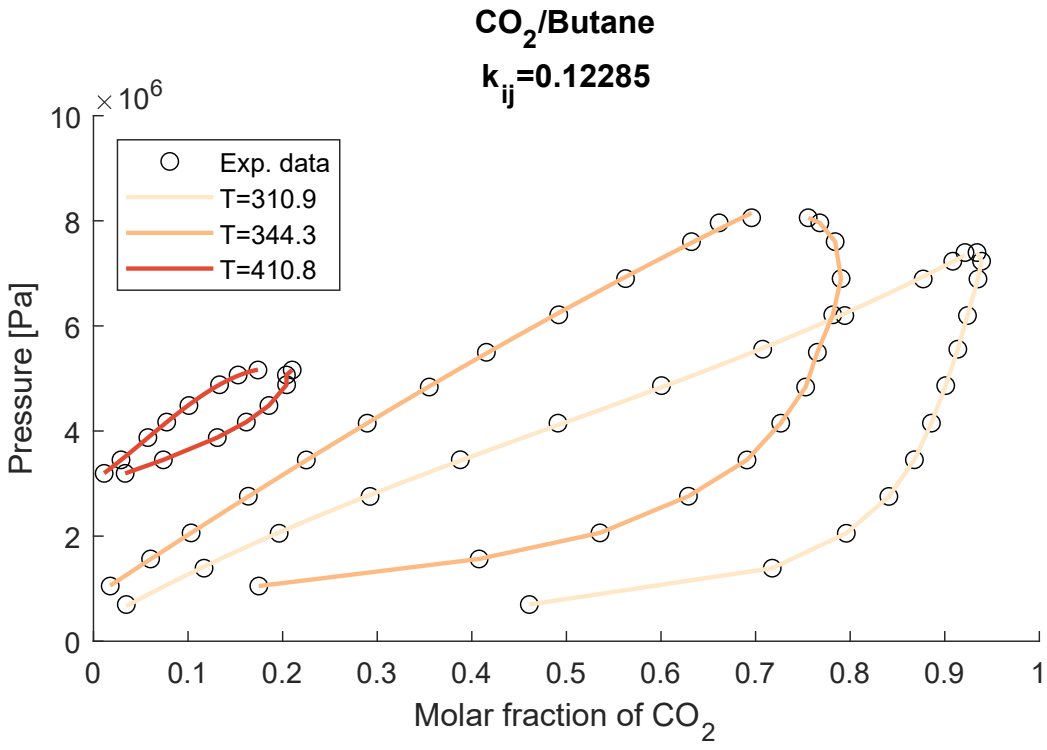

Figure B.5: Phase diagrams for the mixture CO_2/Butane. Solid lines represent the results of PR EoS

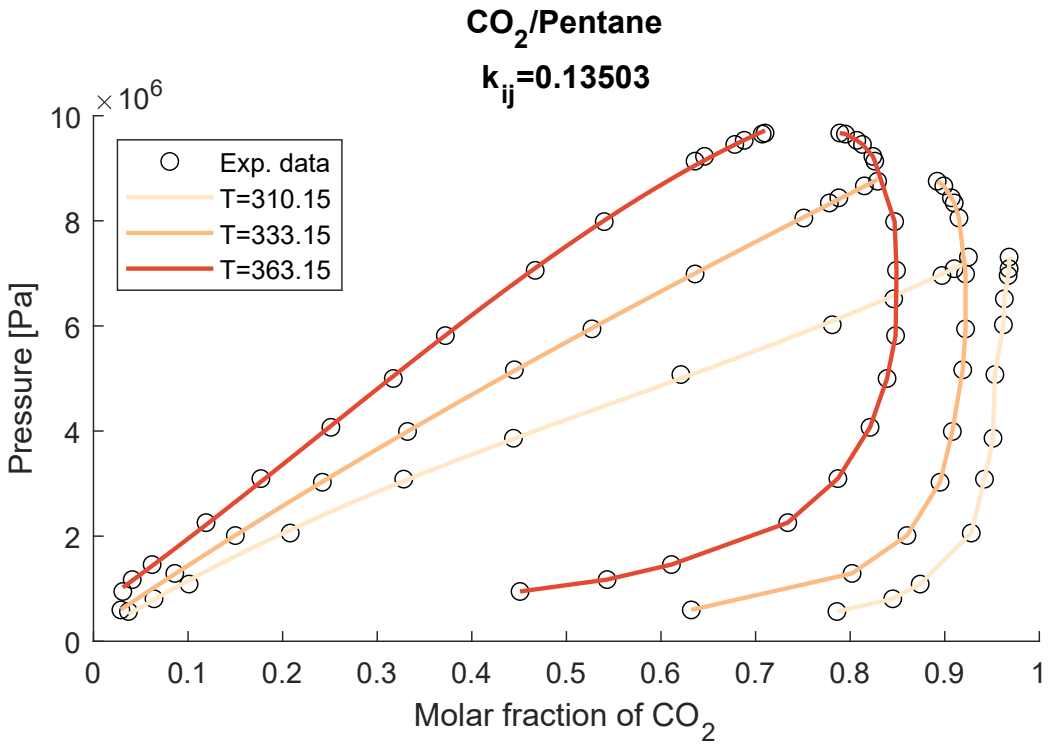

Figure B.6: Phase diagrams for the mixture CO_2/Pentane. Solid lines represent the results of PR EoS

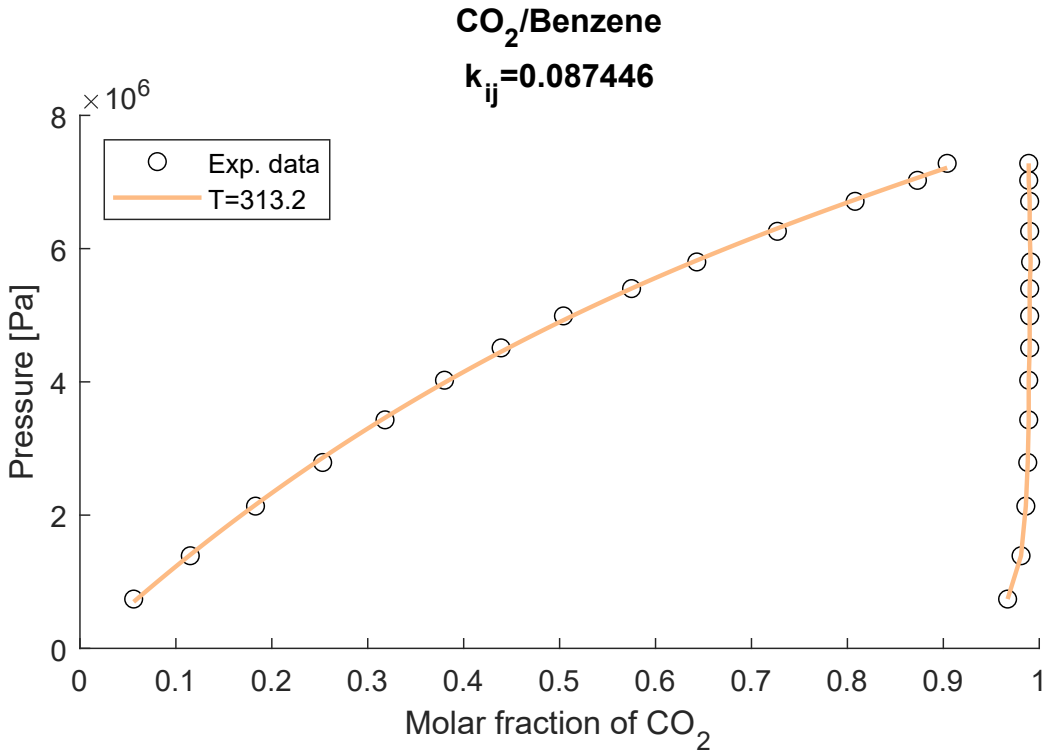

Figure B.7: Phase diagrams for the mixture CO_2/Benzene. Solid lines represent the results of PR EoS

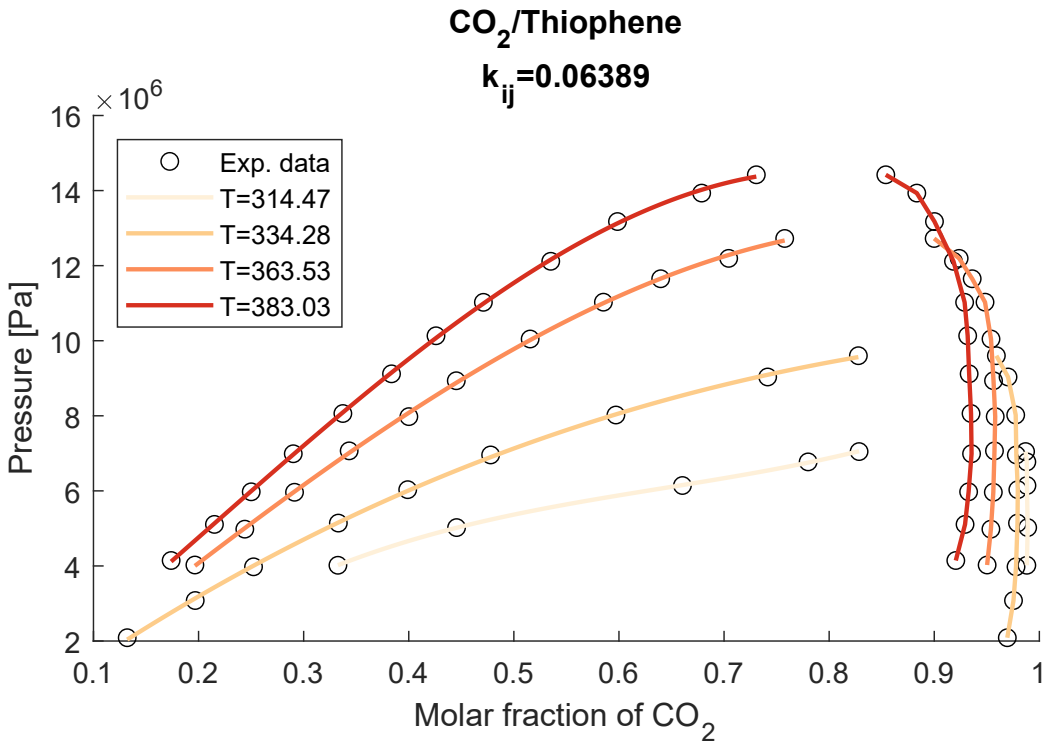

Figure B.8: Phase diagrams for the mixture CO_2/Thiophene. Solid lines represent the results of PR EoS